DE GRUYTER
OLDENBOURG

Jürgen Brillo

THERMOPHYSICAL PROPERTIES OF MULTICOMPONENT LIQUID ALLOYS

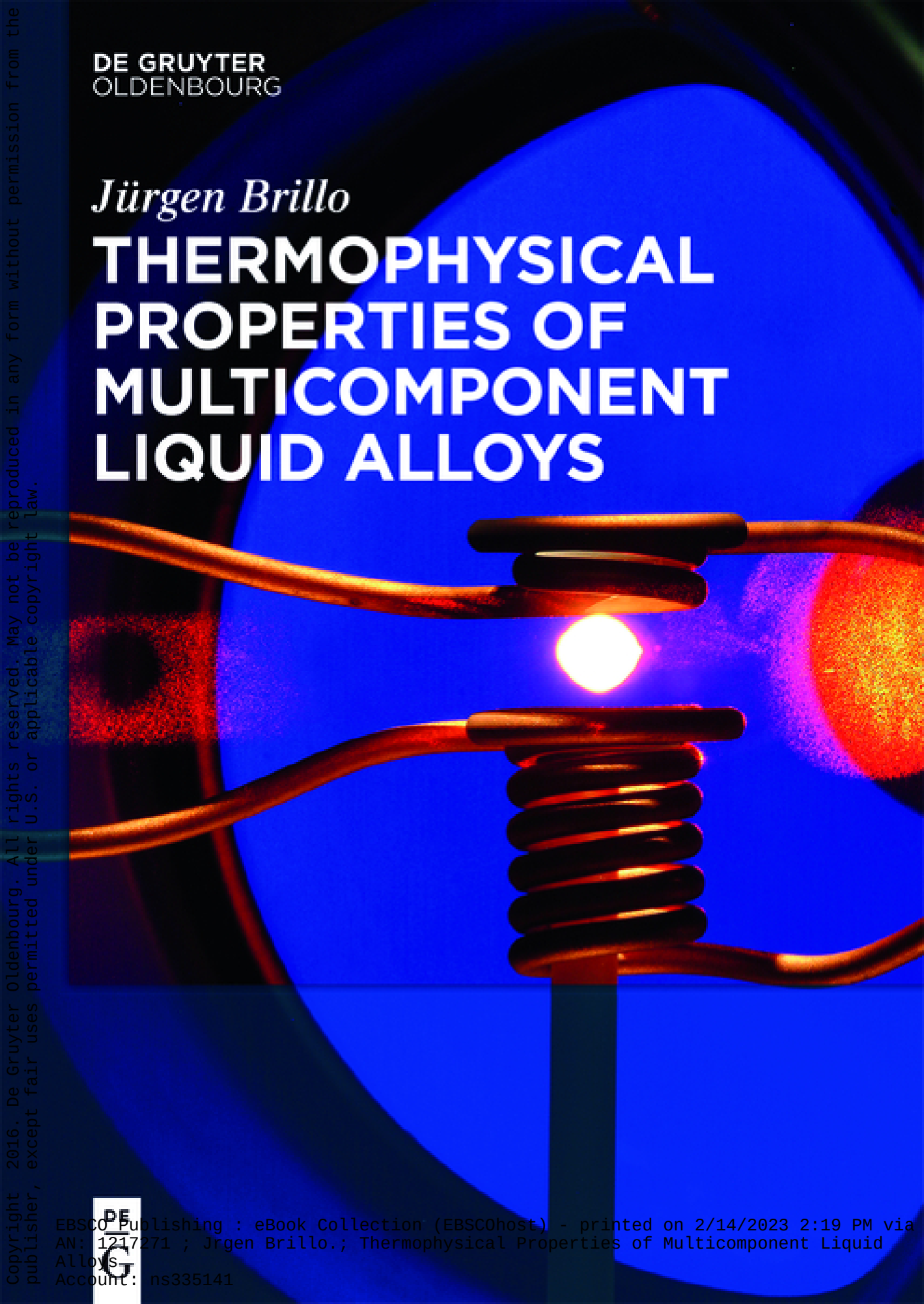

Jürgen Brillo

Thermophysical Properties of Multicomponent Liquid Alloys

Also of interest

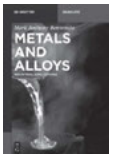

Alloys and Metals
Mark Anthony Benvenuto, 2016
ISBN 978-3-11-040784-6, e-ISBN 978-3-11-044185-7,
e-ISBN (EPUB) 978-3-11-043352-4

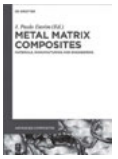

Metal Matrix Composites
J. Paulo Davim (Ed.), 2014
ISBN 978-3-11-031541-7, e-ISBN 978-3-11-031544-8,
e-ISBN (EPUB) 978-3-11-038201-3, Set-ISBN 978-3-11-031545-5

Machinability of Fibre-Reinforced Plastics
J. Paulo Davim (Ed.), 2015
ISBN 978-3-11-029222-0, e-ISBN 978-3-11-029225-1,
e-ISBN (EPUB) 978-3-11-038887-9, Set-ISBN 978-3-11-029226-8

High Temperature Materials and Processes
ed. by Hiroyuki Fukuyama
ISSN 2191-0324

Journal for Manufacturing Science and Production
ed. by Ramana G. Reddy
ISSN 2191-4184

Jürgen Brillo

Thermophysical Properties of Multicomponent Liquid Alloys

DE GRUYTER
OLDENBOURG

Author
Priv.-Doz. Dr. Jürgen Brillo
Institute of Materials Physics in Space
German Aerospace Center (DLR)
51170 Köln
Germany
Juergen.Brillo@dlr.de

ISBN 978-3-11-046684-3
e-ISBN (PDF) 978-3-11-046899-1
e-ISBN (EPUB) 978-3-11-046692-8
Set-ISBN 978-3-11-046900-4

Library of Congress Cataloging-in-Publication Data
A CIP catalog record for this book has been applied for at the Library of Congress.

Bibliographic information published by the Deutsche Nationalbibliothek
The Deutsche Nationalbibliothek lists this publication in the Deutsche Nationalbibliografie; detailed bibliographic data are available on the Internet at http://dnb.dnb.de.

Cover image: Institut für Materialphysik im Weltraum, Deutsches Zentrum für Luft- und Raumfahrt (eV)
Printing and binding: CPI books GmbH, Leck
♾Printed on acid-free paper
Printed in Germany

www.degruyter.com

to my father†

Acknowledgement

I wish to acknowledge the support this work received from various persons and institutions:

First of all, I would like to thank Prof. Dr. Andreas Meyer, director of the Institute of Materials Physics in Space of the German Aerospace Center (DLR), for granting me the opportunity to perform this work. I also wish to thank Prof. Dr. Florian Kargl who read this booklet from its beginning to the end and who provided me with useful comments.

Equally well, I acknowledge the attendance and support I received from Prof. Dr. Andreas Bührig-Polaczek, head of the Foundry Institute of the RWTH-Aachen University, and the stimulating discussions I had with him.

This work would simply not exist without the initial spark lit by Prof. Dr. Ivan Egry in 2002. I'm also grateful to my other colleagues from DLR. In particular, I wish to mention the members of the workshop as well as Frau Astrid Bölt and Frau Regina Kraus from the library.

My greatest credit, however, is due to my co-authors with whom I truly enjoyed working together. Although I cannot name any of them personally here, I wish to mention that this work would not have been possible in its current form without the contributions they made over all the years.

Last, but not least, I acknowledge financial support from the following agencies: German Science Foundation (DFG), Department of Education and Research (BMBF), European Space Association (ESA), German Academic Exchange Service (DAAD) and ERASMUS foundation.

Contents

1 Introduction

The casting of metals and the continuous improvement of materials and their production and development processes are crucial for a society from an economic, social, and cultural point of view. As available computer power and numerical algorithms have drastically improved during the past 30 years, computer aided material design is limited by the accuracy of available material property data serving as input parameters. Current approaches seek to establish comprehensive material databases in order to solve this problem. The present work aims, as an alternative, to gain a basic understanding on how thermophysical properties change as a function of alloy composition and complexity. In order to reach this goal, data needs to be collected on density, surface tension and viscosity as functions of alloy composition and temperature. Such data is measured and discussed for pure liquid elements, liquid binary-, and ternary alloys.

1.1 New materials

Throughout the history of human culture, the development and application of new materials, in particular metals, have played crucial roles. New materials are responsible for such Epochs as “stone-age”, “bronze-age”and “iron-age”, marking the great phases in cultural evolution. For instance, gold is the first metal used on a regular basis since 6000 BC. Nearly 2000 years later, copper and silver were discovered and mined. After another 1800 years the mining of tin and the production of bronze started a new social, cultural, and economic era [1].

Gaining a technological advantage distinguishes between the rise and fall of entire civilizations. The ancient Egyptian empire became mighty due to the availability of weapons made from copper. Later on, the manufacture of improved iron weapons made the Romans become superior over their neighbors.

Still nowadays, the development of a society strongly correlates with the degree of maturity of its metal producing sector and other key industries. Developing countries, therefore, aim to build up these industries first. In Europe, the industrial revolution went hand-in-hand with the development, production and improvement of new metallic alloys such as cast iron, steel and brass. In 1860 more than 60 % of all globally produced metal ores came from European mines [2].

Due to its rapid economic growth, China, at present, has become the world’s largest steel producer, measured in tons per year, the world’s largest steel consumer, steel exporter, and iron ore importer [2]. At the same time, China is the third largest iron ore producer and the third largest steel importer [2]. Figure 1.1 shows the share of the world largest countries in casting production. Among them, China as the largest producer, covering 43 % [3].

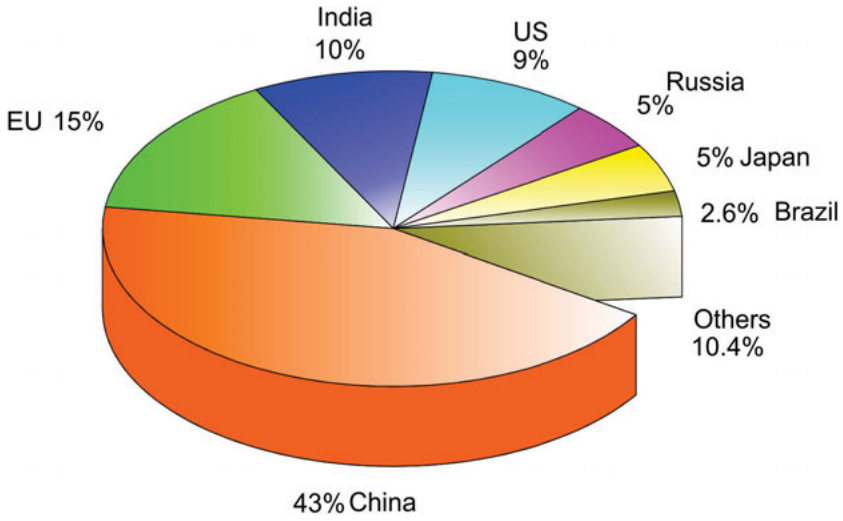

Fig. 1.1. Leading countries in the world casting production [3].

The vast majority of metals produced is gray iron, followed by ductile iron, non-ferrous metals, and steels [3]. Among the non-ferrous metals, alumunium based alloys occupy the largest share [3]. The production volume from casting is shown in Tab. 1.1.

Classically, metals and metallic alloys are used in the automotive industry, in aerospace- and military applications, in railway applications, civil engineering, shipbuilding, cutlery, wire products, for bridges, jewelry, toolmaking, mechanical and technical engineering, for the production of cans, and for electromechanical applications. Market composition is shown in Fig. 1.2. Applications in automotive industry demand almost 50 % of cast metals in Europe [3; 4]. The engineering industry consumes 30 % of the cast metals and building and construction works demand 10 % [3].In Europe, the metals and metal products manufacturing sector is the largest among the industrial economic sectors [4].

Throughout the member states, there are about 400,000 enterprises with ≈ 5 million employees, corresponding to almost 4 % of the productive work force [4].

Within this sector, the foundry industry is an economic branch of key importance. In terms of turnover, value added and number of employees, the foundry sub-sector corresponds to about 5 % [4]. The German foundry industry generated a turnover of 12.8 billion EUR with 71,500 employees in 2013 [5].

As the vast majority of metals and alloys are produced directly from the melt, casting is crucial for the entire manufacturing of metals and their products.

Hence, from an economic point of view, optimization of casting processes is of tremendous importance. The basic physical understanding of the liquid phase is indispensable for this purpose. The liquid phase is also involved in certain metal works

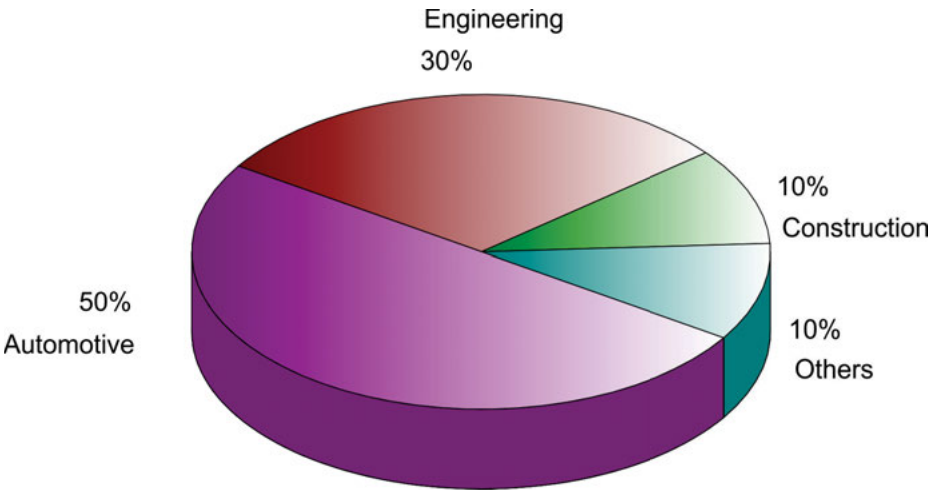

Fig. 1.2. Main markets served by the European foundry industry [3].

Table 1.1. Casting production volume of metals in the categories gray iron, ductile iron, steel, and nonferrous (NF) metals. Shown are the production numbers of the 10 largest producing countries in 2010 [3].

Product	Volume (1000 t)
Grey Iron	38 723
Ductile Iron	20 560
Steel	8 998
NF metals	11 748

operation steps, such as welding, soldering, and joining. Liquid metals also seem to become more and more important for the storage and transportation of energy, for example, in automotive applications for recovering heat from exhaust fumes [4].

Developed (western) countries are now facing new challenges: As cheap labor power and low fixed costs cause a shift of production to Asia, western steel and metal plants are no longer running at full capacity [6; 7]. At the same time, issues of energy effectiveness, CO_2 reduction, the saving of resources, sustainability and productivity become urgent [6].

In order to save resources of naturally available metals, new techniques of scrap recycling need to be developed. Parts of the metals and metal products manufacturing sector are highly energy consumptive. Energy costs for metals and their products accounted in 2006 for 4.4 % of the purchase of goods and services in the European Union. With respect to the casting sector only, this figure is nearly twice as high (7.2 %). Again, this puts a special focus on the liquid phase from a developers point of view [4; 6].

While low production costs serve as an advantage for developing countries, developed, i.e. western, countries can play on their technological and scientific infrastructure. The high education standard in Europe, in particular, of engineers and scientists, is a great advantage compared to low cost developing countries.

European commission has recognized this situation and proposed a number of possible measures [4]. Among which, the development of new specialized products, i.e. high-tech materials, as well as the development of new production processes for the casting industry, play emphasized roles. As an example for new, specialized products, alloys with certain properties, such as low density and high tensile ductility are used for aerospace applications. The development of new techniques of scrap recycling, and/or casting processes, could tremendously save resources and energy [4] which significantly contributes to CO_2-reduction, the increase of productivity and competitiveness.

The future development of new materials and new casting processes is essential for economic, technological, environmentalenvironmental progress, and social progress.

1.2 Materials and process design

Estimated costs of new product development and demonstration in the European steel industry are around 55–75 billion EUR yearly [4].

One reason for such a large sum is that alloys intended for certain applications are developed in trial-and-error procedures where compositions and/or production processes are varied until the desired properties are obtained. In view of the fact, that most alloys used in technical applications are multicomponent, it becomes clear that this kind of development is highly time and money consuming.

"Computer Aided Materials Design from the Melt" might offer an alternative. During the past 20–30 years, computer power and algorithms, have drastically improved. Commercial software tools like ProCAST™, MAGMASOFT™, StarCAST™ [8], MICRESS™, DICTRA™, PANDAT™, FactSage™, ThermoCalc™, just to name a few, have become standard in industrial casting simulation and materials development.

ProCAST™, MAGMASOFT™, and StarCAST™ are based on finite element methods (FEM) combined with an engine for the simulation of fluid flow, and partially with models about heat exchange and diffusion. They are used in order to simulate the casting process and the thermal and mechanical performance of the product on a macroscopic scale. DICTRA™ is a tool for the 1-dimensional modelling of diffusion in multiphase systems. Packages like MICRESS™ employ the phase field method. This method allows simulation of processes and structures on a microscopic (μm-) scale. For instance, the morphology of dendrites can be predicted.

In this context, one often speaks of a *multi scale approach*. The atomic scale, hereby, can be covered by molecular dynamics (MD) simulations, Monte Carlo (MC)

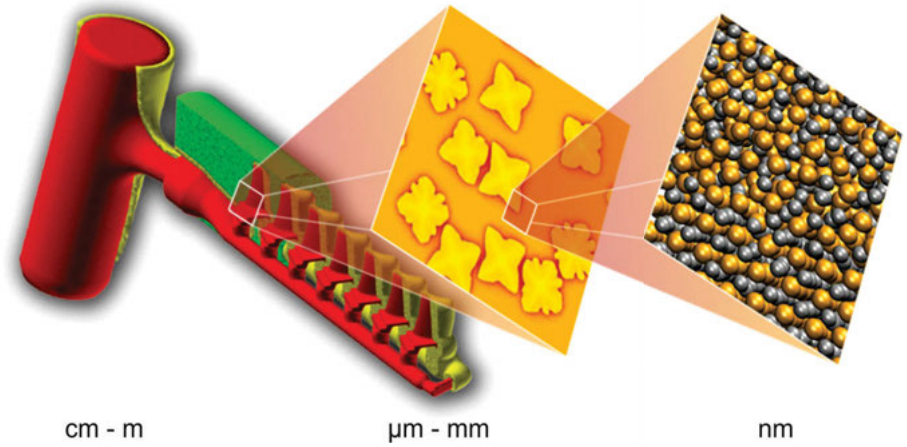

Fig. 1.3. "Computer Aided Materials Design from the Melt" is a multi scale business. Simulations are performed on an atomic (nm) scale, on a micro-meter scale, where dendrites and grains can be observed, and on the macroscopic scale of the dimensions of the work piece.

simulations, or quantum mechanical ab initio methods. The relation between the different length scales is illustrated schematically in Fig. 1.3.

The philosophy behind products like PANDAT™, FactSage™, and ThermoCalc™ is slightly different from the multi scale approach. Instead of simulating structures with spatial resolution, these packages calculate phase equilibria using the CALPHAD method. In the CALPHAD method, each phase is represented by parameterizations of the corresponding free energies, G, which are obtained from assessments of experimental phase diagram and thermodynamic data. Macroscopic properties of a single phase material can further be derived via a suitable model from its free energy, provided, such a model exists. For instance, if G was known as function of pressure, P, the molar volume can be obtained from $\partial G/\partial P$.

Recently, it has been demonstrated that CALPHAD and phase field methods can successfully be joined [9].

Currently, all these tools require information about thermophysical properties. The main limiting factor for the accuracy of the calculations is, in fact, the accuracy of the experimentally measured input data. In many cases, this data are not even available. Unfortunately, this is especially true in the case of liquid metals. As the liquid phase is involved in all casting simulations, this problem is severe.

The computer aided materials design from the melt is still an ideal conception and there are currently different approaches working towards its full implementation. Two of these approaches will be described in the following.

1.3 Challenges

As one approach for the implementation of a computer aided materials design from the melt, it has become customary to experimentally determine a maximum of macroscopic properties of materials of interest and store them into databases. Such a database is then accessed by the simulation software. Projects aiming to establish material property databases currently receive generous funding from the public and private sector.

For instance, the comprehensive measurement of thermophysical properties of different commercial alloys is the main goal of the ESA funded project THERMOLAB [10]. Beside ground based, terrestrial experiments, it is also planned in this project to carry out containerless measurements under microgravity conditions on board the International Space Station ISS. Alloys of interest are Ni-based superalloys, Ti-based, Fe-based, and Cu-based alloys for aerospace, biomedical, automotive, and electronical (soldering) applications, respectively. The THERMOLAB project is carried out under participation of DLR. Among the partners there are roughly 20 industrial ones from foundry to simulation software developing companies.

However, this concept has also an inherent disadvantage: Namely that the properties of an alloy and it's involved phases must be known in advance. The development of new materials with a priori unknown properties and their prediction is not advanced this way. The initial problem, thus, still remains.

Moreover, progress in predicting required property data from modeling suffers currently from a severe lack of systematic experimental data of liquid alloys. The word "systematic", hereby, implies that even benchmark data on simple model systems, i.e. binary or ternary alloys, are missing.

At least for mono-atomic alloys, some thermophysical property data exists. Data collections like Refs. [11]–[13], and [14] provide data on density, ultra sound velocity, vapor pressure, viscosity, surface tension, electrical resistivity, and thermal conductivity for a large set of liquid metallic elements. However, even in the case of pure elements, the currently available information is incomplete or outdated. The viscosity of liquid gold may serve as an example: The most recent data is from 1956 deviating from a previous measurement by more than 30 % and from our very recent data by more than 100 % [15]. In other cases, plenty of results are available. However, they partially contradict each other. The surface tension of liquid Si may serve as another prominent example: Two classes of data sets exist in literature [16]. One indicating a "small" value of the surface tension around 0.75 Nm^{-1} at the liquidus and another one is in agreement with a rather "large" value of ≈0.84 Nm^{-1}. The uncontrolled presence of surface impurities seems to be the main cause for this non-unique behavior [16]. In view of the significant industrial importance of Si, a final clarification is overdue.

The composition in binary alloys can also be varied. This leads to the expansion of a 2D parameter space with an additional degree of freedom. At least, in the majority of systems, information about their thermodynamics exist; like a known phase diagram

and determined heats and free energies of mixing. Information about thermophysical properties is significantly sparse. When this work first began in 2002, little data existed on density and even less on viscosity. The situation can be illustrated by the following: Ref. [11] reports density data of ≈ 80 binary liquid alloys out of roughly 350 binary systems that are listed. For only 20 out of these 350 systems, surface tension data is known. A similar situation is evident from other data references, such as Ref. [13].

Information about liquid ternary systems is even more limited, i.e. systematic data is available only in exceptional cases. Not only that thermophysical property data is missing in most cases, also thermodynamic information, such as phase diagram and heat of mixing, does not exist.

Due to this lack of systematic experimental thermophysical property data, it is also not possible to validate existing models predicting them. These include computer simulation techniques using specific model potentials, ab initio methods, and phenomenological as well as semi-empirical models. Such models exist, for instance, in the case of surface tension and viscosity. They will be introduced and discussed further below. For the prediction of density, no thermodynamic relation exists up to now. The current knowledge of how thermophysical properties of liquid alloys change as a function of their composition, i.e. of the corresponding mixing relations, is still very incomplete.

Generally, accurate experimental thermophysical property data is hard to obtain. The main reason is due to the increased chemical reactivity of liquid metals, especially at high temperature. Due to reactions with the container, the sample might become contaminated and the results of the measurements become uncertain. The development of containerless processing techniques, such as electromagnetic levitation and corresponding diagnostical techniques, have relaxed the situation slightly [18; 19].

In the case of density, the problem is underestimated or not fully recognized. For instance, it is claimed in Ref. [20] that, because atomic hard sphere radii are almost equal for most metals, the excess volume may be neglected. Consequently, it should be possible to approximate the density of a liquid alloy by the one of its ideal solution.

The example of liquid binary Cu-Ni demonstrates that this is not true even though this system is fully miscible and the atomic radii are nearly identical (see Tab. 3.11). Figure 1.4 shows the isothermal densities ρ of the system as a function of the Ni mole fraction x_{Ni}. The values are hereby interpolated - or extrapolated - from regression lines, fit for each alloy to the temperature dependend raw data $\rho(T)$, to $T = 1545$ K.

In addition, densities calculated from the ideal solution model, Eq. (3.15), are shown. Obviously, the latter underestimates the experimental data significantly and there is also a pronounced qualitative disagreement. Thus, even in the case of a putatively simple system, the mixing behavior is not understood in detail.

Multicomponent alloys exhibit a much higher degree of complexity. Before these systems can reasonably be studied, it is necessary to understand the much simpler and more well defined binary and ternary systems first.

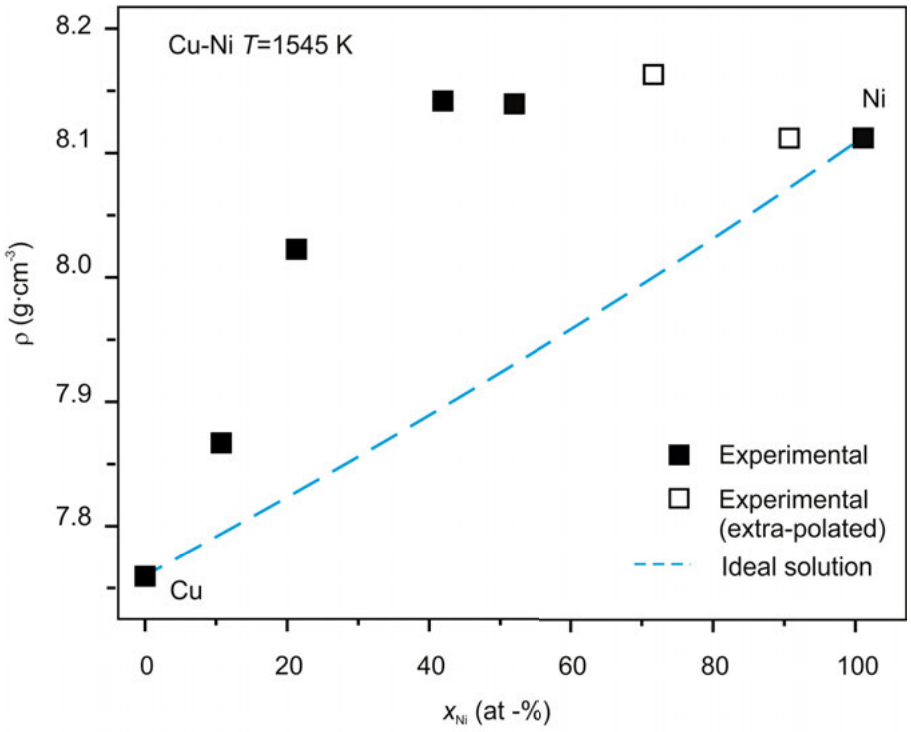

Fig. 1.4. Density of liquid Cu-Ni versus Ni-mole fraction x_{Ni} (symbols). The data are interpolated (solid) or extrapolated (hollow) from the measured raw data to 1545 K. Some of the liquid alloys are undercooled. In addition the ideal solution model (dashed) is shown [17].

1.4 Goals

In addition to the establishment of comprehensive databases of complex alloys and materials, the second approach for the implementation of computer aided materials design from the melt consists of the systematic investigation of binary and ternary model systems. It is aimed to create a general understanding of the mixing behavior of liquid alloys with respect to their thermophysical properties. This concept will be pursued in the present work. For instance, Fig. 1.5 compares various commercial (multicomponent) alloys having Al-Ni as a binary basis. All of these alloys are liquid at 1773 K. Their density at this temperature is shown in Fig. 1.5 as a function of (1.0-x_{Al}) with x_{Al} being the Al-mole fraction. Apparently, there is a weak tendency of the values to increase with decreasing x_{Al}. The same figure shows calculated densities of binary Al-Ni obtained from Ref. [21]. These calculations are performed once for the ideal solution and once while including a term for the excess volume determined experimentally [21]. Both calculations reproduced the trend observed for the commercial systems: namely that their densities increase with decreasing x_{Al}. The overall better

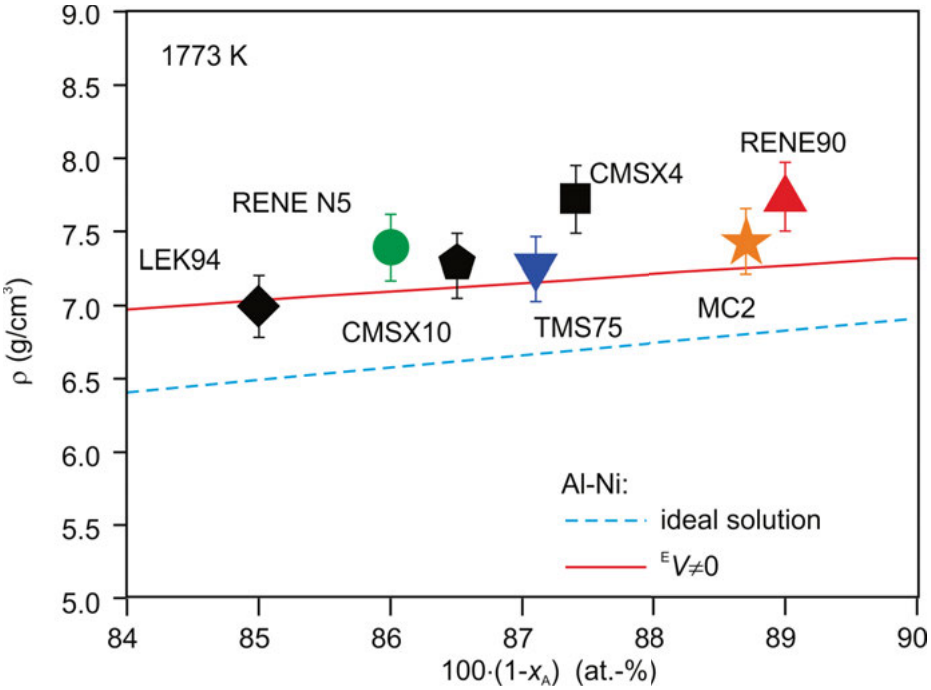

Fig. 1.5. Density of various Al-Ni based multicomponent liquid alloys at 1773 K versus (100 at.-% -x_{Al}). In addition, calculations [21] of the density of binary Al-Ni are shown taking the ideal solution model (dashed) and a model involving the excess volume into account (solid). (with courtesy of Enrica Ricci, CNR, Genua).

correlation between the data and the calculation is obtained when the excess volume is included. Hence, within limits and apart from the systems CMSX4 and RENE90, the densities of the multicomponent alloys in Fig. 1.5 can be approximated by their binary basis, if the excess volume of the latter is included. This implies that an understanding of Al-Ni, as in this example, would also contribute to an understanding of the Ni-based multicomponent alloys.

It is the primary goal of the present work to principally establish such an understanding by systematically studying thermophysical properties of binary and ternary liquid alloys with respect to their mixing behavior. Measuring thermophysical properties as a function of temperature and alloy composition varied over a broad range allows the drawing of conclusions on excess properties and identifying potentially existing commonalities among them. This is the prerequisite of any phenomenological model or simulation.

A secondary goal pursued within the scope of this work consists of reducing the existing lack of available experimental data by accurately measuring them.

1.5 Questions

In order to reach the goals formulated in the previous section, the following key questions must be answered:

Q:1. Is there any general rule for predicting the mixing behavior? Moreover, are there commonalities with respect to the mixing behavior among similar materials?

Answering this question could already contribute substantially to the development of simple and easy-to-implement models. As a special case of question **Q:1**, one may also ask the following:

Q:2. Is it possible to establish relations between excess thermophysical properties and thermodynamic potentials? If such relations exist, how well will they perform?

Provided the answers to questions **Q:1** and **Q:2** are negative, the measured excess properties need to be accepted as a given. One could then try to use these excess properties in order to predict those of higher component systems. For this purpose, the following question must be answered as a necessary pre-condition:

Q:3. Is it possible to relate thermophysical properties of a multicomponent alloy to those of its constituent subsystems?

The first three questions imply that different properties of the same material can be derived from a common basis, as for instance, free energy. It is also a commonly accepted statement in literature that, generally, macroscopic properties of one material are determined by it's "structure". In the case of a melt, this refers to the atomic short range order. If this is true, then it should be possible to relate different properties of a specific material to each other. Hence:

Q:4. Is it possible to identify inter-property relations in selected cases? If yes, what are their forms and how well do they perform?

1.6 Strategy and procedure

In order to answer these questions, a strategy, described in the following, is chosen. The works concentrate on density, surface tension and viscosity as key properties.

Density is a fundamental property that plays a central role in materials science. Its precise knowledge is necessary, not only for the experimental determination of other thermophysical properties from the measured raw data. It is also crucial for the layout of technical processes, such as casting. Last, but not least, density is also interesting from a pure academic point of view due to its intimate relation to the atomic short range order.

Surface tension is firstly selected, because it plays a central role in technical applications which are driven by surface and interfacial free energies. Such an application

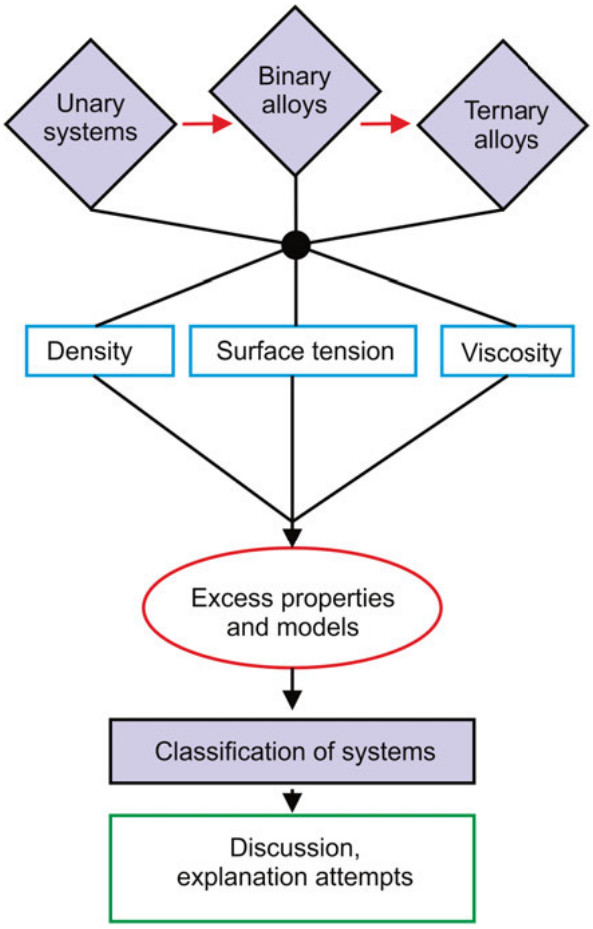

Fig. 1.6. Strategic flow chart of the present work.

is welding, for instance. With regards to casting applications, surface tension data is needed in the context of mould filling.

Lastly, viscosity, is needed for the description of mass and heat transport in applications where fluid flow needs to be considered. "Buoyancy driven convection" is the buzz-word in this context. Currently, viscosity is an intensively studied property in order to obtain an understanding of systems with glass-forming ability [22].

These key properties are subsequently measured through liquid unary, binary, and ternary metallic alloys as functions of temperature and alloy composition.

The data of the pure components is hereby determined with great care. It is crucially required in order to apply mixing rules to the results of binary and ternary alloys.

In addition, data obtained of the pure components is carefully compared with results from literature, provided that the latter exist.

After completion of the works on pure elements, density, surface tension and viscosity are measured on binary systems combined from the unary ones studied before. Subsequently, excess properties are determined. In the case of surface tension and viscosity, various thermodynamic relations will be tested and discussed.

Finally, the same measurements are carried out on a number of ternary alloys containing the binary alloys investigated before as subsystems. Excess properties are determined and, in the cases of surface tension and viscosity, phenomenological models are tested.

The results obtained for the binary and ternary systems are then compared with each other. In some cases, it is possible to relate the excess properties of the ternary alloys directly to those of the binary systems.

The systems investigated are classified according to their composition and miscibility, helping to identify potentially existing similarities among them. The procedure described above is illustrated by the flow chart of Fig. 1.6.

As for identical systems, where different properties are measured, it is possible to study inter-property relations in Chap. 6. Here, it lends itself to the discussion of a predicted relation between surface tension and viscosity [23]–[24]. Moreover, the Stokes-Einstein relation [25; 26] is discussed in Chap. 6.

Chapter 7, finally, presents results on topics related to the main topic of this work but with a strong emphasis on application. Apart from showing "things that also exist", it is analysed from A to Z how the establishment of a complete and accurate set of thermophysical property data can improve "process design" in a specific example. Generally, representations of the discussed density-, surface tension-, and viscosity data are listed in Appendix A. Used parameterizations of the excess free energy are listed in Appendix B.

1.7 Thermophysical properties

The term thermophysical properties is not uniformly defined. The syllable "thermo" is the Greek word for heat and "thermophyiscal properties" can be considered as physical properties that change with temperature. It appears to be common agreement that "thermophysical properties" are all those properties that describe the macroscopic, thermal and physical behavior of a substance. Generally, this behavior could be "mechanical", "optical", "electrical", "magnetical", and "calorical".

In fact, thermophysical properties are defined only for a homogeneous, i.e. single phase system, which is in thermodynamic equilibrium. Often, they are related to the transport and storage of heat or to general transport processes. Indeed, most thermophysical properties can be interpreted as response functions, L_k, describing the

systems response, J_k, to an externally applied force X_k:

$$J_k = L_k X_k \tag{1.1}$$

Hereby, J_k is the current of a physical scalar quantity k and X_k denotes its gradient. For example, the following thermophysical properties fall under this definition: emissivity, specific heat capacity, thermal or electrical conductivity, thermal expansion, viscosity, mass and thermal diffusion, and speed of sound.

In addition, density,[1] surface tension, and interfacial energy are considered thermophysical properties, as well.

Enthalpy, internal energy, entropy, and free energy are not considered as thermophysical properties in this work as there are fundamental thermodynamic relations between these thermodynamic potentials and several thermophysical properties.

Apart from the field of materials and process design, thermophysical properties play key roles in many different applications. Prominent examples are metrology, nuclear technology, thermal insulation, quality assurance and the deep-freezing of food.

In metrology, thermophysical properties play key roles for the development of standards for the calibration of instruments and the definition of physical constants.

Fuel rods in nuclear reactors exhibit extremely large thermal gradients. Inside, a fuel rod can reach temperatures of nearly 2300 K depending on the material, whereas its outside temperature is only roughly 700 K. The exact knowledge of thermal transport properties, specific heat and the thermal expansion, in particular as functions of temperature, is crucial in such applications.

1 or, equivalent, molar volume

2 Experimental methods

In this chapter, the experimental techniques used in this work are presented. The containerless techniques of electromagnetic and electrostatic levitation are described in detail as well as the diagnostic methods for the measurement of density, surface tension, and viscosity. In addition, the containerbased oscillating cup method for the measurement of viscosity is explained.

2.1 Conventional techniques

Conventional techniques for the measurement of thermophysical properties of liquids are containerbased. This means that the liquid is in contact with a crucible or a substrate. Prominent techniques are, for instance: archimedian methods, bubble pressure methods, capillary flow, capillary rise-, gamma ray absorption technique, oscillating cup methods, pycnometer method, sessile drop method, and the vibrating wire technique.

A comprehensive overview of these methods and their detailed descriptions is given in Ref. [27]. Moreover, they are listed Tab. 2.1 together with the properties that can be measured by them.

Table 2.1. Some conventional techniques for the measurement of thermophysical properties of liquids [27].

Conventional technique	Property
Archimedian methods	density
Bubble pressure	density, surface tension
Capillary flow	viscosity
Capillary rise	surface tension, interfacial energy
γ-ray absorption	density
Oscillating cup	viscosity
Pycnometer method	density
Sessile drop technique	density, surface tension, interfacial energies
Vibrating wire	viscosity

2.2 Levitation techniques

The techniques mentioned in Sec. 2.1 are standard for the investigation of liquids at low temperature. They are also applied to liquid metals, although the investigation of liquid metals often involves processing at high temperatures. Under these conditions, the chemical reactivity of a melt may be strongly increased and the sample is easily contaminated from coming in contact with a wall. In a containerbased environment, an accurate measurement of thermophysical properties is possible only under great care. Finding the right substrate or crucible and the right settings of the process parameters is often a tedious and time consuming task. One may also come to the conclusion that carrying out the desired measurement is not possible at all.

As an alternative, containerless investigation techniques using levitation [28; 29] circumvent this problem. For extremely reactive materials, such as Ti- or Zr- based alloys, they are in fact the only option. The use of levitation techniques offers the additional advantage that, due to the absence of heterogeneous nucleation sites, deep undercoolings can be reached. Processes like non-equilibrium solidification [30] or metastable demixing [31] can therefore be studied.

The most prominent and, in the context of this work, most relevant techniques are electrostatic and electromagnetic levitation. All of which have specific advantages and disadvantages, so that they are used in separate fields of application.

In the present work, electromagnetic levitation (EML) is mainly used. An experiment using electrostatic levitation (ESL) is performed in one case [32]. Therefore, the ESL technique will be described briefly while the EML technique will be elaborated upon in more detail.

2.2.1 Electromagnetic levitation

The principle of electromagnetic levitation was first described in 1954 in a patent by Westinghouse [33]. The technique was then widely known as “levitation melting” and mostly applied as a preparation technique for the manufacturing of alloys [18]. With an increase of opportunities to perform materials science experiments under microgravity during the 1980’s, this attitude shifted and the electromagnetic levitation technique was also recognized as a containerless processing technique for scientific investigations [34].

The principle of electromagnetic levitation is based on the fact that an electrically conducting material experiences a Lorentz force, $\vec{F_L}$, when the magnetic flux changes with time. For an electrically conducting body $\vec{F_L}$ is given by the following expression [18]:

$$\vec{F_L} = -\frac{\nabla \vec{B}^2}{2\mu_0}\frac{4\pi}{3}R^3 Q_{\mathrm{EML}}(q_{\mathrm{EML}}) \tag{2.1}$$

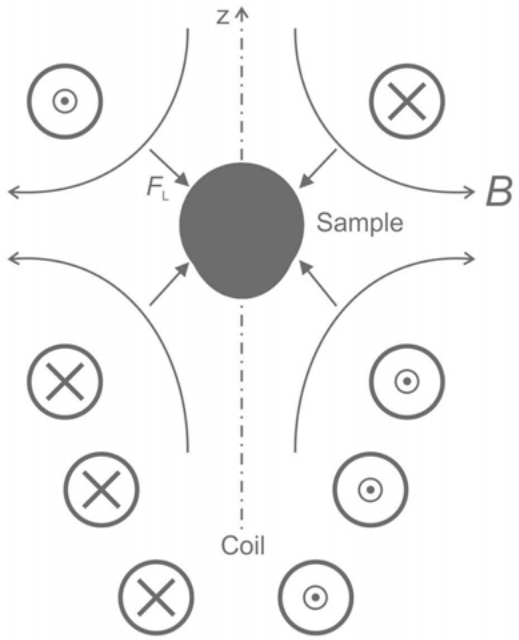

Fig. 2.1. Sketch of a levitation coil with levitating sample. The forces acting on the sample point into the direction of $-\nabla\vec{B}^2$, i.e. away from areas with high field densities.

Here, μ_0 is the magnetic permeability, R is the radius of the sample with approximated spherical shape, $q_{\mathrm{EML}} = R/\delta$ is a dimensionless quantity and δ is the penetration depth of the field $\vec{B}$ depending on the frequency ω and the samples' electrical conductivity [35]. The function $Q_{\mathrm{EML}}(q_{\mathrm{EML}})$ can be interpreted as an efficiency ratio. It takes into account that the field has only a limited penetration depth into the bulk. For a spherical sample, Q_{EML} is given by the following expression [34; 36]:

$$Q_{\mathrm{EML}}(q) = \frac{3}{4}\left(1 - \frac{3}{2q_{\mathrm{EML}}}\frac{sinh(2q_{\mathrm{EML}}) - sin(2q_{\mathrm{EML}})}{cosh(2q_{\mathrm{EML}}) - cos(2q_{\mathrm{EML}})}\right) \tag{2.2}$$

As a necessary condition for levitation, the component of $\vec{F_{\mathrm{L}}}$ in the vertical, i.e. z-, direction must compensate for the gravitational force $\vec{F_{\mathrm{g}}} = \vec{g}\rho V$, when V is the volume of the sample, ρ is it's density, and $\vec{g}$ is the gravitational acceleration. For a spherical sample, Eq. (2.1) becomes [34]:

$$\rho\vec{g} = -\frac{\nabla_z\vec{B}^2}{2\mu_0}Q_{\mathrm{EML}}(q_{\mathrm{EML}}) \tag{2.3}$$

From this condition one can read the factors governing the levitation process: In particular, Eq. (2.3) does not depend on the mass of the sample but on its density ρ, in-

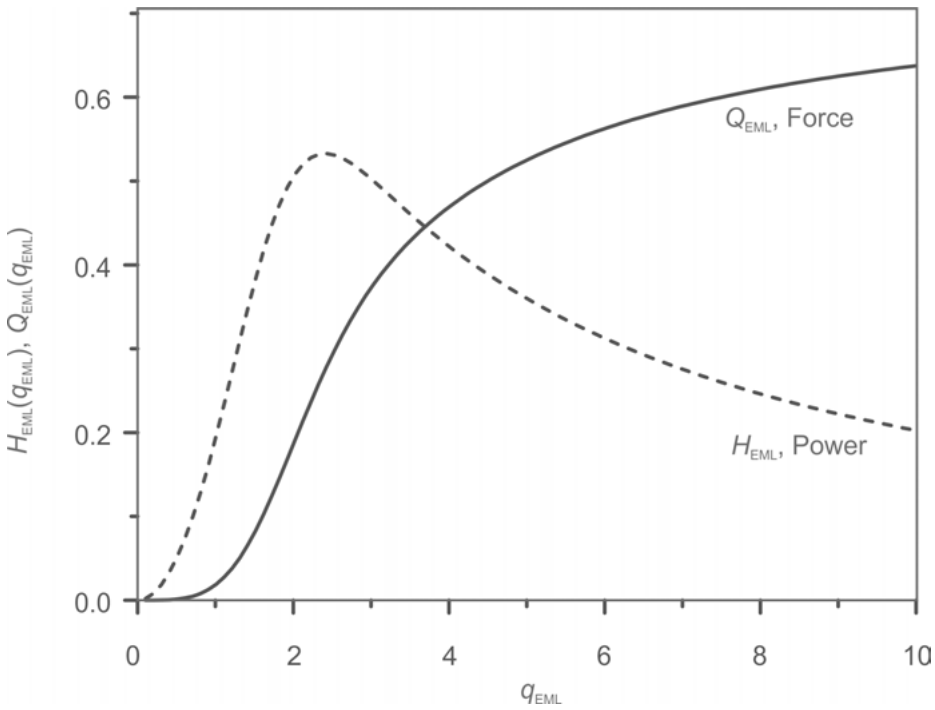

Fig. 2.2. Efficiency ratios $Q_{\mathrm{EML}}(q_{\mathrm{EML}})$ (solid line) and $H_{\mathrm{EML}}(q_{\mathrm{EML}})$ (dashed line) of an electromagnetic field versus $q_{\mathrm{EML}} = R/\delta$ with R being the sample radius and δ the skin depth [18].

stead. Samples with a low density, will be easier to levitate than samples with a comparatively high density. The force acting on the sample scales with $-\nabla B^2$. Hence, it is always directed away from the field. This is illustrated in Fig. 2.1:

In electromagnetic levitation, positioning and heating are not decoupled from each other. The oscillating field induces eddy currents within the sample. As the latter has finite electrical conductivity, the heating power P_{H} will be absorbed due to ohmic losses. The amount of P_{H} is given by [18]:

$$P_{\mathrm{H}} = \frac{\vec{B}^2\omega}{2\mu_0} \cdot \frac{4\pi}{3} R^3 \cdot H_{\mathrm{EML}}(q_{\mathrm{EML}}) \tag{2.4}$$

The function $H_{\mathrm{EML}}(q_{\mathrm{EML}})$ in Eq. (2.4) plays a similar role as $Q_{\mathrm{EML}}(q_{\mathrm{EML}})$ in Eq. (2.1). It can be interpreted as an efficiency ratio for the absorption of power. One can understand from the right hand side of Eq. (2.4) that P_{H} is proportional to the power density, $B^2\omega/(2\mu_0)$ and the volume of the sample. The effect of the latter is reduced by H_{EML} as the field can only act inside its boundary layer. H_{EML} is given by the following function [34]:

$$H_{\mathrm{EML}}(q_{\mathrm{EML}}) = \frac{9}{4{q_{\mathrm{EML}}}^2} \left(q_{\mathrm{EML}} \frac{sinh(2q_{\mathrm{EML}}) + sin(2q_{\mathrm{EML}})}{cosh(2q_{\mathrm{EML}}) - cos(2q_{\mathrm{EML}})} - 1 \right) \tag{2.5}$$

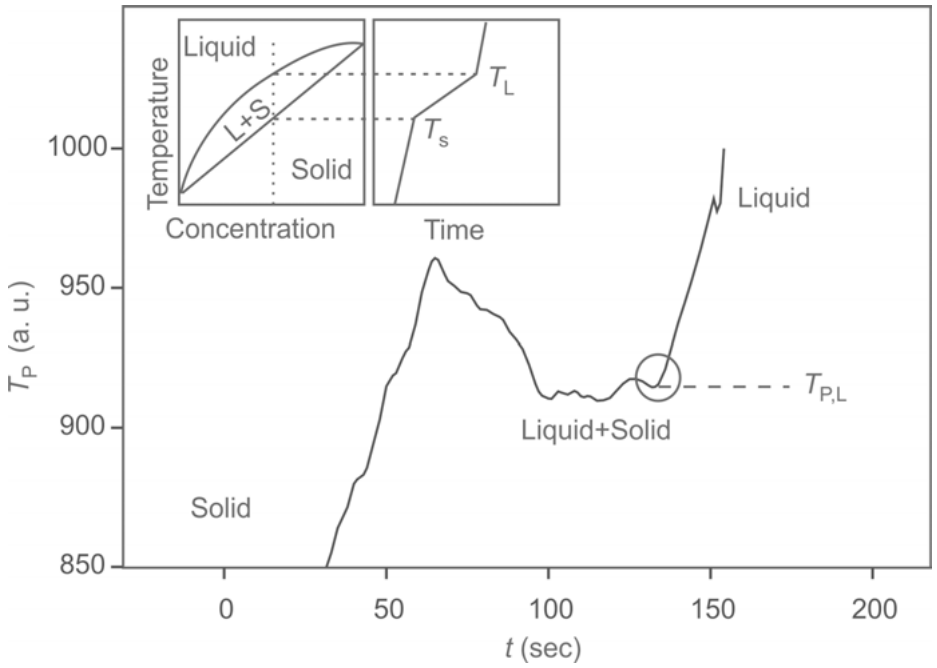

Fig. 2.3. Typical pyrometer output, T_P, when the sample melts. The value $T_{P,L}$ is used to calibrate the pyrometer signal with respect to the known liquidus temperature T_L. $T_{P,L}$ is identified by a sudden change in the slope of the curve as illustrated by the inset (from Ref. [37]).

In Fig. 2.2, Q_{EML} and H_{EML} are plotted versus q_{EML}. Both functions are zero for $q = 0$. This situation corresponds to a perfect insulator (or to an experimental situation where $\omega \approx 0$). Then, neither levitation nor heating is possible. In the case of $q \to \infty$, $H_{EML}(q_{EML})$ vanishes but $Q_{EML}(q_{EML}) > 0$, i.e. levitation occurs, but there is no heating. This latter case applies, for instance, in the limit of a perfectly conducting sample. Between these extreme cases, the ratio between heating and positioning can be adjusted, within limits, by changing the frequency and the power of the electromagnetic field, or by changing its gradient using coils of different geometry [18; 34].

The setups used at the "Institut für Materialphysik im Weltraum" of the German Aerospace Center (DLR) in Cologne are accommodated inside vacuum chambers which can be evacuated down to 10^{-8} mbar in order to remove impurities (adsorbed water, CO, CO_2, hydrocarbons, and others). Levitation experiments are carried out under protecting atmospheres so that pronounced evaporation of the sample is minimized or avoided. For this purpose, the chamber is refilled with 500 – 900 mbar of the processing gas having a purity of 99.9999 vol.-%. Ar or, due to its good cooling properties, He, or mixtures of both are used as processing gasses. An advantage of He, as compared to Ar, results from its lower condensation temperature, the reason for it's

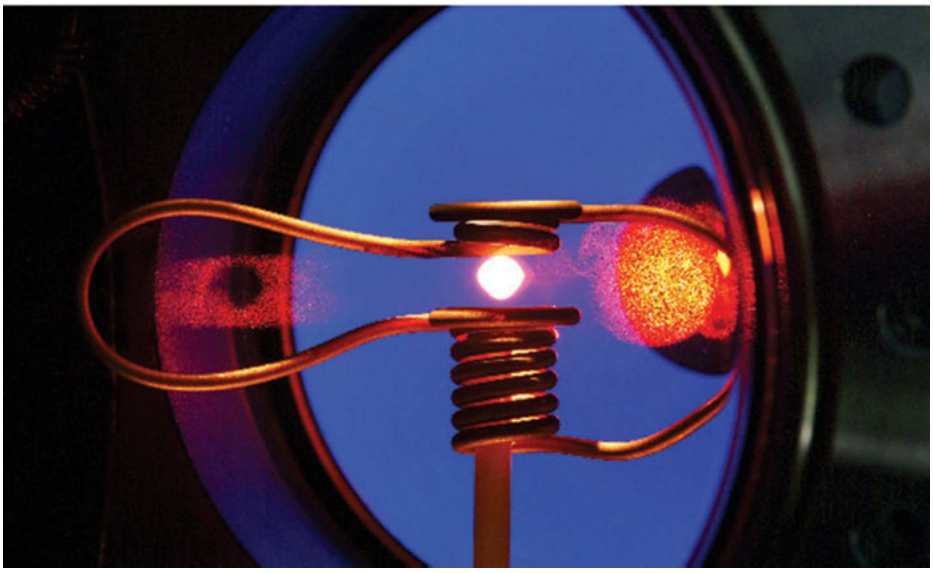

Fig. 2.4. Photograph of a levitated liquid Cu sample at ≈1600 K. The back light illumination using an expanded red laser is clearly visible on the right hand side as well as the sample shadow reflected from the window on the left hand side.

lack of most of the gaseous impurities. In order to reduce oxide traces, mixtures of He containing up to 10-vol% H_2 are also used.

At the beginning of each experiment, the sample is placed on top of a vertical ceramic tube and located in the center of the water-cooled induction coil. Typical dimensions of the coil are 40×15 mm. Its geometry is similar to the one shown in Fig. 2.4. It consists of a lower part, being its main body, and a top part with only a few windings with opposite polarity. Through this, it is assured that in the center B^2 has a minimum and that any dislocation of the sample will be answered by a restoring force.

The typical current through the coil is 200 A with a frequency of ≈ 300 kHz and the power is either 5 kW or 10 kW maximum, depending on which type of generator is used. A typical sample has a diameter of 5 mm. Depending on the material and the available power, temperatures far above the respective melting points are accessible. In some exceptional cases, temperatures of up to even ≈2700 K can be reached. As in EML, heating and positioning are not decoupled from each other, a certain desired temperature is best adjusted by cooling of the specimen against the inductive heating. This is performed by exposure to a laminar flow of the processing gas. The gas is admitted via a small ceramic nozzle located at the bottom of the droplet.

The temperature, T, is measured using an infrared pyrometer aimed at the sample either from the top or from the side. In each measurement, it is necessary to recalibrate the pyrometer signal T_P with respect to the liquidus temperature, T_L, which must be known in advance. The real temperature T is obtained using the following approxi-

mation derived from Wien's law [38]:

$$\frac{1}{T} - \frac{1}{T_\mathrm{P}} = \frac{1}{T_\mathrm{L}} - \frac{1}{T_\mathrm{L,P}} \tag{2.6}$$

In Eq. (2.6), $T_\mathrm{L,P}$ is the pyrometer signal at the liquidus temperature. It is identified by a sudden increase in the slope of T_P which occurs when the melting process is completed and the sample temperature, T, exceeds T_L [37]. This is illustrated in Fig. 2.3. Equation (2.6) is valid only if the sample emissivity at the operating wavelength of the pyrometer $\epsilon_\lambda(T)$ remains constant over the experimentally scanned range of temperature [17]. This is a good approximation for most metals; see Refs. [38; 39]. A photograph of a levitating droplet is shown in Fig. 2.4.

Due to the induction coil's cylindrical symmetry, the sample shape deviates from that of a perfect sphere. This has been described and discussed in previous works [40; 41]. When the volume of the sample is thought to be divided into horizontal discs of thickness dz with cross sections $A_\mathrm{i} = 4\pi R_\mathrm{i}$ and R_i being the radius of one of these discs, then the vertical force, $F_\mathrm{i,z}$ acting on such a disc equals:

$$F_{i,z} = -\frac{\nabla B^2}{2\mu_0} A_i Q_\mathrm{EML}(q_\mathrm{EML}) dz \tag{2.7}$$

For a sample with an initially spherical shape, the sections in the middle contribute most to the levitation force while the forces acting on the sections at the top and bottom are comparatively small. This is due to the quadratic dependence of A_i on R_i. In other words, the sample is suspended on a virtual disc in it's middle. If it was liquid, the top part would virtually flow around and, if the surface tension was large enough, hang like a suspended droplet underneath. The resulting shape is that of a levitating drop which is flat at the top and elongated at the bottom, see Fig. 2.4. A physically more complete analysis is provided, for instance, in Refs. [42; 43]. It is shown in these works that the fluid flow inside the sample also needs to be taken into account in order to correctly understand the sample shape.

Fluid flow is driven by the electromagnetic field. It is crucial for EML experiments that this flow can be turbulent under the correct conditions [42]–[45]. A turbulent flow inside the sample might have some homogenizing effect on it, for instance, with respect to temperature and composition. However, it can also cause strong oscillations of the sample around it's equilibrium position and, in particular, rotations around any axis. These instabilities are only limited by the viscosity of the melt. They may become so intense that an accurate measurement is no longer possible [46; 47].

When the sample is exposed to the magnetic field, surface oscillations of the droplet are strongly damped. This, and energy consumption by the turbulent flow inside the melt, prohibit the measurement of the viscosity under terrestrial conditions [48].

Electromagnetic levitation has also a number of advantages. As mentioned above, it is intrinsically stable. Therefore, active position control is not needed. Electromagnetic levitation is tolerant to ambient conditions and a large number of materials can

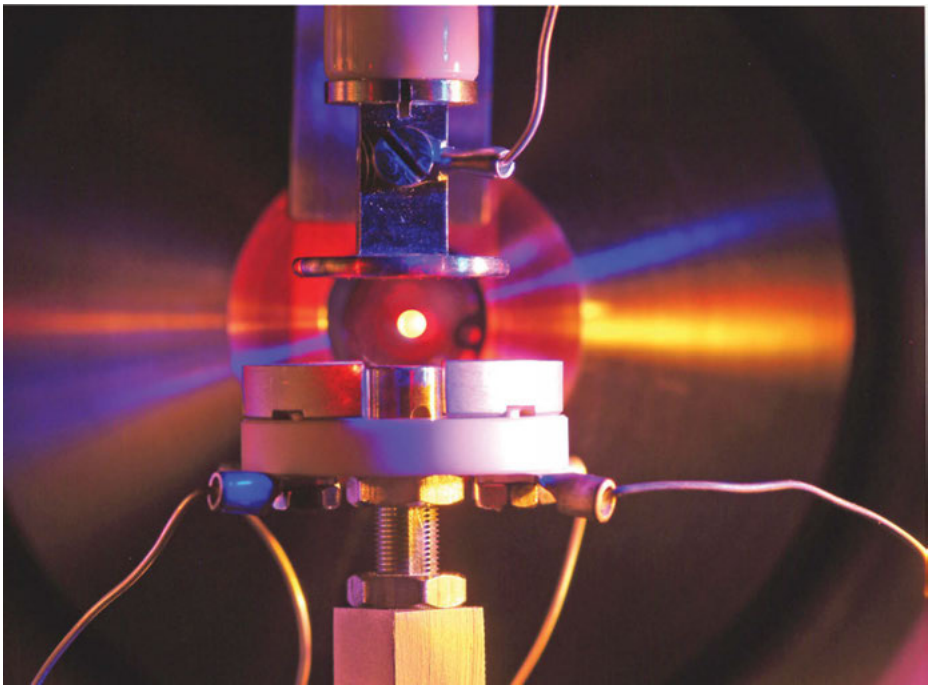

Fig. 2.5. Photograph of a levitated Al sample at ≈900 K. The electrode system is clearly visible as well as a part of the UV lamp whose opening is right behind the specimen.

easily be processed. The turbulent flow inside the melt leads to a spontaneous excitation of surface oscillations. This is very convenient for surface tension measurements. Electromagnetic levitation allows access to high temperatures, provides access to broad temperature ranges, deep undercoolings, and allows the processing of highly reactive materials. At the present point in time, electromagnetic levitation is still the most suitable and indicated technique for the investigation of electrically conductive materials such as liquid metals, alloys, or even semiconductors, such as Si [49].

2.2.2 Electrostatic Levitation

The concept of electrostatic levitation was introduced in order to avoid the disadvantages and restrictions of the electromagnetic levitation technique [50; 51; 52] namely, the turbulent flow, the non-sphericity of the sample and the restriction of the technique to electrically conducting materials. Since the mid 1990's when the ESL technique was first discovered, a number of investigations on thermophysical properties, structural investigations, and solidification studies have been performed. A compre-

hensive overview on the history and the current status of the ESL technique is published by Paradis et. al. [19].

In electrostatic levitation, the sample is electrically charged with a charge q_{charge} and positioning takes place by Coulomb forces $\vec{F}_{\text{C}}$ in a vertical electric field $\vec{E}$:

$$\vec{F_{\text{C}}} = q_{\text{charge}} \cdot \vec{E} \tag{2.8}$$

Typical samples have diameters between 1.5 and 3 mm with masses from 20 – 90 mg [53]. Depending on charge and field strength, larger samples with masses of up to 1 g can be levitated [54]. Positioning takes place between two parallel disk-like electrodes, typically 15 mm apart from each other. Horizontal stabilization is accomplished by four lateral electrodes beneath the specimen.

In contrast to electromagnetic levitation, ESL is not intrinsically stable. According to the Maxwell equations, $\nabla \cdot \vec{E} = 0$. Thus, a potential minimum cannot be generated by static electric fields [35]. Due to this so called Earnshaw theorem, active position control is required in ESL which is performed, in most cases, by sophisticated PID controllers, [55]. In DLR position control is accomplished by an adaptive real time controller developed by T. Meister [53]. The latter has the particular advantage that it can equalize abrupt movements of the sample caused, for example, by a sudden loss of charge.

As part of the control loop, two expanded He/Ne lasers, arranged perpendicular to each other, and associated x,y - position sensitive detectors (PSD) probe the sample position in three dimensions.

From Eq. (2.8) one can easily estimate that, in order to levitate a 50 mg sample, it must be charged with $\approx 5 \cdot 10^9$ e when a voltage of 10 kV is applied. Charging of the sample is therefore crucial for process stability. At the beginning of an experiment, when the sample is cold and solid, it may rest on the lower electrode and becomes charged due to polarization as soon as a voltage is applied. During the levitation experiment the sample may lose part of its charge. This can occur through contact with residual gas atoms or by desorption or evaporation of charged surface atoms. The latter can become a significant problem during the phase of heating and melting. Then, it is often encountered that the sample drops for no obvious reason. In order to compensate for the charge loss, an attempt to re-charge the sample by exposure to UV-light emitted from a He/H_2 lamp is made. At high temperature charging will take place by itself due to thermionic emission. Therefore, electrostatic levitation works best with materials having a high melting point, a low work function, and a low vapor pressure. Such materials are Zr, Ti, Nb, Mo, Pd, and other refractory metals.

Heating and melting of the specimen is achieved by laser power. In electrostatic levitation, positioning and heating are strictly independent from each other. Using the setup in this work, this is accomplished by two IR laser, each having a maximum power of 25 W. The lasers are focused on the sample in a small point where the temperature might be increased. Due to the absence of strong fluid flows, temperature homogenization may be challenging. Temperature gradients across the surface will

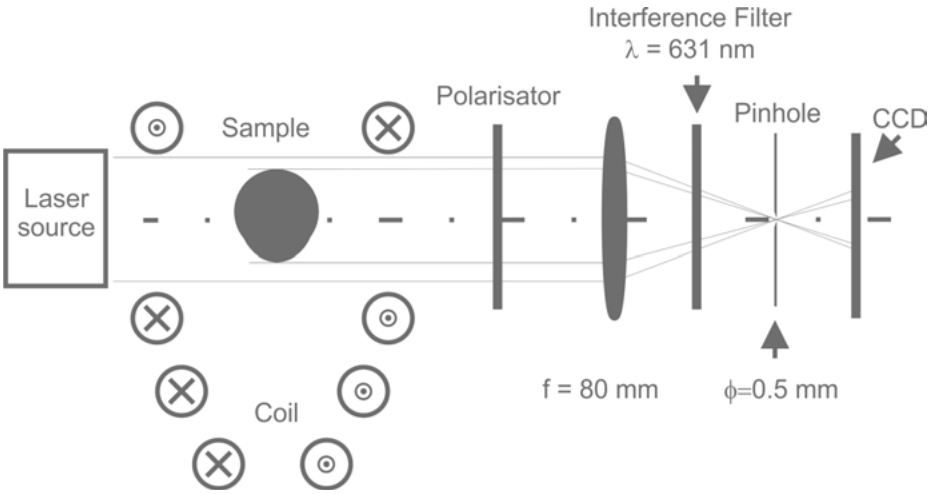

Fig. 2.6. Schematic diagram of the optical setup used for the optical dilatometry method [17].

generate gradients in surface tension which then triggers Marangoni (or thermocapillary) convection [56]. In addition, a non-uniform temperature distribution is always disturbing when precise data needs to be measured. For the setup used in this work, it has been shown that temperature gradients over the sample are so small that they can be neglected [54]. Slow sample rotations even lead to a further homogenization. Other groups sometimes use arrangements of three or more lasers in order to improve the temperature profile [19]. A picture of an electrostatically levitating sample is shown in Fig. 2.5.

Due to its working principle, electrostatic levitation is *a priori* not restricted to a certain materials class. Measurements can be carried out under high vacuum and atmospheric conditions. Devices working under high pressures of even up to 5 bar already exist [19; 57]. Once the sample is liquid and levitates, it is stable with a nearly spherical shape. Electrostatic levitation is potentially available for the measurement of all thermophysical properties.

The method application is however by no means straightforward. Position control requires high efforts. Samples often fall over due to charge loss or other instabilities. And, although electrostatic levitation has been demonstrated to work for all classes of materials [19], it works best for refractory metals Zr, Ti, V, and W and their alloys.

2.3 Optical dilatometry

In order to carry out containerless measurements, corresponding diagnostics have been be developed. For the measurement of density and thermal expansion, a technique has emerged which is known under the term “optical dilatometry”. This tech-

nique [58] was further developed and optimized by the author of the present work [18].

Density and thermal expansion are determined from the liquid sample by measuring it's volume. This is accomplished by illuminating the sample from one side by a light source while a camera records shadow graph images on the other side. The following description mainly refers to the setup used in combination with the EML experiments. However, the optical dilatometry technique can also be applied to electrostatically levitated samples where only a few modifications are necessary [19; 32; 59; 60].

The optical path of such a setup is schematically shown in Fig. 2.6. In this setup, a polarized laser beam is produced by a (He/Ne) laser equipped with a spatial filter, a beam expander and a collimator. The collimator is adjusted such that the beam is parallel [17]. The diameter of the spot produced is 25 mm. The light is shone at the sample from the rear. Due to scattering and diffraction at the chamber windows and at the surface of the sample, a certain part of the light is deflected. These non-parallel components must be removed in order to obtain a sharp shadow graph image that is free of noise, interferences and diffraction patterns [17]. This task is performed by the lens (f = 80 mm) and the pinhole (ϕ = 0.5 mm) acting together as an optical Fourier filter [17]. In order to vary the intensity of the light, a polarization filter is added to the setup. The interference filter and the pinhole, finally, remove contributions due to the samples' thermal radiation [17]. In this way, a uniform background is produced and the contrast of the image is independent on the brightness of the sample. This latter point is crucial for edge detection.

The shadow graph principle also becomes clear from the photograph shown in Fig. 2.4. In this figure, the expanded laser beam appears on the right hand side as a bright red circle. The shadow of the sample is visible in the reflection of the beam at the chamber window on the left hand side.

An example of a shadow image obtained from an electromagnetically levitated liquid copper sample is shown in Fig. 2.7. These images are then recorded by means of a digital CCD camera and fed into a computer. The images are analyzed in real time by an algorithm which detects the edge curve of the sample.

The points $\tilde{x}_{\mathrm{Edge}}$ of this edge curve are conveniently expressed in polar coordinates, (R,φ), with respect to the approximate drop center (x_0,y_0). R is hereby the radius and φ the polar angle, see Fig. 2.7 [17].

In levitation experiments, however, the surface of the droplet is undergoing oscillations. These oscillations can become very strong. Each frame, therefore, shows a droplet that is distorted from its ideal equilibrium shape [17]. As long as the amplitudes of these oscillations are comparatively small with respect to the average radius of the sample, the equilibrium shape can be obtained by averaging $R(\varphi)$ over a number of frames larger than or equal to 1000. In a next step Legendre polynomials of order

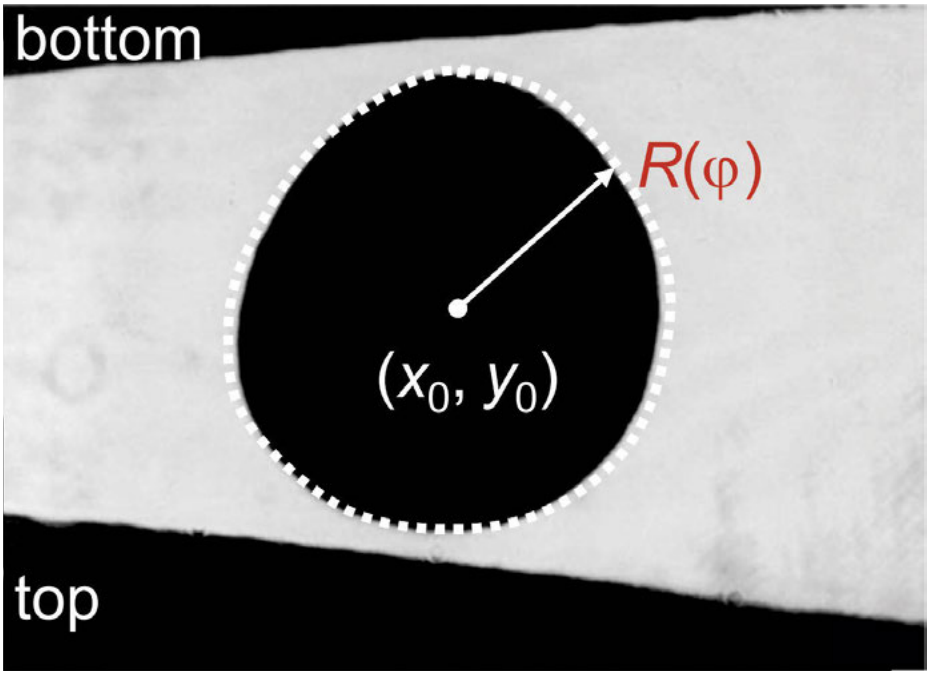

Fig. 2.7. Shadow graph image of an electromagnetically levitated sample. Due to the arrangement of the focusing lens, the sample appears upside down. The black regions at the top and bottom margins correspond to shadows thrown by the windings of the coil. The samples' entire edge curve is marked. In addition, a single edge point and its coordinates (R,φ) with respect to the center of mass, (x_0, y_0), is highlighted.

≤ 6 are fitted to the averaged edge curve $< R(\varphi) >$:

$$< \mathrm{R}(\varphi) >= \sum_{\mathrm{i}=0}^{6} \mathrm{a_i P_i}(\cos(\varphi)) \tag{2.9}$$

with P_i being the i^{th} Legendre polynomial.

At this point, an important assumption is made in order to evaluate the volume: It is assumed that the equilibrium shape of the droplet exhibits rotational symmetry with respect to the vertical axis. If this assumption is valid, the volume can be calculated using the following integral [17]:

$$V_{\mathrm{Pixel}} = \frac{2}{3}\pi \int_0^{\pi} < R(\varphi) >^3 \sin\varphi d\varphi \tag{2.10}$$

In Eq. (2.10), V_{Pixel} is the volume in pixel^3 units. For the calculation of the real volume, V_{Real}, i.e. in cm^3, it is necessary to calibrate the system. As described in Ref. [17], this is performed by the use of differently sized ball bearings.

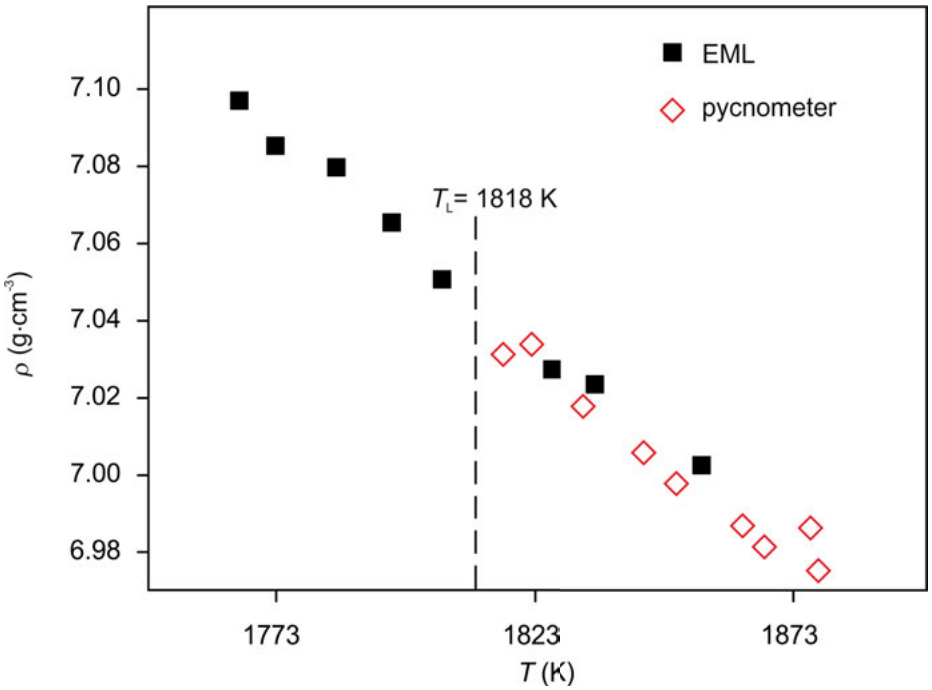

Fig. 2.8. Density of pure liquid iron versus temperature (solid). For comparison, data obtained by Sato using a pycnometer is also shown (open) [18].

Measured density data is shown versus temperature in Fig. 2.8. It is obtained for the case of pure liquid iron [61]. As visible from the figure, it is also possible to obtain data in the undercooled region. The thermal expansion coefficient can be obtained from the slope. In addition, the figure shows data measured for liquid iron by Sato using a classical pycnometer method [18; 62; 63]. The agreement between the two sets is excellent and the deviation of both is less than 0.1 %.

In order to estimate the accuracy of this method, it is necessary to identify factors which contribute to the error budget. Such factors are: strong sample movements, mass loss due to evaporation, errors in the temperature reading, and uncertainties in the calibration. In fact, these factors are mutually dependant. For instance, as a consequence of strong evaporation the sample is losing mass. This can lead directly to a change of the measured density as the density is proportional to the mass, or to a change in the chemical composition which also changes the density. Finally, condensation of the vapor on the windows will lead to a change of the calibration factor and can also influence the temperature reading of the pyrometer. Strong sample movements, such as sample rotations, can lead to a flattening of the sample and a permanent break of the axis-symmetry. In this case, the pre-condition of Eq. (2.10) is not fulfilled and the results may become extremely wrong.

Table 2.2. Sources of error and their impact on a density measurement.

Source of error	Impact
Evaporation	severe
Strong sample rotation	severe
Optics, edge detection	medium
Calibration	± 1.0 % (EML: Ref. [37])
Temperature reading	uncritical (ΔT± 10 K)
Lateral sample movements	uncritical

Among these factors, strong sample movements and mass loss due to evaporation are the most critical. The effect of mass loss is severe, because mass and density are directly proportional to each other. Provided, one of these factors is pronounced, an accurate measurement is no longer possible.

On the other hand, if these factors are avoided, highly accurate data can be obtained. In this case, the overall uncertainty can be estimated as $\Delta\rho/\rho \leq 1.0$ %. This value corresponds to the uncertainty of the calibration [37].

The optical dilatometry method is also successfully applied in combination with electrostatic levitation [19]. Here, it benefits from the additional advantage that due to the absence of turbulent fluid flow strong rotations and oscillations are rather rare. In addition, calibration should also be more precise, resulting in an overall increased accuracy of the data.

2.4 Oscillating drop method

The oscillating drop technique can be used in order to measure surface tension and viscosity of a levitating droplet. Hereby, it is used that the droplet performs oscillations around its equilibrium shape. The time dependent deformation of the droplet can be described as normal modes by spherical harmonics $Y_{\mathrm{n,m}}$ [40]:

$$R(\theta, \varphi, t) = \sum_{l=0} \sum_{l=-l}^{+l} a_{\mathrm{l,m}}(t) Y_{\mathrm{l,m}}(\theta, \varphi, t) \tag{2.11}$$

when R is the radius of the drop depending on the polar and azimuthal angles, θ and φ, respectively, and the time t. $a_{\mathrm{l,m}}(t)$ describes a time dependent deformation, l and m are the integers characterizing the oscillation mode.

Surface tension is obtained from the frequencies of the surface oscillations while viscosity is obtained from the time constant of their decay. In electromagnetic levitation, surface tension can be measured on earth and under microgravity. Viscosity, however, can only be determined under microgravity. A containerless determination of the viscosity on earth is currently only possible using electrostatic levitation.

2.4.1 Surface tension

For a spherical and non-rotating droplet of mass M, Rayleigh [64] has proposed the following relation between the surface tension y and the surface oscillation frequencies $\omega_{l,m}$ [40; 41]:

$$\omega_{l,m}^2 = l(l+2)(l-1)\frac{4\pi}{3M}y \tag{2.12}$$

The frequencies in Eq. (2.12) do not depend on the index m. This is different for a deformed sample [18; 40; 41]. A comparison with Eq. (2.11) reveals the meaning of the first three modes [41]: The mode associated with $l = 0$ corresponds to an isotropic oscillation. As the liquid is assumed to be incompressible, this mode does not appear in practice. The mode associated with $l = 1$ is the translational oscillation of the entire droplet. It is important for the measurement process but it does not contain information about the surface tension. Consequently, the fundamental mode is $l = 2$. It is fivefold degenerate (-2 .. 0 .. +2) and the lowest possible surface mode. The frequency $\omega_{2,0}$ is called Rayleigh frequency ω_R [18; 41]:

$$\omega_R^2 = \frac{32\pi}{3M}y \tag{2.13}$$

For sample masses of around 1 g, $\omega_R/2\pi$ is typically around 40 Hz [18].

Equation (2.12) has successfully been applied to samples levitated in microgravity [28; 65]. On earth, the samples are not spherical. They are also not force-free. The electromagnetic field imposes an additional, so called magnetic pressure, on their surface. In general, electromagnetically levitated samples are also not free of rotations. This whole system of problems has been investigated theoretically by Cummings and Blackburn [40] who finally made the oscillating drop technique applicable. They found that, first of all, the deviation of the droplet from the spherical shape partially removes the degeneracy of the $l = 2$ modes. The frequencies ω_R split up into a set of three frequencies, $\omega_{2,\pm2}$, $\omega_{2,\pm1}$, and $\omega_{2,0}$. Furthermore, it is assumed, that the magnetic field varies linearly, $\partial B_z/\partial z = const$, in the vertical direction [40]. Then, $\omega_{2,\pm2}$, $\omega_{2,\pm1}$, and $\omega_{2,0}$ are related to the Rayleigh frequency ω_R as follows:

$$\omega_{2,0}^2 = \omega_R^2 + \overline{\omega^2}_{Tr}\left(3.832 - 0.1714\left(\frac{g}{2a\overline{\omega^2}_{Tr}}\right)^2\right) \tag{2.14}$$

$$\omega_{2,\pm1}^2 = \omega_R^2 + \overline{\omega^2}_{Tr}\left(3.775 - 0.5143\left(\frac{g}{2a\overline{\omega^2}_{Tr}}\right)^2\right) \tag{2.15}$$

$$\omega_{2,\pm2}^2 = \omega_R^2 + \overline{\omega^2}_{Tr}\left(-0.9297 - 2.571\left(\frac{g}{2a\overline{\omega^2}_{Tr}}\right)^2\right) \tag{2.16}$$

In these equations, a is the mean sample radius, g is the gravitational acceleration and $\overline{\omega^2}_{Tr}$ denotes the mean quadratic translation frequency. It is calculated as

$\overline{\omega^2}_{\mathrm{Tr}} = \frac{1}{3}(\omega_{\mathrm{X}}^2 + \omega_{\mathrm{Y}}^2 + \omega_{\mathrm{Z}}^2)$ with ω_{X}, ω_{Y}, and ω_{Z} being the frequencies of the sample translations in the three spatial directions x, y, and z, respectively [18; 40; 41]. $\omega_{2,\pm2}$ and $\omega_{2,\pm1}$ are pairwise degenerate. In reality, however, this degeneracy is lifted due to the fact that the sample rotates. In a spectrum, therefore, peaks at five distinguishing frequencies become visible. If the frequency of a rotation around the vertical axis is Ω_{rot} and if Ω_{rot} is smaller than $\omega_{\mathrm{l,m}}$ [41] it has been shown by Busse [66; 41] that

$$\omega'_{\mathrm{l,m}} \approx \omega_{\mathrm{l,m}} + \frac{m}{2}\Omega_{\mathrm{rot}} \tag{2.17}$$

with $\omega'_{\mathrm{l,m}}$ being the shifted frequency.

Equations (2.14)–(2.16) can be combined with Eqs. (2.12) and (2.17) so that the sum-rule of Cummings and Blackburn is obtained, from which the surface tension can be obtained in practical applications, [18]:

$$y = \frac{3M}{160\pi}\sum_{m=-2}^{+2}\omega'^2_{2,\mathrm{m}} - \underbrace{1.9\overline{\omega^2}_{\mathrm{Tr}} - 0.3\left(\frac{g}{a\overline{\omega^2}_{\mathrm{Tr}}}\right)^2}_{\text{Correction term}} \tag{2.18}$$

The correction term in this equation accounts for the influence of the magnetic pressure which is estimated from the translational motion of the sample. If this term is neglected, as discussed in Ref. [41], the resulting surface tension values would be severely overestimated. Depending on the mass of the droplet, discrepancies of more than 30 % can easily be obtained.

The setup for monitoring the surface oscillations in electromagnetic levitation is shown in Fig. 2.9. It is hereby assumed that, in electromagnetic levitation, the surface oscillations are spontaneously excited due to the induced fluid flow inside the sample. Artificial excitation of the modes is therefore not necessary. In an experiment, the liquid sample is observed at constant temperature by a camera directed at it from the top, see Fig. 2.9. The frame rate of the camera must at least be twice as large as the highest frequency occurring in the spectrum. In practice, a frame rate of 130 Hz is sufficient for a sample of ≈1 g. In the setup used for the present work, however, the frame rate of the camera is 400 Hz allowing to record images with a resolution 400x400 pixel.

For each temperature, either 4096 or 8192 frames are recorded. After finishing the measurement, the images are analyzed by a program extracting the following parameters as a function of time: the center of mass, $(x_0(t), y_0(t))$, the visible droplet area, $A(t)$ and two perpendicular radii $r_{\mathrm{x}}(t)$ and $r_{\mathrm{y}}(t)$. Then, these are fast-Fourier-transformed (fft) and spectra are obtained from the translation in x- and y- direction, $\mathrm{fft}(x_0(t))$, $\mathrm{fft}(y_0(t))$, of the area, $\mathrm{fft}(A(t))$, of the sum, $\mathrm{fft}(r_x(t) + r_y(t))$ and of the difference, $\mathrm{fft}(r_x(t) - r_y(t))$ of the two perpendicular radii.

Typical spectra of the translations in x- and y- direction are shown in Fig. 2.10 [67]. The frequencies ω_{x} and ω_{y} appear as pronounced peaks at approximately 5.5 Hz and 6.0 Hz, respectively. In the ideal case of a perfect coil, both frequencies should be identical [41]. Small deviations between them point towards distortions in the coil geometry. In order to determine $\overline{\omega^2}_{\mathrm{Tr}}$, the vertical movement must also be known. This is

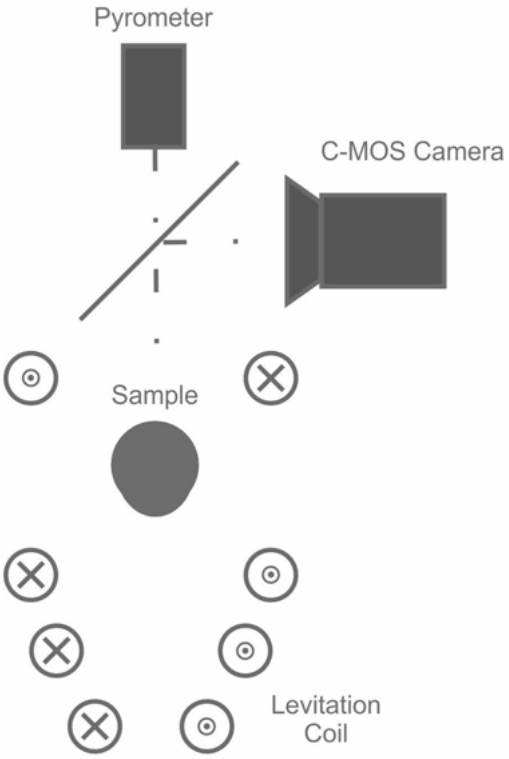

Fig. 2.9. Schematic diagram of the optical setup used in order to measure surface tension in electromagnetic levitation [18].

slightly more difficult when, as in the setup of the present work, no horizontal camera is used. However, ω_z is visible in the spectrum of the area. If the sample moves towards or away from the camera, it's apparent size changes which is visible in fft($A(t)$) as a weakly pronounced peak (see Fig. 2.10). Obviously, it is sometimes hard to distinguish this peak from the background noise. It can be helpful, in this context, that $\omega_z \approx 2\omega_x \approx 2\omega_y$ [18; 40; 41].

Figure 2.11, finally, shows spectra of the sum and the difference of the two perpendicular radii [67]. The $m = 0$ mode can be identified, because it appears in the sum spectrum but not in the difference [18; 41]. Just as straightforward, the $m = \pm 2$ modes are identified, because they should[1] only appear in the difference spectrum [18; 41]. Finally, the peaks appearing in both, the sum and the difference, belong to the $m = \pm 1$

1 Deviations from this ideal rule, as in the case of the $m = -2$ mode in Fig. 2.11, are owed to the fact that the assumptions (spherical sample, coil with circular cross section, linear variation of $\vec{B}$ along z-axis) made in the theory of Cummings and Blackburn are not always fulfilled in a strict sense.

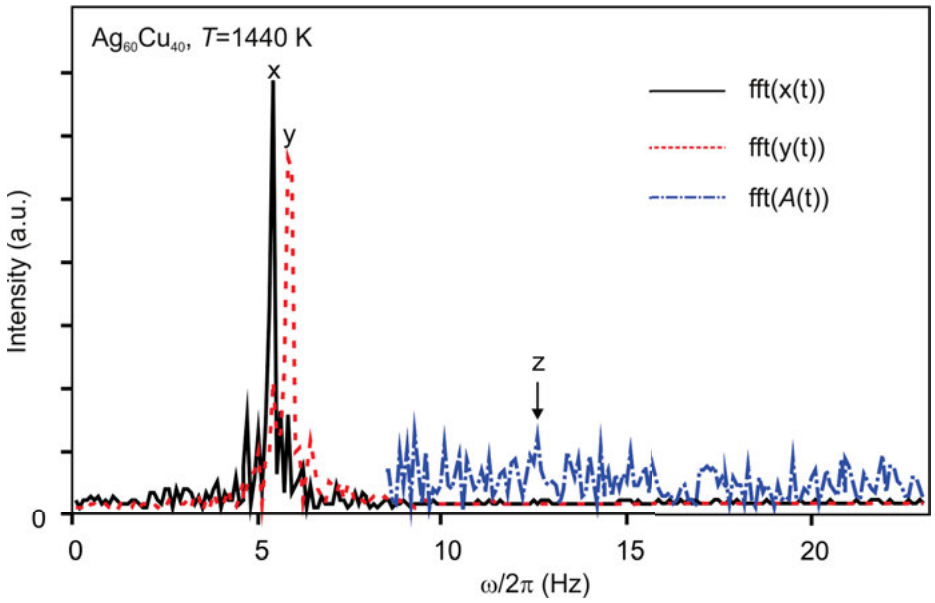

Fig. 2.10. Spectra of the translational movements in the horizontal directions, *x* and *y*, as well as of the area signal *A*(*t*). The peaks corresponding the translational modes of the sample are marked by x,y, and z [67].

mode. This way, all five frequencies, $\omega'_{2,\mathrm{m}}$ for the evaluation of Eq. (2.18) can be identified.

In a conservative approach, a maximum error of the surface tension $\Delta y/y \leq 5$ % [68] is estimated by assuming numerical errors of the parameters entering Eq. (2.18). For instance, the uncertainty of the frequency reading is estimated as 0.5 Hz which, in practice, is in the upper limit. In many systems, such as Fe-Ni [68] or Al-Cu [69], the variation of the surface tension, with temperature or concentration, is much smaller than these 5 %. However, it will be useful to analyze and exclude potential sources of error. Like for the density measurement, such factors are: evaporation and mass loss, strong sample rotation, and uncertain temperature readings. In addition, the purity condition of the sample and its environment, is crucial. It turns out, that from experiment mass loss due to evaporation, strong sample rotations and poor purity conditions can be true show-stoppers, if they occur.

In Eq. (2.18), *y* is directly proportional to the mass. An error in the mass would directly cause an error of the same order of magnitude in the surface tension. Strong sample rotations lead to a flattening of the sample. In a spectrum, only a single but extremely pronounced peak is then visible at double the frequency in this rotation. In addition, the pre-condition of Eq. (2.18), a negligible sample rotation, is violated.

Finally, the purity condition is crucial. Already a few ppm of some surface active species, such as oxygen or sulphur, can drastically decrease the surface tension by

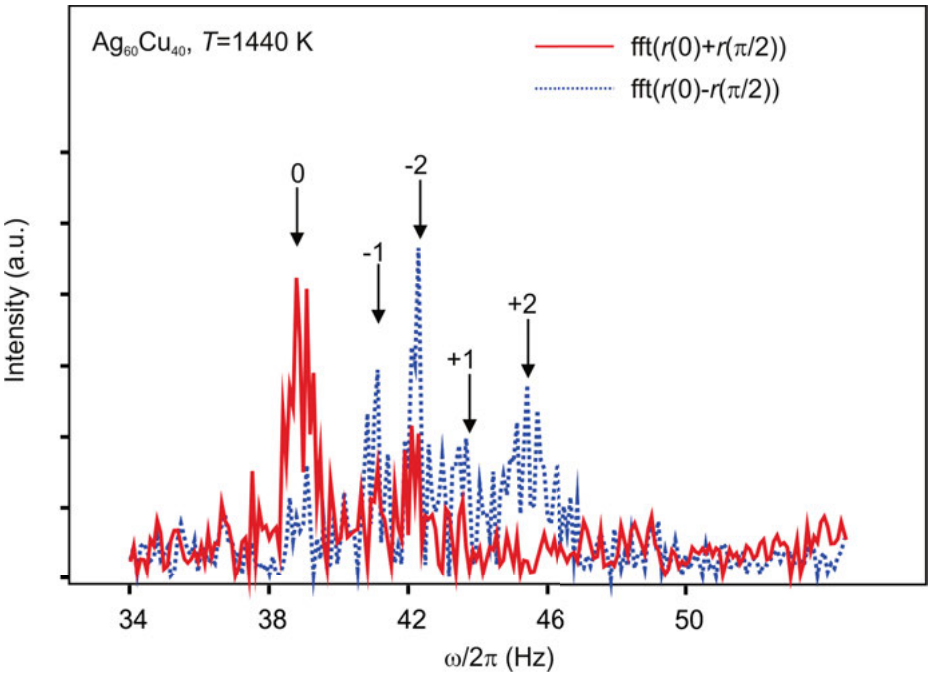

Fig. 2.11. Frequency spectra of the surface oscillation of a $Ag_{60}Cu_{40}$ sample at 1440 K. The solid curve is the Fourier transform of the sum signal of two perpendicular radii and the dotted curve is the Fourier transform of the difference signal. The peaks corresponding to $\omega'_{2,m}$ are marked by arrows [67].

more than 30 % and even reverse the temperature coefficient [70]. Oxygen can be adsorbed at the liquid metal surface from the gas phase. It is, therefore, important to keep the environment clean. Sometimes, hydrogen is added to the process gas in order to reduce the surface. On the other hand, the impurities may already linger inside the raw materials due to the way, these have been manufactured. Finding a clean material and providing the optimum conditions for the measurement is often a challenging task. Table 2.3 lists factors influencing the accuracy of surface tension measurement.

2.4.2 Viscosity

The oscillation drop technique can also be used for the determination of viscosities. This has been performed, for instance, by Egry during the shuttle missions IML-2 (1994) and MSL-1 (1997) [71; 72]. On the ground, these measurements can only be performed if magnetic damping and strong fluid flow is prohibited [48]. Electrostatic levitation provides a promising platform for such investigations. Corresponding experiments have been performed, for instance, by Ishikawa [73], Paradis [60],

Mukherjee [74], Rhim [75], Brillo [32], Bradshaw et al. [76] and others. These activities and the current status of the ESL technique are summarized in a review paper published recently by Paradis [19].

The influence of the viscosity on the droplet oscillations was studied mainly by Lamb [77] and Chandrasekhar [78]. They derived a formula for the viscosity, η, of a liquid spherical drop which is called Lambs law [41]:

$$\eta = \frac{\rho a^2 \Gamma}{(l-1)(2l+1)} \tag{2.19}$$

In this equation, Γ is the damping constant of the surface oscillation and a is the radius of the spherical droplet.

Unlike in electromagnetic levitation, the oscillations are not self excited. Hence, in an experiment, a sinusoidal electric field with an amplitude of 0.4 – 2 kV is superimposed to the vertical positioning field with a frequency between 100 and 400 Hz [19; 32]. In this way, a $Y_{2,0}$ oscillation mode is excited. It is important, however, that the amplitude of this mode does not exceed 5 % of the sample radius. Larger amplitudes can trigger flow vortices inside the droplet and consume additional energy [79].

When the $Y_{2,0}$-mode has stabilized, the excitation field is switched off and the oscillations start to decay due to inner friction. During this decay, shadow graphs are recorded of the sample.

The use of a high-speed camera (frame rate > 2000 FPS) allows the collection of 10 – 20 data points per oscillation, if the viscosity of the sample is below 100 mPa · s. The vertical radius $a_z(t)$ can be determined as a function of time t with a precision of better than 1 % [32]. For further analysis, $a_z(t)$ is fitted by a damped sine function

$$a_z(t) = a_0 + a_0 \exp(-\Gamma t) sin(\omega t + \delta_0) \tag{2.20}$$

where a_0 is the amplitude, Γ is the damping constant, ω is the frequency, and δ_0 is a constant phase shift. From the obtained value of Γ, the viscosity is calculated according to Lamb's law, Eq. (2.19).

Table 2.3. Sources of error and their impact on a surface tension measurement.

Source of error	Impact
Evaporation	severe
Strong sample rotation	severe
Optics, edge detection	uncritical
Temperature reading	uncritical ($\Delta T \pm$ 10 K)
Lateral sample movements	uncritical
Purity conditions	severe

2.5 Oscillating cup viscometry

Measuring viscosity by means of the oscillating drop technique has many convincing advantages.

On earth, however, it will only work in combination with electrostatic levitation which has no straightforward application. In many cases, a certain element or alloy material cannot be processed at all.

Hence, for the measurement of the viscosities of liquid metals at high temperature, the classical oscillating cup technique, is still standard [70]. In this technique, the liquid alloy is in contact with a crucible and one has to struggle with all the shortcomings described in section 2.2.

The cylindrical crucible containing the liquid is suspended by a wire and performs torsional oscillations around it's vertical axis. Due to the inner friction of the liquid, these oscillations are damped. The viscosity can be obtained from the time decay of the oscillation amplitude.

This can be achieved by formulating the Navier-Stokes equations for the problem. Depending on which approximation is used, different working equations are obtained [80], which need to be solved numerically. The most prominent of which is the Roscoe equation [81; 82], where the viscosity η is given by the following expression:

$$\eta = \left(\frac{I\delta}{\pi R^3 H_{\mathrm{osc}} Z}\right)^2 \frac{1}{\pi \rho_{\mathrm{T}}} \tag{2.21}$$

Here, I is the moment of inertia of the oscillating system, δ is the logarithmic decrement, T_{period} is the oscillation period time, ρ is the density of the liquid, R is the inner radius of the crucible, and H_{osc} is the height of the sample. The parameter Z_{osc} is given by

$$Z_{\mathrm{osc}} = \left(1 + \frac{R}{4H_{\mathrm{osc}}}\right) c_{\mathrm{osc},0} - \left(\frac{3}{2} + \frac{4R}{\pi H_{\mathrm{osc}}}\right) \frac{1}{p_{\mathrm{osc}}} + \left(\frac{3}{8} + \frac{9R}{4H_{\mathrm{osc}}}\right) \frac{c_{\mathrm{osc},2}}{2p_{\mathrm{osc},2}} \tag{2.22}$$

with

$$p_{\mathrm{osc}} = \left(\frac{\pi\rho}{\eta T_{\mathrm{osc}}}\right)^2 R \tag{2.23}$$

and

$$c_{\mathrm{osc},0} = 1 - \frac{3}{2}\left(\frac{\delta}{2\pi}\right) - \frac{3}{8}\left(\frac{\delta}{2\pi}\right)^2 \tag{2.24}$$

$$c_{\mathrm{osc},2} = 1 + \frac{1}{2}\left(\frac{\delta}{2\pi}\right) + \frac{1}{8}\left(\frac{\delta}{2\pi}\right)^2 \tag{2.25}$$

The above equations form a self-consistent system and viscosity can be obtained by numerical solution. Alternative analyses have become popular during the past years. Here, the analysis of Beckwith and Newell [63; 83; 84] must be mentioned, as well as the analysis of Brockner [63; 85].

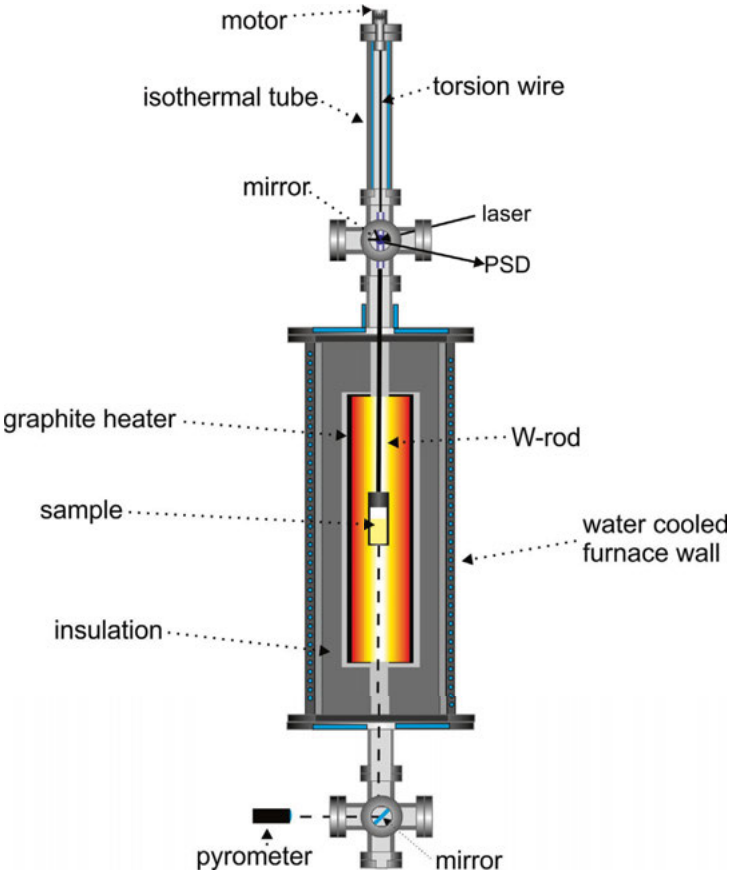

Fig. 2.12. Scheme of the viscometer [80].

The apparatus used for the present work was designed and set up by Kehr during the work for his Ph.-D. thesis [86]. It is described in detail in Refs. [86; 80]. A scheme of the setup is shown in Fig. 2.12. It consists roughly of two main parts: the furnace and the oscillation system. The heart of the oscillation system is the torsional steel wire with a diameter of 0.228 mm. It's length is approximately 1.3 m and it is accommodated in a tube-housing held at a constant temperature of 28 °C. A mirror holder with attached mirror is fixed at the end of the wire for the oscillation detection. The mirror holder continues with a tungsten rod reaching inside the furnace. This rod holds the graphite container with the sample crucible inside. Its length is adjusted such that the sample is located right in the center of the furnace as the temperature here is where homogeneity is best.

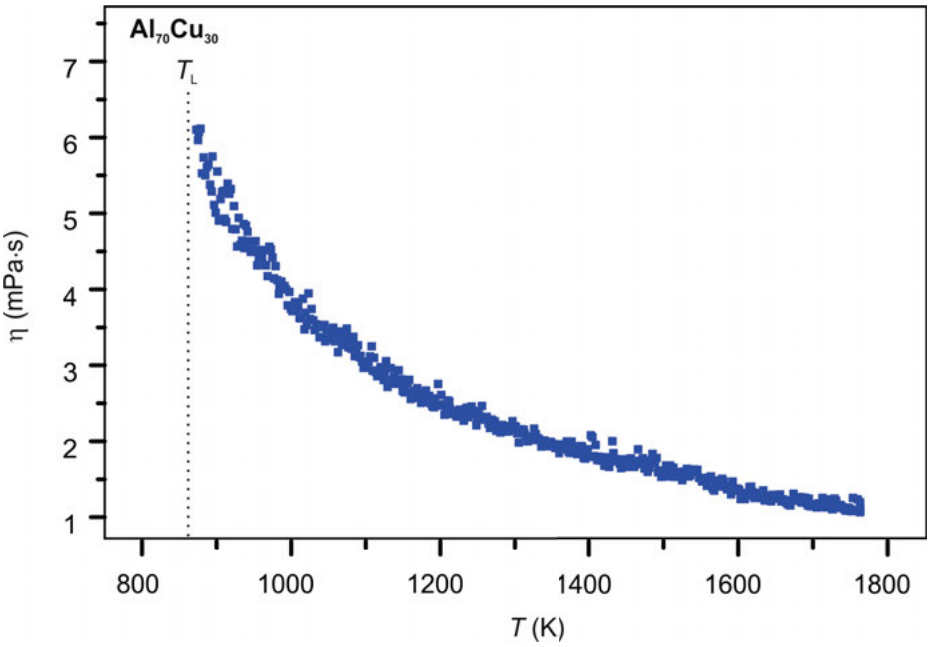

Fig. 2.13. Viscosity of liquid $Al_{70}Cu_{30}$ versus temperature [87].

In order to monitor the oscillations, a laser is shone at the mirror and the reflected beam is accepted by a position sensitive detector (PSD) in order to measure the angle of torsional displacement [80].

The furnace consists of a graphite resistance heater with an inner diameter of 100 mm and the length of the isothermal hot zone is 450 mm [80]. Magnetic fields at the position of the sample are reduced to a minimum due to the meander shaped design of the heater. Thermal insulation is achieved by a graphite felt wrapped around the heater. The overall thickness of the insulation is 10 – 15 cm. The outer wall of the furnace is a water-cooled steel tube [80]. Using this setup, a maximum temperature of ≈2600 K is obtained. The maximum operating temperature of the vast majority of currently existing viscometers is nearly 800 K lower.

During operation, a pyrometer is used in order to record the furnace and sample temperatures. The pyrometer is directed via a mirror to the bottom face of the crucible container. The emissivity of the crucible container is determined using the melting points of several pure metals (Al, Cu, Ni, Co, Fe) as reference temperatures.

The furnace is part of a high vacuum system. Prior to an experiment, it is evacuated to a pressure of $<10^{-6}$ mbar and then backfilled with Ar of high purity 99.9999 vol-%, so that the measurements can be carried out under a protective atmosphere. In order to avoid that the oscillations interfere with the gas convection flow, its pressure is reduced to 400 mbar.

During an experiment, torsional oscillations of the suspended crucible are excited by an electric motor [87]. The position sensitive detector is read out by a software [86] which solves the Roscoe equation, Eq. (2.21), and calculates the viscosity. During data acquisition, the temperature is slowly decreased in steps of 1 K/min [87]. In contrast to strictly isothermal measurements, a smooth and continuous curve is obtained over a wide temperature range with several hundred data points, see Fig. 2.13.

In Ref. [80] Kehr specifies an estimated uncertainty of the viscometer of less than 6 %. This value is calculated from estimated uncertainties of the input parameters of the Roscoe equation. However, the uncertainty of the data reported in the same article is larger, namely 15 %. The authors identify the crucibles as the main reason for this discrepancy. Due to chemical reactions, most cups would change their inner diameter during the measurement [80]. In addition, the sample becomes "dirty" from these reactions and it's properties would change. Another severe problem in this context affects the wetting behavior of the melt at the container wall. The Roscoe equation is derived assuming that, in a hydrodynamic sense, the liquid sticks to the wall and that there is also no meniscus at its surface. Chemical reactions, such as oxidation, might destroy these preconditions: If a meniscus forms and if slipping between the liquid and the container occurs, the sheared volume differs from the actual volume and Eq. (2.21) can no longer be applied [63]. As a consequence, errors in the viscosity of more than 50 % are easily encountered.

3 Density

In this chapter, systematic density measurements of a number of liquid pure metals as well as binary and ternary alloys are presented. The measurements are carried out without a container using the optical dilatometry technique in combination with electromagnetic levitation. The degree of complexity of the sample materials is increased stepwise from mono-atomic systems to binary and ternary alloys. The results are discussed using the excess volume as the key mixing parameter. There is no general rule of thumb whether or not it is positive, negative or zero. However, it is found that demixing systems tend to exhibit a positive excess volume while strongly mixing systems show a negative excess volume. For alloys of which the components are chemically similar, the excess volume is almost zero.

3.1 Formalism

In this section, the mathematical formalism and the terminology used to analyze and discuss the measured density data will be briefly recalled. The fundamental equation for the free energy G reads as follows [88]:

$$dG = Vdp - SdT + \sum_i \mu_i dn_i \tag{3.1}$$

Here, V is the volume, p the pressure, S the entropy, T is the temperature, μ_i the chemical potential of component i in the mixture and n_i its number of moles. From Eq. (3.1), the following basic relation can be derived for the volume:

$$\left(\frac{\partial G}{\partial p}\right)_{T,n_i} = V \tag{3.2}$$

For a mixture of different components i with mole fractions $x_i = n_i / \sum_i n_i$, G can be written:

$$G = \sum_i x_i G_i^0 + \Delta G \tag{3.3}$$

where G_i^0 is the free energy of the pure component i and ΔG is the mixing free energy. The corresponding excess property, the excess free energy ${}^{E}G$, is related to ΔG via the mixing free energy of the ideal solution, ${}^{id}\Delta G$ which equals $RT \sum_i x_i \ln(x_i)$:

$${}^{E}G = \Delta G - {}^{id}\Delta G = \Delta G - RT \sum_i x_i \ln(x_i) \tag{3.4}$$

Applying Eq. (3.2) to Eq. (3.3) using Eq. (3.4), yields the following relation for the molar volume of the mixture, V, with V_i being the molar volume of component i and ${}^{E}V$ the molar excess volume which equals ΔV, the mixing molar volume:

$$V = \sum_i x_i V_i + {}^{E}V \tag{3.5}$$

This equation is intuitively clear: The volume of the mixture is given by the volumes of the pure components, weighed by their corresponding mole fractions, and an additional contribution, ${}^{\mathrm{E}}V$, originating from the interaction between the particles.

The density, ρ, is generally given by mass M divided by volume V. As the mixture consists of atoms i with molar masses M_i and $\rho_\mathrm{i} = M_\mathrm{i}/V_\mathrm{i}$ is the density of pure component i, ρ is obtained from Eq. (3.5) as:

$$\rho = \frac{\sum_i x_\mathrm{i} M_\mathrm{i}}{\sum_i x_\mathrm{i} \frac{M_\mathrm{i}}{\rho_\mathrm{i}} + {}^{\mathrm{E}}V} \tag{3.6}$$

Molar volume and density depend on temperature. For the molar volume, this is expressed by the thermal volume expansion coefficient β. It describes the change of the volume relative to a fixed reference point. In a liquid alloy, such a reference point is usually the liquidus temperature T_L at which the molar volume equals V_L. Then, $V(T)$ is given by:

$$V(T) = V_\mathrm{L}(1 + \beta(T - T_\mathrm{L})) \tag{3.7}$$

This can be written into a power series expansion for the density:

$$\rho(T) = \rho_\mathrm{L} + \rho_\mathrm{T}(T - T_\mathrm{L}) + \rho'_\mathrm{T}(T - T_\mathrm{L})^2 \tag{3.8}$$

whereas $\rho_\mathrm{L} = \rho(T_\mathrm{L})$ is the density at the liquidus temperature and $\rho_\mathrm{T} = \partial\rho/\partial T$ denotes the linear temperature coefficient. The second order temperature coefficient $\rho'_\mathrm{T} = \partial^2\rho/\partial T^2$ accounts for a possible deviation ρ from the linear law. Hints that this may indeed be possible exist in the case of liquid silicon. Here, a maximum of the density as a function of temperature is discussed, [89]. In most other cases, in particular in all of those discussed in the present work, ρ'_T =0 and the density obeys a linear law:

$$\rho(T) = \rho_\mathrm{L} + \rho_\mathrm{T}(T - T_\mathrm{L}) \tag{3.9}$$

There is also a useful relation between ρ_L and β as long as T is in the vicinity of T_L:

$$\beta \approx -\frac{\rho_\mathrm{T}}{\rho_\mathrm{L}} \tag{3.10}$$

Differentiating Eq. (3.6) with respect to temperature, the following expression is obtained for the temperature coefficient of the mixture:

$$\rho_\mathrm{T} = \left[\sum_i x_\mathrm{i} M_\mathrm{i}\right] \times \left[\sum_\mathrm{i} x_\mathrm{i} \frac{M_\mathrm{i}\rho_{\mathrm{T,i}}}{\rho_\mathrm{i}^2} - \frac{\partial {}^{\mathrm{E}}V}{\partial T}\right] V^{-2} \tag{3.11}$$

In order to apply this expression, the excess volume as well as its temperature dependence need to be known.

3.1.1 Ideal solution

Excess properties are zero for an ideal solution. In particular, ${}^{\mathrm{E,id}}G = 0$ for all values of p. Moreover, it follows strictly from Eq. (3.2) that:

$$ {}^{\mathrm{E,id}}V = {}^{\mathrm{id}}\Delta V = 0 \tag{3.12} $$

with ${}^{\mathrm{E,id}}V$ being the excess volume and $\Delta^{\mathrm{id}}V$ being the mixing volume in an ideal solution. Hence, the following conclusion is justified:

$$ \text{ideal solution} \Longrightarrow^{\mathrm{E,id}} V = 0 \tag{3.13} $$

The reverse conclusion, however, is not allowed. A mixture with zero or vanishing excess volume is not necessarily ideal. This is seen from integration of Eq. (3.12) with respect to pressure, yielding an integration constant C. In general, $C \neq 0$.

In fact, it is not straightforward to decide, whether or not an alloy is an *ideal solution*, even, if ${}^{\mathrm{E}}G$ is reported as zero. The difficulty comes from the fact that for liquid metals and alloys, the pressure dependence of ${}^{\mathrm{E}}G$ is insufficiently known. For a system exhibiting ${}^{\mathrm{E}}G = 0$ at ambient pressure, it's partial derivative with respect to p may be unequal to zero. Therefore, one may find ${}^{\mathrm{E}}V \neq 0$ even if the system is apparently ideal. The following possible approach for a model doesn't work in general: ${}^{\mathrm{E}}V \propto {}^{\mathrm{E}}G$.

Combining Eq. (3.12) and Eq. (3.5) the molar volume of an ideal solution, ${}^{\mathrm{id}}V$, is obtained as:

$$ {}^{\mathrm{id}}V = \sum_i x_{\mathrm{i}} V_{\mathrm{i}} \tag{3.14} $$

Equation (3.14) is a linear combination of the molar volumes of the pure elements. In some publications, it is known as *Vegards law* [90]. Vegards law has been derived empirically in order to describe the observation that the observed lattice constants in solid crystalline materials change linearly in composition. In the present work, Eq. (3.14) will be referred to as *ideal law* in order to emphasize the subtle difference between mixtures with vanishing excess volume, ${}^{\mathrm{E}}V = 0$ and an actual *ideal solution*, see Eq. (3.13). Now, from Eq. (3.6) one may also note the corresponding expression for the ideal density, ${}^{\mathrm{id}}\rho$:

$$ {}^{\mathrm{id}}\rho = \frac{\sum_i x_{\mathrm{i}} M_{\mathrm{i}}}{\sum_i x_{\mathrm{i}} \frac{M_{\mathrm{i}}}{\rho_{\mathrm{i}}}} \tag{3.15} $$

3.1.2 Sub-regular solution

In literature, one distinguishes between *regular*, *sub-regular* and *sub-(sub-)regular* solution models. As the difference between these terms is not relevant in this work and as their correct definition is sometimes confused in literature, the term *sub-regular* solution is preferred in this chapter with the following meaning: A sub-regular solution

is a solution that can be described by the Redlich-Kister-Muggianu polynomial with non-vanishing interaction parameters, [91].

For a binary alloy with components i, j the excess free energy ${}^{\mathrm{E}}G$ written in the Redlich-Kister form is given by:

$$ {}^{\mathrm{E}}G_{\mathrm{i,j}} = x_{\mathrm{i}}x_{\mathrm{j}} \sum_{\nu=0}^{N_{\mathrm{i,j}}} {}^{\nu}L_{\mathrm{i,j}}(T)(x_{\mathrm{i}} - x_{\mathrm{j}})^{\nu} \tag{3.16} $$

The binary interaction parameters, ${}^{\nu}L_{\mathrm{i,j}}(T)$ ($\nu = 0 \ldots N_{\mathrm{i,j}}$), describe the interaction between particles of different kind. They may depend on temperature, but not on composition. In a thermodynamic assessment, which is commonly regarded as "good", the order of this polynomial is small, typically, $N_{\mathrm{i,j}} \leq 2$[1]. In addition, ${}^{\nu}L_{\mathrm{i,j}}(T)$ should decrease with increasing ν. For a mixture of three or more components the Redlich-Kister-Muggianu form reads as follows [91]:

$$ {}^{\mathrm{E}}G_{1,2,3} = \sum_{i<j} x_{\mathrm{i}}x_{\mathrm{j}} \sum_{\nu=0}^{N_{\mathrm{i,j}}} {}^{\nu}L_{\mathrm{i,j}}(T)(x_{\mathrm{i}} - x_{\mathrm{j}})^{\nu} + {}^{\mathrm{T}}G(T, x_1, x_2, x_3)x_1x_2x_3 + \ldots \tag{3.17} $$

The parameters ${}^{\nu}L_{\mathrm{i,j}}(T)$ are identical with those in Eq. (3.16). In addition, there is also a parameter ${}^{\mathrm{T}}G$ accounting for a possible ternary interaction. ${}^{\mathrm{T}}G$ depends on T and, generally also on composition. However, the composition dependence is usually very weak and, ideally, the influence of the ternary term on the excess free energy should be comparatively small. If ${}^{\mathrm{T}}G \approx 0$, the excess free energy of a ternary system can be predicted from the binary subsystems.

Using Eq. (3.2), Eq. (3.16) and Eq. (3.17) can be transformed into similar expressions for the molar volume with binary volume interaction parameters ${}^{\nu}V_{\mathrm{i,j}}(T)$ and a ternary parameter ${}^{\mathrm{T}}V(T)$, assumed independent on composition. This is first exercised for a binary system whereas the polynomial is truncated for $\nu > 1$:

$$ {}^{\mathrm{E}}V_{\mathrm{i,j}} = x_{\mathrm{i}}x_{\mathrm{j}} \left[{}^{0}V_{\mathrm{i,j}}(T) + {}^{1}V_{\mathrm{i,j}}(T)(x_{\mathrm{i}} - x_{\mathrm{j}}) \right] \tag{3.18} $$

The general form of Eq. (3.18) is that of a distorted parabola. The term $x_{\mathrm{i}}x_{\mathrm{j}}{}^{0}V_{\mathrm{i,j}}(T)$, describes this parabola. Deviations from it are taken into account by the second term, ${}^{1}V_{\mathrm{i,j}}(T)(x_{\mathrm{i}} - x_{\mathrm{j}})$, inside the square brackets. In most cases, these deviations are so small that ${}^{1}V_{i,j}$ can be neglected. Hence, the molar volume of a binary alloy can be approximated by the following parabola:

$$ {}^{E}V_{\mathrm{i,j}} \approx x_{\mathrm{i}}x_{\mathrm{j}}{}^{0}V_{\mathrm{i,j}}(T) \tag{3.19} $$

1 This originates from a point of view according to which a model is generally worsening as more free parameters are needed in order to achieve agreement with the data. On the other hand, a maximum number of free parameters of 2 (i.e. $N_{\mathrm{i,j}} < 2$) may cause problems in certain applications involving the thermodynamic factor, which is defined as $\Phi = \frac{\partial^2 G}{\partial x^2}$.

The derivation for a ternary system is performed analogously, whereas the ternary parameter ${}^{\mathrm{T}}G$ in Eq. (3.17) transforms into a corresponding ternary parameter ${}^{\mathrm{T}}V = \partial {}^{\mathrm{T}}G/\partial p$ for the volume. The following equation is obtained for the isothermal excess volume, ${}^{\mathrm{E}}V_{1,2,3}$, of a ternary mixture as a function of the concentrations x_{i}:

$$ {}^{\mathrm{E}}V_{1,2,3} = \overbrace{\sum_{i<j} {}^{\mathrm{E}}V_{\mathrm{i,j}}(T)}^{\text{binary term}} + \overbrace{x_1 x_2 x_3 \, {}^{\mathrm{T}}V(T)}^{\text{ternary term}} \tag{3.20} $$

The right side of Eq. (3.20) consists of two terms. The left term, accounts for the binary interactions. As already discussed for Eq. (3.17), ${}^{E}V_{\mathrm{i,j}}(T)$ is identical with the excess volume of the binary subsystem and can be determined from an independent measurement.

It is desirable with respect to question **Q:3**, see Chap. 1, that, like the parameter ${}^{\mathrm{T}}G$ in Eq. (3.17), ${}^{\mathrm{T}}V$ is also very small. This would have the advantage that the excess volume of a ternary alloy could easily be predicted from the excess volumes of it's binary boundary systems. However, $\partial {}^{\mathrm{T}}G/\partial p \neq 0$ even if ${}^{\mathrm{T}}G = 0$ at ambient pressure. Therefore, ${}^{\mathrm{T}}V$ can be quite large, even if ${}^{\mathrm{T}}G$ was practically zero. On the other hand, the integral, $\int {}^{\mathrm{T}}V dp$ is determined apart from an integration constant. Thus, even if ${}^{\mathrm{T}}V$ was zero, ${}^{\mathrm{T}}G$ could in principle be large.

The temperature dependencies of the interaction parameters ${}^{\nu}V_{\mathrm{i,j}}(T)$ and ${}^{\mathrm{T}}G(T)$ are generally weak. As will be shown below, they can be assumed linear in some cases:

$$ \begin{aligned} {}^{\nu}V_{\mathrm{i,j}}(T) &= {}^{\nu}A_{\mathrm{i,j}} + {}^{\nu}B_{\mathrm{i,j}} T \\ {}^{\mathrm{T}}V(T) &= {}^{\mathrm{T}}A + {}^{\mathrm{T}}B T \end{aligned} \tag{3.21} $$

A and B are constants in Eq. (3.21). From a practical point of view, it is usually more convenient to treat the volume interaction parameters as being independent of T, i.e. as constants.

3.2 Unary systems

In order to evaluate the excess volume of binary, ternary, and multicomponent systems, ${}^{\mathrm{id}}V$ must be known precisely. Therefore, the densities of the pure elements are determined with great care.

Figure 3.1 shows those sections of the periodic table being relevant in this context. The marked elements are those of which densities are measured. These are Al, the group Ib noble metals Cu, Ag, and Au, as well as the transition metals Ni, Co, Fe, and Ti. The latter are all from the fourth period.

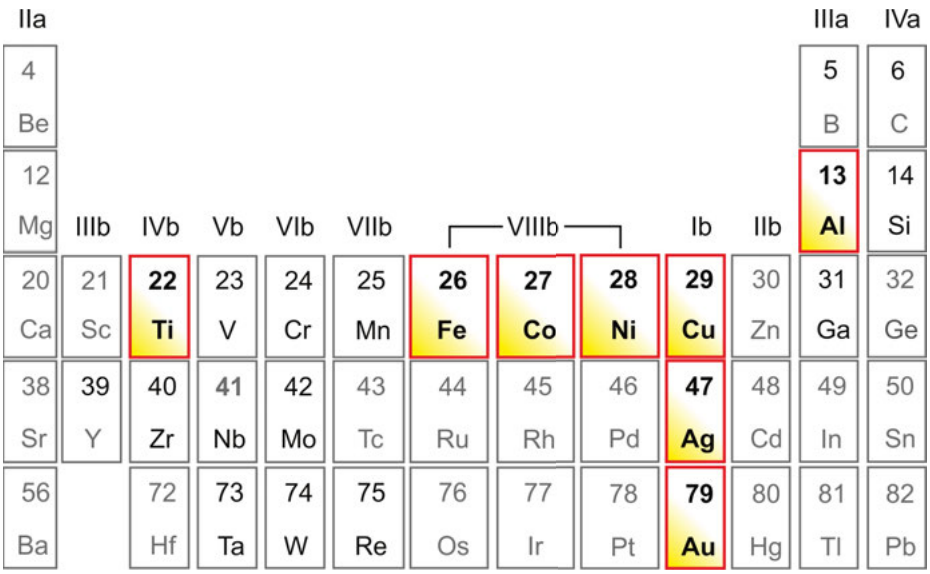

Fig. 3.1. Relevant section of the periodic table. Densities of the highlighted elements are measured in the liquid state and will be discussed below.

Table 3.1. Key of methods for density determination used in the tables below [27].

Key	Name
A	Archimedian methods
BP	Bubble pressure
EML	Electromagnetic levitation
ESL	Electrostatic levitation
EW	Exploding wire
G	γ-Absorption dilatometry
P	Pycnometer method
R	Recommended from literature review
SD	Sessile drop

The results for the density are compared with each other and with selected literature data in Figs. 3.2–3.4. Moreover, they are summarized in Tabs. 3.2–3.9 and compared therein with published results from literature. These are attached with a *key* specifying the method used for their determination. These keys are defined in Tab. 3.1. The key *R*, meaning "recommended", specifies that the listed value is obtained from a literature review. To some of them, the results of the present work have contributed as well (see, Refs. [63; 92; 93; 94; 95]). Furthermore, some of the literature data is picked from these or other review articles in which it partially went through a pre-selection process making sure that their error in accuracy is under a certain arbitrarily chosen

threshold. This threshold is around ±1.0 % in most cases. For this reason, the listed literature values are not strictly independent from one another.

3.2.1 Liquid Al

Density data of liquid Al is obtained in Refs. [15; 96; 97] as functions of temperature over ranges of $T_L \leq T \leq T+ 300$ K. Undercooling is not achieved.

The data is shown in Fig. 3.2 together with reference data from Assael [63] and Mills [12]. In the cases of the data published in Refs. [96] and [97], the densities change over the investigated temperature ranges linearly from ≈2.35 g · cm^{-3} at T_L to approximately 2.3 g · cm^{-3} at ≈ 1230 K. This data is in agreement with the results of Assael [63] with an overall deviation of less than 1.0 %. The recommended values of Mills [12] are only slightly larger. The data reported in Ref. [15] is approximately 2 % smaller than the ones of Refs. [96] and [97]. However, is is still within the margin of acceptance.

Equation (3.9) is fitted to the data and the obtained parameters ρ_L and ρ_T are listed in Tab. 3.2 together with other results from literature. Agreement is obtained in this table within ± 1.0 % for ρ_L and within ± 19.0 % for ρ_T. The uncertainty of ρ_T is generally much larger than for the density itself. This is because the temperature coefficient of the density is exposed to specific sources of error, such as evaporation, see Chap. 2. In addition, ρ_T is harder to measure as for its precise determination, data must be recorded over a sufficiently large temperature range. Often, this range is not fully accessible.

Table 3.2. Parameters ρ_L and ρ_T for the density of pure liquid Al measured in this work [96; 15; 97] (bold). The data is compared with selected data from literature. The experimental methods used are specified in the third column.

ρ_L (g · cm^{-3})	ρ_T (10^{-4}g · cm^{-3}K^{-1})	Method	Source
2.37	-2.6	A	[98]
2.39	-3.9	BP	[99]
2.37	-2.6	SD	[100]
2.38	-3.3	SD	[101]
2.37	-3.1	G	[102]
2.38	-2.3	G	[103]
2.38	-2.3	R	[12]
2.37	-3.1	R	[63]
2.36 ± 0.03	**-3.3 ± 0.03**	**EML**	**[96]**
2.36 ± 0.03	**-3.0 ± 0.03**	**EML**	**[97]**
2.29 ± 0.03	**-2.5 ± 0.03**	**EML**	**[15]**

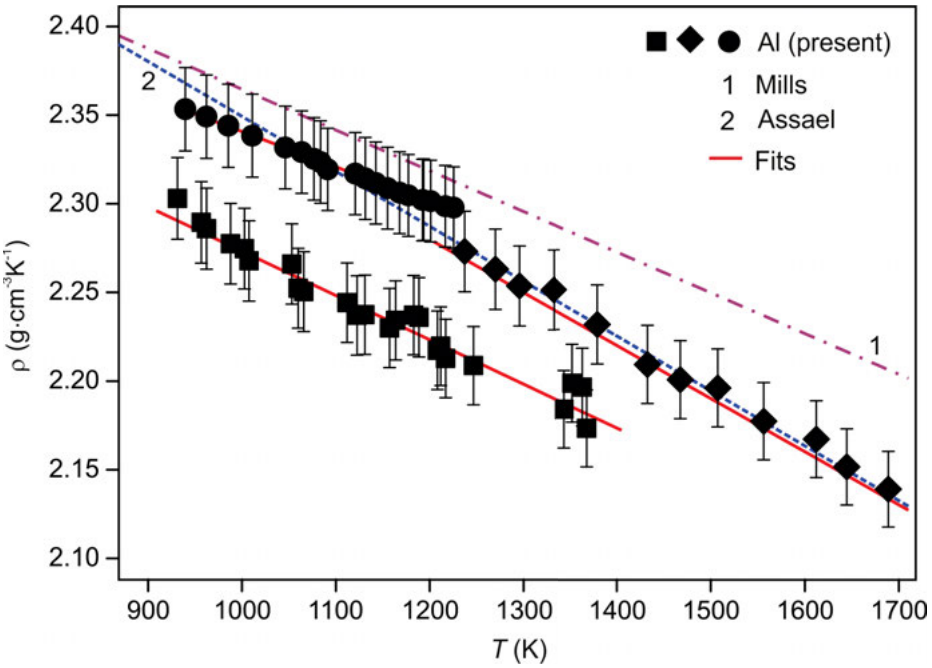

Fig. 3.2. Density of pure Al versus temperature [96; 97; 15] (symbols). For comparison, the representations reported by Mills [12] (1) and Assael [63] (2) are shown as lines as well.

On the other hand, ρ_T is relatively small compared to ρ. The ratio of the error in ρ_T to ρ, i.e. $\Delta\rho_T/\rho$, is in the order of 10^{-5}. Hence, over a temperature range of several 100 K, an uncertainty in ρ_T will not cause a significant uncertainty in the density with respect to the experimental accuracy of ρ.

3.2.2 Noble metals (Cu, Ag, Au)

Measured densities of the pure liquid noble or semi-noble metals, Cu [17], Ag [37], and Au [104] are plotted in Fig. 3.3 versus temperature. Again, all experimental data can be described by linear laws, i.e. by Eq. (3.9). Undercoolings are not achieved. Data is measured over temperature ranges of almost 400 K for Cu and 450 K for Au. In the case of liquid Ag, evaporation becomes pronounced and the corresponding mass loss becomes unacceptable when the temperature exceeds roughly T_L+200 K.

In addition to the strong evaporation at higher temperatures, another problem renders the levitation of pure liquid Ag, and Ag- containing alloys: An extended film of sulphur appears on top of the samples' surface as soon as it is molten. This occurs even though nominally high purity material is obtained from the supplier. The sulphur originates from chemical reactions of the solid material with gaseous or dissolved SO_2

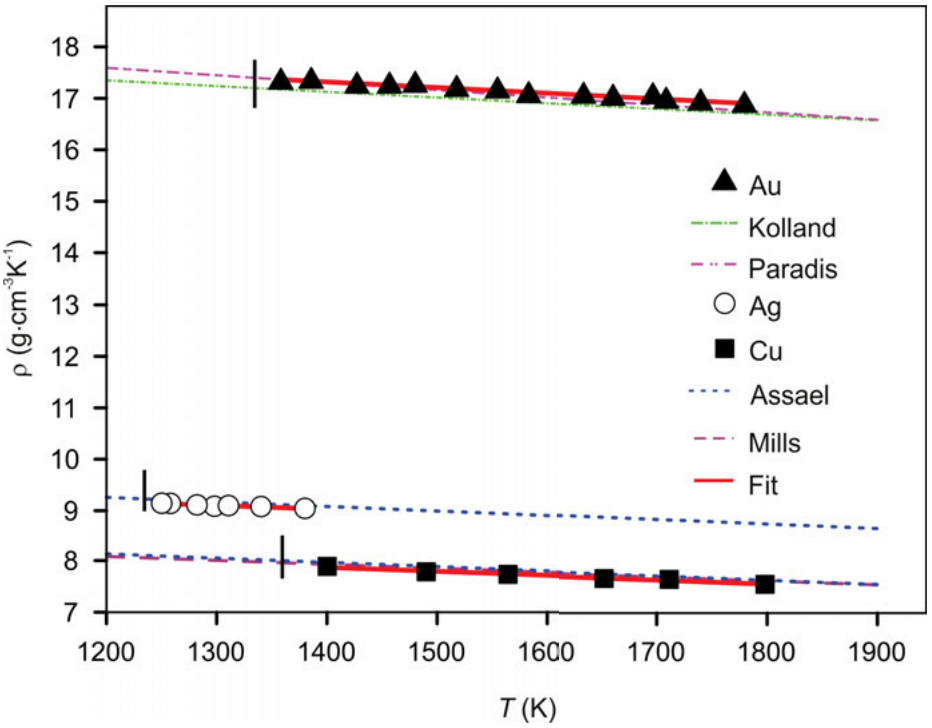

Fig. 3.3. Density of the pure metals Cu [17] (squares), Ag [37] (circles), and Au [104] (triangles) versus temperature. For comparison, the representations reported by Mills [12] and Assael for Cu [93], Assael for Ag [94] and Paradis [95] for Au are shown as lines, as well. The short vertical lines mark the positions of the corresponding liquidus temperatures, T_L.

when being *ex situ* in contact with water or air. The sulphur cannot be removed under the reducing conditions of a levitation experiment[2]. It is a particular problem for the temperature measurement as its emissivity is not constant with respect to time and temperature. Under these conditions, reliable temperature measurements are possible only, if the pyrometer is focused on a clean section of the surface area. In addition, the pyrometer signal, $T_{P,L}$, needs to be checked several times at the liquidus temperature T_L upon melting and solidification. As long as the temperature measurement can be carried out reliably, the sulphur layer on top of the droplet is not considered a severe problem for the density measurement. The error encountered this way is ≈ ±1.5 %, see Tab. 3.4.

2 As proved in later experiments, see Chap. 4, the sulphur layer can effectively be removed if, prior to the actual experiment, the silver is levitated and melted in air.

Table 3.3. Parameters ρ_L and ρ_T for the density of pure liquid Cu measured in this work [17] (bold). The data are compared with selected data from literature. The experimental methods used are specified in the third column.

ρ_L (g·cm^{-3})	ρ_T (10^{-4} g·cm^{-3}K^{-1})	Method	Source
8.03	-7.9	MBP	[105]
8.09	-9.4	EML	[106]
7.92	-8.4	EML	[107]
7.96	-7.6	R	[12]
8.02	-6.1	G	[103]
8.06	-7.8	A	[108]
8.00	-8.2	R	[93]
8.00	-10.0	BP	[109]
8.00	-8.3	A	[110]
8.03	-8.2	BP	[111]
8.05	-10	SD	[112]
8.18	-4.5	EW	[14]
7.98	-15	A	[113]
7.90 ± 0.1	**-7.65 ± 0.5**	**EML**	**[17]**

Table 3.4. Parameters ρ_L and ρ_T for the density of pure liquid Ag measured in this work [37] (bold). The data is compared with selected data from literature. The experimental methods used are specified in the third column.

ρ_L (g·cm^{-3})	ρ_T (10^{-4} g·cm^{-3}K^{-1})	Method	Source
9.23	-8.8	R	[94]
9.31	-9.7	G	[114]
9.32	-10.5	A	[115]
9.29	-8.3	BP, A	[116]
9.33	-11.1	BP	[111]
9.32	-9.8	A	[117]
9.28	-9.0	A	[118]
9.24	-6.5	A	[113]
9.29	-11.75	SD	[119]
9.15 ± 0.12	**-7.4 ± 0.8**	**EML**	**[37]**

The parameters ρ_L and ρ_T, obtained from fitting Eq. (3.9) to the experimental data, are listed in Tabs. 3.3–3.5 together with their respective uncertainties [17; 37; 104]. The concurrance with the literature data, also listed in Tabs. 3.3-3.5, is generally good. Over the investigated temperature ranges, the overall deviations between the literature data and the ones of the present work are approximately ±1.0 %. This is also seen in Fig. 3.3 where the experimental data is plotted together with the corresponding reference data of Mills [12], Assael [93; 94] and Paradis [95]. The relative uncertainties $\Delta\rho_T/\rho_T$ are about ±10 %.

Table 3.5. Parameters ρ_L and ρ_T for the density of pure liquid Au measured in this work [104] (bold). The data is compared with selected data from literature. The experimental methods used are specified in the third column.

ρ_L (g·cm^{-3})	ρ_T (10^{-4} g·cm^{-3}K^{-1})	Method	Source
17.3	-12.3	A	[118]
17.3	-13.4	A	[120]
17.2	-14.4	EW	[14]
17.4	-14.4	ESL	[95]
17.2	-12.7	SD	[121]
17.4	-16.1	A	[122]
17.3	-12.0	A	[113]
17.4 ± 0.1	**-11.0 ± 0.6**	**EML**	**[104]**

Table 3.6. Parameters ρ_L and ρ_T for the density of pure liquid Ni measured in this work [17; 123] (bold). The data is compared with selected data from literature. The experimental methods used are specified in the third column.

ρ_L (g · cm^{-3})	ρ_T (10^{-4}g · cm^{-3}K^{-1})	Method	Source
7.86	-6.7	ESL	[124]
7.89	-6.5	ESL	[125]
7.89	-12.1	EML	[126]
7.91	-11	EML	[107]
7.85	-12	R	[12]
7.68	-12.7	SD	[127]
7.81	-7.3	G	[103]
7.87	-9.9	R	[94]
7.89	-11.9	SD	[128]
7.84	-11.2	P	[62]
7.77	-16.8	A	[129]
7.76	-10.7	A	[130]
7.97	-11.6	A	[131]
7.94	-11.1	EML	[132]
7.91	-11.7	G	[116]
8.02	-12	BP	[133]
7.93 ± 0.1	**-10.1 ± 0.5**	**EML**	**[17]**
7.82 ± 0.1	**-8.6 ± 0.6**	**EML**	**[123]**

3.2.3 Transition metals (Ni, Co, Fe, Ti)

Density data of the pure liquid transition metals, Ni, [17; 123], Co [134], Fe [61; 123], and Ti [135] is plotted in Fig. 3.4 versus temperature. Undercoolings are archieved for all materials. In the case of Ni, data is obtained in a temperature range of approximately

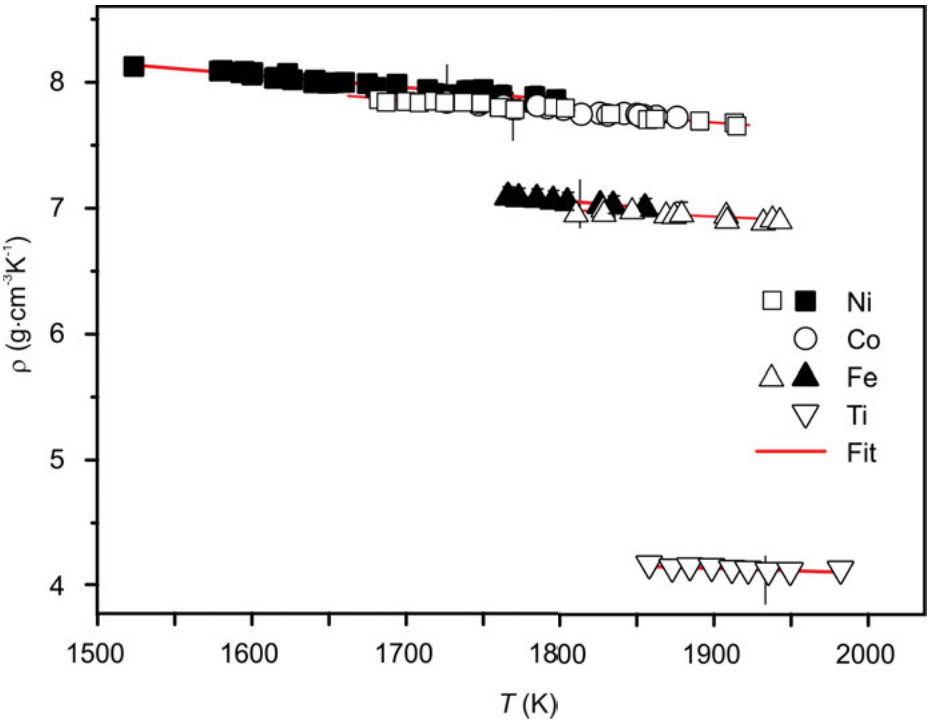

Fig. 3.4. Densities of liquid Ni [17; 123] (squares), Co [134] (circles), Fe [61; 123] (solid triangles), and Ti [135] (open triangles) versus temperature. The short vertical lines mark the positions of the corresponding liquidus temperatures, T_L.

$T_L - 220\ K \leq T \leq T_L + 200\ K$. For Co, the temperature range is $T_L - 70\ K \leq T \leq T_L + 100\ K$, for Fe, it is $T_L - 70\ K \leq T \leq T_L + 120\ K$, and in the case of Ti, data is obtained in a temperature range of approximately $T_L - 90\ K \leq T \leq T_L + 50\ K$.

Ni exhibits the largest and Ti the smallest density. The densities of Co and Ni are closer together. In fact, the density of Co is only 1.0 % smaller than that of Ni.

The obtained respective fit parameters ρ_L and ρ_T are listed in Tabs. 3.6–3.9 together with their corresponding uncertainties. In the cases of Ni, Co, and Fe, the observed temperature coefficients, ρ_T, are similar to each other, i.e. roughly $-10.0 \times 10^{-4} g \cdot cm^{-3} K^{-1}$.

Tables 3.6–3.9 also show parameters ρ_L and ρ_T of available literature data. Concurrence, within ±1.0 %, is obtained for Fe, Ni, and Co. In the case of pure Ti, the overall agreement is also good. However, the base of available literature data is smaller than for the other metals. In addition, the deviation among all data in Tab. 3.9 is almost 10 % and thus larger compared to the other metals.

The increased relative inaccuracy of the Ti data can be explained by three causes, acting together to some degree: The density of Ti is lower than that of the other metals.

Table 3.7. Parameters ρ_L and ρ_T for the density of pure liquid Co measured in this work [134] (bold). The data is compared with selected data from literature. The experimental methods used are specified in the third column.

ρ_L ($g \cdot cm^{-3}$)	ρ_T ($10^{-4} g \cdot cm^{-3} K^{-1}$)	Method	Source
7.81	-7.0	G	[136]
7.67	-11.8	A	[129]
7.76	-12.3	BP	[137]
8.02	-10.6	SD	[138]
7.78	-10.2	EML	[132]
7.76	-16.5	BP	[109]
7.75	-11.0	BP	[133]
7.75	-11.0	R	[12]
7.83	-9.4	R	[92]
7.81 ± 0.1	**-8.9 ± 0.1**	**EML**	**[134]**

A certain absolute error would have a larger impact on a relative scale. The processing temperature of Ti is larger than that of the other metals (T_L=1941 K). Evaporation is therefore more critical. In addition, Ti is chemically highly reactive. This provides an additional challenge at the high processing temperatures applied.

Table 3.8. Parameters ρ_L and ρ_T for the density of pure liquid Fe measured in this work [61; 123] (bold). The data is compared with selected data from literature. The experimental methods used are specified in the third column.

ρ_L ($g \cdot cm^{-3}$)	ρ_T ($10^{-4} g \cdot cm^{-3} K^{-1}$)	Method	Source
7.04	-8.2	P	[62]
7.18	-16.6	A	[129]
7.02	-8.5	EML	[132]
7.08	-12.3	BP	[109]
7.02	-9.3	A	[139]
6.98	-9.4	A	[130]
7.00	-8.2	EW	[14]
6.98	-5.7	G	[103]
6.98	-9.5	BP	[133]
7.04	-8.6	BP	[140]
7.03	-8.6	R	[12]
7.03	-9.3	R	[63]
6.99 ± 0.1	**-5.6 ± 0.2**	**EML**	**[123]**
7.04 ± 0.07	**-10.8 ± 0.1**	**EML**	**[61]**

Table 3.9. Parameters ρ_L and ρ_T for the density of pure liquid Ti measured in this work [135] (bold). The data is compared with selected data from literature. The experimental methods used are specified in the third column.

ρ_L ($g \cdot cm^{-3}$)	ρ_T ($10^{-4} g \cdot cm^{-3} K^{-1}$)	Method	Source
4.17	-2.2	ESL	[141]
4.10	-9.9	ESL	[142]
4.21	-5.1	ESL	[19; 143; 144]
4.14	-2.25	R	[12]
4.29	-2.3	EW	[14]
4.1 ± 0.4	**-3.3 ± 0.4**	**EML**	**[135]**

Table 3.10. Density of the investigated liquid elements. For each dataset, the table shows the name of the element, its atomic number Z, the liquidus temperature T_L, the parameters ρ_L and ρ_T including their uncertainty, and the literature reference.

Element	Z	T_L (K)	ρ_L ($g \cdot cm^{-3}$)	ρ_T ($10^{-4} g \cdot cm^{-3} K^{-1}$)	Source
Al	13	933	2.36 ± 0.03	-3.3 ± 0.03	[96]
			2.29 ± 0.03	-2.5 ± 0.03	[15]
			2.36 ± 0.03	-3.0 ± 0.03	[97]
Cu	29	1358	7.90 ± 0.1	-7.65 ± 0.5	[17]
Ag	47	1233	9.15 ± 0.12	-7.4 ± 0.8	[37]
Au	79	1333	17.4 ± 0.1	-11.0 ± 0.6	[104]
Ni	28	1727	7.93 ± 0.1	-10.1 ± 0.5	[17]
			7.82 ± 0.1	-8.56 ± 0.6	[123]
Co	27	1768	7.81 ± 0.1	-8.9 ± 0.1	[134]
Fe	26	1818	7.04 ± 0.07	-10.8 ± 0.1	[61]
			6.99 ± 0.1	-5.6 ± 0.2	[123]
Ti	22	1941	4.1 ± 0.4	-3.3 ± 0.4	[135]

3.2.4 Synopsis

For the pure elements discussed above, the obtained parameters ρ_L and ρ_T are listed together in Tab. 3.10. In addition, the appropriate liquidus temperatures T_L are also shown. The nearly monotone relation between ρ_L and the atomic number Z is obviously due to the fact that ρ is directly proportional to the molar mass. This also explains the observed large differences in density among the elements.

The physically relevant property which needs to be discussed is, however, the molar volume, V_m. It is shown in Tab. 3.11 for each of the investigated pure liquid el-

Table 3.11. Molar volumes of the investigated liquid elements. For each dataset, the table shows the atomic number Z, the molar volume V_L at T_L, the thermal expansion coefficient, β, atomic radii after Miracle, r_M [145], and Pauling, r_1 [146], as well as respective packing fractions δ_M and δ_1.

Element	Z	V_L (cm^3mol^{-1})	β (10^{-4} K^{-1})	r_M(Å)	r_1(Å)	δ_M	δ_1
Al	13	11.48	0.40	1.41	1.25	0.616	0.427
		11.79	1.10			0.600	0.416
		11.48	1.27			0.616	0.427
Cu	29	8.04	0.97	1.26	1.17	0.627	0.506
Ag	47	11.79	0.81	1.44	1.34	0.640	0.514
Au	79	11.32	0.63	1.43	1.34	0.652	0.531
Ni	28	7.40	1.27	1.26	1.16	0.682	0.532
		7.51	1.09			0.672	0.525
Co	27	7.55	1.14	1.24	1.16	0.638	0.518
Fe	26	7.93	1.53	1.26	1.17	0.636	0.503
		7.99	0.8			0.632	0.499
Ti	22	11.68	0.8	1.42	1.32	0.618	0.501

ements. Here, V_L, denotes the molar volume at the liquidus temperature and β the thermal volume expansion coefficient calculated from ρ_T using Eq. (3.10).

For all elements in Tab. 3.11, the thermal volume expansion coefficient β is of the order of 1.0×10^{-4} K^{-1} and almost constant. A significant scatter of ± 50 % is found, even among different measurements for the same element.

It is striking from Tab. 3.11 that, with respect to their molar volume, the listed elements can be subdivided into two groups: one group where V_L is between 11.0 and 12.0 cm^3mol^{-1} and another one with V_L attaining values around 7.5 cm^3/mol. The first group consists of Al, Ti, Ag, and Au. The second group contains the remaining transition metals, Ni, Fe, Co, and Cu.

In order to elucidate this observation, the corresponding atomic radii r_{at} are discussed as following. The concept of atoms having a radius is based on the idea that, under some circumstances, it is useful to describe them as hard spheres with defined radii. The volume of such a sphere is then given by $4/3\pi r_{at}^3$ and the total compact volume for one Mol of spheres is given by $V_{m,c} = 4/3\pi r_{at}^3 N_{Av}$ with $N_{Av} = 6.023 \times 10^{23} mol^{-1}$ being the Avogadro number.

The power of this concept, however, comes down to the right definition of r_{at}. In Ref. [146] two kinds of atomic radii, r_1 and r_{12}, are reported for each element: r_{12} corresponds to the half of the mean bond distance between atoms in a hexagonal close packed (hcp) structure with coordination number 12. These values are re-assessed by Miracle [145]. The corresponding radii, r_M, are listed in Tab. 3.11 as well. r_1 in Ref. [146] denotes the radius of an atom bonded in a dimer with the formal coordination number 1. The radii r_1 are approximately 5 % smaller than r_M and r_{12}. In a number of cases the Stokes-Einstein relation could partially be validated using r_1 for the hydro-

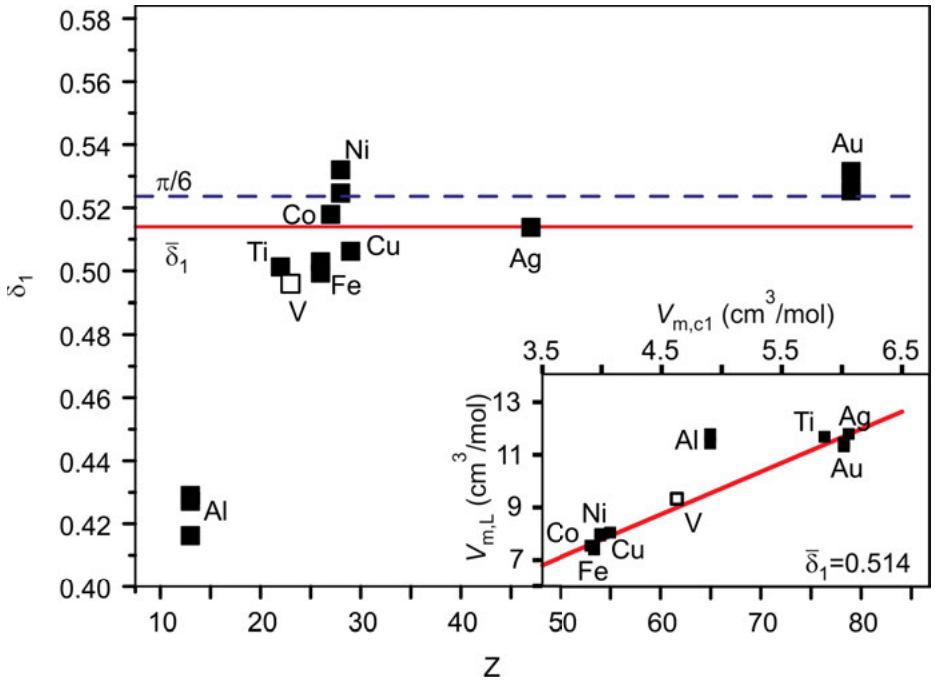

Fig. 3.5. Packing fraction δ_1 at liquidus versus atomic number Z. The inset shows V_L versus compact molar volume calculated using r_1. The solid line hereby corresponds to a fit of Eq. (3.22). Solid symbols: data measured in this work. Hollow symbol: Vanadium [149].

dynamic radius [147; 148]. Hence, r_1 may be more suited for the study of systems with mobile atoms. Such systems are liquid metals at $T > T_L$. For each element Tab. 3.11 also lists r_1.

Figure 3.6 shows a plot of the measured V_L versus $V_{m,c}$ calculated from the atomic radii r_M. Obviously, the two quantities are linearly related via the average volume packing fraction $\overline{\delta}$:

$$V_{m,c} = \overline{\delta} V_L \tag{3.22}$$

This also explains the fact why there are apparently two groups of elements with respect to their molar volume in Tab. 3.11. This is simply, because only elements with two classes of radii, smaller ones around 1.26 Å and larger ones around 1.41 Å, have been investigated. Vanadium, for instance, has an atomic radius of $r_{M,V}$ =1.35 Å [145] lying in between. Using the density data published by Paradis [149], it becomes obvious that the molar volume is also in the middle between the two groups. As shown in Fig. 3.6, Vanadium fits nicely into the scheme of Eq. (3.22).

If Eq. (3.22) is fitted to the plot in Fig. 3.6, a value of 0.633 is found for $\overline{\delta}$. This value is very close to the known packing fraction calculated by Bernal [150] for a dense stochastic mixture of spheres which is δ_{Stoch} =0.637.

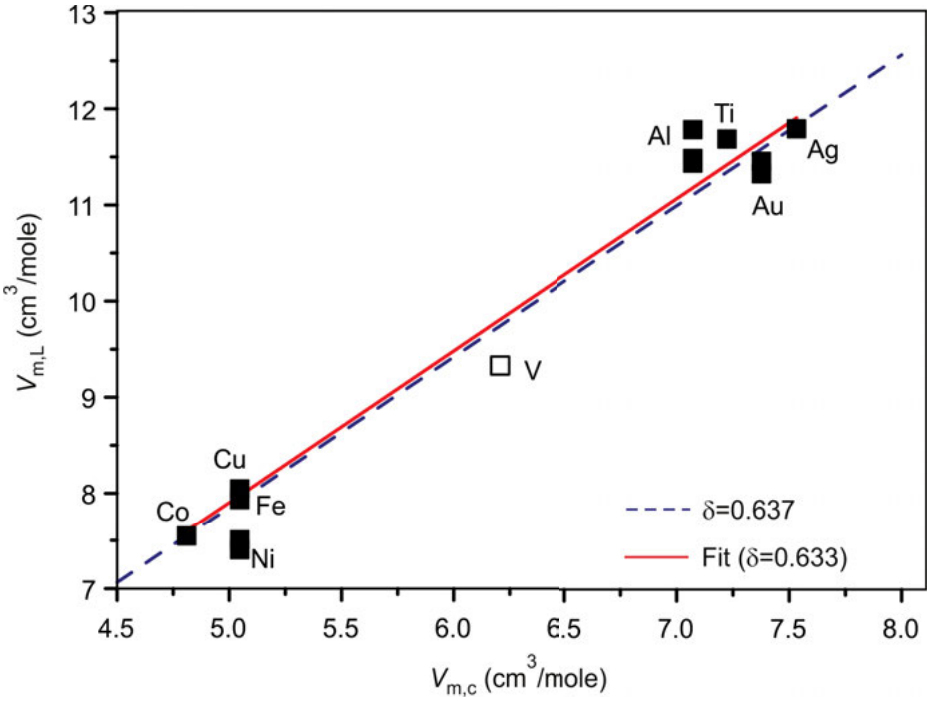

Fig. 3.6. Molar volume at liquidus temperature, V_L versus compact molar volume calculated using r_M for the data measured in this work (solid) and for Vanadium (hollow) [149]. The solid line represents a linear fit of Eq. (3.22). The dashed line represents a plot of Eq. (3.22) using for $\overline{\delta}$ the value of dense stochastic spheres, 0.637.

In colloidal systems, the critical packing fraction at the glass transition is 0.515. Hard sphere systems at the glass transition exhibit critical packing fractions of approximately 0.56. Hence, from the standpoint of dynamics, a packing fraction of 0.633, as obtained above, is rather non-physical in liquid metals at temperatures far above their glass transition temperature T_g.

Table 3.11 also lists packing fractions δ_1 calculated from r_1. As visible, δ_1 scatters around 0.5. This value seems to be physically more realistic. Figure 3.5 shows a plot of δ_1 versus the atomic number Z. With the exception of Al, the packing fractions are distributed around a mean value of $\overline{\delta}_1$ =0.514. This is remarkably close to the value of 0.515 for which colloidal systems perform the glass transition. Pure Al exhibits a significantly smaller packing fraction of δ_1=0.42.

In addition, the inset in Fig. 3.5 shows a plot analogous to Fig. 3.6 where V_L is plotted for each element versus the compact molar hard sphere volume $V_{m,c} = 4/3\pi r_1^3 N_{Av}$. Again, the validity of Eq. (3.22) is found for all the investigated elements, except Al.

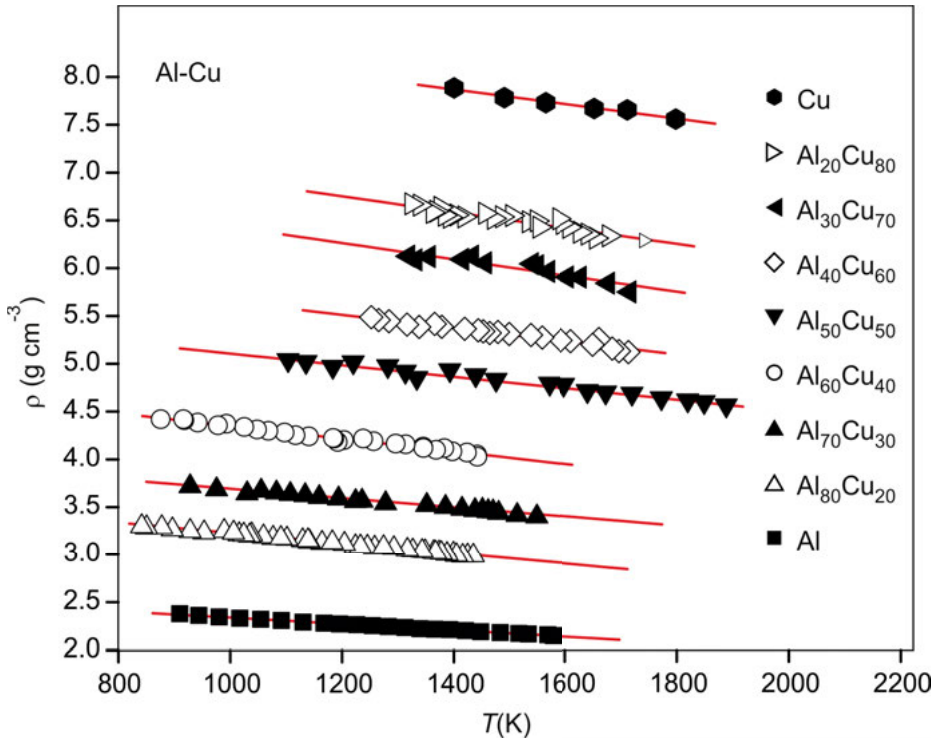

Fig. 3.7. Density of liquid Al-Cu versus temperature. The different symbols correspond to measurements for alloys with different composition. The lines represent fits of Eq. (3.9).

3.3 Binary systems

Starting from mono atomic systems, the investigations are now extended to their binary combinations. The following binary systems are investigated systematically: Cu-Ni [17], Cu-Fe [61], Co-Cu [134], Ag-Cu [37], Au-Cu [104], Ag-Au [37], Fe-Ni [61; 123], Co-Fe [134], Cr-Ni [123], Cr-Fe [123], Cu-Ti [135], Al-Cu [96], Al-Au [15], Ag-Al [96], Al-Ni [21], Al-Fe [21], Cu-Si [151], and Al-Si [97].

As an example, the binary Al-Cu [96] system is discussed in detail. Figure 3.7 shows the measured density data versus temperature for pure Al and Cu as well as for the binary alloys with Al concentrations ranging from 0 to 100 at.-%. Due to the good levitation stability and low vapor pressure of the Al-Cu samples, precise data is obtained, even in the broad temperature range of $T_L \leq T \leq T_L + 1000$ K. In order to analyze the concentration dependence, ρ is calculated using the corresponding parameters ρ_L and ρ_T from Eq. (3.9). This calculation is done for each composition at a constant temperature of 1400 K. This temperature is chosen so that it lies in the center

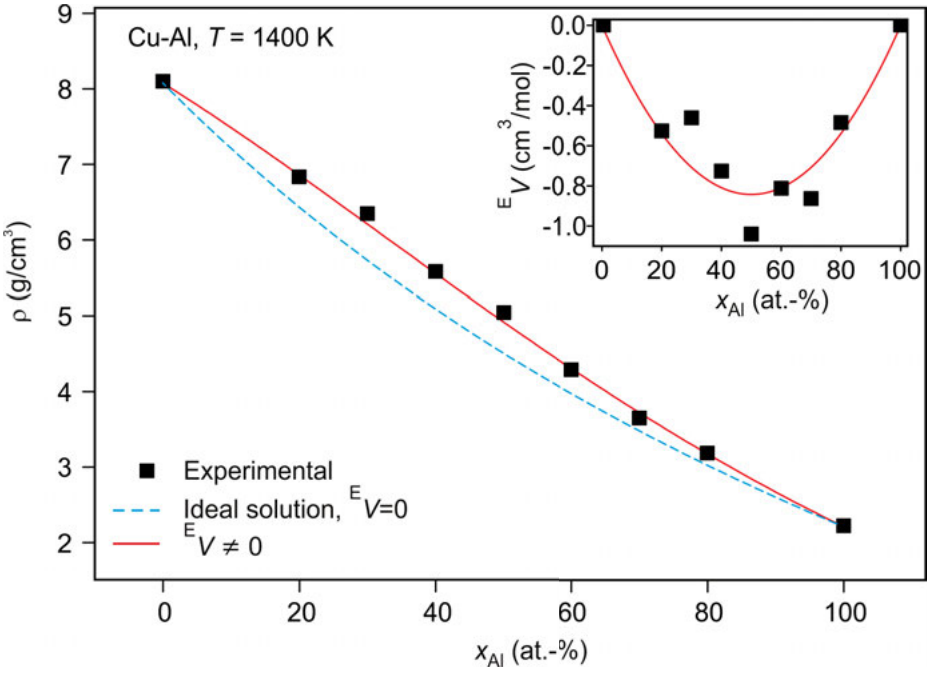

Fig. 3.8. Isothermal density of Al-Cu versus aluminium concentration x_{Al} (symbols) for T =1400 K. The solid line represents Eq. (3.6) with the excess volume adjusted in Eq. (3.19). The dashed line corresponds to the ideal solution, Eq. (3.15). The inset shows the measured excess volume versus x_{Al} which can be described by adjusting Eq. (3.19) (line).

of the temperature range common to all data in Fig. 3.7. The result is the isothermal density which is plotted in Fig. 3.8 versus the Al-mole fraction x_{Al}.

As visible from this figure, the density decreases with an increase of the Al concentration from a value of $\approx 8.0\ g \cdot cm^{-3}$, corresponding to the density of pure Cu, down to approximately $2.2\ g \cdot cm^{-3}$, which is the density of pure liquid Al at this temperature.

The dashed line in Fig. 3.8 represents the density of the ideal law, i.e. Eq. (3.15) where the excess volume ${}^{E}V_{Al,Cu} = 0$. A deviation of the measured density data from the ideal law towards larger values is clearly visible. In Fig. 3.8 it amounts to nearly 8 % of the magnitude of the ideal density and is largely compared to the experimental error of <1.5 %. Therefore, the excess volume ${}^{E}V_{Al,Cu}$ is negative in Al-Cu.

The solid line in Fig. 3.8 shows Eq. (3.6) with ${}^{0}V_{Al,Cu}$ obtained from a fit of Eq. (3.19). As visible, the agreement with the experimental data is far better than in the case of the ideal law. The experimental density data can also be used as an input to Eq. (3.6) in order to calculate the corresponding excess volumes as a function of the respective Al-mole fraction x_{Al}. This is shown by the inset in Fig. 3.8. In agreement with Eq. (3.19) the excess volume as a function of x_{Al} can be described by a parabola for Al-Cu. Equation (3.19) is found to be applicable to nearly all binary alloy systems

investigated in the present work. There are only two exceptions: Cu-Ti and Cu-Si. Their cases will be discussed further below. However, they still correspond with Eq. (3.18) of which Eq. (3.19) is a special case.

Generally speaking, the excess volume can be zero, positive, or negative. A negative excess volume is commonly associated with a process where smaller atoms fill voids between larger atoms. Such a process has been investigated in ball bearing mixtures [152], for instance, and a negative excess volume is found in all cases. Whether or not this simple picture can be transferred to liquid metals is, however, more than questionable [153]. For the investigated alloys, all the assumed cases are observed. Binary systems for which the excess volume is zero, or almost zero, are Fe-Ni, Co-Fe, Au-Cu, Ag-Cu, Ag-Au, and Al-Si. Binary alloy systems, for which a negative excess volume is found are Cu-Ni, Al-Cu, Ag-Al, Al-Au, Al-Ni, Al-Fe and Cu-Si. Alloys with a positive excess volume are Cr-Ni, Cr-Fe, Cu-Fe, Co-Cu, and Cu-Ti. The corresponding interaction parameters ${}^0V(T)_{i,j}$ and ${}^1V(T)_{i,j}$ according to Eq. (3.18) are listed for each binary system in Tab. 3.12. They are hereby assumed independent of temperature. Only for Cu-Ti is a small linear temperature dependence considered for both parameters.

Table 3.12. Parameters ${}^0V_{i,j}$ and ${}^1V_{i,j}$ used in Eq. (3.18) for the calculation of the excess volume of binary liquid alloys. In addition, the absolute maximum value of the excess volume relative to the ideal volume is shown.

System i,j	${}^0V_{i,j}$ (cm^3mol^{-1})	${}^1V_{i,j}$ (cm^3mol^{-1})	$\lvert {}^EV/{}^{id}V\rvert_{max}$	Source
Ag, Au	0		0	[37]
Ag, Cu	0		0	[37]
Al, Si	0		0	[97]
Au, Cu	0		0	[104]
Co, Fe	0		0	[134]
Fe, Ni	0		0	[61]
Ag, Al	-2.68		3.2 %	[96]
Al, Au	-2.24		5.0 %	[15]
Al, Cu	-3.37		7.7 %	[96]
Al, Fe	-1.7		14 %	[21]
Al, Ni	-5.0		22 %	[21]
Cu, Ni	-0.85		2.9 %	[17]
Cu ,Si	0	-5.45	6.5 %	[151]
Co, Cu	0.45		1.5 %	[134]
Cu, Fe	0.65		2.0 %	[61]
Cu, Ti	$1.97+1.15\cdot10^{-3}T$	$6.81-2.65\cdot10^{-3}T$	16 %	[135]
Cr, Fe	0.28		1.0 %	[123]
Cr, Ni	0.74		2.0 %	[123]
Fe, Ni	0.51		1.5 %	[123]

In order to discuss the non-ideality of the investigated alloys, the absolute maximum value of the excess volume relative to the ideal volume, $\alpha = |{}^{\mathrm{E}}V/{}^{id}V|_{\max}$ is shown in Tab. 3.12. Values range from 1.5 % for Co-Cu to 22 % for Al-Ni. With the exception of Cu-Ti, the largest values of α are found in systems with a negative excess volume. From large values of α to smaller ones, the investigated systems can be arranged in the following order: Al-Ni > Cu-Ti > Al-Fe > Al-Cu > Al-Au > Ag-Al > Cu-Ni > Cu-Fe > Cr-Ni > Co-Cu > Fe-Ni > Cr-Fe. Hence, with respect to the molar volume, Al-Ni is the most non-ideal and Cr-Fe the least non-ideal among the non-ideal binary systems investigated.

The systems Cu-Ti and Cu-Si in Tab. 3.12 form exceptions. Unlike the other alloys, their excess volumes cannot be represented using Eq. (3.19) with ${}^{0}V(T)_{\mathrm{i,j}}$ being the only parameter. For Cu-Ti, two parameters, ${}^{0}V(T)_{\mathrm{Cu,Ti}}$ and ${}^{1}V(T)_{\mathrm{Cu,Ti}}$ are necessary in Eq. (3.18) to account for the deviation of the excess volume from the parabolic shape [135]. It has already been suggested in section 3.1 that this case is theoretically possible. Here, an example is presented, where this actually occurs in a liquid metallic system.

The inclusion of higher order terms in Eq. (3.18) may become necessary, if the sizes of the particles in the mixture strongly deviate from one another. In organic chemistry, this is long known [88]. In fact, the mismatching of the atomic radii (r_{M} or r_1, see Tab. 3.11), is up to ≈12 % for Cu and Ti [135]. This is the largest mismatch among the systems investigated. The difference among the atomic radii is also quite large in Al-based systems. A small first order term, ${}^{1}V(T)_{\mathrm{i,j}}$, can, in principle, be adjusted to the excess volumes of the other systems as well. A small deviation of ${}^{\mathrm{E}}V$ from the parabolic shape is evident in every system. As long, as this deviation is small, it should be ignored, i.e. ${}^{1}V_{\mathrm{i,j}}(T)$ ≈0, in order minimize the number of free parameters in Eq. (3.18). On the other hand, there is no obvious reason, why a situation where ${}^{0}V(T)_{\mathrm{i,j}} = 0$ and ${}^{1}V(T)_{\mathrm{i,j}} \neq 0$ should be forbidden. It would correspond to a case in which the excess volume as a function of concentration is changing sign. Cu-Si [151] seems to be an example for such a system. In the work of Adachi [151] alloys with a Si content of up to 40 at.-% are processed. For higher Si-concentrations, levitation becomes difficult. Sample rotations in particular become too strong and the droplet is also no longer fully visible. In the data obtained so far, a minimum of the negative excess volume is found at x_{Cu}=80 at.-%, as shown in Fig. 3.9. The position of this minimum is believed in Ref. [151] to be associated to the composition of the intermetallic phase, Cu_3Si. Although intermetallic phases are stable at lower temperatures and in the solid state only, it is sometimes believed that precursors already exist in the melt, if the temperature is close to, or even smaller than T_{L}. For Cu-Si, most likely, this interpretation is wrong: Adjusting Eq. (3.18) to the excess volume in Fig. 3.9 yields ${}^{0}V(T)_{\mathrm{Cu,Si}}$ ≈0 and ${}^{1}V(T)_{\mathrm{Cu,Si}}$ =-5.46 cm^3/mol, see Tab. 3.12. Using these parameters, Eq. (3.18) is plotted in Fig. 3.9. As is visible, the curve predicts a change of sign of the excess volume as a function of composition: ${}^{\mathrm{E}}V_{\mathrm{Cu,Si}}$ is negative for x_{Cu} > 50 at.-% with the minimum reproduced correctly at x_{Cu} =80 at.-%. In addition, ${}^{\mathrm{E}}V_{\mathrm{Cu,Si}}$ is positive for x_{Cu} < 50 at.-% with a predicted maximum at x_{Cu} =20 at.-%. At this composition, no intermetallic

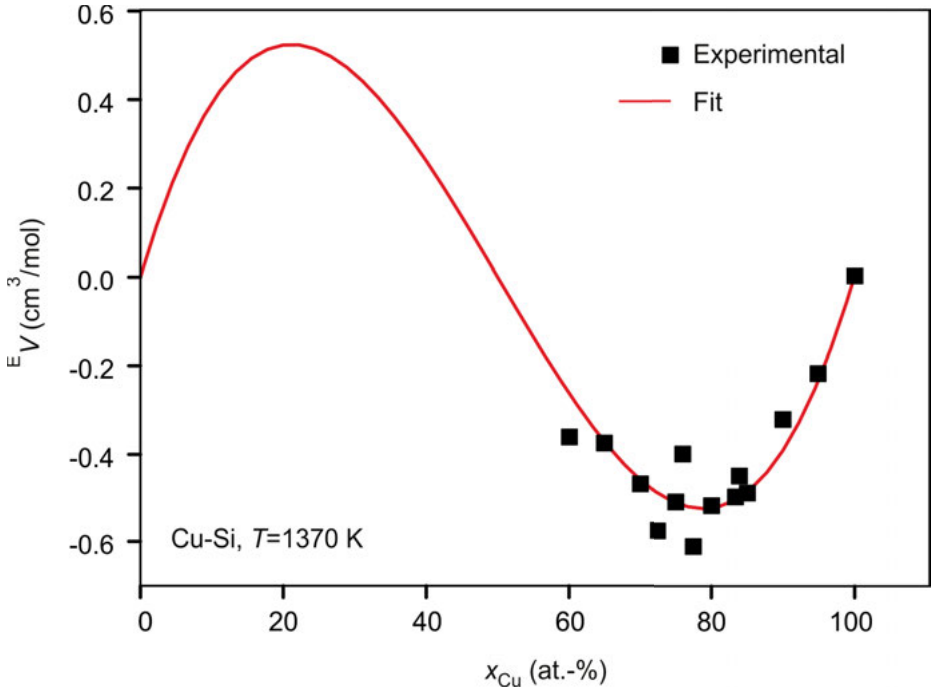

Fig. 3.9. Excess volume of binary Cu-Si at 1370 K. The solid line is a fit of Eq. (3.18) yielding ${}^0V_{Cu,Si} = 0$ and ${}^1V_{Cu,Si} \neq 0$.

phase is evident in the phase diagram [154]. For $x_{Cu} = 50$ at.-% ${}^{E}V$ equals zero, even though Cu-Si is by no means an *ideal* system.

Coming back to the example of Al-Cu [96], a plot of the temperature coefficient, $\rho_T = \partial\rho/\partial T$ versus x_{Al}, is shown in Fig. 3.10. With increasing aluminium concentration, there is a general tendency of ρ_T towards larger values. A weak minimum exists at $x_{Al} \approx 30$ at.-%. With respect to the uncertainty of the data it may, however, be negligible [155]. The dashed curve in Fig. 3.10 shows a calculation of ρ_T according to Eq. (3.11) with the excess volume being set to zero, i.e. in the case of the ideal law. In addition, the temperature derivative of the excess volume $\partial^{E}V/\partial T$ is usually very small [15; 17; 96; 37]. Therefore, it, too, is neglected. Although there are systematic deviations of the experimental data from this curve, the agreement can be regarded as positive with respect to the experimental error. An even better agreement can be obtained, if the excess volume is not ignored in Eq. (3.11). In this case, even the small minimum $x_{Al} \approx 30$ at.-% is reproduced correctly.

Setting $\partial^{E}V/\partial T = 0$, Eq. (3.11), becomes:

$$\rho_T = \frac{\left[\sum_i x_i M_i\right] \times \left[\sum_i x_i \frac{M_i \rho_{T,i}}{\rho_i^2}\right]}{({}^{id}V + {}^{E}V)^2} \tag{3.23}$$

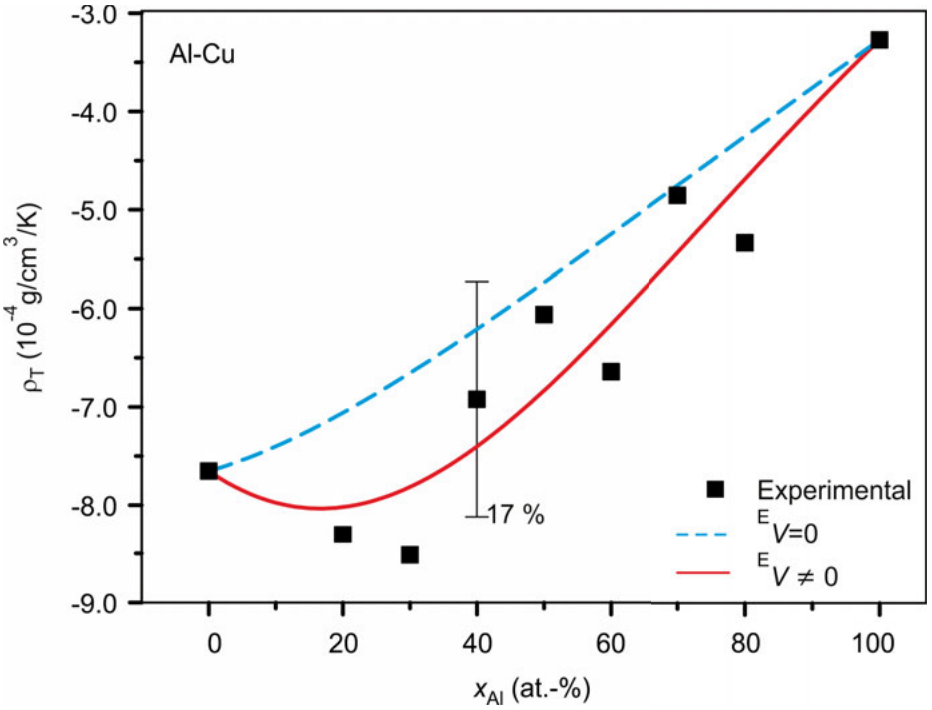

Fig. 3.10. Temperature coefficient ρ_T of liquid Al-Cu versus x_{Al}. The dashed line is calculated from Eq. (3.24) and the solid line from Eq. (3.23).

It is noteworthy to mention that, except for the excess volume, this formula depends only on properties of the pure elements. Therefore, the problem of predicting the thermal expansion coefficient can be reduced to understanding the excess volume. If even the excess volume is ignored, a simple recipe is obtained for the estimation of the thermal expansion coefficient of the density of alloys from only the pure elements:

$$\rho_T \approx \frac{\left[\sum_i x_i M_i\right] \times \left[\sum_i x_i \frac{M_i \rho_{T,i}}{\rho_i^2}\right]}{(^{id}V)^2} \tag{3.24}$$

Equations (3.23) and (3.24) are found to be applicable to all alloy systems, binary and ternary, being investigated in the present work.

3.4 Ternary systems

The investigations of the binary systems can be extended to ternary alloys. The focus hereby is put on the question whether or not results obtained for the binary alloys are transferable to a ternary system, i.e. if the ternary term needs to be included into Eq. (3.20) (**Q:3**). For example, Fig. 3.11 shows a plot of the isothermal density of a section

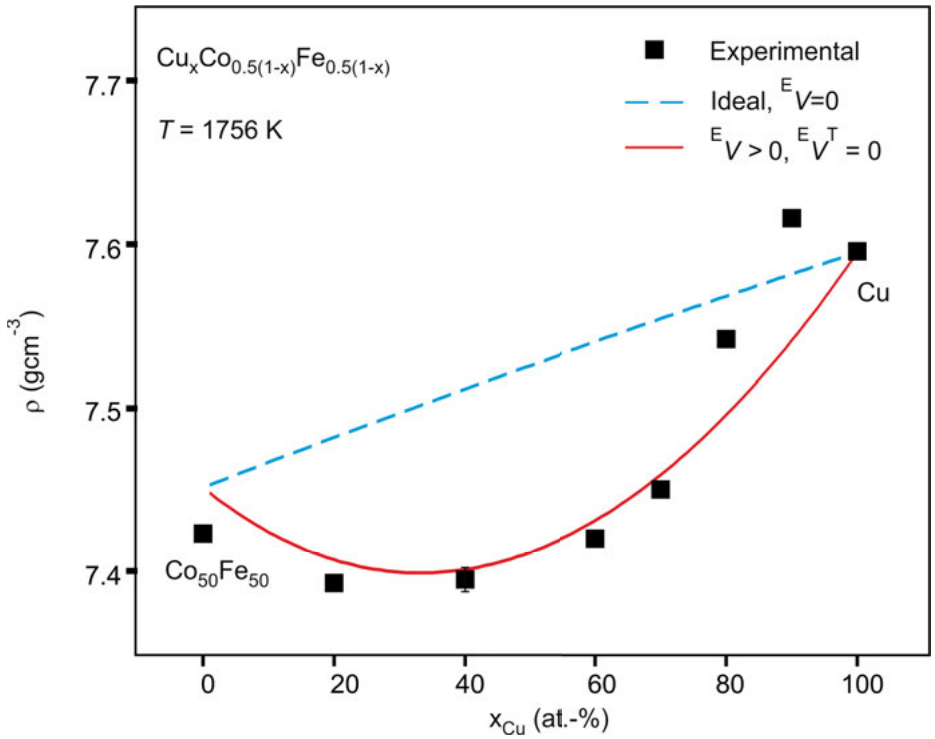

Fig. 3.11. Isothermal densities of liquid Co-Cu-Fe alloys at T=1756 K plotted versus x_{Cu} along a section from $Co_{50}Fe_{50}$ to pure copper. The lines represent calculations of Eq. (3.20) for ^{E}V=0 (dashed) and $^{E}V_{i,j} \neq 0$ (solid). In both cases, the ternary volume interaction parameter ^{T}V equals zero.

through the ternary Co-Cu-Fe system versus the copper concentration x_{Cu} at T =1756 K [134]. In this section, x_{Cu} is varied from 0 to 100 at.-% and the ratio of x_{Co} to x_{Fe} is 1:1. The involved binary subsystems are Co-Cu [134], Cu-Fe [61], and Co-Fe [134], see Tab. 3.12.

The obtained densities are all in a range between 7.4 to 7.6 g·cm^{-3}. For x_{Cu} > 80 at.-% they are identical with the corresponding ideal law and appear significantly lower for x_{Cu} < 80 at.-%. In this concentration range, the excess volume is positive and the experimental data agrees well with a calculation using Eq. (3.20) with the ternary interaction parameter ^{T}V being set to zero and binary volume interaction parameters $^{v}V_{i,j}$ from Tab. 3.12. In the same way, the density measured along a second cut through the ternary system can also be derived from the binary boundary systems [134]. Hence, in this special case the densities can be predicted from those of the binary subsystems using Eq. (3.20) [156].

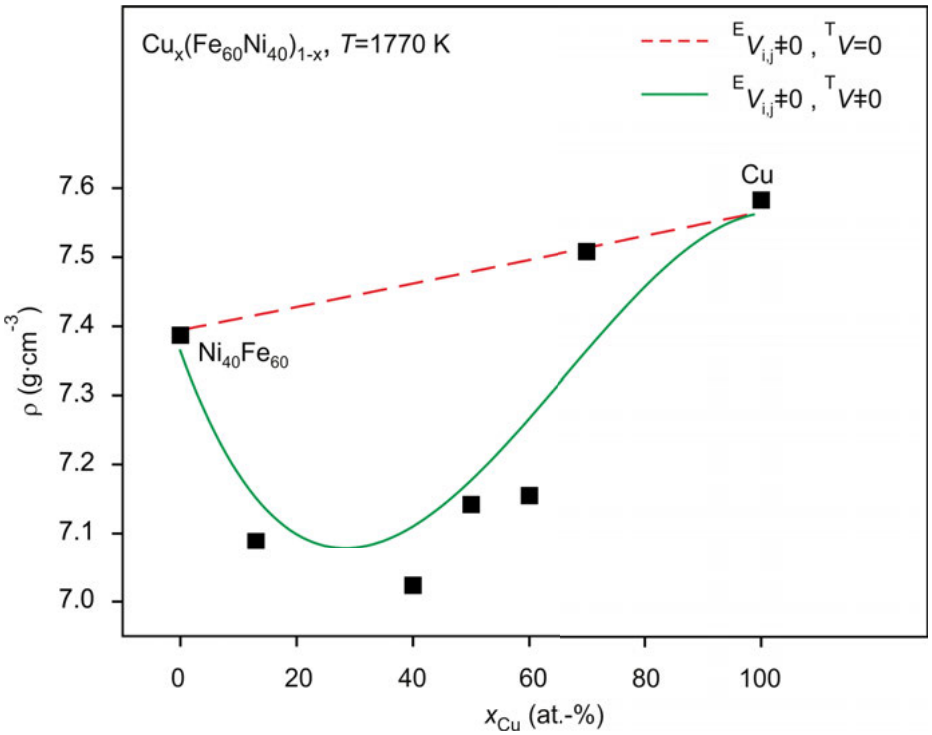

Fig. 3.12. Isothermal densities of liquid Cu-Fe-Ni alloys at T=1770 K plotted versus x_{Cu} along a section from $Ni_{40}Fe_{60}$ to pure copper. The lines represent calculations of Eq. (3.20) with $^{E}V \neq 0$ and $^{T}V = 0$ (dashed) as well as $^{E}V_{i,j} \neq 0$ and $^{T}V \neq 0$ (solid).

Table 3.13. Ternary volume interaction parameter ^{T}V for the investigated ternary alloys.

System	^{T}V (cm^{3}mol^{-1})	Reference
Ag-Al-Cu	0	[157]
Al-Cu-Si	19.7	[158]
Co-Cu-Fe	0	[134]
Co-Cu-Ni	-12.0	[159]
Cr-Fe-Ni	0	[160]
Cu-Fe-Ni	11.5	[161]

Similar results are found for the systems Cr-Fe-Ni [160], and Ag-Al-Cu [157]. However, ^{T}V is generally not zero. This is shown in Fig. 3.12 and 3.13 for two sections through the ternary system Cu-Fe-Ni, respectively [161].

In these figures, the measured density data is significantly smaller than the curve predicted only from the binary phases, i.e. where $^{T}V = 0$. If a positive ternary parameter, ^{T}V =11.5 cm^{3}mol^{-1}, is taken into account, the densities can be reproduced for both

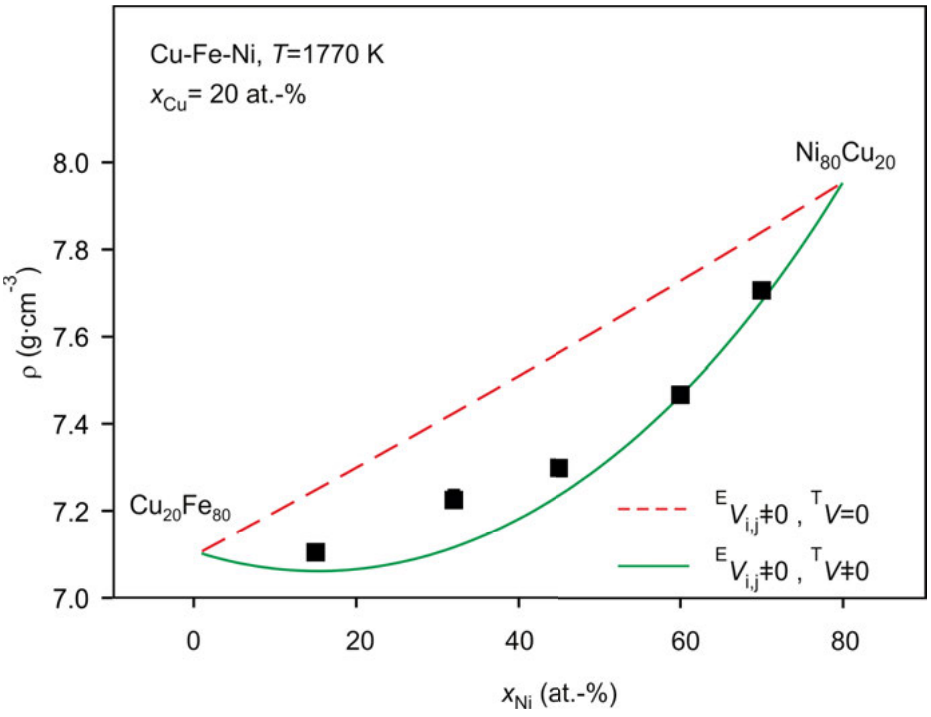

Fig. 3.13. Isothermal densities of liquid Cu-Fe-Ni alloys at T=1770 K plotted versus x_{Ni} along a section from $Cu_{20}Fe_{80}$ to $Cu_{20}Ni_{80}$. The lines represent calculations of Eq. (3.20) with ${}^{E}V \neq 0$ and ${}^{T}V = 0$ (dashed) as well as ${}^{E}V_{i,j} \neq 0$ and ${}^{T}V \neq 0$ (solid).

sections. Co-Cu-Ni [159] and Al-Cu-Si [158] are two other systems, where a ternary volume interaction parameter is needed. In Co-Cu-Ni, the excess volume is negative and the ternary interaction parameter, ${}^{T}V$ =-12.0 cm^3mol^{-1}.

These examples show that the influence of the ternary parameter, ${}^{T}V$, on the density can be quite large. In Cu-Fe-Ni and Co-Cu-Ni, ${}^{T}V$ actually dominates the density.

Results on densities of the investigated ternary systems are summarized in Tab. 3.13 by means of their ternary volume interaction parameter, ${}^{T}V$.

3.5 Observed trends

With regard to the question whether there is any rule of thumb for the prediction of the excess volume and the density of a multicomponent system (**Q:1**), the molar volume V_m at 1773 K is plotted versus the compact molar volume, $V_{m,cM}$, in Fig. 3.14 for all investigated alloys. A similar plot to the one shown in Fig. 3.6 for the pure elements is produced for the alloys. $V_{m,cM}$ is calculated from $r_{M,Alloy}$ whereas $r_{M,Alloy}$ is obtained

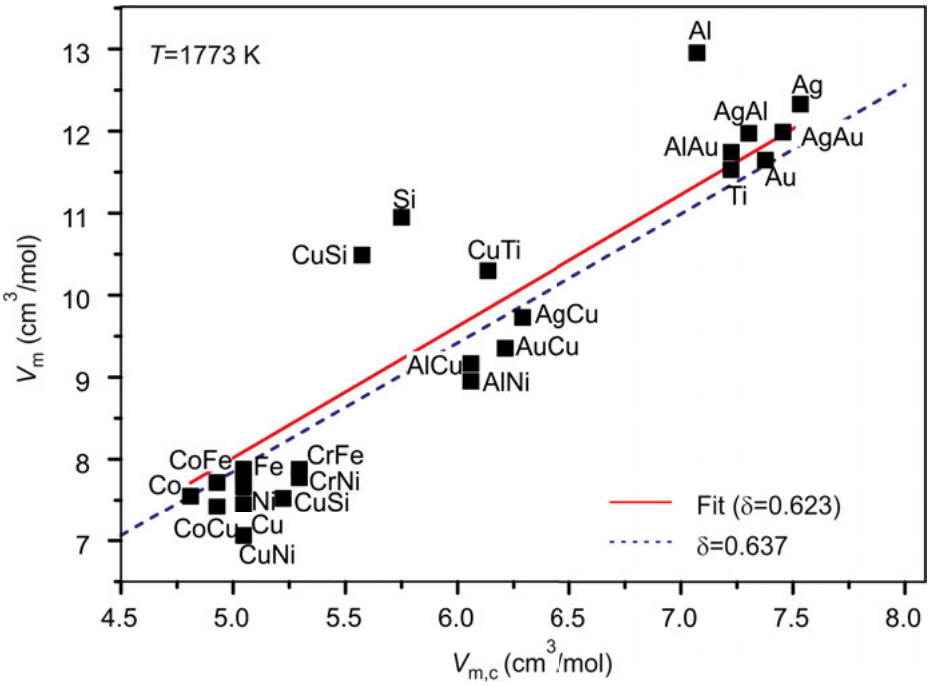

Fig. 3.14. Molar volume V_m versus compact molar volume $V_{m,cM}$ at 1773 K for all investigated alloys and pure elements. The solid line represents a fit of Eq. (3.22). The dashed line shows a calculation of Eq. (3.22) with an average packing fraction $\overline{\delta}$ of 0.637 corresponding the an irregularly packed dense mixture of spheres [150].

from the atomic radii $r_{M,i}$ [145] (i =element) according to $r_{\mathrm{M,Alloy}} = \sum_i x_i r_{\mathrm{M,i}}$. The data scatter in Fig. 3.14 around the straight line of Eq. (3.22) with $\overline{\delta}$ =0.623. Again, this value is close to the packing fraction of a dense mixture of stochastically arranged spheres, which is 0.637 [150].

The investigated alloys can roughly be assigned to three distinct classes as shown in Tab. 3.14:

Class I contains systems with positive excess free energy, ${}^{\mathrm{E}}G > 0$, and in which one element is Cu and the others are transition metals.

Class II contains alloys, in which the elements are similar with respect to their electronic configuration, i.e. which either belong to the same group of the periodic table or which are all transition metals. Al and Si do not belong to the same group of the period table. Moreover, Al is a metal and Si a semiconductor[3].

3 Si becomes metallic at high temperatures and its electronic configuration, $[\mathrm{Ne}]2s^2 3p^2$ is similar to one of Al which is $[\mathrm{Ne}]2s^2 3p^1$. They form a eutectic system and weakly interact in the liquid ${}^{\mathrm{E}}G \approx 0$. For the latter reasons, Al-Si is also assigned to class II.

Table 3.14. Observed trends in the excess volume of the investigated alloys.

Class	System	Sign of ${}^{E}V$	Reference
I	Cu-Fe	+	[61]
	Co-Cu		[134]
	Cu-Co-Fe		[134]
	Cu-Fe-Ni		[161]
	Cu-Ni	-	[17]
	Co-Cu-Ni		[159]
II	Ag-Au	≈0	[37]
	Ag-Cu		[37]
	Al-Si		[97]
	Au-Cu		[104]
	Co-Fe		[134]
	Fe-Ni		[61]
	Cr-Fe-Ni	+	[160]
	Fe-Ni		[123]
	Cr-Ni		[123]
	Cr-Fe		[123]
III	Ag-Al	-	[96]
	Al-Au		[15]
	Al-Cu		[96]
	Al-Fe		[21]
	Al-Ni		[21]
	Cu-Ti	+	[135]
	Cu-Si	+/-	[151]
	Al-Cu-Si	≈ 0	[158]
	Ag-Al-Cu		[157]

Class III, finally, contains systems with strong attractive interactions, i.e. where ${}^{E}G << 0$. Such systems are the Al-based alloys, except Al-Si. In addition, Cu-Si and Cu-Ti are also assigned to the third class as ${}^{E}G << 0$ for these systems. As Ti is a transition metal, the Cu-Ti system could also have been assigned to class I, but its strongly negative excess free energy is rather typical for alloys in class III.

Obviously, the systems in class I have a positive excess volume. Among the six systems listed, Cu-Ni and Co-Cu-Ni are the only exceptions where negative excess volumes are exhibited.

In class II, the excess volumes of the systems are approximately zero. This class contains 10 systems and is the largest among the three. In Ref. [61] it is claimed that Fe-Ni is an ideal system and that its excess volume is negligible. Measurements recently performed by Kobatake [123] using the same apparatus indicate that ${}^{E}V_{Fe,Ni}$ might indeed be slightly positive. Exceptions in this class are the systems Fe-Ni, Cr-Fe, and Cr-Ni for which ${}^{E}V_{i,j} > 0$ [123].

The systems in class III exhibit a negative excess volume, except Cu-Ti, of which the excess volume is positive, Cu-Si of which the excess volume changes sign as a function of composition, Ag-Al-Cu and Al-Cu-Si. In the cases of Ag-Al-Cu and Al-Cu-Si, the binary margins are the highly non-ideal systems Al-Cu, Ag-Al and Cu-Si. Thus, one would expect that the ternary systems would also exhibit pronounced excess volumes. However, this is not the case. The ternary volume interaction parameters ${}^{T}V$ compensate for the effect of the binary systems. For the other systems in this class the excess volume is large compared to the corresponding ideal volume (see also Tab. 3.12). These systems are, therefore, highly non-ideal, not only with respect to their free energy G, but also due to their molar volume.

The scheme in Tab. 3.14 can be interpreted as a rough tendency that alloys with a positive excess free energy also have a positive excess volume and alloys with negative excess Gibbs energy exhibit a negative excess volume. However, this scheme is by no means a strict rule. The latter becomes evident from the exceptions in Class I, Cu-Ni and Co-Cu-Ni, and the exceptions in Class III, Cu-Ti and Cu-Si. For Cu-Ni and Co-Cu-Ni ${}^{E}G > 0$ but the excess volume is negative. For Cu-Ti, on the other hand, ${}^{E}G << 0$ with ${}^{E}V >> 0$. For Cu-Si, finally, ${}^{E}G << 0$ and the excess volume can be positive and negative.

Therefore, a tendency for the excess volume is evident but there is no strict correlation between ${}^{E}V$ and ${}^{E}G$.

This finding is in agreement with the results of a simulation study performed by Amore and Horbach [162] on symmetric binary modified Lennard-Jones mixtures. The term “symmetric” here means identical interaction potentials are used in order to describe the interactions between the same kind of particles (A-A and B-B). For different kind of particles (A-B) a distinguished potential is used. The excess volume and the energy of mixing are calculated as function of composition whereas the influence of the depth of the A-B potential as well as its long range attractive part are studied. The main result of their study is that the sign of the excess volume is determined from a subtle interplay between the long range and short range parts of the interatomic potentials. For both, mixing and demixing systems, negative, zero, or positive excess volumes are found.

3.6 Explanation attempts

In order to understand the physics causing an excess volume and, thus, trying to understand the scheme of Tab. 3.14, it is no longer sufficient to study the systems on a macroscopic level. In fact, additional methods, such as X-ray- or coherent neutron diffraction analysis, need to be employed in order to yield information about the atomic short range order.

Another option, is provided by the opportunity to carry out molecular dynamics simulation (MD) studies. Provided, a suitable interaction potential exists, density and excess volume can be calculated and compared with the experimental data. In

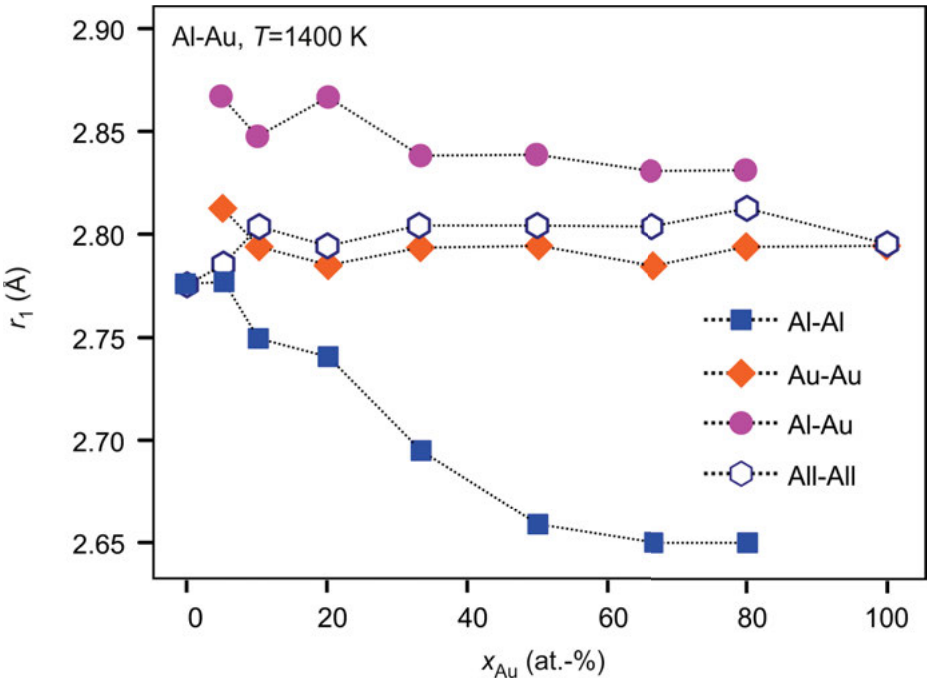

Fig. 3.15. Evolutions of the first maxima, $r^{(1)}$, of the partial radial distribution functions $g_{i,j}(r)$, with i, j as labeled, and the total RDF $g(r)$ (labeled "all"), with x_{Au}.

addition, radial distribution functions (RDF's) $g_{i,j}(r)$ can be determined providing information about the short range order.

Such investigations are carried out for the system Al-Au [15]. For this purpose, an embedded atom model (EAM) potential is developed and adjusted to the available experimental data, Tab. B.4, according to a procedure described in Ref. [15]. The potential developed this way correctly predicts the measured density, thermal expansion, excess volume and viscosity.

As further discussed in Ref. [15], the calculated radial partial distribution functions of unlike atoms, $g_{Al,Au}(r)$, do not vary with composition for x_{Au} ≥10 at.-%. This suggests that in these alloys, the main effect of mixing takes place by Au atoms effectively replacing Al atoms when x_{Au} is increased. Moreover, the radial distribution functions, $g_{Al,Au}(r)$, exhibit a pronounced split in the second maximum which is about 20 % of the atomic radii. This rules out pure geometric packing arguments as a potential cause. Instead, it can be concluded that in liquid Al-Au alloys, densely packed units [15] arise through chemical interaction. These units lead to an overall reduction in volume.

Such features are also observed experimentally in the systems Al-Cu and Al-Ni, investigated in x-ray diffraction experiments [163].

The evolutions of the first maximum $r^{(1)}$ of the different partial RDF's as functions of x_{Au} are shown in Fig. 3.15 for a temperature of 1400 K.

For Al-Au- and Au-Au bonds, $r^{(1)}$ varies only weakly with composition. Moreover, the Al-Al nearest-neighbor distance decreases monotonically with increasing x_{Au} [15]. This observation drastically contradicts any theory according to which the packing of atoms can be described by hard-spheres. In effect, Al becomes compressed in the presence of a second, more densely packed species. The observed behavior indicates that the Al-Al interactions are descriptively "softer" as those of Au-Au. Thus, Al atoms are able of becoming accommodated in the Au-dominated structure by reducing their interatomic distances.

This, together with the fact that mixing in Al-Au occurs mainly by substitution of foreign atoms into the denser structure, explains the large negative excess volume of this particular system [15].

In the scheme of Tab. 3.14, Al-Au belongs to class III. It is striking that members of this class are mostly Al-based alloys which all exhibit an extremely large negative excess volume. The underlying mechanism, which is clarified in the case of Al-Au, is probably the same for all alloys of class III, as well. This will have to be shown in future. In future, similar MD-studies will be carried out on representative systems of class I and class II.

3.7 Summary and conclusions

Systematic investigations of the densities of several liquid metal systems, i.e. pure elements, binary and ternary alloys are performed. From the results presented in this chapter and with respect to questions **Q:1** and **Q:2** formulated in Chap. 1, it can be concluded that, *ad hoc*, there is no general rule or model in order to predict the excess volume or its sign. In the case of ternary alloys, the excess volumes can be determined from those of the binary phases only in a number of some special cases. In general, however, a ternary volume interaction parameter ${}^{T}V$ needs to be taken into account (question **Q:3**).

Despite this fact, the following trends can be identified for the excess volume (see **Q:1**):

- Alloys consisting of elements with similar electronic structure exhibit no or only a very small excess volume.
- Cu-based alloys with a positive excess free energy containing one or more transition metals tend to show a positive excess volume.
- Al-based alloys with an exothermic mixing behavior show excess volumes which are strongly negative.
- Exceptions from this scheme exist in all three cases.

Further investigations, involving elements from sections of the periodic table that are not taken into focus yet, will have to show whether or not this scheme can be maintained. Understanding of the observed behavior, however, can only be obtained if, in addition to the density measurements, other techniques of analysis are employed. This is demonstrated in the case of Al-Au. Systematic structural investigations, using simulation- as well as scattering techniques, will play an even more important role in the future.

4 Surface tension

Surface tension data is measured on pure liquid elements, binary and ternary alloys. The measurements are carried out containerlessly using the oscillating drop technique in combination with electromagnetic levitation. The degree of complexity of the sample material is stepwise increased from mono-atomic systems to binary and ternary alloys. Data is obtained as functions of temperature and, in the case of alloys, of their corresponding compositions. The results are discussed using thermodynamic models. The performances of the different models are compared with each other. Generally, it is found that systems with negative excess free energies exhibit a weak surface segregation while systems with positive excess free energies exhibit a pronounced segregation.

4.1 Formalism and models

4.1.1 Definition

Surface tension as a macroscopic property is sensitively linked to the microscopic configuration of the interface and can be interpreted as a mechanical tension applied to the surface [164]. Upon increasing the surface area, a force acts on its circumference which is proportional to its length. The surface tension, y, is also related to a difference in pressure, ΔP, between the two sides of a curved surface [165]. If the curvature of the surface in any point is characterized by two radii, r_1 and r_2, vertical to each other, the following relation is valid:

$$\Delta P = y\left(\frac{1}{r_1} + \frac{1}{r_2}\right) \tag{4.1}$$

Equation (4.1) is called *Laplace equation*. It forms the basis for the description of mechanical equilibria at surfaces and interfaces [70].

Atoms in the surface are generally on a higher energy level compared to those in the bulk [165]. Creating a surface, therefore, costs energy. For a liquid, the surface tension is identical with the energy per surface area A [164]. If A is increased by dA, a mechanical work, $dw = ydA$ is required. Hence, it is possible to express the surface tension by the coresponding change in the free energy G [165]:

$$y = \frac{\partial G}{\partial A}|_{P,V,T} \tag{4.2}$$

Finally, the surface tension results from a change of the atomic distribution near the interface and the resulting difference in the net binding energy [20]. y can therefore be obtained from the normal $p_\perp$ and parallel $p_\parallel$ compound of the pressure tensor. Close

to the surface, $p_\perp > p_\parallel$ [20; 70] and y equals

$$y = \int_{-\infty}^{+\infty} p_\perp - p_\parallel dz \tag{4.3}$$

In general, the pressure, P, can be written as $PV = E_k - \left\langle \sum \vec{r} \cdot \vec{F} \right\rangle$ with E_k denoting the mean kinetic energy, $\vec{r}$ denotes the position of each particle to which a force $\vec{F}$ is applied, and $\langle \dots \rangle$ indicates thermal averaging [166]. If this is applied to Eq. (4.3), one obtains [41]:

$$y = \frac{1}{2} \int_{-\infty}^{\infty} dz \int \frac{X^2 - Z^2}{R} \vec{F}(R) g(z, \vec{R}) d\vec{R} \tag{4.4}$$

In this equation, $\vec{R} = (X, Y, Z)$ is a spatial relative vector and z is a position vertical to the interface. $\vec{F}$ is the force between two neighboring particles in a distance R from each other. $g(z, \vec{R})$ finally, is a z-dependent pair correlation function. The latter can be approximated by a product, $g_z(z)g(R)$, of a part depending on z and another one depending on r [20]. If, furthermore, g_z is approximated by a step function, the integral can be solved and the following result, known as *Fowlers formula* is obtained [20]:

$$y \approx \frac{\pi n^2}{8} \int_0^{\infty} dR R^4 F(R) g(R) \tag{4.5}$$

This equation neglects electronic contributions. The latter might play an important role in liquid metals. Moreover, the pair correlation function $g(r)$ as well as the interatomic potentials need to be known precisely. Equation (4.5) has been tested successfully in a few cases [20].

4.1.2 Gibbs formalism

According to Gibbs [165], the surface (S) of a liquid can be described as the boundary of a bulk phase (B) with a gas phase (G). Both phases are treated as homogeneous up to their interface. Consequently, the number densities, $\widehat{\rho_i}^B$ and $\widehat{\rho_i}^G$, of particles of kind i are also taken as constant. Moreover, the interface is associated with a plane, the *Gibbs dividing plane*, (S) separating the two phases from each other. At the position of (S), which is chosen arbitrarily, the number density changes abrutly from $\widehat{\rho_i}^B$ to $\widehat{\rho_i}^G$. If V^B is the volume of the bulk phase and V^G is the volume of the gas phase, the number of moles of particles is given by $n_i^B = \widehat{\rho_i}^B V^B$ for the bulk phase and by $n_i^G = \widehat{\rho_i}^G V^G$ for the gas phase [165].

Realistically, however, the number density does not suddenly change. Instead, it transits continuously within a limited zone including the interface. The thickness of

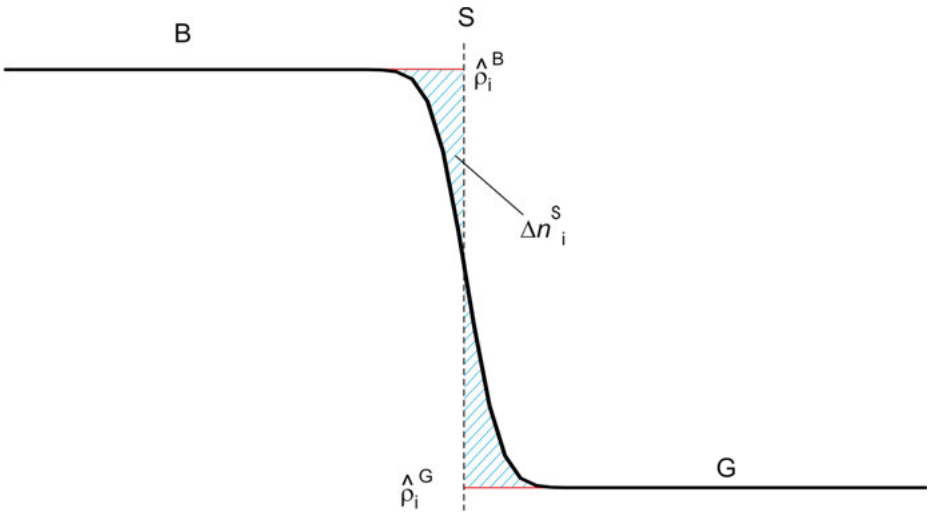

Fig. 4.1. The Gibbs picture of an interface: The two phases, liquid bulk (*B*) and gas (*G*), are assumed to be homogeneous with both having constant number densities $\widehat{\rho}_i$ up to the position of the dividing plane (*S*) (dashed) where an assumed abrupt change of $\widehat{\rho}_i$ occurs. The real density, however, deviates from this idealized situation causing an excess of particles, Δn_i^S, at the interface (shaded areas).

this zone, $\Delta\delta$, is typically of the order of several Å which corresponds to a few atomic diameters. The situation is schematically shown in Fig. 4.1 [165].

The smooth transition of the number density, $\widehat{\rho}$, at the interface causes a deviation, Δn_i^S, of the sum, $n_i^B + n_i^G$, from the total number of moles, n_i, in the entire system. This is illustrated by the shaded areas in Fig. 4.1. Δn_i^S is the excess number of moles. It can be positive, negative or even zero, depending on the position of the diving plane [165]. The thermodynamic potentials can be written as a sum of their contributions from the surface-, bulk- and gas-phase. Using the thermodynamic definition of y, Eq. (4.2), the fundamental equation of the molar free energy of the surface, G^S can directly be followed for a mixture of N components, ($i = 1..N$) [165]:

$$dG^S = -S^S dT + V^S dP - A dy + \sum_i^N \mu_i d\Delta x_i^S \tag{4.6}$$

In this equation, S^S is the molar entropy in the surface phase, V^S is its molar volume, P is the pressure, A is the molar surface area, and $\Delta x_i^S = \Delta n_i^S / \sum_i^N \Delta n_i^S$ is the excess surface mole fraction. The term Ay denotes in Eq. (4.6) the mechanical work needed in order to create a new surface with an area A. Integration of Eq. (4.6) for constant P, T, and y yields:

$$G^S = \sum_i^N \mu_i \Delta x_i^S \tag{4.7}$$

Differentiation of Eq. (4.7) and comparison with Eq. (4.6) leads to [165]:

$$S^S dT - V^S dP + A dy + \sum_i^N \Delta x_i^S d\mu_i = 0 \tag{4.8}$$

This equation is called *Gibbs-Duhem relation for surfaces*. It can be used in order to derive a number of useful relations, such as, for instance, the one for the temperature coefficient of the surface tension, $y_T = dy/dT$:

$$y_T = -(\frac{S^S - S^B}{A}) \tag{4.9}$$

Obviously, y_T can be interpreted as the change in entropy needed to create a surface. For pure elements, y_T is usually negative [20]. For systems with more than one component, y_T may also be positive under certain conditions [155].

At the critical point, $T = T_C$ it is no longer possible to distinguish between liquid and vapor and the surface tension equals zero. Close to the critical point, y decays as function of T according to a power law [165]:

$$y \propto \left(1 - \frac{T}{T_C}\right)^{\upsilon} \tag{4.10}$$

with a critical exponent $\upsilon \approx \frac{11}{9}$. In the high temperature limit, thus, y_T is always negative. At temperatures sufficiently smaller than T_C, y depends linearly on T:

$$y(T) = y_L + y_T(T - T_L) \tag{4.11}$$

In Eq. (4.11) y_L denotes the surface tension at $T = T_L$.

Another consequence of the Gibbs-Duhem relation of surfaces, Eq. (4.8) is the so called *Gibbs adsorption isotherm*. For constant temperature and pressure Eq. (4.8) transforms into the *Gibbs relation*:

$$dy + \sum_i^N \Gamma_i d\mu_i = 0 \tag{4.12}$$

Here, $\Gamma_i = \Delta x_i^S / A$ denotes the so called *adsorption* of component i. It can be interpreted as an excess surface density.

Equation (4.12) can be combined with the following expression for the composition dependent chemical potential of a solution, μ_i:

$$\mu_i = \mu_i^0 + RT \ln(a_i) \tag{4.13}$$

In this equation, R is the molar gas constant, μ_i^0 is the chemical potential of the standard (bulk) state, independent of composition, and a_i is the activity. The Gibbs adsorption isotherm follows as the result [165]:

$$-dy = \sum_i^N RT\Gamma_i d\ln(a_i) \tag{4.14}$$

Equation (4.14) describes the dependence of surface tension on the composition of an alloy at constant temperature. Depending on the purpose, Eq. (4.14) may have different forms [165]. For instance, in the case of a binary alloy, $N = 2$, the position of the dividing plane can be adjusted such, that $\Gamma_2 = 0$. In this case, Eq. (4.14) reads:

$$dy = -RT\Gamma_1 d\ln(a_\mathrm{i}) \tag{4.15}$$

Equation (4.15) plays an important role in processes where surface active gas phase atoms adsorb at the liquid surface. A prominent example is the reduction of the surface tension of liquid metals under the influence of an oxygen containing atmosphere [167; 168]. In technical processes, such as welding, this has enourmous consequences for the quality of the final product [169; 170].

4.1.3 Quantities of mixing

Based on the Gibbs adsorption isotherm, Eq. (4.14), it is possible to formally develop an expression for surface tension in terms of mixing and excess properties. For this purpose, the Gibbs adsorption isotherm is written in differential form. Subsequent integration leads to the expression below in which x_i^B denotes the mole fraction of component i in the bulk phase:

$$y = \sum_i^N x_\mathrm{i}^\mathrm{B} y_\mathrm{i} - \sum_i^N RT\Gamma_\mathrm{i} \ln(a_\mathrm{i}) \tag{4.16}$$

Without violating the general case, the integration constant is written as $\sum_i x_\mathrm{i}^\mathrm{B} y_\mathrm{i}$ and the activity term is expressed by $RT\ln(a_\mathrm{i}) = RT\ln(x_\mathrm{i}^\mathrm{B}) + {}^\mathrm{E}G_\mathrm{i}$ with ${}^\mathrm{E}G_\mathrm{i}$ being the partial excess free energy. Then, Eq. (4.16) becomes:

$$y = \overbrace{\sum_i^N x_\mathrm{i}^\mathrm{B} y_\mathrm{i} - \underbrace{\sum_i^N RT\Gamma_\mathrm{i} \ln(x_\mathrm{i}^\mathrm{B})}_{\Delta^\mathrm{id} y}}^{{}^\mathrm{id} y} - \underbrace{\sum_i^N \Gamma_\mathrm{i}\, {}^\mathrm{E}G_i}_{{}^\mathrm{E} y} \tag{4.17}$$

In this equation, the right hand side consists of three terms: The first is a linear combination of the surface tensions of the pure individual components in x_i^B. The second term denotes the surface tension of mixing, $\Delta^\mathrm{id} y$, for the ideal solution case. The last term can be interpreted as the excess surface tension, ${}^\mathrm{E} y$. Moreover, the ideal surface tension, ${}^\mathrm{id} y$, equals the sum of the first two terms. The sum of the last two terms corresponds to the surface tension of mixing, Δy, for the real solution case. Using this nomenclature, Eq. (4.17) can be written in its generalized form:

$$y = {}^\mathrm{id} y + {}^\mathrm{E} y \tag{4.18}$$

Equations (4.17) and (4.18) provide a formalism similar to the one developed for the excess volume in section 3.1. Hence, the excess surface tension may also be written in Redlich-Kister form and the following is valid for a binary system with components i and j:

$$^{E}y_{i,j} = x_i^B x_j^B \left[{}^0u_{i,j} + {}^1u_{i,j}(x_i^B - x_j^B) \right] \tag{4.19}$$

The coefficients ${}^0u_{i,j}$ and ${}^1u_{i,j}$ are generally temperature dependent.

The predictive power of the Gibbs model is rather small. The principle problem arises from a difficulty with the determination of Γ_i [165]. This is problematic both, experimentally and theoretically. The Gibbs formalism has provided a basic thermodynamic theory of surfaces and interfaces. In fact, the Gibbs adsorption isotherm has generally been accepted as being thermodynamically exact. In order to predict the surface tension numerically, other, more suitable, models exist.

4.1.4 Butler model

One of the first analytic models for the prediction of surface tension is the Butler model [171]. It differs form the Gibbs model in the description of the surface. The Butler model considers the surface as a separate thermodynamic phase which is in equilibrium with the bulk. In an alloy system, the mole fractions of components in the surface, x_i^S, generally differ from those in the bulk, x_i^B. Moreover, the surface is considered in the Butler model as a monolayer of atoms, Fig. 4.2. The latter is assumed for mathematical reasons: If the surface is a monolayer, one may write $1 = \sum_i \Gamma_i A_i$ with A_i being the area that one mole of atoms of type i occupies [20]. Furthermore, the gas phase is completely neglected.

The following derivation of the concept is adopted from a similar derivation of a model for liquid-liquid interfaces [172]: If G^{tot} is the free energy of the total system, the surface tension corresponds to its change upon changing the surface area. Hence, using the definition of y, Eq. (4.2), one can write:

$$y = \frac{dG^{tot}}{dA} = \frac{\partial G^{tot}}{\partial A}\frac{dn_i^S}{dn_i^S} = \sum_i \frac{dG^{tot}}{dn_i^S}\frac{\partial n_i^S}{\partial A} \tag{4.20}$$

with n_i^S being the number of moles of particles of kind i in the surface layer. n_i^S will change by ∂n_i^S if the surface area A is changed by ∂A. Hence, in Eq. (4.20) y can be interpreted as the energy needed per unit area to move a particle from the bulk phase (B) to the surface (S). If n_i^B is the number of moles of particles in the bulk, then:

$$\frac{dG^{tot}(n_i^S, n_i^B)}{dn_i^S} = \frac{\partial G^{tot}}{\partial n_i^S} - \frac{\partial G^{tot}}{\partial n_i^B} \tag{4.21}$$

Introducing the partial molar surface area, $A_i = \partial A / \partial n_i^S$, Eq. (4.20) can be transformed into the following equation using Eq. (4.21):

$$y = (u_i^S - \mu_i^B)A_i^{-1} \tag{4.22}$$

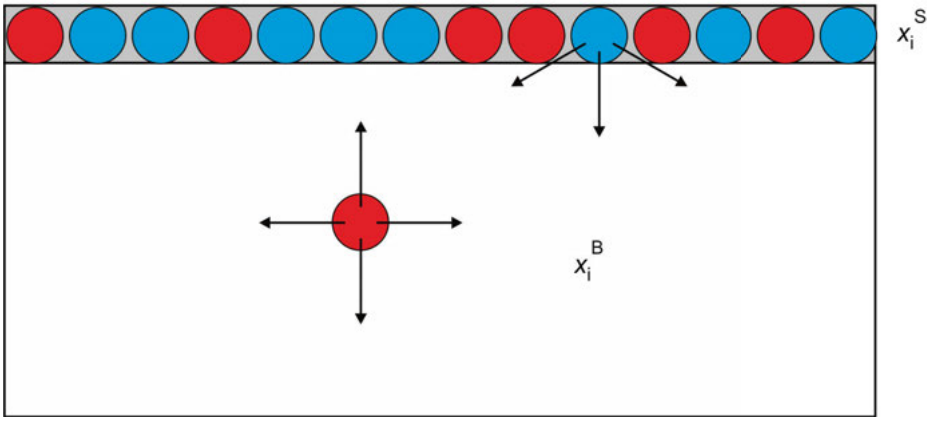

Fig. 4.2. The Butler model of a liquid surface: The surface is considered as a monolayer of atoms. It forms an individual phase with their own thermodynamic potentials and composition, x_i^S. x_i^B = mole fraction of component *i* in the bulk.

whereas in Eq. (4.22) $\partial G^{tot}/\partial n_i^S$ and $\partial G^{tot}/\partial n_i^B$ are abreviated by u_i^S and μ_i^B, respectively. μ_i^B is the chemical potential of a particle of kind *i* in the bulk phase. The chemical potential of the surface, μ_i^S, includes the interfacial energy. μ_i^S, therefore, consists of one part, yA_i, depending on the interfacial energy and the partial molar area, and another one, u_i^S, including the rest:

$$\mu_i^S = u_i^S - yA_i \tag{4.23}$$

In Eqs. (4.22) and 4.23, u_i^S can be interpreted as the chemical potential of a particle of kind *i* which is not on the surface, but instead, in a bulk phase with a composition identical to the surface [172].

In case of thermodynamic equilibrium, Eq. (4.23) allows that the chemical potentials, μ_i^S and μ_i^B, can, indeed, be equal without violating Eq. (4.22). Equations (4.22) and (4.23) can be combined with Eq. (4.13) and Eq. (4.22), which allows for determining the surface tension of the pure component, y_i as $(\mu_i^{0,S} - \mu_i^{0,B})/A_i$, so that the following relation is obtained:

$$y = y_i + \frac{RT}{A_i} \ln\left(\frac{a_i^S}{a_i^B}\right) \tag{4.24}$$

In Eq. (4.24), a_i^S is the activity of an element *i* in the surface and a_i^B is the corresponding activity in the bulk phase. Equation (4.24) must produce identical results for different choices of *i* and it is therefore possible to eliminate *y* from Eq. (4.24). Equation (4.24) is called the *Butler equation*. In the form of Eq. (4.24) it is most general.

4.1.5 Ideal solution

Before the Butler equation is discussed in greater detail, one of its special cases, the ideal solution, will be emphasized. For the ideal solution model, $RT\ln(a_i) = RT\ln(x_i)$ with x_i being the mole fraction of component i in any phase. Then, the Butler equation, Eq. (4.24), turns into:

$$^{id}y = y_i + \frac{RT}{A_i}\ln\left(\frac{x_i^S}{x_i^B}\right) \tag{4.25}$$

For an alloy with N components, $i = 1, ..N$, Eq. (4.25), results in N equations with N unknowns: y and $N - 1$ independent surface concentrations, $x_1^S, .., x_{N-1}^S$ for which $x_1^S + .. + x_N^S = 1$. Correspondingly, the system can be solved.

In the case of a binary alloy with components A and B, Eq. (4.25) can even be solved analytically, using the approximation $A_A \approx A_B :\approx A$. Then, the surface concentration x_A^S of a component A becomes:

$$x_A^S = \frac{x_A^B}{x_A^B + x_B^B S_e(T)} \tag{4.26}$$

and for component B:

$$x_B^S = \frac{x_B^B}{x_B^B + x_A^B / S_e(T)} \tag{4.27}$$

with $S_e(T)$ being the so called segregation factor. It is written as

$$S_e(T) = \exp\left(\frac{(y_A - y_B)A}{RT}\right) \tag{4.28}$$

Equation (4.26) is plotted in Fig. 4.3. Negative values of $\ln(S_e)$ are equivalent to $y_A < y_B$. The curves in Fig. 4.3 exhibit a convex shape as $x_A^S > x_A^B$. This effect is called *segregation* or *surface segregation*. It is more pronounced if the difference between the surface tensions of the pure components is increased. Surface segregation can be understood as a process of energy minimization: In order to minimize the energy of the total system, G^{tot}, the component with the smaller surface tension becomes enriched in the surface layer. Figure 4.3 also shows that segregation takes place already within the ideal solution model.

Knowing x_A^S and x_B^S from Equations (4.26) and (4.27), the surface tension of an ideal solution can be calculated as a linear composition of y_i in the surface concentrations:

$$^{id}y(T) = x_A^S y_A(T) + x_B^S y_B(T) \tag{4.29}$$

This equation even holds for an N-component system:

$$^{id}y(T) = \sum_i^N x_i^S y_i(T) \tag{4.30}$$

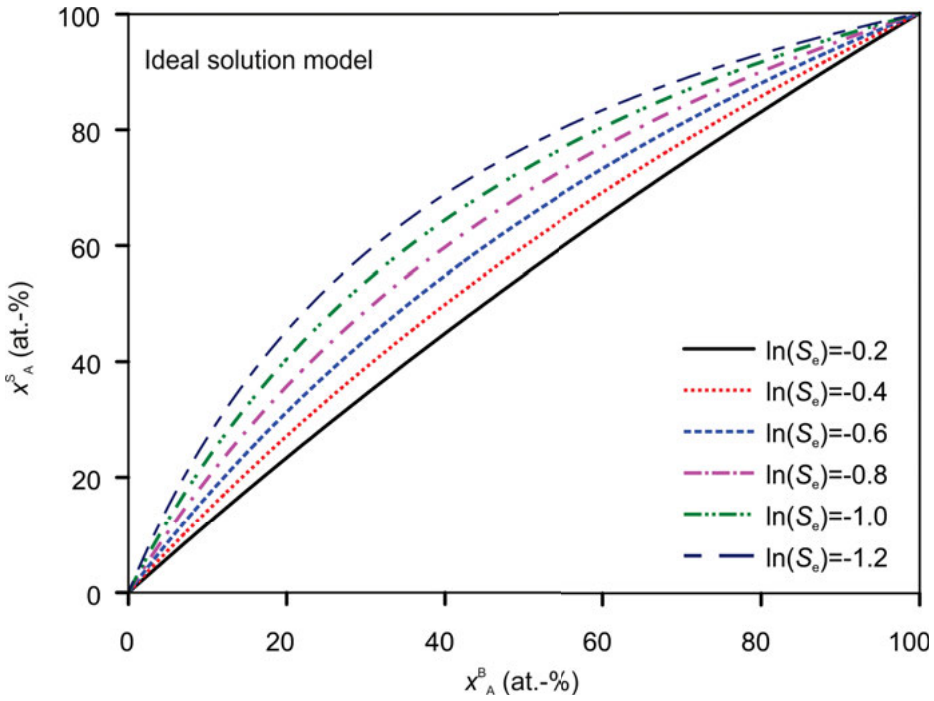

Fig. 4.3. x_A^S versus x_A^B for the ideal solution model plotted for different choices of the segregation factor S_e.

In order to calculate ${}^{id}y$ for the systems investigated in the present work, i.e. binary and ternary alloys, Eq. (4.25) is solved numerically. For this purpose, the partial molar surface areas need to be precisely known. Following a strict route, A_i has to be calculated from the molar volume. However, the latter is not always known. On the other hand, the effect of ${}^{E}V$ on the surface tension is very small and can be neglected. Hence, A_i is usually approximated from the molar volume, V_i of the pure components according to the following rule [173]:

$$A_i \approx f \times (N_A)^{\frac{1}{3}} V_i^{\frac{2}{3}} \tag{4.31}$$

In this equation, $N_A = 6.023 \times 10^{23}$ is the Avogadro number and V_i is the molar volume of the liquid pure element. Moreover, $f = 1.091$ is the geometrical factor [174; 175]. This value corresponds to an assumed atomic arrangement in the surface similar to an fcc (111) plane with a coordination number in the bulk of $z = 12$ [176].

4.1.6 Sub-regular solution

Usually, the ideal solution fails to predict experimental data correctly. This is due to the fact that, in most systems, ${}^{\mathrm{E}}G \neq 0$. For a non-ideal system, the Butler equation can be expressed using the partial excess free energies, ${}^{\mathrm{E}}G_{\mathrm{i}}^{\mathrm{S}}$ and ${}^{\mathrm{E}}G_{\mathrm{i}}^{\mathrm{B}}$, for the surface and the bulk, respectively:

$$y = y_{\mathrm{i}} + \frac{RT}{A_{\mathrm{i}}} \ln\left(\frac{x_{\mathrm{i}}^{\mathrm{S}}}{x_{\mathrm{i}}^{\mathrm{B}}}\right) + \frac{1}{A_{\mathrm{i}}} \left({}^{\mathrm{E}}G_{\mathrm{i}}^{\mathrm{S}}(T, x_1^{\mathrm{S}}, .., x_{\mathrm{N}}^{\mathrm{S}}) - {}^{\mathrm{E}}G_{\mathrm{i}}^{\mathrm{B}}(T, x_1^{\mathrm{B}}, .., x_{\mathrm{N}}^{\mathrm{B}}) \right) \tag{4.32}$$

The difficulty with Eq. (4.32) is obvious: While ${}^{\mathrm{E}}G_{\mathrm{i}}^{\mathrm{B}}$ may be known for the bulk from thermodynamic databases, the thermodynamic potentials of the surface phase, in particular ${}^{\mathrm{E}}G_{\mathrm{i}}^{\mathrm{S}}$, are generally unknown. *A priori* it is not even clear which functional forms they should have.

In an attempt to overcome this hurdle, Hoar and Melford proposed that ${}^{E}G_{i}^{S}$ should have the same functional form as by the bulk, apart from a factor ξ which accounts for a reduced coordination of atoms in the surface layer with respect to the bulk [177]:

$${}^{\mathrm{E}}G_{\mathrm{i}}^{\mathrm{S}}(T, x_1^{\mathrm{S}}, .., x_{\mathrm{N}}^{\mathrm{S}}) \approx \xi {}^{\mathrm{E}}G_{\mathrm{i}}^{\mathrm{B}}(T, x_1^{\mathrm{S}}, .., x_{\mathrm{N}}^{\mathrm{S}}) \tag{4.33}$$

Depending on the atomic short range order within the liquid, ξ varies from 0.5 to 1.0 [175; 177; 178; 179]. A value of 0.75 was initially suggested by Tanaka and Iida [175] as a default for liquids with an unknown structure. Later, they replaced this value by 0.83 based on a more detailed analysis published in Ref. [180]. This value of ξ shall be used in the present work as well.

The partial excess free energies ${}^{\mathrm{E}}G_{\mathrm{i}}^{\mathrm{B}}$ are derived from the excess free energy ${}^{\mathrm{E}}G^{\mathrm{B}}$ by partial derivatives with respect to concentration.

For an N-component system, Eq. (4.32), again, forms a system of N equations with N unknowns, y and $N - 1$ independent surface concentrations. Up to $N = 3$, Eq. (4.32) can be solved numerically. For systems with more components, it might become more difficult to solve Eq. (4.32) accurately, as the minimum in which the solution converges becomes broader with an increasing number of components. For true multicomponent systems different models, based on Gibbs energy minimization, need to be employed [181].

4.1.7 Chatain model

The Butler equation has often been criticized. For instance, the assumption of Eq. (4.33) appears arbitrary. It moves the Butler model close to semi-empiric methods. Furthermore, the mono-layer assumption might not always be justified. In reality, there would be a vertical gradient of composition in the near-to surface region [182]. The associated surface thicknesses even diverge in real systems, for temperatures close to

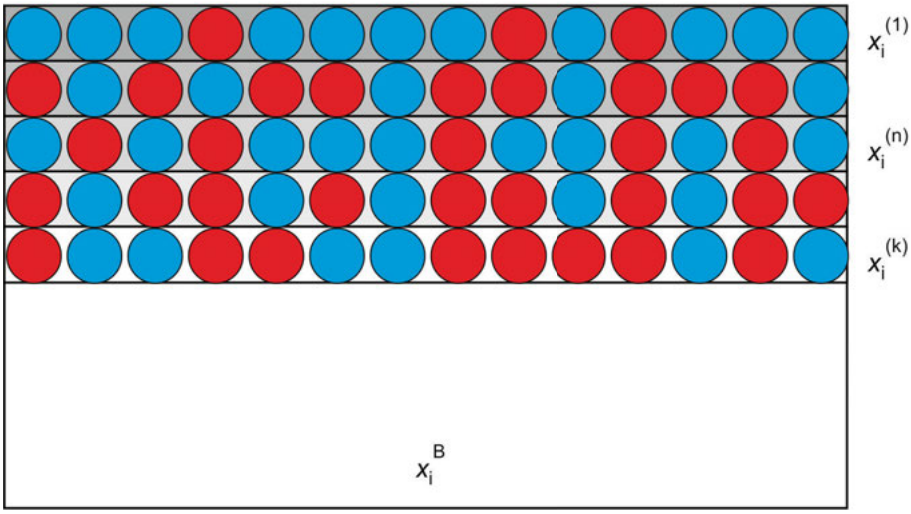

Fig. 4.4. The Chatain model of a liquid surface: The surface is considered as a stack of k atomic monolayers with each layer n, $n = 1, .., k$, having its individual composition, $x_i^{(n)}$.

the critical temperature of demixing [182]. Last but not least, the Butler model is in disagreement with the Gibbs-adsorption isotherm. For this reason, the Butler model has even been regarded as being non-physical.

The latter problem, at least, can be diminished by considering instead of just one monolayer, a stack of multiple layers with each layer having its own composition, see Fig. 4.4. The concept of such a multilayer model is not new [20]. It dates back to the works of Defay and Prigogine in 1950 [183] and Taylor in 1956 [184], and others [185; 186].

The most important and recent development of a multilayer model is the one proposed by Wynblatt and Chatain [187]. In its current form, the model is defined solely for binary systems. It is based on the regular solution or sub-regular solution model [188]. A recent modification of the model also describes oxygen adsorption at liquid copper surfaces [189].

In the Chatain model [187], the atoms of the liquid are assumed to reside on cubic lattice sites with a coordination number $z = 12$ in the bulk and a lateral coordination number $z_l = 6$. The number of neighboring atoms in an adjacent atom layer is $z_v = 3$. Interactions among atoms take place only with the nearest neighbors, whereas $\Phi_{i,j}$ denotes a single bond energy for a bond between atoms of kind i and j.

If G^S is expressed in Eq. (4.7) by the internal energy, U^S with $-Ay$ being included into the usual expression of the mechanical work, the surface tension appears as

$$y = \frac{U^S}{A} - T\frac{S^S}{A} - \sum_i \mu_i \Gamma_i \tag{4.34}$$

In order to determine y, the three terms, i.e. the internal energy term, the entropy term and the adsorption term, need to be evaluated separately. This is done layer by layer. The index $(k+1)$, hereby refers to the bulk, i.e. $x_i^{(k+1)} = x_i^B$. In addition, it is assumed that the area per atom is the same for both elements and in each layer.

Moreoever, it is assumed that the entropy S^S equals the ideal entropy of mixing and the chemical potentials of the components are written for a binary regular solution as

$$\mu_i = \frac{z}{2}[2x_i^B\omega + \Phi_{i,i}] + RT\ln(1 - x_i^B) \tag{4.35}$$

where ω is the regular solution constant given by: $\omega = \Phi_{A,B} - (\Phi_{B,B} + \Phi_{A,A})/2$. Assuming further that $y_i = -z_v\Phi_{i,i}/(2A)$, the following expression for the surface tension of a binary alloy is obtained:

$$\begin{aligned} Ay &= Ay_B x_B^{(1)} + Ay_A x_A^{(1)} \\ &- z_v\omega(x_B^{(1)} - 2x_B^B x_B^{(1)} + (x_B^B)^2 - 2z_v\omega\textstyle\sum_{n=1}^{k}(x_B^{(n)} - x_B^B)\times(x_A^{(n)} - x_A^B) \\ &- nz_1\omega\textstyle\sum_{n=1}^{k}(x_B^{(n)} - x_B^B)^2 \\ &+ RT\textstyle\sum_{n=1}^{k}\left[x_B^{(n)}\ln\left(\frac{x_B^{(n)}}{x_B^B}\right) + x_A^{(n)}\ln\left(\frac{x_A^{(n)}}{x_A^B}\right)\right] \end{aligned} \tag{4.36}$$

Equation (4.36) is solved by minimization of y. Typically, this is performed using a Monte Carlo algorithm with random sampling. The parameters $\Phi_{i,i}$ and ω are related to standard thermodynamic potentials as follows [187; 190]:

$$\Phi_{i,i} \approx A \cdot y_i \quad , \qquad \omega \approx \frac{{}^0L(T=0)}{z} \tag{4.37}$$

The Chatain model is in agreement with the Gibbs adsorption isotherm [187]. The model is able to predict the composition in the surface near region and its dependence on the layer number [190; 191]. As a particular strength, it can be used in order to investigate surface phase transitions [187]. This is demonstrated, for instance, in the case of the metastable demixing in liquid Co-Cu [188].

However, it is fair to mention that the Chatain model also has disadvantages. First of all, it exhibits a small mathematical inconsistency: While ω and $\Phi_{i,i}$ are initially taken as constants, Eq. (4.35), they tacitly become temperature dependent when linking them later to y_i in Eq. (4.37). In addition, the assumption of atoms being arranged on a lattice does not reflect the reality of a liquid and the assumption of an ideal entropy offers room for improvement. A more serious disadvantage of the model is related to Eq. (4.37) where ω is linked to the first Redlich-Kister coefficient, ${}^0L(T = 0)$. As the majority of systems involve at least two or three parameters, the field of application is, thus, narrowed for the Chatain model. In order to overcome this problem, a more recent version of the model is developed [188]. An exotic quadratic dependence on temperature is used therein for the interaction parameters. This brings up difficulties for the matching with existing thermodynamic assessments, as by most of them, the temperature dependence is either linear or logarithmic.

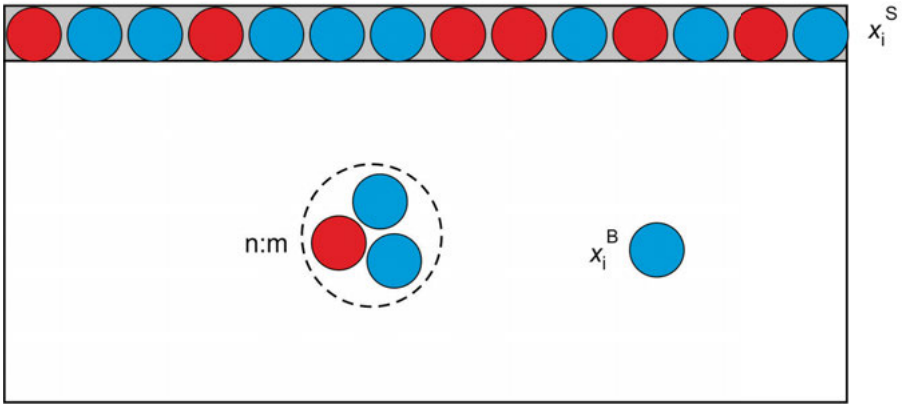

Fig. 4.5. The Egry model [193] for the surface tension of a liquid compound forming alloy: The surface is considered as a monolayer. Compounds forming in the bulk with a stoichiometric ratio of $n : m$ cannot segregate to the surface (encircled).

For some systems, the Chatain model is shown to correctly predict surface tension [190; 191]. A systematic comparison, which is still outstanding, is performed within the present work.

4.1.8 Egry model

Another interesting topic of surface tension measurement is linked to the idea that, in liquid metals, so called *compounds* may form under certain conditions. Such compounds would exist in systems which exhibit congruently melting intermetallic phases [192]. It is assumed that, at temperatures only a little above T_L, the intermetallic phase partially survives in the form of a preferred pronounced structural configuration called compound, see Fig. 4.5.

In order to elucidate the impact that compound formation would have on the surface tension, Egry proposed a simple and easily applied model [193] based on the ideal solution approximation described in section 4.1.5.

The main assumption of this model is that compounds do not segregate to the surface. In a binary system A, B, with compounds A_nB_m, the segregation factor then changes in the exponent by an additional contribution $f_{se} \cdot (n + m)(x_A^B)^n(x_B^B)^m$, where f_{se} is related to the energy of a single bond in the compound. Hence, Eq. (4.28) changes into:

$$S_e(T) = \exp\left(\frac{A(y_A - y_B) - f_{se} \cdot (n + m)(x_A^B)^n(x_B^B)^m}{RT}\right) \tag{4.38}$$

The factor f_{se} is an adjustable parameter [193].

4.1.9 Empirical models

Other empirical models exist, such as, for instance, the model of Allen [194] which links the surface tension of a liquid element at its liquidus, y_L to T_L, ρ_L, and its molar mass, M:

$$y_L = 3.6 T_L \left(\frac{M}{\rho_L}\right)^{-\frac{2}{3}} \tag{4.39}$$

This model has been improved by Kaptay [195], whereas the basic theoretical framework has been published by him earlier [179]. In his model, the concept was developed that the surface free energy is related to the cohesive energy and its difference with respect to the bulk- and the surface phase. In addition, it is found empirically that the cohesive energy is proportional to the liquidus temperature:

$$y_L (N_A)^{1/3} V_{L,i}^{2/3} \cong \alpha_K T_L \tag{4.40}$$

In Ref. [195], Kaptay also reports a value for the empirical parameter α_K which is α_K =38(±10) JK^{-1}. In the same work [195], Eq. (4.40) was optimized along existing data. The new, optimized form of Eq. (4.40) reads:

$$y_L (N_A)^{1/3} V_{L,i}^{2/3} \cong \alpha_K T_L + \beta_K {T_L}^2 \tag{4.41}$$

with α_K = 41 JK^{-1} and a second parameter $\beta_K = -3.3 \times 10^{-3}$ JK^{-2}.

Differentiation of Eq. (4.41) with respect to temperature, leads to a formula for the estimation of the temperature coefficient y_T [195]:

$$y_T \cdot A \cong 0.182 C_p - 1.2 - \frac{2}{3} \beta y_L \cdot A \tag{4.42}$$

In this equation, C_p is the molar heat capacity and β the thermal expansion coefficient.

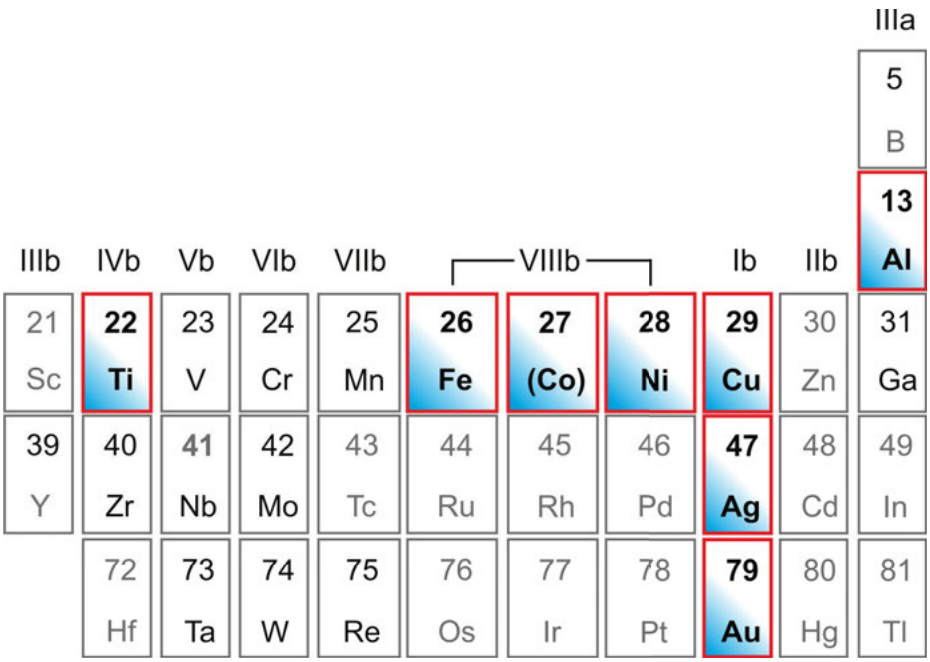

Fig. 4.6. Relevant section of the periodic table. Surface tensions of the highlighted elements are measured in the liquid state and will be discussed below. In the case of Co, data measured by Eichel [196] will be discussed.

4.2 Unary systems

In order to discuss the surface tension of binary and ternary liquid alloys, it is first necessary to determine the surface tensions of their pure components. For elements like Al, Ti and others, this is already a difficult task, due to their high chemical reactivity. Even now, the surface tensions of liquid aluminium [197] and/or silicon [16; 168; 198] are still subject to discussion.

Figure 4.6 shows the section of the periodic table which is relevant in this context. The marked elements are those for which the surface tension is measured in this work. These are Al, the group Ib noble metals Cu, Ag, and Au, as well as the transition metals metals Ni, Fe, and Ti. The latter are all from the fourth period. In addition, the surface tension of liquid Co is also discussed, which was previously determined [196].

The experimental results for the surface tension of the pure components are summarized in Tabs. 4.2–4.9 and compared therein with published results from literature. The corresponding experimental methods are specified in these tables by a certain *key*, defined in Tab. 4.1. The key *R*, means "recommended" and specifies that the listed values are obtained from literature reviews. From these, some of the cited original data is

also chosen for this work. Hence, the reference data is not strictly independent from one another. Moreover, the results are shown in Figs. 4.7–4.10.

Table 4.1. Key of methods for surface tension determination used in the tables below [27].

Key	Name
CR	Capillary rise method
DC	Draining crucible
DW	Drop weight
EML	Electromagnetic levitation
μg-EML	Electromagnetic levitation under microgravity
ESL	Electrostatic levitation
R	Recommended from literature review
SD	Sessile drop method and its variants

Table 4.2. Parameters γ_L and γ_T for the surface tension of pure liquid Al measured in this work [199] (bold). The data is compared with selected data from literature. The experimental methods used are specified in the third column.

γ_L ($N \cdot m^{-1}$)	γ_T ($10^{-4} N \cdot m^{-1} K^{-1}$)	Method	Source
0.865	-1.2	SD	[200]
0.873	-1.2	SD	[201]
0.865	-1.5	SD	[202]
0.867	-1.5	SD	[164]
0.871	-1.55	R	[12]
0.914	-3.5	R	[175]
0.866 ± 0.04	**-1.46 ± 0.1**	**EML**	**[199]**

4.2.1 Aluminium

Surface tension data of liquid Al [199] is plotted in Fig. 4.7 versus temperature. The temperature ranges over more than 500 K from $T_L + 100$ K to $T_L + 650$ K. Undercoolings are not observed.

The obtained values of y change linearly over the investigated temperature range from ≈0.85 Nm^{-1} at 1050 K to 0.78 Nm^{-1} at around 1550 K, see Fig. 4.7. Equation (4.11) can be fitted to the experimental data, and the corresponding fit parameters y_L and y_T are listed in Tab. 4.2 together with corresponding results from literature. Excellent agreement is obtained with the results of Refs. [164; 200; 201; 202] and [12].

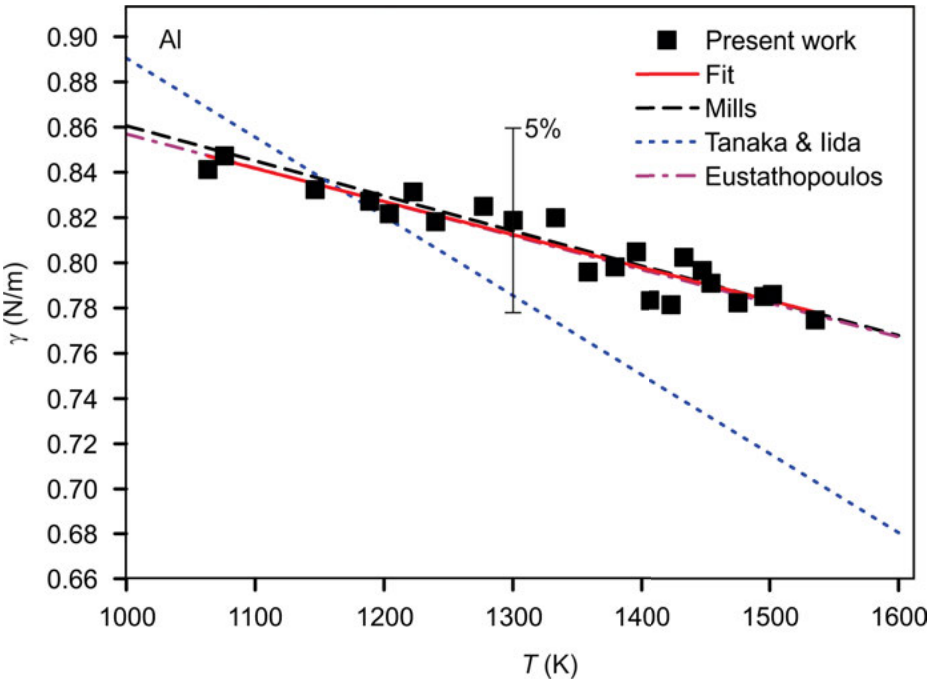

Fig. 4.7. Surface tension of pure Al versus temperature [199] (symbols). For comparison, the representations reported by Mills [12], Tanaka [175], and Eustathopoulos [164] are shown as lines as well.

There is, however, a disagreement with the values reported by Tanaka, [175], for which y_L =0.914 Nm^{-1} and y_T =-3.5 $10^{-4} Nm^{-1}K^{-1}$.

This is also observed in Fig. 4.7 where, in addition to the experimental data of the present work [199], linear representations of the reference data of Mills [12], Tanaka [175] and Eutstathopoulos [164] is shown. While the agreements between the results of the present work and those of Refs. [12] and [164] are nearly perfect, the slope of the surface tension reported in Ref. [175] deviates significantly.

On the other hand, the increased affinity of Al to oxygen cannot be ignored. It is mentioned in Ref. [12] that, using the maximum bubble pressure method, Garcia-Cordovilla et al. [203], Goumiri et al. [204] as well as Pamies et al. [201] reported values of y around 1.0 Nm^{-1} under, as declared by them, oxygen-free conditions. Hence, surface tension values around 0.86 Nm^{-1}, as found in this work and by most of the authors cited in Tab. 4.2, are interpreted by them as being related to an Al-surface saturated in oxygen [12; 205]. In a recent work of Molina [197], it is noted that, if this interpretation is correct, the scatter of the available experimental data should be increased. However, as visible in Tab. 4.2, this is not the case. In fact the deviation of the available data from each other is not much larger as for other materials. The influence

of oxygen on the surface tension of liquid Al is discussed in detail by these authors. They came to the conclusion, that the value of $y \approx 0.85\ \mathrm{Nm}^{-1}$ should correspond to a virtually oxygen free surface. This is in agreement with the results presented here[1].

4.2.2 Noble metals (Cu, Ag, Au)

The surface tensions of Cu [67; 191; 206], Ag [67], and Au [199] are plotted in Fig. 4.8 versus temperature. For pure Cu and Ag, surface tensions are measured over almost 300 K. For both systems, the maximum temperature is limited by evaporation. For liquid Au, data is obtained in a broad temperature range of $T_L \leq T \leq T_L + 600$ K. Undercoolings are not observed.

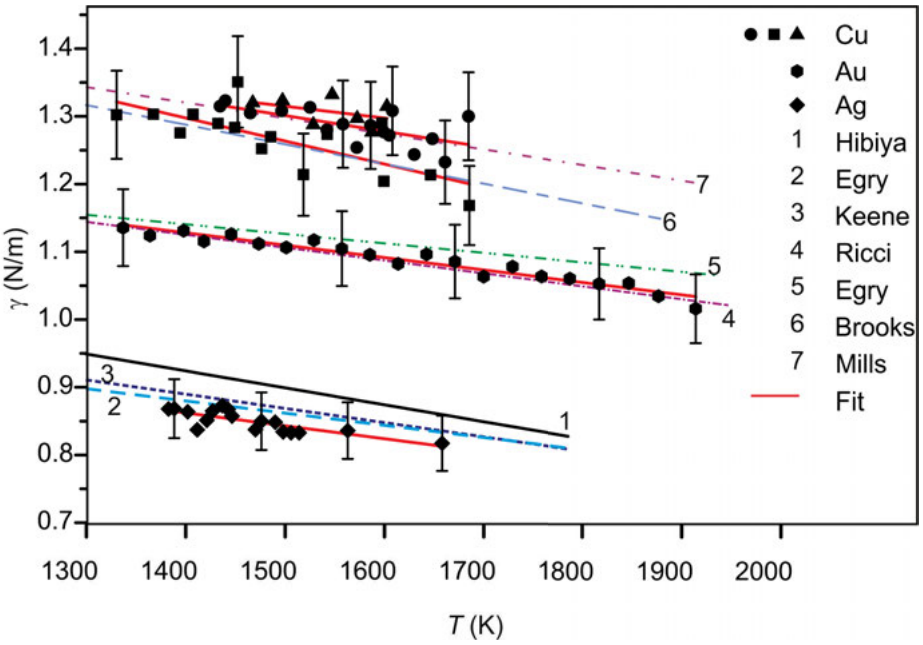

Fig. 4.8. Surface tension of pure Cu [67; 191; 206], Ag [67], and Au [199] versus temperature (symbols). In comparison, representations are shown for Cu [12; 207] for Ag [208; 209], and for Au [210; 211]. Representations of Ag: 1: Ref. [208], 2: Ref. [209], 3: Ref. [205]. Representations of Au: 4: Ref. [210], 5: Ref. [211]. Representations of Cu: 6: Ref. [207], 7: Ref. [12].

1 It must be noted, however, that very recent measurements performed by Kobatake using electromagnetic levitation under controlled atmosphere seem to be rather in agreement with the data of Ref. [175].

Again, the data can be described by Eq. (4.11) and the adjusted parameters, y_L and y_T, are listed in Tabs. 4.3–4.5. Among the three metals, Au exhibits the smallest relative scatter in the surface tension. In the case of Ag, the scatter is slightly larger. The largest scatter in the data, however, is found among the different measurements for Cu. Not only the curves obtained for each run deviate from each other by up to 10 %, but also the relative scatter in a single run is nearly (± 5 %). In Fig. 4.8 the data of Ref. [191] is obviously about 3 % smaller than that of Refs. [67; 206]. The reason is unclear.

In general, the agreement with the literature data listed in Tabs. 4.3–4.5 is good. The measured surface tensions of Ag deviate from the literature values systematically by 3 %, tending towards lower values, if the results of Hibiya [208] are ignored in Tab. 4.4. The agreement among the different data sets of gold including the results of the present work, is also within ± 3 %.

Figure 4.8 displays representations of some of the literature data. These are the reviews [12; 205; 207] for Cu, plus some representative studies for Ag [208; 209] and for Au [210; 211]. For the latter system, no specific review data seems to be available.

As mentioned already in Sec. 3.2, the levitation of liquid silver and its alloys comes with the particular problem that a visibly bright and extended film of some impurity appears the surface of the droplet as soon as it becomes molten. From EDX-analysis, it is evident that this film consists of sulphur originating from chemical reactions when the solid sample comes in contact with air prior to the measurement. With respect to the surface tension, the action of sulphur can be fatal. Like oxygen, only a few ppm of sulphur can drastically decrease y and may even reverse the sign of its temperature coefficient y_T. In order to obtain reliable surface tension data, therefore, it is imperative to remove these impurities from the surface *in situ*, i.e. during the levitation experiment.

In Ref. [67] this is achieved by exposing the liquid sample at high temperature to an oxygen partial pressure of more than 10^3 Pa. This way, volatile SO_2 forms and the surface is cleaned efficiently within a few minutes.

Table 4.3. Parameters γ_L and γ_T for the surface tension of pure liquid Cu measured in this work [67; 191; 206], (bold). The data is compared with selected data from literature. The experimental methods used are specified in the third column.

γ_L (N·m^{-1})	γ_T (10^{-4}N·m^{-1}K^{-1})	Method	Source
1.33	-2.6	EML	[196]
1.30	-2.3	EML	[107]
1.33	-2.3	R	[12]
1.30	-2.9	R	[207]
1.30	-2.5	SD	[212]
1.29	-1.6	SD	[202]
1.34	-1.8	SD	[213]
1.31	-1.1	SD	[214]
1.30	-2.1	SD	[215]
1.30 ± 0.07	**-2.64 ± 0.1**	**EML**	**[191]**
1.33 ± 0.07	**-2.6 ± 0.1**	**EML**	**[67]**
1.33 ± 0.07	**-2.3 ± 0.1**	**EML**	**[206]**

Table 4.4. Parameters γ_L and γ_T for the surface tension of pure liquid Ag measured in this work [67] (bold). The data is compared with selected data from literature. The experimental methods used are specified in the third column.

γ_L (N·m^{-1})	γ_T (10^{-4}N·m^{-1}K^{-1})	Method	Source
0.966	-2.5	EML	[208]
0.91	-1.8	EML	[209]
0.925	-2.1	R	[216; 205]
0.916	-2.28	SD	[215]
0.914	-1.5	SD	[213]
0.912	-2.0	SD	[217]
0.919	-1.76	SD	[119]
0.911	-1.53	SD	[214]
0.894±0.05	**-1.9±0.1**	**EML**	**[67]**

Table 4.5. Parameters γ_L and γ_T for the surface tension of pure liquid Au measured in this work [199] (bold). The data is compared with selected data from literature. The experimental methods used are specified in the third column.

γ_L ($N \cdot m^{-1}$)	γ_T ($10^{-4} N \cdot m^{-1} K^{-1}$)	Method	Source
1.143	-1.4	SD	[218]
1.121	-0.9	EML	[41]
1.138	-1.9	SD	[210]
1.15	-1.4	EML	[211]
1.140±0.06	**-1.83±0.11**	**EML**	[199]

Table 4.6. Parameters γ_L and γ_T for the surface tension of pure liquid Ni measured in this work [68] (bold). The data is compared with selected data from literature. The experimental methods used are specified in the third column.

γ_L ($N \cdot m^{-1}$)	γ_T ($10^{-4} N \cdot m^{-1} K^{-1}$)	Method	Source
1.778	-3.8	R	[175]
1.770	-3.3	EML	[107]
1.770	-3.3	EML	[41]
1.796	-3.5	R	[205]
1.781	-2.85	R	[12; 207]
1.77	**-3.30**	**EML**	[68]

Table 4.7. Parameters γ_L and γ_T for the surface tension of pure liquid Co measured in Ref. [196]. The data is compared with other selected data from literature. The experimental methods used are specified in the third column.

γ_L ($N \cdot m^{-1}$)	γ_T ($10^{-4} N \cdot m^{-1} K^{-1}$)	Method	Source
1.873	-4.9	R	[175]
1.944	-6.666	SD	[214]
1.89	-3.30	EML	[196]

Table 4.8. Parameters γ_L and γ_T for the surface tension of pure liquid Fe measured in this work [68] (bold). The data is compared with selected data from literature. The experimental methods used are specified in the third column.

γ_L (N·m^{-1})	γ_T (10^{-4}N·m^{-1}K^{-1})	Method	Source
1.896	-9.5	SD	[219]
1.872	-4.9	R	[175]
1.843	-1.86	SD	[214]
1.92	**-3.97**	**EML**	[68]

4.2.3 Transition metals (Ni, Co, Fe, Ti)

Surface tension data of the pure liquid transition metals, Ni, [68], Fe [68], and Ti [206] are plotted in Fig. 4.9 versus temperature. In addition, the representation of liquid Co, obtained by Eichel [196], is shown. The latter has been measured using the same electromagnetic levitation furnace and under similar conditions as the data for Ni and Fe of the present work. In order to remove residual oxides from the surface, the experiments on Ni, Co,

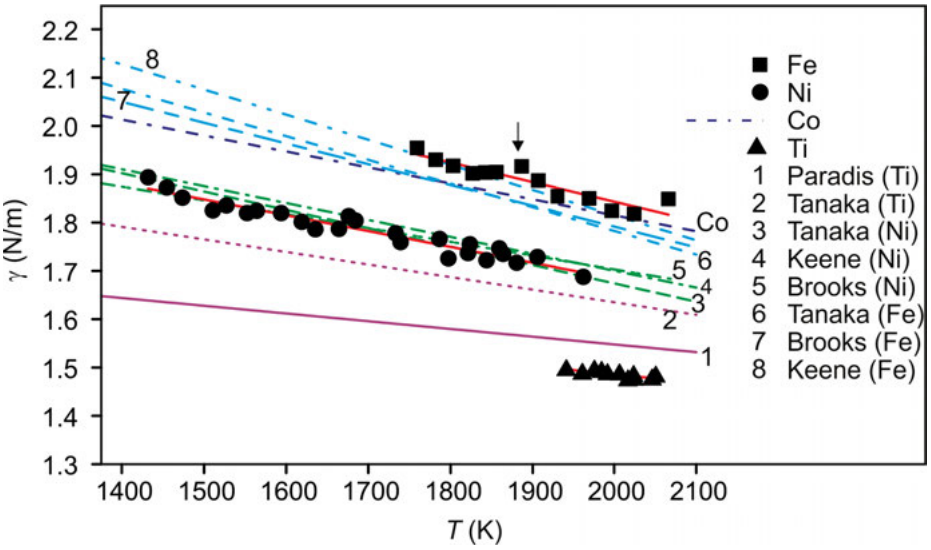

Fig. 4.9. Surface tension of pure Ni [68], Fe [68], and Ti [206] versus temperature (symbols). The data is shown together with results from literature: 1: Ref. [220], 2,3,6: Ref. [175], 4,8: Ref. [205], 5: Ref. [207].

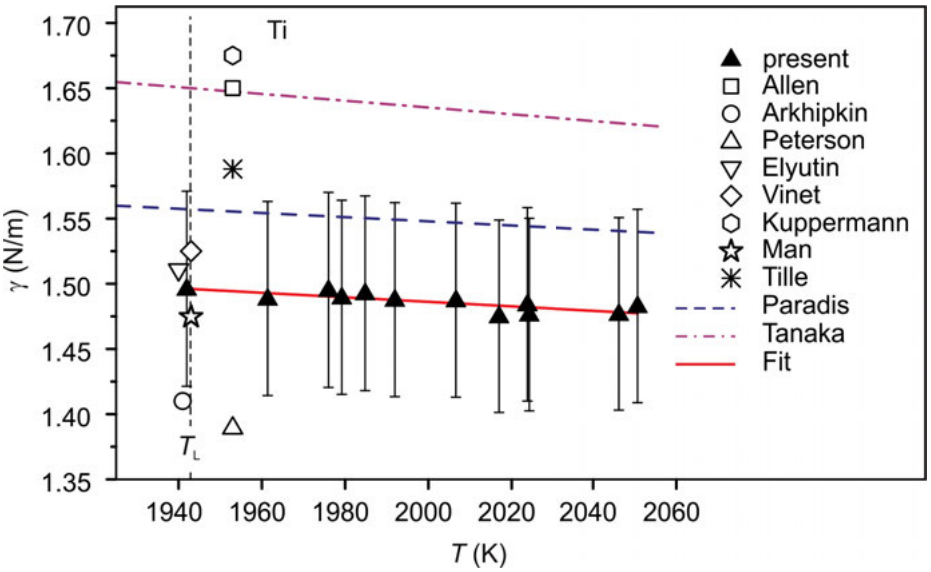

Fig. 4.10. Surface tension of pure Ti as function of temperature [206] (solid symbols). The data is shown together with the γ-T representations published in Ref. [175] ("Tanaka") and Ref. [220] ("Paradis"). In addition, data measured by means of various container-based methods is also shown: [221]–[222] (open symbols).

and Fe are performed by adding hydrogen (≤ 8 vol.-%) to the process gas. As visible in Fig. 4.9, undercoolings are obtained for each material. In the case of Ni, data is obtained in a temperature range of $T_L - 320\,K \leq T \leq T_L + 220\,K$. In the case of Fe, it is obtained in a range of $T_L - 100\,K \leq T \leq T_L + 230\,K$ and for Ti, a temperature range of $T_L \leq T \leq T_L + 110\,K$ is covered. Fe exhibits the largest and Ti the smallest surface tension. The results for Co and Fe lie closely together and overlap within an error margin of ±3 %.

The usage of hydrogen gas and its reducing action is discussed by Ozawa [223]. In fact, the kinetics of the reduction is temperature dependent: At low temperature, the equilibrium may be on the reducing side. In contrast to this, desorption of oxygen dominates at high temperature. In the regime of medium temperatures, adsorption of oxygen may become significant which is associated with a sign reversal of y_T. Following this argumentation, Ozawa identified in Ref. [223] a small kink in the data of liquid iron [68] measured in the present work. He explained this kink by the action of the added hydrogen. It is marked in Fig. 4.9 by an arrow. Obviously, this feature is still beyond the error margin of ±5 %.

The respective fit parameters y_L and y_T are listed for Ni, Fe, and Ti in Tabs. 4.6, 4.8, and 4.9 together with their corresponding uncertainties. In addition, the fit parameters for liquid Co are listed in Tab. 4.7.

Table 4.9. Parameters γ_L and γ_T for the surface tension of pure liquid Ti measured in this work [206] (bold). The data is compared with selected data from literature. The experimental methods used are specified in the third column.

γ_L ($N \cdot m^{-1}$)	γ_T ($10^{-4} N \cdot m^{-1} K^{-1}$)	T_{ref} (K)	$\gamma(T_{ref})$ ($N \cdot m^{-1}$)	Method	Source
		1953	1.65	SD	[221]
		1953	1.588	DW	[224]
		1941	1.41	DC	[225]
		1953	1.39	DW	[226]
		1940	1.51	CR	[227]
		1943	1.525	PD/DW	[228]
		1953	1.675	μg-EML	[229]
		1943	1.475	SD	[222]
1.650	-2.6			R	[175]
1.557	-1.6			ESL	[220]
1.49±0.08	**-1.7±0.1**			**EML**	**[206]**

The tables also show available literature data. Correspondance is obtained for Fe, Ni and also for Co. In the case of pure Ti, there is a big scatter among the published data. At temperatures close to T_L, surface tensions vary from 1.39 Nm^{-1} [226] to 1.675 Nm^{-1} [229]. This is further illustrated in Fig. 4.10. y is measured as a function of temperature for only three datasets: the one published in Ref. [175], which is taken from the review of Keene, [205], another one measured by Paradis [220], using electrostatic levitation and the data measured by Amore [206] within the frame of the present work. The large variation among the data originates from the high chemical reactivity and the high melting point of Ti.

For surface tension measurements, the purity of the sample and its surface is crucial. Hence, container-based processing cannot seriously be employed. Among the data measured by containerless techniques, those of Paradis [220] are closest to the ones of the present work. In electrostatic levitation, however, the effect of the surface charge on the surface tension measurement is still unclear [19]. At the present point in time, the only reliable data for the surface tension of pure Ti are those of the present work [206]. This fact is very astonishing, in particular, in view of the enormous technical importance of Ti and Ti-based alloys.

4.2.4 Synopsis

The surface tension results discussed in the previous section are summarized for each element by their parameters y_L and y_T in Tab. 4.11 together with their corresponding liquidus temperatures T_L. Obviously, there is a rough tendency for the surface tension to nearly monotonically increase with the liquidus temperature. However, Ti forms

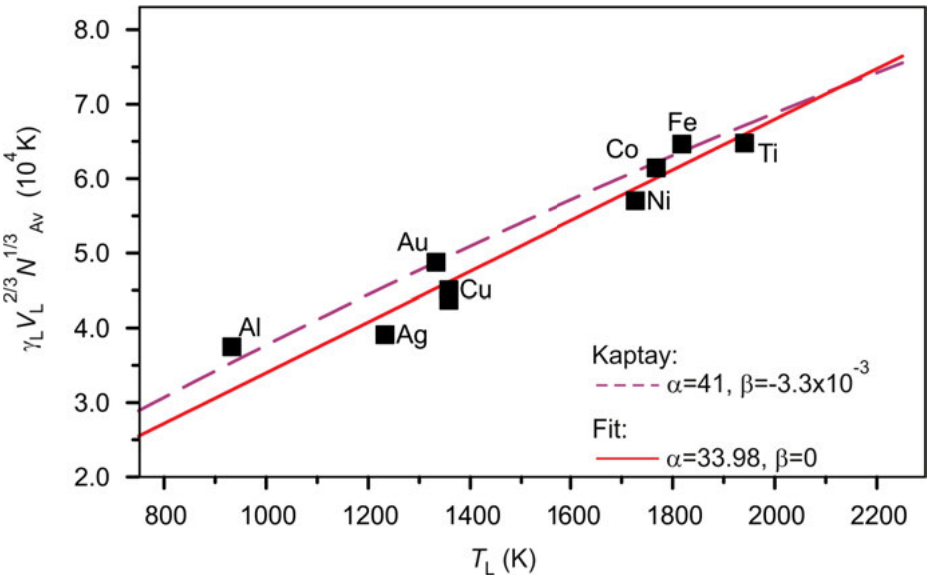

Fig. 4.11. $\gamma_L V_L^{\frac{2}{3}} N_A^{\frac{1}{3}}$ calculated from measured quantities versus T_L (symbols). In addition, the lines show calculation of Eq. (4.40) (solid) and Eq. (4.41) (dashed).

an exception from this trend: It has the largest liquidus temperature but its surface tension ranges fairly in the middle between the others.

As discussed in Sec. 4.1.9, the molar surface area A, which is calculated in Eqs. (4.26) and (4.40) from the molar volume, must also be taken into account. Hence Tab. 4.11 also lists molar volumes selected from Tab. 3.11.

Figure 4.11 also shows a plot of Kaptays optimized formula, Eq. (4.41), using values of the free adjustable parameters α_K and β_K recommended by him as $\alpha_K = 41$ and $\beta_K = -3.3 \times 10^{-3}$ [195]. Obviously, the agreement of Eq. (4.41) with the experimental data is also very good, but the mean square deviation is smaller for the linear, unoptimized, relation of Eq. (4.40). On the other hand, Eq. (4.41) is adjusted in Ref. [195] to a much larger set of data covering also a different T_L-range from 1728 K to 3600 K. Hence, it is justified to assume that Eq. (4.41) provides the better overall agreement.

Figure 4.11 shows for each element a plot of $y_L(N_A)^{1/3} V_{L,i}^{2/3}$ versus T_L. Obviously, the linear relation of Eq. (4.40) can be adjusted to this plot. The adjustable free parameter, α_K, turns out from Fig. 4.11 as $\alpha_K = 33.98$. This agrees within the margins with the value given by Kaptay α_K =38±10, see Sec. 4.1.9.

Table 4.10. Auxiliary data for the calculation of the γ_T in Eq. (4.42). For each element, the table shows the liquidus temperature, T_L, the molar volume V_L, the thermal expansion coefficient β and the molar heat capacity at constant pressure, C_p. The parameters V_L and β are picked from Tab. 3.11. Data of C_p are obtained from Ref. [230]. ([1)]: Average molar volume).

Element	T_L (K)	V_L (cm^3mol^{-1})	β ($10^{-4}K^{-1}$)	C_p (J/mol)
Al	933	11.6[1)]	1.116[1)]	31.78
Cu	1358	8.04	0.97[1)]	32.66
Ag	1233	11.79	0.81	33.49
Au	1333	11.4[1)]	0.64	33.38
Ni	1727	7.45[1)]	1.18	43.12
(Co)	1768	7.55	1.14	40.53
Fe	1818	7.96[1)]	1.16[1)]	45.05
Ti	1941	11.68	0.8	37.68

Table 4.11. Surface tension of the investigated elements. For each dataset, the table shows the parameters T_L, γ_L, γ_T, V_L, and the corresponding literature source. The molar volume V_L is picked from Tab. 3.11. ([1)]: Average molar volume).

Element	T_L (K)	γ_L (Nm^{-1})	γ_T ($10^{-4}Nm^{-1}K^{-1}$)	V_L (cm^3mol^{-1})	Source
Al	933	0.866	-1.46	11.6[1)]	[199]
Cu	1358	1.30	-2.64	8.04	[191]
		1.33	-2.6	8.04[1)]	[67]
		1.33	-2.3	8.04[1)]	[206]
Ag	1233	0.894	-1.9	11.79	[67]
Au	1333	1.140	-1.83	11.4	[199]
Ni	1727	1.77	-3.30	7.45[1)]	[68]
(Co)	1768	(1.89)	(-3.30)	7.55	[196]
Fe	1818	1.92	-3.97	7.96[1)]	[68]
Ti	1941	1.49	-1.7	11.68	[206]

The relation for y_T, Eq. (4.42), can be validated in the same way. The parameters needed in Eq. (4.12) are listed in Tab. 4.10. The molar heat capacities, C_p, are taken from Ref. [230] and the thermal expansion coefficients, β, are picked from Tab. 3.11. y_L, finally, is taken from Tab. 4.11. The result is shown in Fig. 4.12, where $y_T A$ calculated from Eq. (4.12) is plotted versus the measured one. As visible, the symbols scatter around the diagonal line qualitatively, confirming Eq. (4.12).

Instead of relating the surface tension to the cohesive energy via T_L, one can also attempt to compare the surface tension y_i of an element i with the free energy of its standard state, $G_i^0(T)$. From Eq. (4.22) it is maintained that $y_i \cdot A = G_i^S - G_i^B$. If, in a

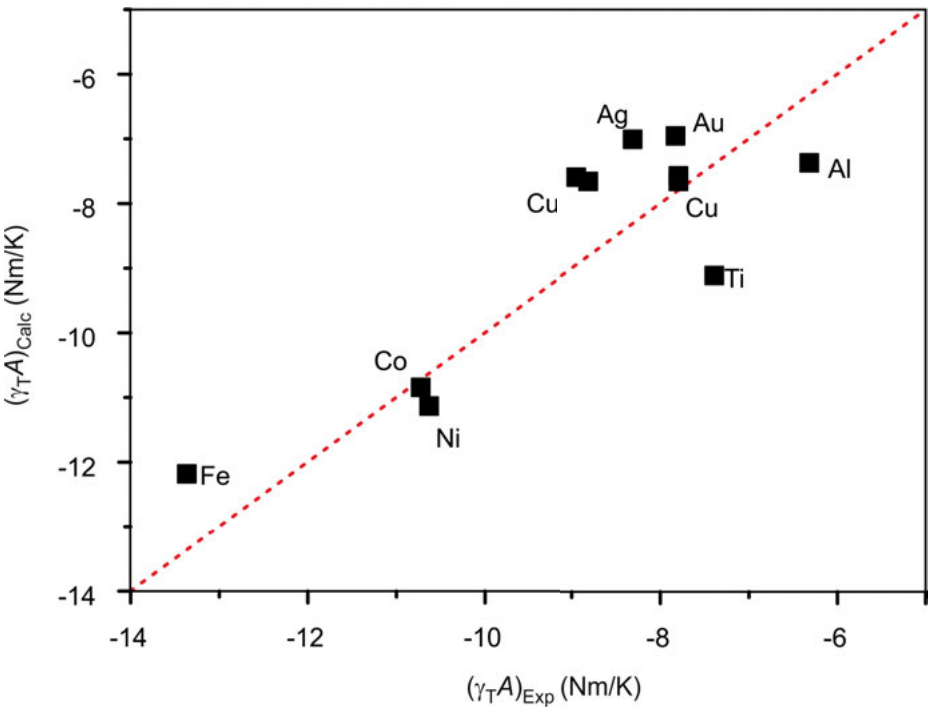

Fig. 4.12. Validation of Eq. (4.12). Predicted values of $\gamma_T A$ versus the experimental ones (symbols). The points scatter around the diagonal line (dashed).

similar approach as in Eq. (4.33), G_i^S is expressed by ζG_i^B the following simple relation is obtained:

$$y \cdot A = (\zeta - 1) G_i^0(T) \tag{4.43}$$

In order to test Eq. (4.43), $G_{\text{Surf}} = y_L \cdot A$ is plotted for each element versus $G_i^0(T_L)$. The corresponding functions for the standard state are taken from the SGTE database, provided in Ref. [231]. The result is shown in the inset in Fig. 4.13. The data is assembled around a straight line with a negative slope of -0.577 corresponding to $\zeta = 0.423$. Al hereby forms an exception as the corresponding data point is shifted along the horizontal axis by roughly 20 kJ/mol.

The parameter ζ can also be calculated for each element separately. This is shown in Fig. 4.13, where ζ is plotted versus the atomic order number, Z. As visible, ζ scatters around its mean value of $\bar{\zeta} = 0.377$ which is very close to the value of 0.423 obtained from the linear fit.

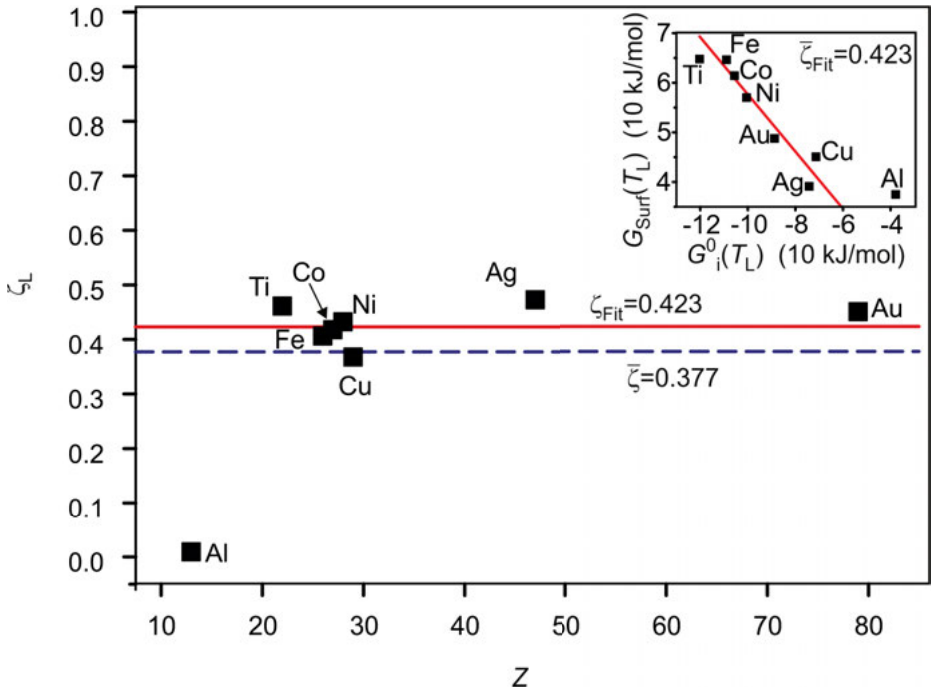

Fig. 4.13. ξ calculated from Eq. (4.43) and plotted versus the atomic order number Z. The dashed line shows the arithmetic average and the solid line corresponds to the slope of $G_{\text{Surf}} = \gamma_{\text{L}} A$ versus G_{i}^{0} shown in the inset.

4.3 Binary systems

In the same way as for the densities in Chap. 3, surface tensions are investigated by a stepwise extension from unary to binary and ternary systems. Regarding the binary systems, results are obtained for Ag-Cu, Al-Au, Al-Cu, Al-Fe, Al-Ni, Cu-Fe, Cu-Ni, Cu-Ti, Cu-Si, and Fe-Ni. Their excess surface tensions are evaluated at fixed temperatures T_{fix} using Eqs. (4.18) and (4.19). The results, i.e. the parameters ${}^{0}u_{\text{i,j}}$ and ${}^{1}u_{\text{i,j}}$, are summarized in Tab. 4.12, allowing for a qualitative discussion of the excess surface tension with respect to sign and magnitude. Moreover, an overview of the segregation behavior is provided for each system.

Systems with a negative excess surface tension, ${}^{\text{E}}y < 0$, are Cu-Ni [68], Cu-Fe [68; 155], Ag-Cu [67], and Cu-Si [151]. Among these, Cu-Fe is a typical representative and will be discussed in more detail:

Cu-Fe consists of two structurally different components, a group Ib noble metal and a transition metal. ${}^{\text{E}}G$ is strongly positive and a metastable miscibility gap exists in the undercooled regime [233].

Table 4.12. Investigated binary systems and parameters ${}^0u_{i,j}$ and ${}^1u_{i,j}$ obtained from fitting ${}^E\gamma$ by Eq. (4.19) at $T = T_{fix}$. The 5^{th} column specifies the segregating species and references to the surface tension data is given in the last column.

System i, j	T_{fix} (K)	${}^0u_{i,j}$ ($Nm^{-1}mol^{-1}$)	${}^1u_{i,j}$ ($Nm^{-1}mol^{-1}$)	Segregating species	Source
Cu,Ni	1400	-0.399	0.793	Cu	[68]
Cu,Fe	1900	-1.124	1.127	Cu	[68]
Cu,Ti	1400	0.118	-0.273	Cu	[206]
Ni,Fe	1800	0.221	0.007	Ni	[68]
Cu,Ag	1400	0.257	0.307	Ag	[67]
Al,Cu	1400	0.475	-0.754	Al	[191]
Al,Fe	1600	1.508	-1.341	Al	[232]
Al,Ni	1600	2.095	-1.624	Al	[232]
Al,Au	1400	0.247	-0.391	Al	[199]
Cu,Si	1400	-1.030	-3.267	Si	[151]

Measured surface tensions of liquid Cu-Fe alloys with Cu concentrations ranging from 20 to 80 at.-% are shown as functions of temperature in Fig. 4.14. Temperature ranges are covered from 1300 K to 2100 K. The data falls between 1.2 and 1.4 Nm^{-1}. Even for $Cu_{20}Fe_{80}$, which has a large iron concentration, the surface tensions are close to those of pure Cu. In order to study the concentration dependence, $y(T)$ is extrapolated in Fig. 4.15 to a temperature of $T = T_{ref}$ =2000 K. This temperature is chosen for the following reasons: First of all, the temperature at which the model calculations are to be performed should be well above the critical temperature of demixing, T_{demix}. In Cu-Fe, T_{demix} is determined experimentally as ≈ 1673 K [234]. This is in agreement with Calphad calculations using the full Redlich-Kister description of ${}^EG$ [235]. Second if, as in the Chatain model [187] only one coefficient ${}^0L(T = 0)$ is used, T_{demix} turns out to be approximately 2100 K. This temperature is, however, far above the maximum temperature at which experimental surface tension data is obtained. As a compromise, therefore, the experimental data is discussed at T_{ref} =2000 K and, in Eq. (4.37), ${}^0L(T = 0)$ is reduced by a factor of α_{demix} =0.9:

$$\alpha_{demix} \cdot {}^0L(T = 0) \rightarrow {}^0L(T = 0) \tag{4.44}$$

This moves T_{demix} back to ≈ 1700 K [190].

In Fig. 4.15, y sharply decreases within the first 30 at.-% of Cu bulk concentration from its initial value of ≈1.85 N/m, corresponding to pure iron, down to ≈1.15 N/m. This latter value corresponds to the surface tension of pure copper. Upon further increase of x^B_{Cu}, y remains practically constant at this level.

The comparison of the experimental data with the model calculations in Fig. 4.15 shows that the ideal solution significantly overestimates the data and, hence, fails to describe it correctly. This is expected, as Cu-Fe is a highly non-ideal system [235]. A far better agreement is obtained for the Butler equation, Eq. (4.32). There is also some

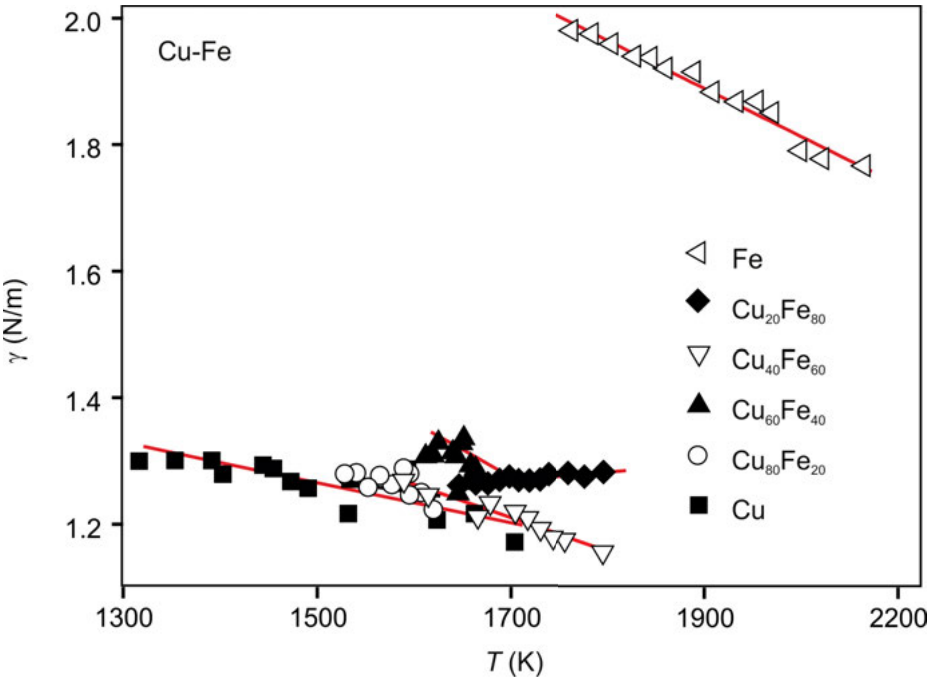

Fig. 4.14. Measured surface tensions γ of liquid Cu-Fe versus temperature T for different compositions (symbols). The solid lines represents fits of Eq. (4.11).

discrepancy for x^{B}_{Cu} >40 at.-% where the experimental data is overestimated by 2–5 %. The linear representation of y, Eq. (4.11), becomes less accurate when T_{ref} becomes too large. Therefore, Fig. 4.15 shows the same comparison also for T =1823 K. Obviously, the agreement is now better.

The Butler equation predicts in Fig. 4.15 that the surface tensions at T =2000 K are lower than for 1823 K as long as x^{B}_{Cu} > 20 at.-%. For smaller concentrations, x^{B}_{Cu} < 20 at.-%, it is predicted that y(2000 K) > y(1823 K). This crossover of the curves is encircled in Fig. 4.15. It is in agreement with the observed positive y_T of the data for $Cu_{20}Fe_{80}$ shown in Fig. 4.14 [68; 155; 190].

In Fig. 4.15 a calculation of the Chatain model, Eq. (4.36) is also shown. The agreement with the data is reasonable. The surface tension and its concentration dependence are predicted to be qualitatively correct but the experimental data is overestimated by at least 10 %. This is due to the above mentioned reduction of ${}^{0}L(T = 0)$ in Eq. (4.44).

According to the Butler model, the concentration of copper in the surface layer, x^{S}_{Cu}, is greater in Fig. 4.16 than approximately 60 at.-%, even for a small copper bulk concentration of only x^{B}_{Cu} ≈15 at.-%. A significant and sharp decrease of x^{S}_{Cu} is found if x^{B}_{Cu} falls below this limit. As shown in Fig. 4.16, an even stronger segregation of

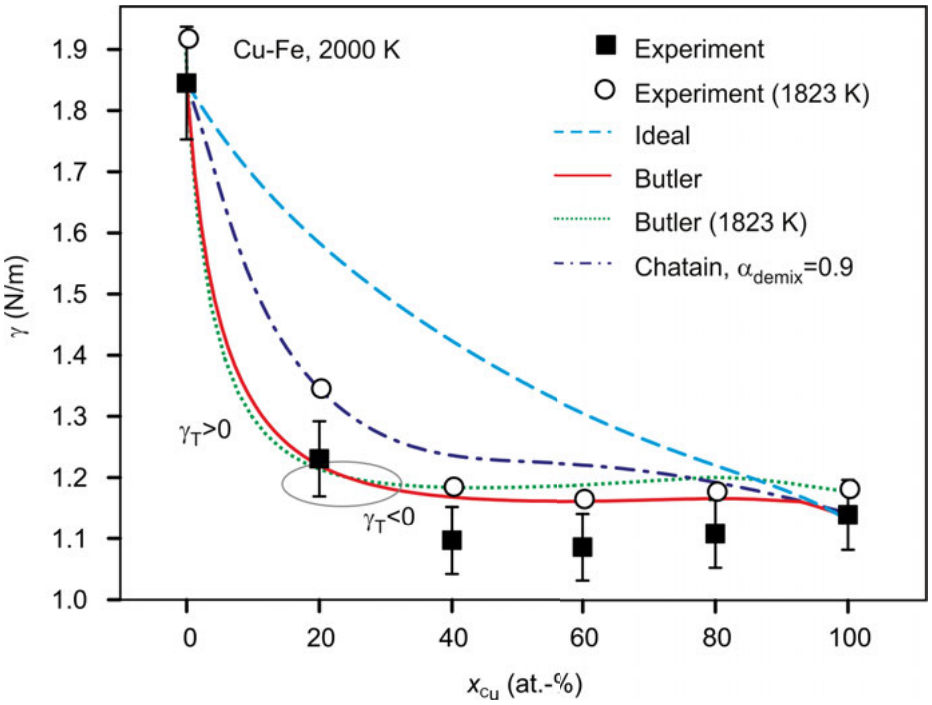

Fig. 4.15. Isothermal surface tension of Cu-Fe versus the bulk mole fraction of copper, x_{Cu}^{B}. The data is plotted for T =2000 K (solid symbols) and T =1823 K (hollow symbols). In addition, model calculations are shown for the ideal solution model (dashed), Eq. (4.29), the Butler equation, Eq. (4.32), at 2000 K (solid line) and at 1823 K (dotted) and the Chatain model, Eq. (4.36), (dash-dotted). The ellipse encircles the transition point from positive to negative values of γ_T.

copper is predicted for the top monolayer by the Chatain model, according to which x_{Cu}^{S} > 95 at.-% if x_{Cu}^{B} >10 at.-%. The figure shows calculations of layer compositions up to the 10^{th} layer from the top. It is seen that the deviation from x_{Cu}^{B} disappears with an increase in the layer number n. Under these conditions, the effective thickness of the surface is approximately 5 – 9 layers [190]. While the Butler equation and the Chatain model may both give a good estimate of the surface tension, as is seen in Fig. 4.16, they may significantly differ in the description of the surface composition [190]. Because the Butler model is restricted to one monolayer, it effectively averages the surface composition [190].

Qualitatively, the same isothermal surface tension curve of Cu-Fe is obtained for Cu-Ni [68] where surface segregation of Cu is also dominant. In the case of Ag-Cu, a similar curve of the surface tension is also obtained except that, instead of Cu, Ag is the segregating species.

As discussed above, the process of segregation results from a minimization of the surface energy. Hence, the element with the smaller surface tension becomes enriched

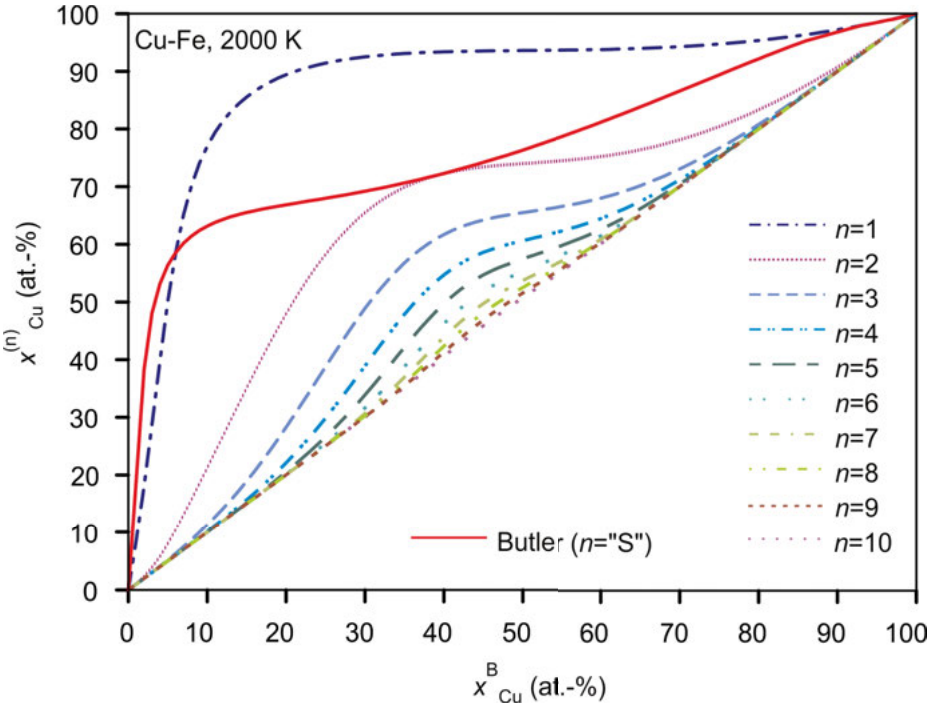

Fig. 4.16. Calculated Cu mole fractions $x^{(n)}_{Cu}$ of the surface near layers n in Cu-Fe at 2000 K as function of the bulk mole fraction, x^{B}_{Cu}. The solid line represents the calculation of Butler model for the top surface layer n ="S". The dashed and/or dotted lines correspond to the Chatain model.

in the surface and determines the surface tension of an alloy. As in the case of Cu-Fe, segregation becomes enhanced if ${}^{E}G > 0$. Alloys for which ${}^{E}G < 0$ display a different behavior. Such alloys are Fe-Ni, Cu-Ti, Cu-Si, Al-Cu, Al-Ni, Al-Fe and Al-Au. Fe-Ni, e.g., is a comparatively simple system composed of two structurally similar elements: Fe and Ni.

For this system, the isothermal surface tension is plotted in Fig. 4.17 versus the bulk nickel concentration, x^{B}_{Ni} at T =1800 K. Upon increasing x^{B}_{Ni}, y decreases from ≈1.92 Nm^{-1}, corresponding to the surface tension of pure Fe, down to ≈1.75 N/m. The latter value corresponds to the surface tension of pure liquid Ni. Over the entire compositional range, y varies, therefore, by ≈ 10 %.

In Fig. 4.17 the experimental data is shown together with the ideal solution model underestimating them by ≈ 2 %. This discrepancy is beyond the estimated error of the experimental method (± 5 %). For Fe-Ni the ideal solution model can, in principle, be regarded as sufficient in order to predict the surface tension. A slightly better agreement is found, of course, when applying the Butler and the Chatain model [190]. Obviously, there is no significant difference among the two models in Fig. 4.17.

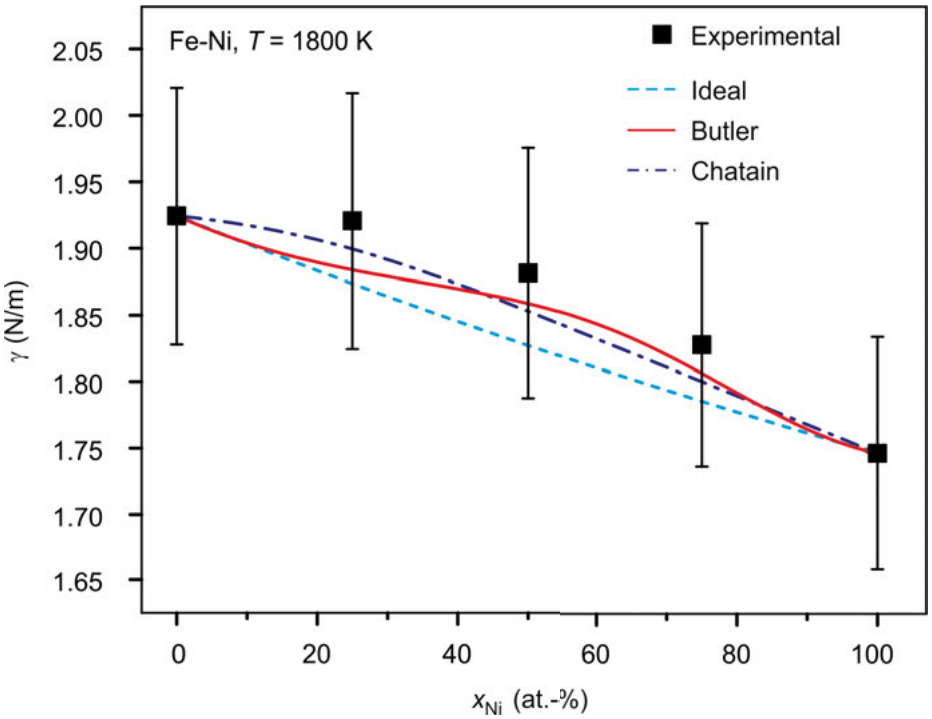

Fig. 4.17. Isothermal surface tension γ versus $x_{\mathrm{Ni}}^{\mathrm{B}}$ for the Fe-Ni system. The plot is shown for a temperature of 1800 K. For comparison, calculations of the ideal solution model, Eq. (4.29) (dashed), the Butler model, Eq. (4.32), (solid) and the Chatain model, Eq. (4.36), (dash-dotted), are also shown. Within the error bars of ± 5 %, the agreements between the models and the data are equally good.

In contrast to Cu-Fe, Cu-Ni, and Ag-Cu, the $\gamma(x_{\mathrm{Ni}}^{\mathrm{B}})$-curve in Fig. 4.17 exhibits a concave shape. In Fe-Ni, the excess free energy is negative and segregation is reduced. This becomes clear from the calculated segregation profile in Fig. 4.18. Again, there is a good agreement between the calculations of the two models for the top monolayer. The concentration of Ni in this layer is predicted by both models to be moderately increased, i.e. by 10 %, with respect to the concentration in the bulk, $x_{\mathrm{Ni}}^{\mathrm{B}}$. Moreover, the Chatain model predicts a depletion of Ni in the second layer. Already in the third layer there is no sign of segregation at all. The most important information from this plot is that the surface concentration can also be predicted by the ideal solution model. Hence, segregation in this system exceeding the one predicted by the ideal solution model is practically suppressed. The systems Al-Ni, Al-Fe, Al-Cu, and Al-Au not only exhibit ${}^{\mathrm{E}}G \ll 0$, their components are also structurally different. In addition, their phase diagrams exhibit intermetallic phases reaching up to the corresponding liquidus temperatures. Compound formation might therefore affect the surface tension.

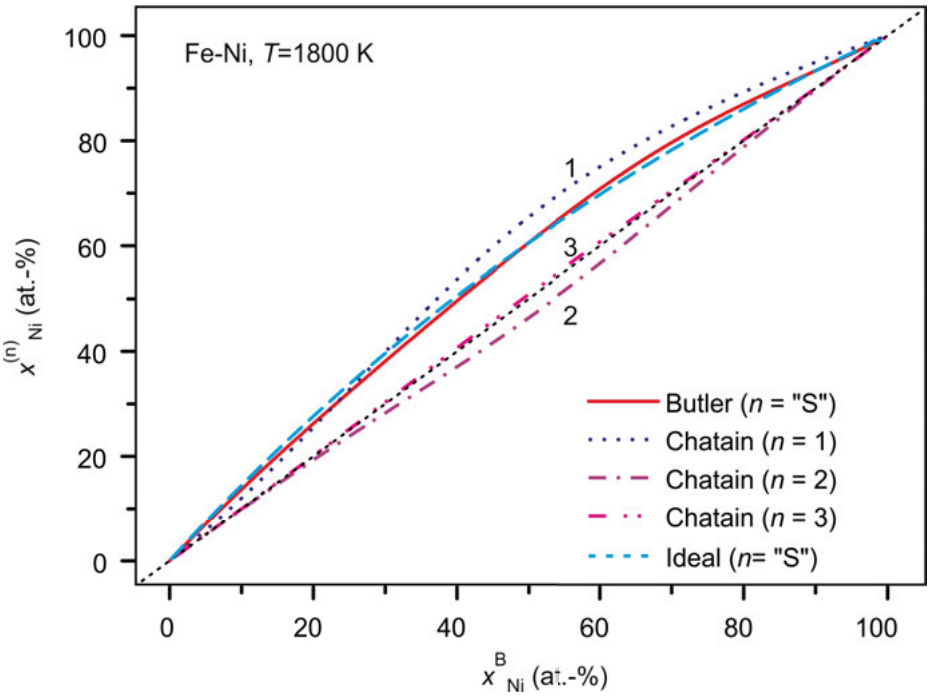

Fig. 4.18. Calculated nickel mole fractions $x^{(n)}_{Ni}$ of the surface near layers in Ni-Fe at 1800 K plotted versus the bulk mole fraction, x^{B}_{Ni}. The solid line represents the calculation of Butler model for the top surface layer n ="S". The dashed and/or dotted lines correspond to the Chatain model calculated up to the third layer.

Figure 4.19, thus, shows a plot of the isothermal surface tension of Al-Ni versus the Al bulk mole fraction x^{B}_{Al}. The plot is shown for a temperature of 1673 K [190]. The data exhibits a broad maximum around x^{B}_{Al} =50 at.-% following a dip at approximately 25 at.-% [190]. Such a feature is believed to be due to compound formation in the liquid, caused at a certain composition by pronounced attractive interactions between unlike atoms. Such interactions would also lead to the formation of intermetallic phases [190; 192]. In Al-Ni, the responsible intermetallic phase exists at 50 at.-% and leads to a dominant maximum in the liquidus at this composition, see inset in Fig. 4.19.

Figure 4.19 also shows the model calculations. The Butler and the Chatain model are in qualitative agreement with the data only for x^{B}_{Al} >40 at.-%. In particular, both models do not reproduce the observed maximum and the dip. This is not surprising as the thermodynamic potentials, ${}^{E}G$, are approximated by the sub-regular solution model. Processes, such as compound formation, are not included [190].

Figure 4.19 also shows a calculation of the compound formation model of Egry, Eq. (4.38). As visible, the agreement with the data is impressively good: Deviations

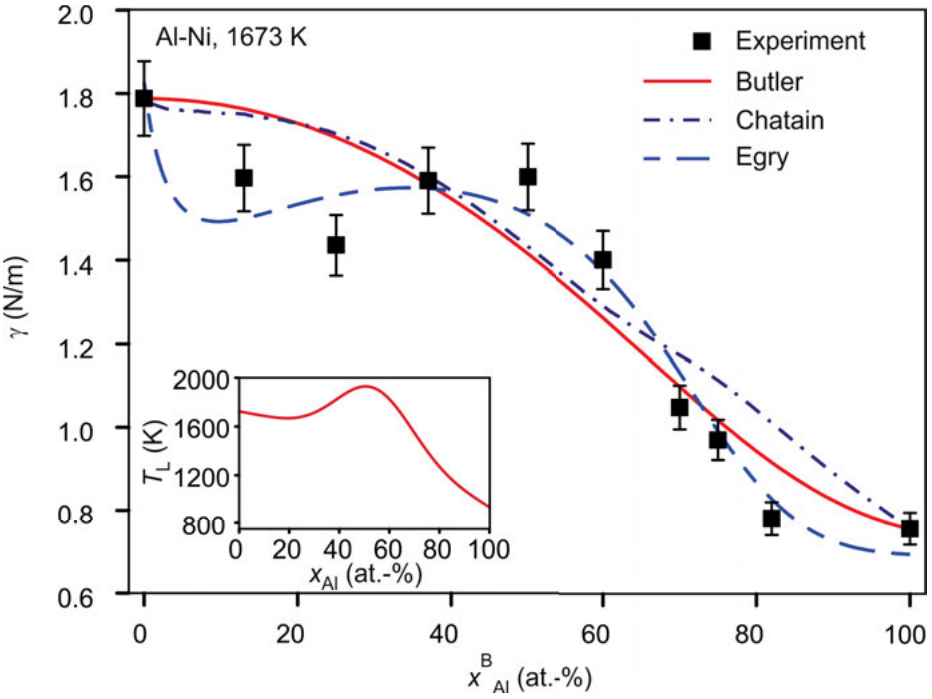

Fig. 4.19. Isothermal surface tension of Al-Ni plotted at 1673 K versus x_{Al}^{B} (symbols). The lines correspond to model calculations of the Butler model, Eq. (4.32), (solid), the Chatain model, Eq. (4.36) (dash-dotted) and the Egry model, Eq. (4.38) (long-short dashed). The inset corresponds to the phase diagram of Al-Ni [154].

are within the error bars and the maximum and the dip are reproduced correctly.

Other systems, studied in this work in which compound formation may play a role and for which a maximum or a shoulder is visible in the isothermal surface tension are Al-Fe [232] and Cu-Si [151]. As for Al-Ni, the Butler- and the Chatain models fail to describe these features correctly whereas the Egry model is successful.

The phenomenon of compound formation and its effect the surface tension is not yet fully understood. There are a number of examples in literature, mainly for solder materials, where the surface tension has successfully been described by a compound formation model [236]–[238]. However, it is a fact that systems exhibiting pronounced intermetallic phases in their phase diagrams do not necessarily exhibit features of compound formation in their surface tension: Such a system is Al-Au which has a dominant intermetallic phase located at x_{Al}=63.3 at.-%, see inset in Fig. 4.20. Due to its color, it is sometimes referred to as the “purple plague” or the “purple pest”.

In the surface tension, no maximum is visible at the corresponding composition. This is also confirmed by surface tension data obtained under microgravity during a parabolic flight campaign (solid circles in Fig. 4.20). Obviously, the data is correctly

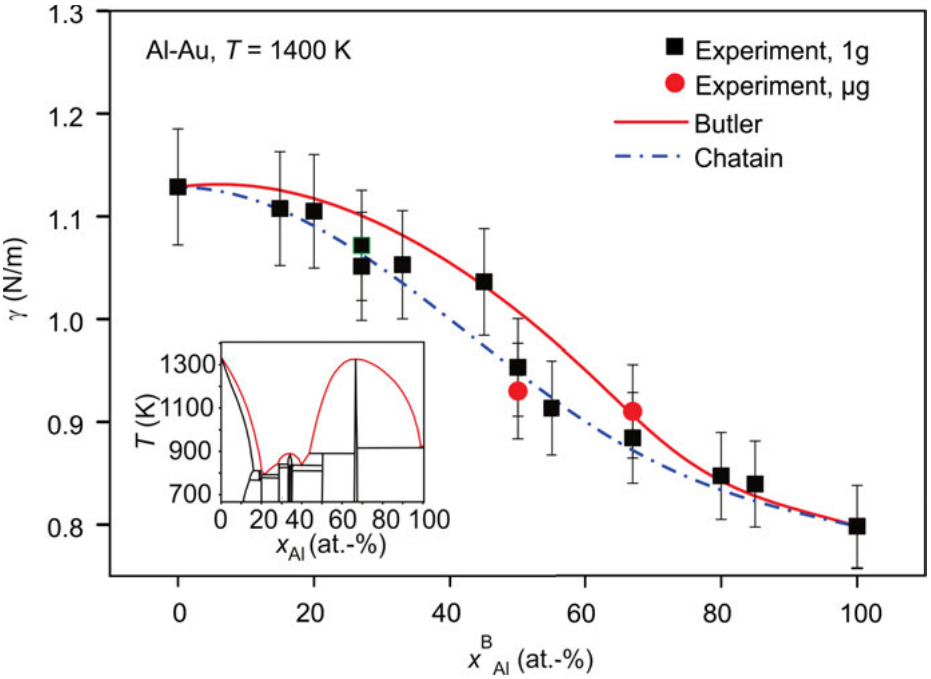

Fig. 4.20. Isothermal surface of Al-Au versus x_{Al}^{B} at 1400 K (symbols). No maximum in γ is evident at x_{Al}^{B} =63.3 at.-%. This is also confirmed by μ-gravity data (circles). The solid line corresponds to the Butler model, Eq. (4.32), and the dash-dotted line to the Chatain model, Eq. (4.36). The inset shows the phase diagram of Al-Au [154].

predicted by the Butler model using the sub-regular solution approximation. Hence, no model involving compound formation needs to be taken into account for this particular system. Al-Cu [191] is another system with intermetallic phases for which the surface tension can be described sufficiently without using any compound formation model.

Figure 4.20 also shows a calculation of the Chatain model, Eq. (4.36). The agreement with experimental data is also positive. Again, the Chatain model does not take any theory into account about compound formation and the sub-regular solution approximation suffices to describe the surface tension.

The Chatain model shall be used for a qualitative discussion of surface segregation in Al-Au, because general features can be explored for a mixing and a demixing system. For this purpose, Fig. 4.21 shows the concentration $x_i^{(n)}$ of each layer plotted against the layer number, (n). For $Al_{50}Au_{50}$, the Al concentration oscillates around its bulk value in the surface near region [199]. Such an oscillation is also observed in the cases of Al-Cu [191], Al-Ni [190] and, less pronounced, in Fe-Ni [190], see Fig. 4.18. This effect is also regarded as *chemical layering*. As one component segregates to the surface, a surplus of the other component in the second layer will energetically be fa-

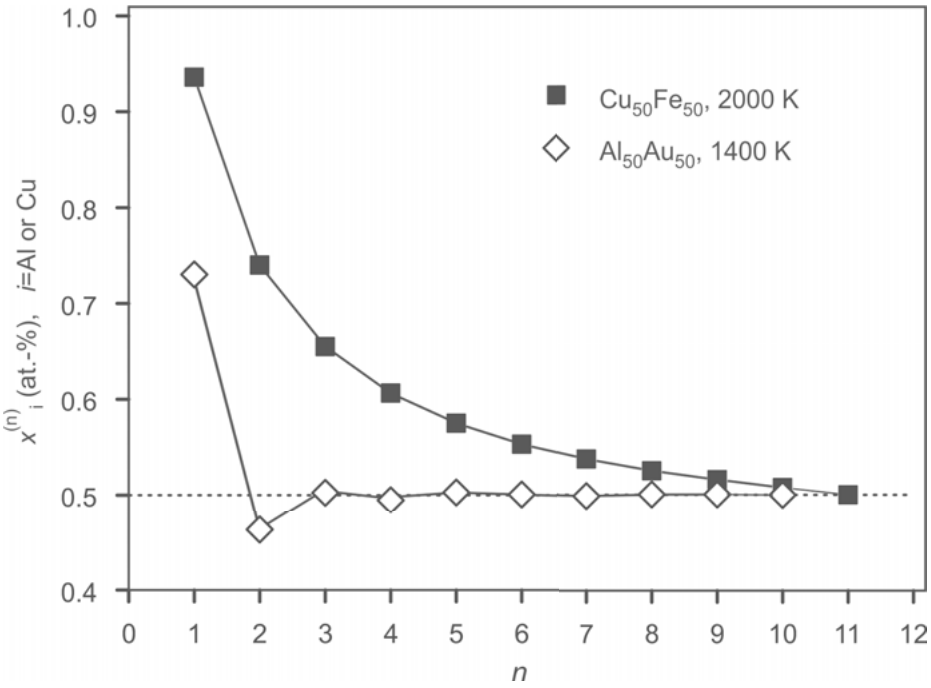

Fig. 4.21. Layer composition $x_i^{(n)}$, calculated from the Chatain model, Eq. (4.36), as function of the layer number n. Solid symbols refer to $Cu_{50}Fe_{50}$ at 2000 K (i=Cu) and hollow symbols refer to $Al_{50}Au_{50}$ at 1400 K (i=Al).

vored due to the negative excess free energy [190]. Such oscillations are not observed in a system with a positive excess free energy, as shown for Cu-Fe [190] in Fig. 4.21.

Table 4.13 summarizes comparisons performed within the present work of different systems with the discussed models. A tested model is hereby rated *OK*, if it agrees with the experimental data within the error bars of ±5 %. A model is rated "reasonable" (*RS*) if its agreement with the experimental data is partially within the error bars. It is rated "failed", i.e. *F*, if it is neither rated *OK* nor *RS*.

In the majority of cases, y is predicted correctly by the Butler model (=*OK*). Exceptions are, Al-Fe [232], Al-Ni [232] and Cu-Si [151]. In these systems, the surface tension is affected by compound formation and the Butler model gives only an estimate of the surface tension (=*RS*). The Chatain model is tested in the cases of Cu-Fe [190], Fe-Ni [190], Al-Cu [191], Al-Au [199], Al-Fe [232], and Al-Ni [190]. Positive agreement is found for Fe-Ni, Al-Cu and Al-Au. The Egry model is successfully tested for Al-Ni, Al-Fe, and Cu-Si. With respect to the experimental accuracy, the surface tension of Fe-Ni can also be described within the ideal solution model.

Table 4.13. Comparison of surface tensions of binary systems with calculations of different models: OK = good agreement (i.e. within error bars), RS = reasonable agreement (partially within error bars), F = fails. The last column specifies the corresponding literature source where the each comparison is discussed in detail.

System (*i*, *j*)	Model tested		Source
Ag-Cu	Butler	OK	[67]
Al,Au	Butler	OK	[199]
	Chatain	OK	
Al,Cu	Butler	OK	[191]
	Chatain	OK	
Al,Fe	Butler	RS	[232]
	Chatain	RS	
	Egry	OK	
Al,Ni	Butler	RS	[190]
	Chatain	RS	
	Egry	OK	
Cu,Fe	Butler	OK	[68]
	Chatain	RS	[190]
Cu,Ni	Butler	OK	[68]
Cu,Si	Butler	RS	[151]
	Egry	OK	
Cu,Ti	Butler	OK	[206]
Fe,Ni	Butler	OK	[68]
	Chatain	OK	[190]
	ideal	OK	[190]

4.4 Ternary systems

4.4.1 Overview

In order to further expand the investigations of ternary alloys, systems listed in Tab. 4.14 are studied. These are in particular the ternary monotectics Cu-Fe-Ni [239], Co-Cu-Fe [240], and Co-Cu-Co [159]. In addition, the ternary eutectic system Ag-Al-Cu is also investigated [176]. The investigations are performed by measuring along different cuts through the corresponding concentration triangles.

Table 4.14. Ternary systems investigated with respect to their surface tensions.

System	Source
Ag-Al-Cu	[176]
Co-Cu-Fe	[240]
Co-Cu-Ni	[159]
Cu-Fe-Ni	[239]

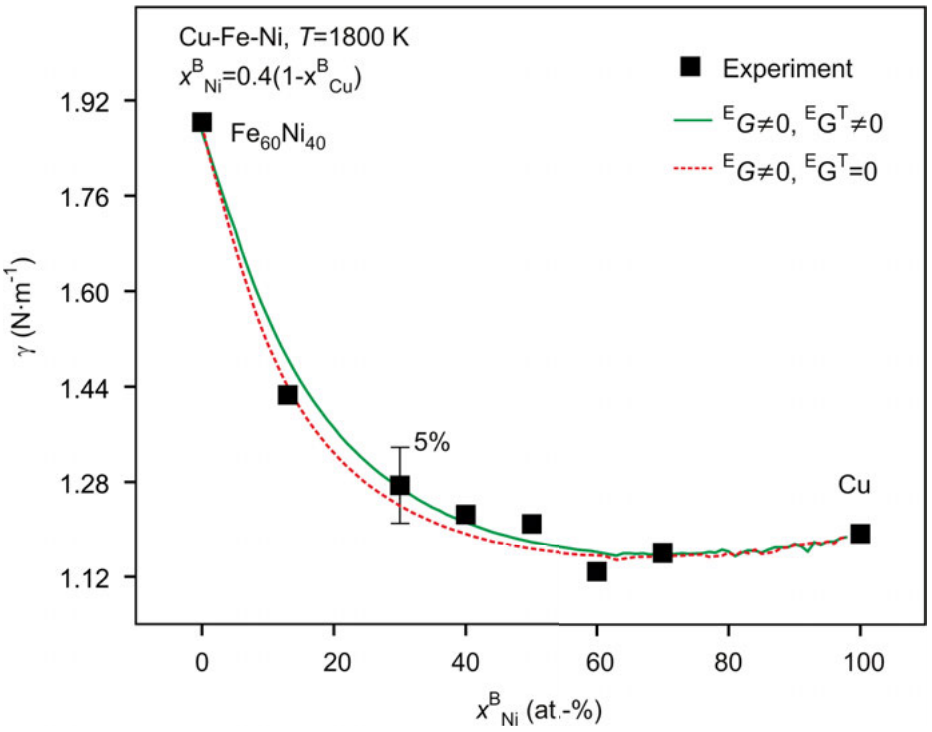

Fig. 4.22. Isothermal surface tension of Cu-Fe-Ni measured at 1800 K along $Cu_xNi_{0.4(1-x)}Fe_{0.6(1-x)}$, $0 \le x \le 1$ (symbols). The lines correspond to calculations of the Butler model, Eq. (4.32), with (solid) and without (dashed) the ternary term ^TG included into the excess free energy.

4.4.2 Monotectic systems

As an example of a comprehensively studied system, results on the surface tension obtained for Cu-Fe-Ni at T = 1800 K are shown in Fig. 4.22. In this figure, y is plotted versus x^B_{Cu} along a section from binary $Fe_{60}Ni_{40}$ to pure Cu, i.e. for $Cu_xFe_{0.6(1-x)}Ni_{0.4(1-x)}$, $0 \le x \le 1$. [155; 239]. The general shape of the curve is the same as for Cu-Fe in Fig. 4.15, i.e. there a strong dependence of y on the bulk concentration of Cu. Again, Cu is the main segregating species [239]. In Fig. 4.22, the experimental data is plotted together with solutions of the Butler model with and without, the ternary term ^TG being included into the excess free energy ^EG, see Eq. (3.17).

Obviously, these two cases cannot be distinguished from each other with respect to the uncertainty of the experimental data [239]. Hence, the ternary term can be neglected in Eq. (3.17) for the description of the surface tension. This result is also obtained for measurements performed along another cut through the system for which x^B_{Cu} is kept constant at 20 at.-% and where only the ratio of x^B_{Ni} to x^B_{Fe} is varied [239], see Fig. 4.23. The observed change of y with concentration is so small that y can be

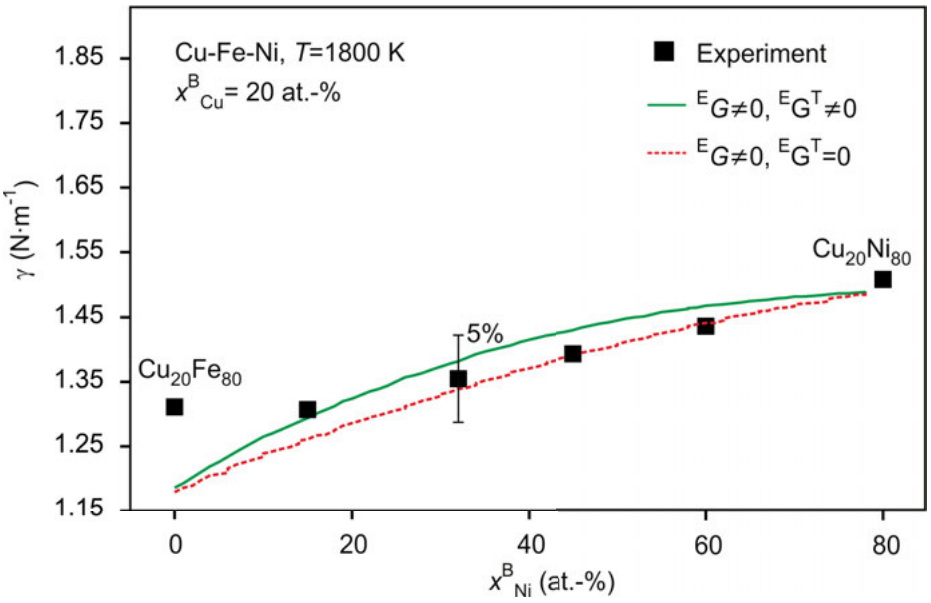

Fig. 4.23. Isothermal surface tension of Cu-Fe-Ni measured at 1800 K along a section for which x^B_{Cu} =20 at.-% (symbols). The lines correspond to calculations of the Butler model, Eq. (4.32), with (solid) and without (dashed) the ternary term ^TG included into the excess free energy.

considered as practically constant [155; 239]. Again, the Butler model yields approximately identical results once the ternary term ^TG is included into the calculations and when it is not.

With respect to surface tension, the systems Cu-Co-Fe [240] and Cu-Co-Ni [159] behave similarly to Cu-Fe-Ni. In all three systems, the surface tensions strongly depend on the concentration of Cu and they are almost invariant against a replacement of the other transition metals with each other [159; 240]. This, and the obvious similarities with the surface tensions of the binary alloys, Cu-Fe [68], Cu-Ni [68], and Co-Cu [196], imply that one may interpret Co-Cu-Fe, Cu-Fe-Ni, and Co-Cu-Ni as quasi binary systems "Cu-TM", where "TM" means "transition metal" [155]. Using a simple model such as the one proposed in [240; 241], it can be shown that, with respect to the surface tension, this is indeed a valid approach [155].

The monotectic systems discussed above can be characterized by their ability to metastably demix in the undercooled regime due to their positive excess free energy.

4.4.3 Ag-Al-Cu

The ternary eutectic system Ag-Al-Cu can be characterized by attractive interactions between its components. Its phase diagram exhibits intermetallic phases as well as

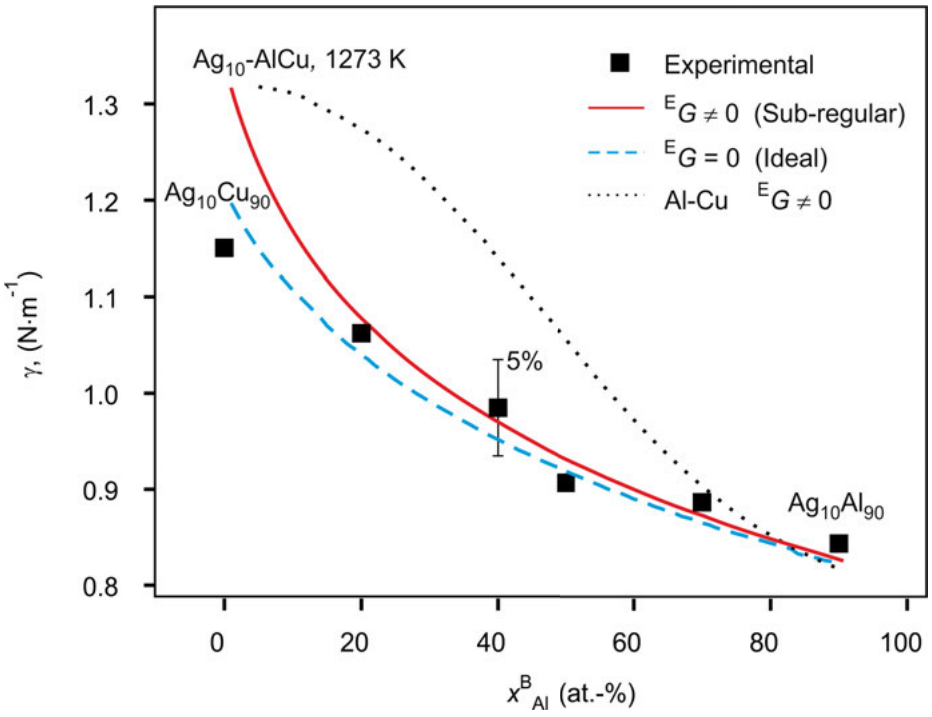

Fig. 4.24. Surface tension of Al-Cu-Ag along a section $Ag_{0.1}Al_xCu_{(0.9-x)}$, $0 \leq x \leq 0.9$, at 1273 K versus x^B_{Al} (symbols). The data is shown in comparison with solutions of the Butler equation, Eq. (4.32), for the ideal (dashed line) and the sub regular solution model (solid line). The dotted line corresponds to a calculation of the sub regular solution model for Al-Cu [191]. (from Ref. [176]).

eutectic and peritectic points [242; 243]. As discussed above Ag-Al-Cu is highly non-ideal, i.e. ${}^{E}G << 0$. Also, its binary margin systems, Al-Cu [191; 96], Ag-Al [96], and Ag-Cu [67] can be labeled as "non-ideal". One may expect, hence, that, with respect to its surface tension, Ag-Al-Cu will also behave highly non-ideal.

However, this is not the case as demonstrated in Fig. 4.24 for a cut along $Ag_{10}Al_xCu_{0.9-x}$, i.e. where the concentration of silver kept at 10 at.-% and x^B_{Al} is varied from 0 to 90 at.-% [176]. The surface tensions plotted in Fig. 4.24 collapse at 1273 K on a concave curve, $y(x^B_{Al})$, which is in a positive agreement with the Butler equation calculated for the (sub-)regular solution model, at least for $x_{Al} \geq 20$ at.-%. In the case of the datapoint at $x_{Al} = 0$ at.-%, which corresponds to $Ag_{10}Cu_{90}$, the deviation between the measured surface tension and the calculated result is larger than 10 %. In fact, the same value of y is reproduced for $Ag_{10}Cu_{90}$ in Ref. [67] so that it can be assumed that this value is correct, compare Tabs. A.7 and A.9. Therefore, the reason for the observed deviation needs to be identified in the thermodynamic assessment used, see Refs. [242; 243] and Tab. B.3.

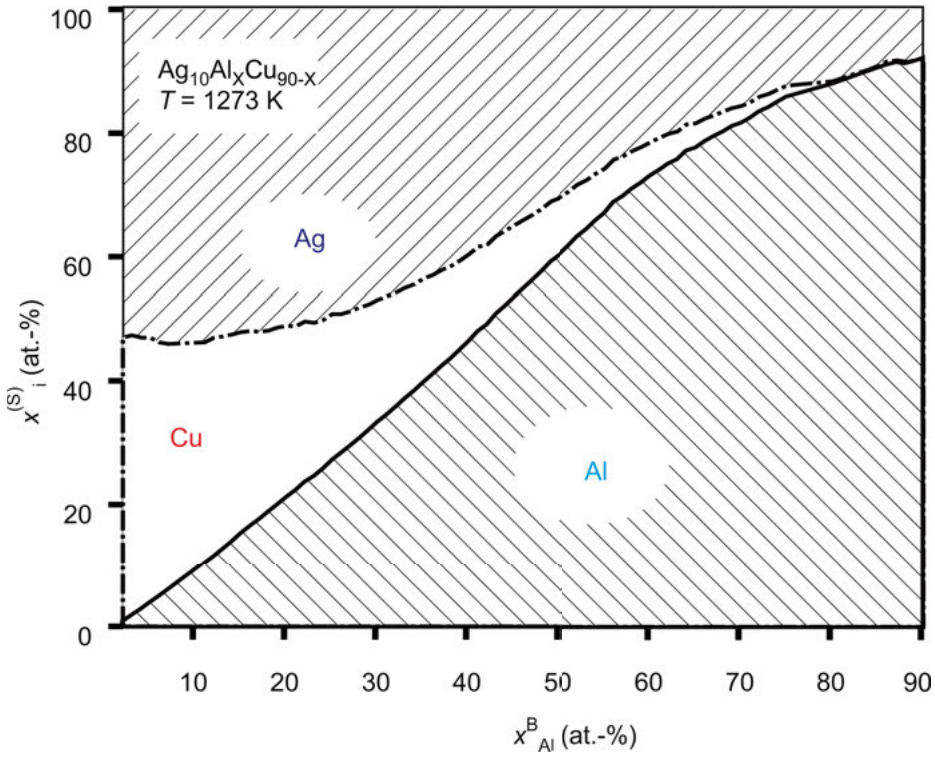

Fig. 4.25. Calculated surface concentrations of Ag, Al, and Cu at 1273 K as function of x^B_{Al} for the section $Ag_{0.1}Al_xCu_{(0.9-x)}$, $0 \le x \le 0.9$. The solid line shows x^S_{Al} and the dash-dotted line corresponds to $x^S_{Al} + x^S_{Cu} = 1 - x^S_{Ag}$, [176].

Surprisingly, an even better agreement with the experimental data is obtained in Fig. 4.24, if, instead of the (sub-)regular solution model, the ideal solution model is used which is also shown in the figure. In fact, the ideal solution model also approximates the surface tension along the two other sections through this system [176].

The comparison [176], with the calculation for the highly non-ideal system Al-Cu reveals both, a qualitative and a quantitative difference, see Fig. 4.24: Instead of concave, a convex curve is obtained and the surface tension values are up to 30 % larger. Obviously, the small addition of 10 at.-% to Al-Cu is sufficient to turn this system from highly non-ideal into ideal [176].

In order to understand this phenomenon, the surface composition needs to be discussed. For this purpose, Fig. 4.25 shows the calculated surface composition along the $Ag_{0.1}Al_xCu_{0.9-x}$-section. Obviously, Al is the main component in the surface. The component with second largest amount is Ag and Cu is the least component. As x^B_{Al} is increased, the concentration of Al in the surface increases on the expense of the two other components. A more detailed analysis [176] reveals a competitive character of

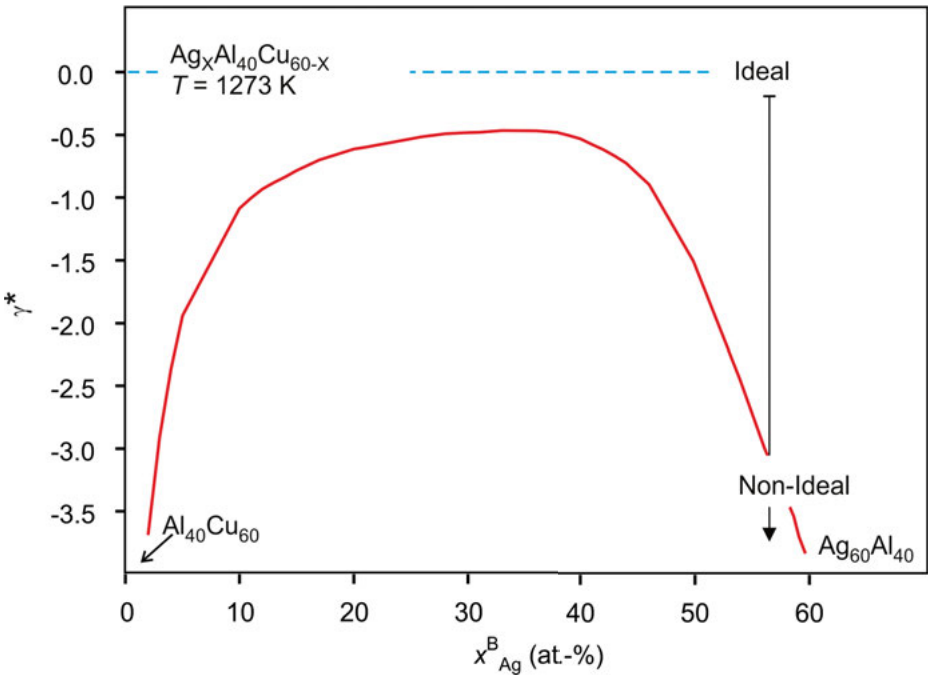

Fig. 4.26. Parameter $^*\gamma$ as function of x^B_{Ag} along a section $Ag_xAl_{0.4}Cu_{(0.6-x)}$ with $0 \le x \le 0.6$. Significant deviations from zero indicate that the system is non-ideal at the corresponding concentrations [176].

the segregation of Al and Ag. As the magnitude of the surface tensions of Ag and Al are similar, $\gamma_{Al} \approx \gamma_{Ag}$, while γ_{Cu} is significantly larger, Cu is suppressed in the surface and Al and Ag form the main chemical species [176].

Once the surface composition is known, it becomes possible to understand the reason why for the vast range of composition γ is in agreement with the ideal solution model. For this purpose, a coefficient $^*\gamma$ is defined as the ratio of the enthalpy- to the ideal entropy term in Eq. (4.32) in the following way [176]:

$$^*\gamma = \frac{\sum_i x_i^B \left({}^E G_i^{(S)}(T, x_i^{(S)}) - {}^E G_i^{(B)}(T, x_i^{(B)}) \right)}{RT \sum_i x_i^B \ln \left(\frac{x_i^{(S)}}{x_i^B} \right)} \tag{4.45}$$

The enthalpy and the entropy term in Eq. (4.45) are taken in their integral forms. The parameter $^*\gamma$ measures the non-ideality of the system. For an ideal system, $^*\gamma = 0$ while it becomes significantly different from zero for a non-ideal system. $^*\gamma$ is plotted in Fig. 4.26 versus x^B_{Ag} for a section where Al is kept constant at 60 at.-% and the concentration of Ag is varied from 0 to 40 at.-%, i.e. for the section $Ag_xAl_{0.4}Cu_{(0.6-x)}$ with $0 \le x \le 0.6$. In the range of 15 at.-% $\le x^B_{Ag} \le$ 45 at.-%, the curve of $^*\gamma(x^B_{Ag})$ is flat and

with ${}^{*}y \approx -0.5$ close to zero. In this range, the surface tension is approximated by the ideal solution model as the excess free energy term cancels out in the Butler equation [176].

4.4.4 Summary on ternary alloys

Summarizing the results on ternary systems, it is possible to draw the following conclusions: The surface tension of ternary Cu-based monotectic alloys of the form "Cu-TM" is determined by the segregation of copper. The corresponding systems can be interpreted as quasi binary [155]. This is different for alloys for which ${}^{\mathrm{E}}G < 0$. These types of system can be described by the ideal solution model in the vast composition range.

For all investigated ternary alloys, the surface tensions are in agreement with the Butler equation. Moreover, the ternary term ${}^{\mathrm{T}}G$ can be neglected in Eq. (3.17) for the prediction of the surface tension. Hence, it is possible to calculate y of a ternary alloy directly from the thermodynamic potentials of its binary subsystems. A thermodynamic assessment on the full ternary system is not necessarily needed [155]. This is in contrast to the results obtained for the density measurements presented in Sec. 3.4. Here, the molar volume may be dominated by a large ternary term ${}^{\mathrm{T}}V$, whereas it is possible to omit ${}^{\mathrm{T}}G$ in applying the Butler equation because, usually, the ternary term in Eq. (3.17) $x_1 x_2 x_3 {}^{\mathrm{T}}G$ is small compared to the binary: $x_1 x_2 x_3 {}^{\mathrm{T}}G << \sum_{i<j} x_{\mathrm{i}} x_{\mathrm{j}} \sum_{\nu=0}^{N_{\mathrm{i,j}}} {}^{\nu}L_{\mathrm{i,j}}(T)(x_{\mathrm{i}} - x_{\mathrm{j}})^{\nu}$.

4.5 Observed trends

With respect to their surface tensions, the systems investigated during this work can be subdivided roughly into two groups: systems tending to demix and systems tending to mix. Systems of the first group have positive excess free energies, ${}^{\mathrm{E}}G > 0$, and systems of the second group exhibit negative excess free energies, ${}^{\mathrm{E}}G < 0$.

Systems belonging to the first group are Cu-Fe-Ni, Cu-Fe, Cu-Ni, Co-Cu-Fe, Co-Cu-Ni, Co-Cu, and Ag-Cu. Their segregation profiles, calculated from the Butler model, Eq. (4.32), are shown in Fig. 4.27. In this figure, the surface concentration of the segregating species, A, $x_{\mathrm{A}}^{\mathrm{S}}$, is plotted versus its bulk concentration, $x_{\mathrm{A}}^{\mathrm{B}}$. In the case of Ag-Cu, the segregating species is Ag. Cu is the segregating species in the other systems. Although each calculation is performed at a different temperature, the curves in Fig. 4.27 exhibit similar features: All of them have a convex shape and, in each curve, $x_{\mathrm{A}}^{\mathrm{S}}$ steeply increases already within the first 20 at.-% of $x_{\mathrm{A}}^{\mathrm{B}}$. For larger bulk mole fractions, $x_{\mathrm{A}}^{\mathrm{B}} > 20$ at.-%, the curves flatten at corresponding values of $x_{\mathrm{A}}^{\mathrm{B}}$ of around 70 – 90 at.-%. Systems with ${}^{\mathrm{E}}G > 0$, hence, exhibit strong segregation.

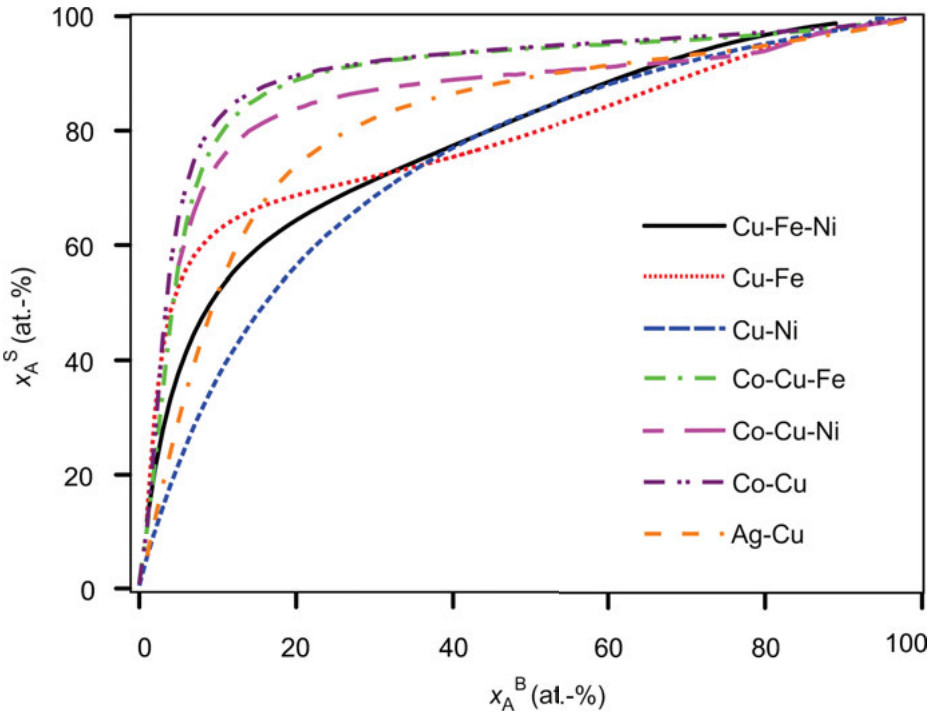

Fig. 4.27. Calculated segregation profiles of liquid binary and ternary alloys with ${}^{E}G > 0$. The plot shows surface concentrations x_A^S of the segregating species A versus their bulk concentrations, x_A^B. The species A corresponds to Ag in Ag-Cu and to Cu for the rest. The temperatures at which these calculations are carried out are different for each system.

The following investigated systems belong to the second group: Al-Cu, Al-Au, Ag-Al-Cu, Al-Fe, Al-Ni, Cu-Ti, and Fe-Ni. In these systems ${}^{E}G < 0$ and, consequently, they tend to mix. In the same way as in Fig. 4.27, their segregation profile is calculated. This is shown in Fig. 4.28. The segregating species is Ni in the case of Fe-Ni, Cu in the case of Cu-Ti, and Al for the rest. Again, the curves are all similar to each other. However, they strongly differ from those shown in Fig. 4.27. Instead of an initial steep increase, x_A^S linearly increases upon increasing x_A^B. The slope dx_A^S/dx_A^B is only slightly larger than 1. A flattening of the segregation curves occurs when x_A^B is already large, e.g. $x_A^B > 60$ at.-%. Hence, systems with ${}^{E}G < 0$ exhibit weak segregation.

In order to compare these findings with the classification scheme introduced in Sec. 3.5, the investigated systems are listed in Tab. 4.15. The table also shows the corresponding signs of ${}^{E}G$, ${}^{E}y$, and denotes whether the systems exhibit weak or strong segregation.

Obviously, systems belonging to class I, see Sec. 3.5, exhibit strong segregation. Their excess free energy is positive and the excess surface tension is negative. Members of this class are Cu-Fe [68], Cu-Ni [68], Co-Cu-Fe [240], Cu-Fe-Ni [161], and

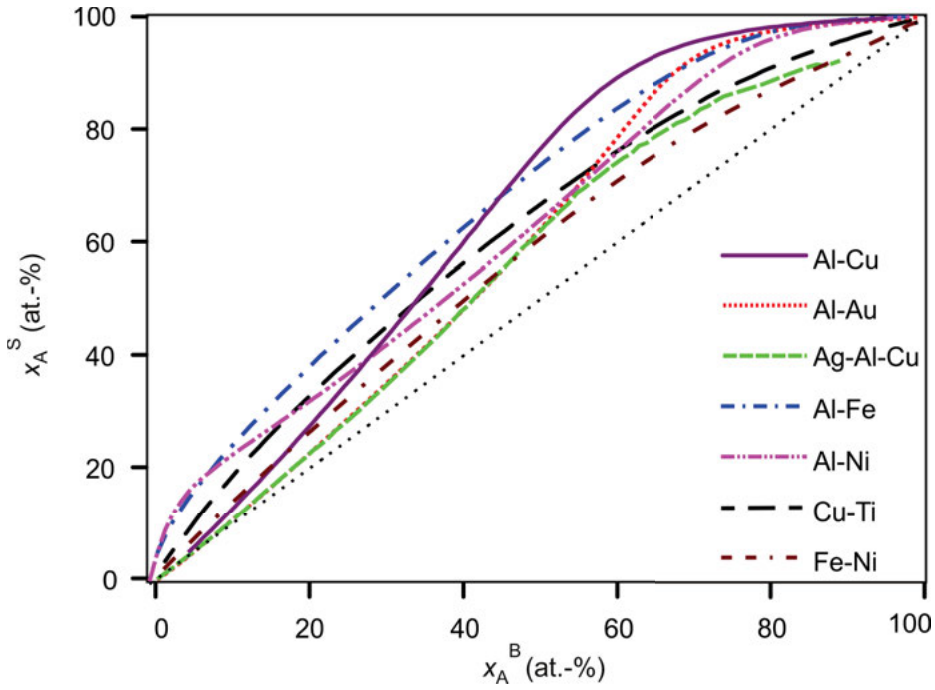

Fig. 4.28. Calculated segregation profiles of liquid binary and ternary alloys with ${}^{E}G < 0$. The plot shows surface concentrations x_A^S of the segregating species A versus their bulk concentrations, x_A^B. The species A corresponds to Cu in Cu-Ti, Ni in Fe-Ni, and to Al for the rest. The temperatures at which these calculations are carried out are different for each system.

Co-Cu-Ni [159]. Except for Cu-Ni, these systems also tend to demix in the liquid and exhibit metastable miscibility gaps in the undercooled temperature domain.

All systems belonging in Sec. 3.5 to class III exhibit a weak segregation behavior. These systems are Al-Au, Al-Cu, Al-Fe, Al-Ni, Cu-Ti and Cu-Si. Their excess free energies are strongly negative, ${}^{E}G << 0$, and ${}^{E}y$ is slightly positive. Compound formation affects the surface tension in Al-Fe [232], Al-Ni [232] and Cu-Si [151].

The segregation behavior is not uniform in class II of Sec. 3.5. As shown in Tab. 4.15, Ag-Cu exhibits strong segregation of Ag. Its excess free energy is slightly positive and ${}^{E}y < 0$. The other systems investigated of this class are Ag-Al-Cu and Fe-Ni. In both systems, ${}^{E}G < 0$ and only weak segregation takes place. Fe-Ni exhibits only a small positive excess surface tension and ${}^{E}y \approx 0$ in Ag-Al-Cu. Both systems are in fairly good agreement with the ideal solution model.

Table 4.15. Observed trends in the surface tensions of the investigated alloys.

Class	System	Sign of ${}^{E}G$	Sign of ${}^{E}\gamma$	Segregation	Source
I	Cu-Fe	+	-	strong	[68]
	Cu-Ni				[68]
	Co-Cu-Fe				[240]
	Co-Cu-Ni				[159]
	Cu-Fe-Ni				[161]
II	Ag-Cu				[67]
	Fe-Ni		≈0		[68]
III	Al-Au	-	+	weak	[199]
	Al-Cu				[191]
	Al-Fe				[232]
	Al-Ni				[232]
	Cu-Ti				[206]
	Cu-Si				[151]
	Ag-Al-Cu		≈0		[176]

4.6 Summary and conclusions

In this chapter, surface tensions of unary, binary and ternary liquid alloy systems are systematically studied.

In the case of unary systems, the obtained surface tensions are in agreement with reference data from literature within ± 5%. The results obtained confirm the validity of a semi-empirical model of Kaptay,Eqs. (4.40)–(4.42), relating the surface tension of a pure element to its liquidus temperature and specific heat. In addition, it is found that for most metals, the surface tension at the melting point y_{L} is proportional to the free energy of the pure component, $G_{\mathrm{i}}^{0}(T_{\mathrm{L}})$.

With regard to questions **Q:1** and **Q:2** (Chap. 1), surface tensions of binary systems are measured and compared to a number of phenomenological models. These are the Butler model, the Chatain model and, in case of compound forming systems, the Egry model. The Butler model predicts the surface tension most reliably. It produces correct results for all sub-regular-solution systems. Surface tensions of so called compound forming systems are best described by the Egry model. The Chatain model is less reliable compared with the two others as it mainly produces reasonable results or even fails.

The Butler and the Chatain models are able to predict the segregation behavior. The Chatain model is hereby more detailed than the Butler model. The latter only predicts the composition of the top monolayer while the Chatain model provides information about the compositions of several monolayers below the surface. Reliable data from experiments on the composition of the surface near region in liquid alloys is yet not available.

The surface tensions of the investigated ternary systems are also well predicted by the Butler model. With respect to question **Q:3** it is shown that equally good results are obtained when the ternary interaction parameters are neglected in the corresponding expressions for ${}^{\mathrm{E}}G$. This result means that, in the case a ternary system, surface tensions can be predicted from the thermodynamic properties of the binary subsystems.

One can identify the following scheme: Systems for which ${}^{\mathrm{E}}G \approx 0$ or ${}^{\mathrm{E}}G > 0$ exhibit segregation, or strong segregation, respectively, of that component with the smallest surface tension. Systems for which ${}^{\mathrm{E}}G \approx< 0$ exhibit no, or only weak, segregation. Alloys belonging to class I exhibit strong segregation and alloys that belong to class III exhibit weak segregation. Systems of class II either exhibit strong or weak segregation, depending on the sign of ${}^{\mathrm{E}}G$.

5 Viscosity

Viscosity is defined as the transport coefficient of momentum diffusion. There are several mathematical forms and phenomenological models describing its dependence on temperature and alloy composition. Viscosity data is measured on pure liquid elements, binary and ternary alloys. The measurements are carried out using oscillating cup viscometry. Data is obtained as functions of temperature and, in case of alloys, of their compositions. The results are accurate within ± 20 %. The results obtained for the pure elements are found in agreement with the Hirai law. Among the phenomenological models, the Kozlov model exhibits the best overall agreement with the measured isothermal viscosities of binary and ternary alloys. This model also works best for systems containing similar elements. In case of systems tending to demix, the Kaptay model works best and in the case of Al- based alloys with a strong attractive interaction, the Brillo/Schick model is the best choice. The majority of the investigated systems exhibit an ideal mixing behavior with respect to viscosity.

5.1 Formalism and models

5.1.1 Definitions

Shear viscosity measures the resistance of a liquid against shear flow. It is commonly associated with the "thickness" of the fluid.

If a small volume of a liquid is confined between two parallel plates with areas A, and if a force F_x is applied to one of these plates in a parallel direction x, the plate moves into that direction with a velocity v_x. Due to the inner friction of the liquid, a velocity gradient $\nabla_y v_x$ is produced along the perpendicular direction y, see Fig. 5.1. The ratio of F_x and A yields a stress, σ_x, which is proportional to $\nabla_y v_{x,y}$. The coefficient, η, between both is defined as the shear viscosity [166]:

$$\sigma_{x,y} = \eta \cdot \nabla_y v_x \tag{5.1}$$

Equation (5.1) can be multiplied by the density ρ and the product, $\rho \nabla_y v_x$, defines a gradient of momentum. Combining Eq. (5.1) with the continuity equation, $\rho \dot{v}_x = \nabla_y \sigma_x$, yields a diffusion equation for the transport of momentum [166]:

$$\rho \frac{\partial v_x}{\partial t} = (\rho^{-1}\eta)\nabla_y^2 (v_x \rho) \tag{5.2}$$

The corresponding transport coefficient is, thus, $\rho^{-1}\eta$.

In equilibrium, thermal fluctuations of the velocities vary locally and lead to fluctuations in $\nabla_y v_x$. According to Eq. (5.1), these will also cause fluctuations in $\sigma_{x,y}$. The Green-Kubo formalism [166; 244] relates the viscosity to the auto-correlation function

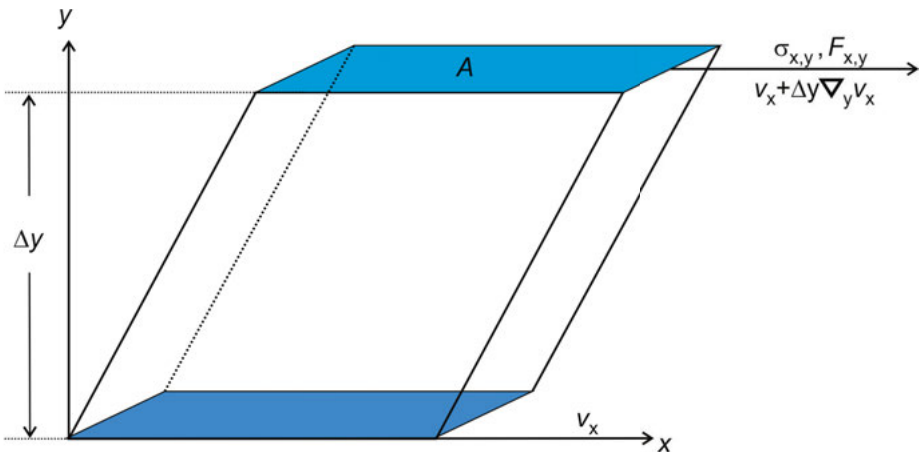

Fig. 5.1. Sheared liquid volume element confined between two parallel plates with areas A (colored). Applying a stress, $\sigma_{x,y}$, to one of the plates in x-direction causes a gradient of v_x, $\nabla_y v_x$, in the vertical direction y.

of $\sigma_{x,y}$ denoted as $\langle \sigma_{x,y}(0)\sigma_{x,y}(\tau)\rangle$:

$$\eta = \frac{1}{Vk_B T}\int_0^\infty \langle \sigma_{x,y}(0)\sigma_{x,y}(\tau)\rangle \, d\tau \tag{5.3}$$

Moreover, $\sigma_{x,y}$ can be expressed by the velocities and positions of the individual atoms [166], if their interaction potential is known. This is useful for the calculation of η in molecular dynamics (MD) simulations [245].

Another expression for the viscosity, involving the radial pair distribution function, $g(r)$, and the pair potential, $\varphi(r)$, was derived earlier by Born and Green [246]:

$$\eta = \frac{2\pi}{15}\sqrt{\frac{\rho}{k_B T}}\int_0^\infty dr r^4 \frac{\partial \varphi(r)}{\partial r} g(r) \tag{5.4}$$

This equation can be used as a good approximation for the viscosity, provided $g(r)$ and $\varphi(r)$ are sufficiently well known.

Equations (5.3) and (5.4) imply that the viscosity is mainly determined by the short range order and the atomic interaction. In contrast to molar volume and surface tension, there is no thermodynamic definition of the viscosity in the sense that η can be expressed through differentiating one of the thermodynamic potentials. This makes a thermodynamic treatment of the viscosity particularly difficult.

5.1.2 Temperature dependences

According to Eq. (5.2), the viscosity can be interpreted as the coefficient of diffusion of momentum vertical to the shear planes. In a concept, developed by Eyring [34], it is assumed that this transport is accomplished by an exchange of atoms taking place with a certain rate k.

In equilibrium and in the absence of externally applied shear, $k(T)$ equals $k_0 \exp(-W/k_B T)$, whereas W is the energy barrier and k_0 is the pre-exponential factor corresponding to an attempt frequency. The difference between jumps in forward- and backward direction, Δk, equals zero under these conditions.

Upon applying an external stress, the energy barrier W is altered by an additional amount ΔW. Δk can then be approximated in first degree of order by

$$\Delta k \approx k(T) \frac{\Delta W}{k_B T} \tag{5.5}$$

Setting $\nabla_y v_x$ equal to Δk and expressing $\sigma_{x,y}$ through $\partial \Delta W / \partial y$ leads to an expression for the viscosity using the particle density, $\hat{\rho}$:

$$\eta = \hat{\rho} \frac{k_B T}{k_0} \exp\left(\frac{\Delta W}{k_B T}\right) \tag{5.6}$$

Obviously, this relation has the general form,

$$\eta \propto T \exp\left(\frac{E_A}{RT}\right) \tag{5.7}$$

whereas, E_A is an activation energy and $R = 8.314$ J/K is the molar gas constant.

As an alternative to Eq. (5.7) another relation for $\eta(T)$ has been proposed, which reads [70]:

$$\eta \propto \frac{1}{T} \exp\left(\frac{E_A}{RT}\right) \tag{5.8}$$

Although Eq. (5.7) and Eq. (5.8) seem to contradict each other, both relations have their particular field of application [70].

In fact, there is a whole zoo of η-T relations for the viscosity. Even worse, they are not consistent with each other. In Ref. [70], Chapman reviewed 17 different forms of $\eta(T)$. In some of them η is related to T just via a power law: $\eta \propto T^n$ with $n \in \Re$ being an index.

Most commonly, the viscosity is expressed by an Arrhenius law, having a pre-exponential factor, η_∞. As function of temperature η then reads:

$$\eta(T) = \eta_\infty \exp\left(\frac{E_A}{RT}\right) \tag{5.9}$$

The pre-exponential factor, hereby, corresponds to an asymptotic viscosity for $T \to \infty$.

The Arrhenius law offers the particular advantage that, when the natural logarithm of η is plotted versus the inverse temperature, a straight line is obtained with a

slope corresponding to E_A/R. In addition, the intersection with the vertical axis corresponds to $\ln(\eta_\infty)$. The Arrhenius law is also used in the present work in order to represent the measured viscosity data by E_A and η_∞.

Another important relation is the Vogel-Fulcher-Tammann (VFT) law [166]:

$$\eta(T) = \eta_\infty \exp\left(\frac{B}{T - T_0}\right) \tag{5.10}$$

In this equation, B corresponds to activation energy and T_0 is a temperature which can be related to the glass transition temperature T_g. Equation (5.10) is important in order to describe the viscosity of glass forming alloys over broad temperature ranges where $\eta(T)$ usually significantly deviates from the Arrhenian behavior.

According to Mode-Coupling theory [247] dynamical freezing sets in closely above a certain critical temperature, T_{Fr}[1]. All dynamic processes then scale with temperature according to the same law. Hence, the inverse viscosity would obey the following relation whereas y_{MCT} is a critical exponent:

$$\eta^{-1} \propto D \propto \left(1 - \frac{T}{T_{Fr}}\right)^{y_{MCT}} \tag{5.11}$$

As a consequence of Eq. (5.11), the product of viscosity and the diffusion coefficient D would become constant at temperatures close to T_{Fr}.

5.1.3 Composition dependences

Despite the problem that there is no thermodynamic definition of the viscosity and that there is no uniform description of its temperate dependence, there is plenty of models relating η and E_A to either the enthalpy of mixing ΔH or the excess free energy ${}^E G$ [248]. An overview on some of these models is given, for instance, in Ref. [249].

The following selection is considered in the present work: the model of Moelwyn/Hughes [250], of Kozlov/Romanov/Petrov [251], the Hirai model [252], the Seetharaman/Du Sichen model [253] and the Kaptay model [254]. For the sake of brevity, the Kozlov/Romanov/Petrov model is just referred to as "Kozlov model". For the same reason, the Seetharaman/Du Sichen model will be called "Seetharaman model".

Recently, a new model has been proposed by Brillo and Schick [87] for liquid Al-Cu binary alloys. This model will be discussed as well. In the following, it will be referred to as "Brillo/Schick model".

In each of these models, the viscosity is predicted as function of the alloy composition. In the Moelwyn/Hughes model [250], the viscosity η is given as a function of

1 In MCT, T_{Fr} is denoted as "T_C". In order not to confuse this with the temperature of the critical point, a different notation is used in the present work.

temperature and composition by the following expression:

$$\eta = (x_A \eta_A + x_B \eta_B)\left(1 - 2\frac{\Delta H}{RT}\right) \tag{5.12}$$

Here, η_i is the viscosity of a pure element i (i = A,B), x_i is the corresponding mole fraction, T is the absolute temperature and R the universal gas constant.

Equation (5.12) is defined purely for binary systems. Details on its application to the ternary system Cu-Fe-Ni are described in Ref. [248]. In the same way, Eq. (5.12) is also applied to Co-Cu-Ni.

Equation (5.12) predicts that the deviation of η from the linear law, $x_A \eta_A + x_B \eta_B$, is related to the enthalpy of mixing. Depending on the system, this deviation can result in positive or negative values.

Among the models discussed, the Kozlov model [251] is the only one that is derived strictly from physical principles. The authors of Ref. [251] relate the viscosity to ΔH by expressing the free energy in terms of atomic vibration frequencies. For an alloy with N components, $i = 1..N$, they obtain:

$$\ln(\eta) = \sum_{i=1}^{N} x_i \ln(\eta_i) - \frac{\Delta H}{3RT} \tag{5.13}$$

The Hirai model [252] relates the activation energy E_A in a semi-empirical way to the liquidus temperature T_L. This leads to the following expression:

$$\eta = 1.7 \cdot 10^{-7} \frac{\rho^{2/3} {T_L}^{1/2}}{M^{1/6}} \exp\left[\frac{2.65 {T_L}^{1.27}}{R} \cdot \left(\frac{1}{T} - \frac{1}{T_L}\right)\right] \tag{5.14}$$

In Eq. (5.14) ρ is the density and M the molar mass of the alloy. The Hirai model has been developed in order to predict the viscosity of pure liquid elements. Here, it is applied to liquid alloys. The input parameters of this model are easily accessible, if the excess volume can be neglected. This circumstance might be seen as an advantage [248].

The Seetharaman model [253] links E_A to ${}^{E}G$. This model is valid for binary systems only. In Ref. [253], however, the authors also give a semi-empirical expression for ternary systems:

$$\eta = \frac{hN_A}{V} \exp\left(\frac{\sum_i^3 x_i G_i^* + 3RT \sum_{i<j}^3 x_i x_j + RT \sum_i^3 x_i \ln(x_i) + {}^{E}G}{RT}\right) \tag{5.15}$$

In Eq. (5.15), $h = 6.626 \cdot 10^{34}$ Js denotes the Planck constant, $N_A = 6.022 \cdot 10^{23}$ mol^{-1} the Avogadro number and V the molar volume. G_i^* is the Gibbs energy of activation for the viscous flow of pure component i. It is defined using the molar volume V_i of the pure component i:

$$G_i^* = RT \ln\left(\frac{\eta_i V_i}{hN_A}\right) \tag{5.16}$$

The Seetharaman model has been improved by Kaptay [249], who relates the activation energy E_A to the enthalpy of mixing ΔH. This is done by introducing a semi-empirical parameter, $\phi = 0.155$. As described in Ref. [249] ϕ has is estimated from the properties of pure metals:

$$\eta = \frac{hN_A}{V} \exp\left(\frac{\sum_i x_i G_i^* + \phi \cdot \Delta H}{RT}\right) \tag{5.17}$$

The Kaptay model has been further developed by describing the shear planes as liquid interfaces with individual compositions obtained from solving the Butler equation for an ideal solution. This model is called Budai/Kaptay model [249]. Although there are hints that this model is successful, it will not be discussed in detail in the present work.

The main assumption of the Brillo/Schick model [87] is that E_A is generally larger if the interactions between the atoms are more attractive. Moreover, it is assumed that $\eta(T)$ follows an Arrhenius type behavior. Hence, the activation energy of viscous flow in an alloy E_A can be written as:

$$E_A = \sum_i x_i E_{A,i} - \Delta H + RT \sum_i x_i \ln(x_i) \tag{5.18}$$

In Eq. (5.18) $E_{A,i}$ is the activation energy of the liquid pure component. The last term in this equation accounts for the entropy of mixing which is assumed as ideal. Therefore, the activation energy becomes temperature-dependent in the Brillo/Schick model [87] yielding an apparent contribution to the pre-exponential factor η_∞ which is expressed as:

$$\ln(\eta) = \sum_{i=1}^{N} x_i \ln(\eta_i) \tag{5.19}$$

For the evaluation of some of these expressions the enthalpy of mixing, ΔH, and the excess free energy, ${}^E G$, are needed. The enthalpy of mixing ΔH is related to ${}^E G$ via $\Delta H = {}^E G + T {}^E S$ with ${}^E S$ being the excess entropy. When ${}^E G$ is known, ΔH can be obtained from $\Delta H = {}^E G - T \partial EG/\partial T$. As can be seen from Tabs. B.4 - B.14, ${}^E G$ depends in most systems linearly on temperature. In these systems, ΔH can easily be obtained from ${}^E G$ by just skipping the temperature dependent terms.

5.2 Unary systems

In this section, the viscosities of pure elements are discussed. Figure 5.2 shows the relevant part of the periodic table with those elements marked of which viscosities are determined within the present work. These are Al, Si, and Cu, as well as the transition metals Ni, Co, and Fe.

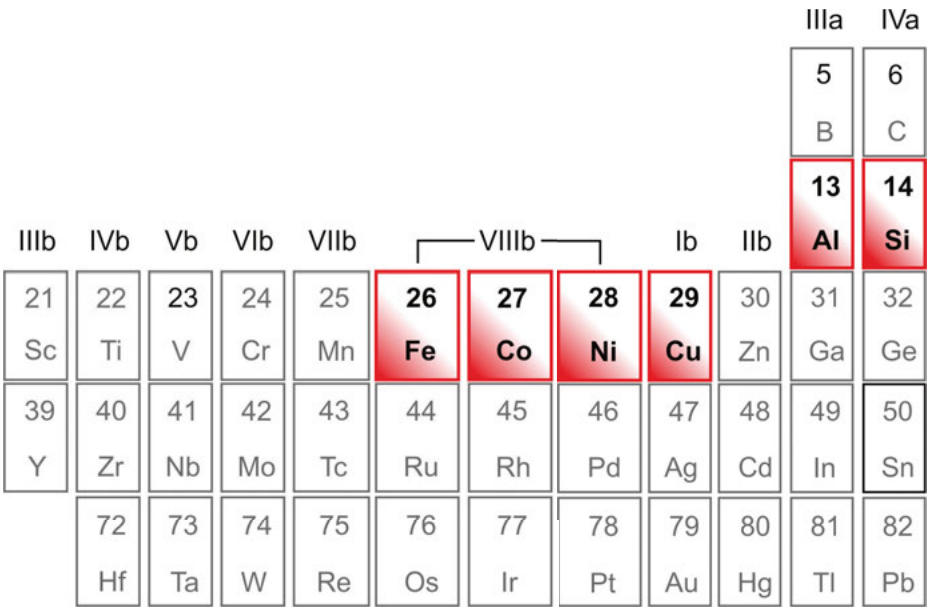

Fig. 5.2. Relevant section of the periodic table. Viscosities of the highlighted elements are measured and discussed below.

The results of the viscosity measurements are presented in Figs. 5.3–5.7 and summarized in Tabs. 5.2–5.7. Therein, they are compared with recommended and/or measured results from literature. These are attached with a *key* specifying the method used for their determination. The keys are defined in Tab. 5.1. *R*, hereby, means "recommended" and specifies that the listed value is obtained from a literature review. The results of the present work contributed to some of them as well. The listed data is not strictly independent from each other. Moreover, the key *HOC* meaning "high temperature oscillating cup" specifies the viscometer at DLR and the key *OCN* specifies the oscillating cup viscometer located at NPL[2] in Teddington, UK where some of the measurements are performed.

2 NPL = National Physical Laboratory

Table 5.1. Keys of methods for viscosity determination used in the tables below. The keys HOC and OCN specify that the corresponding data is obtained using the oscillating cup viscometer at DLR or NPL, respectively.

Key	Name
R	Recommended from literature review
OC	Oscillating cup
HOC	High temperature oscillating cup (DLR)
OCN	Oscillating cup (NPL)

5.2.1 Al and Si

Measured viscosity data $\eta(T)$ of Al [158] and Si [158] is plotted versus temperature in Fig. 5.3. Obviously, the viscosities decay according to an exponential law and the Arrhenius law of Eq. (5.9) can be used for their representation. This is shown by the solid lines. The obtained parameters, η_∞ and E_A, are listed in Tab. 5.2 for Al and in Tab. 5.3 for Si. Obviously, they are quite similar. They are compared in these tables with corresponding results from literature.

For Al, these are the recommended values by Assael, [63], by Mills [12] and by Shiraishi [11]. The latter results are identical with those reported by Iida and Guthrie [13]. The results reported by Kehr [86] are shown as well. They are obtained by means of the same viscometer as used in the present work. The Arrhenius law, Eq. (5.9), is also plotted in Fig. 5.3 for the literature data.

Obviously, the agreement among the different curves is within ± 20 %. The largest deviation is, hereby, observed for the results of Mills [12]. The overall deviation between the different datasets is worse than in the cases of density and surface tension. This is mainly due to the container based nature of the oscillating cup technique. Chemical reactions between the melt and the crucible might effectively change the sheared volume. Oxidation of the free liquid surface can cause a meniscus which also changes the effective sheared volume of the liquid. Last but not least, the diameter of the crucible must precisely be known. Small deviations from its real value can lead to stronger systematic errors in the measured data.

In the case of liquid Si, the number of available literature data is more limited. Table 5.3 lists the recommended values of Assael [92] which are also plotted in Fig. 5.3. Although the parameters, η_∞ and E_A, recommended in Ref. [92], strongly differ from those of the present work, see Tab. 5.3, the two curves still agree with each other in the experimentally covered temperature interval from 1600 K to 1900 K, see Fig. 5.3.

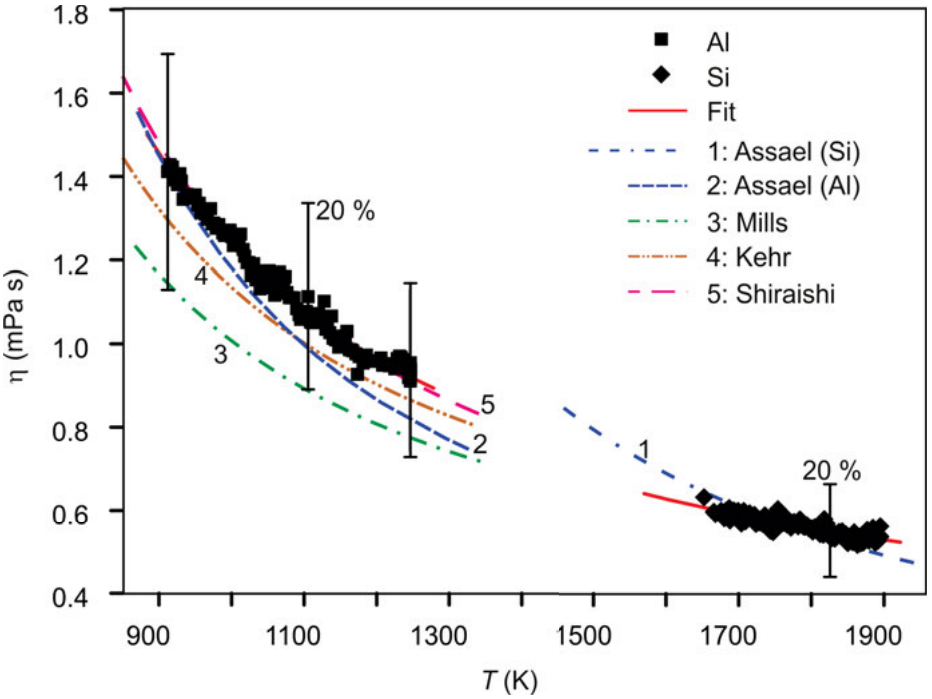

Fig. 5.3. Viscosity η of Al (squares) and Si (diamonds) versus temperature. The data is shown together with results from literature: 1: data of Si recommended by Assael [92]. Data of Al, recommended by Assael [63] (2), by Mills [12] (3), by Shiraishi, Iida and Guthrie [11; 13] (5), and measured by Kehr [86] (4), using the same viscometer (HOC).

Table 5.3. Parameters η_∞ and E_A for the viscosity of pure liquid Si measured in this work (bold) [158]. The data are compared with selected results from literature. The methods used for their determinations are specified in the third column.

η_∞ (mPa · s)	E_A (10^4J/mol)	Method	Source
0.214 ± 0.02	**1.43± 0.1**	**HOC**	**[158]**
0.082	2.831	R	[92]

5.2.2 Cu

For liquid Cu, two sets of data are established: one is obtained using the viscometer at National Physical Laboratory (NPL), Teddington, UK [248] and the other one is obtained using the viscometer at DLR, [158]. The results are shown in Fig. 5.4. Again, η can be fitted by Eq. (5.9) and the resulting parameters are listed in Tab. 5.4 together with corresponding results from literature. These are the recommended data

Table 5.2. Parameters η_∞ and E_A for the viscosity of pure liquid Al measured in this work (bold) [158]. The data is compared with selected results from literature. The methods used for their determinations are specified in the third column.

η_∞ (mPa · s)	E_A (10^4J/mol)	Method	Source
0.281 ± 0.02	**1.23 ± 0.08**	**HOC**	**[158]**
0.268	1.10	R	[12]
0.185	1.54	R	[63]
0.288	1.14	HOC	[86]
0.257	1.31	R	[11; 13]

Table 5.4. Parameters η_∞ and E_A for the viscosity of pure liquid Cu measured in this work (bold [158; 248]). The data is compared with selected results from literature. The methods used for their determinations are specified in the third column.

η_∞ (mPa · s)	E_A (10^4J/mol)	Method	Source
0.522 ± 0.05	**2.36± 0.1**	**OCN**	**[248]**
0.657 ± 0.04	**2.15± 0.1**	**HOC**	**[158]**
0.378	2.67	R	[93]
0.466	2.41	HOC	[86]
0.529	2.39	R	[11]
0.527	2.39	R	[12]

of Assael, [93], of Mills, [12] and of Shiraishi [11]. The two latter are identical with each other. Mills [12], however, uses a representation of data which is different from Eq. (5.9). The small deviation in η_∞ between the two datasets in Tab. 5.4 originates from a rounding error that occurs when the representation is being converted. Finally, the data measured by Kehr [86] is also shown. These measurements have been carried out in the same machine, i.e. (HOC).

As visible in Fig. 5.4, all reported data lie within a band of ± 10 %. The upper limit is given by the results of Mills [12], Shiraishi [11], and the data of the present work [158] measured at DLR (HOC). These agree with each other within less than ±5 %. The lower limit of the band is determined by the data of Kehr [86] and Assael [93]. However, these two latter curves are not independent from each other. In fact, the data of Kehr were considered in Ref. [93] and significantly contributed to the final result as, in Ref. [93], the individual data sets were weighed by the number of data points. The DLR viscometer produces continuous curves, $\eta(T)$, so that the number of experimental points is far larger as in the other sets of data considered in Ref. [93].

The data measured at NPL [248] lie right in the middle of the band. Apart from a small kink at $T \approx 1520$ K, which corresponds to demixing of CuO_2 [154], these data nicely obey an Arrhenius law.

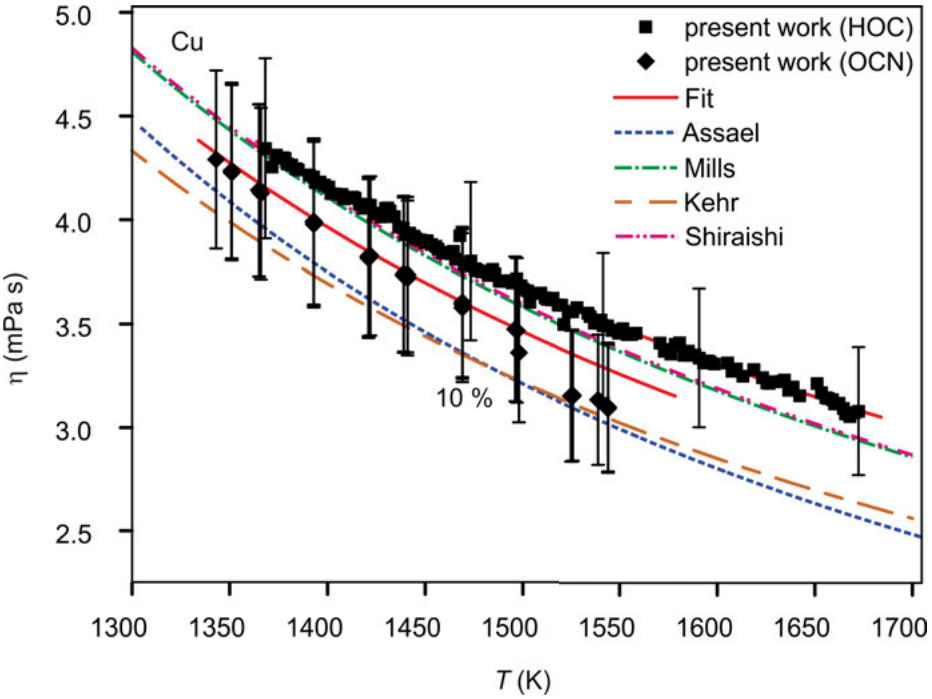

Fig. 5.4. Viscosity η of Cu versus temperature, measured at NPL using the viscometer (OCN) (diamonds, [248]) and at DLR using the viscometer (HOC) (squares, [158]). The data is shown together with results from Assael [93], Mills [12], Shiraishi [11], and Kehr [86].

5.2.3 Ni, Co and Fe

Measured viscosities of the transition metals Ni, Co and Fe are plotted versus temperature T in Figs. 5.5–5.7. The corresponding parameters obtained from the Arrhenius law, Eq. (5.9), η_∞ and E_A, are listed in Tabs. 5.5 – 5.7.

For liquid Ni, the following literature sources were discussed in Tab. 5.5: the reviews by Assael [94] and Mills [12], as well as the data measured by Kehr [86] using the DLR viscometer. The results of Mills [12] are identical with the results of Andon [255] obtained in the viscometer at NPL (OCN). The corresponding representations, Eq. (5.9), are shown in Fig. 5.5 as well.

All curves agree with each other within a band of ± 20 %. The viscosities recommended by Assael [94] form the upper limit of this band and the data of Kehr [86] the lower limit.

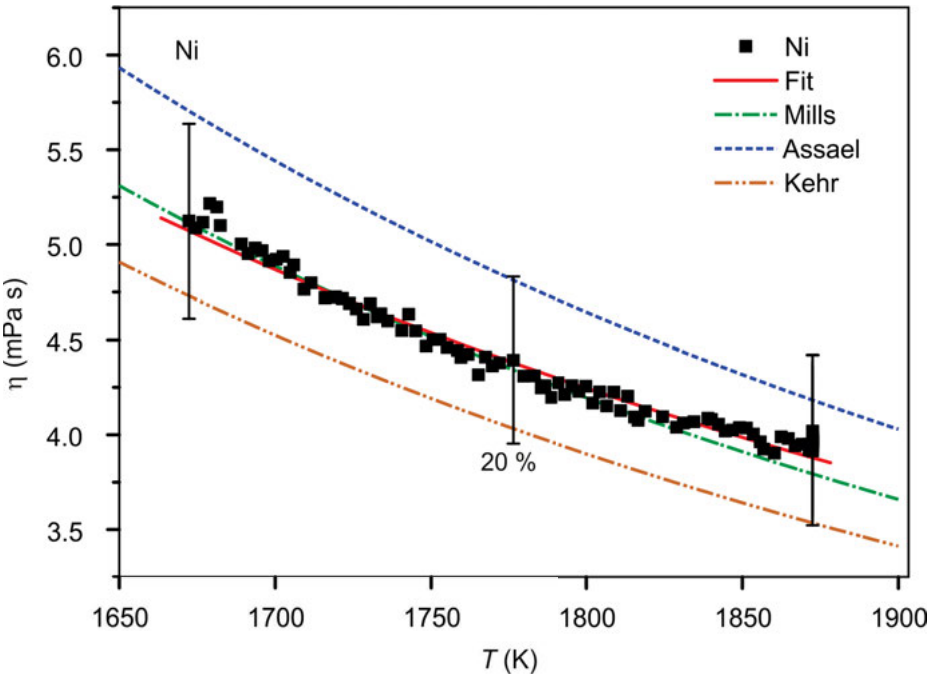

Fig. 5.5. Viscosity η of Ni [160] versus temperature using the viscometer (HOC) (squares) at DLR. The data is shown together with results from Assael [94] and Mills [12].

Table 5.5. Parameters η_∞ and E_A for the viscosity of pure liquid Ni measured in this work (bold) [160]. The data is compared with selected results from literature. The methods used for their determinations are specified in the third column.

η_∞ (mPa · s)	E_A (10^4J/mol)	Method	Source
0.413 ± 0.02	**3.487± 0.1**	**HOC**	**[160]**
0.313	3.884	R,OCN	[12; 255]
0.313	4.036	R	[94]
0.31	3.789	HOC	[86]

The data obtained in the present work [160], shown in Fig. 5.5 as symbols, lies almost in the middle of the band. Within roughly ± 5 %, it is in agreement with the results of Mills, [12]. With regard to the data of Kehr, it is demonstrated that results obtained even in the same machine, can deviate from each other by as much as ±20 %.

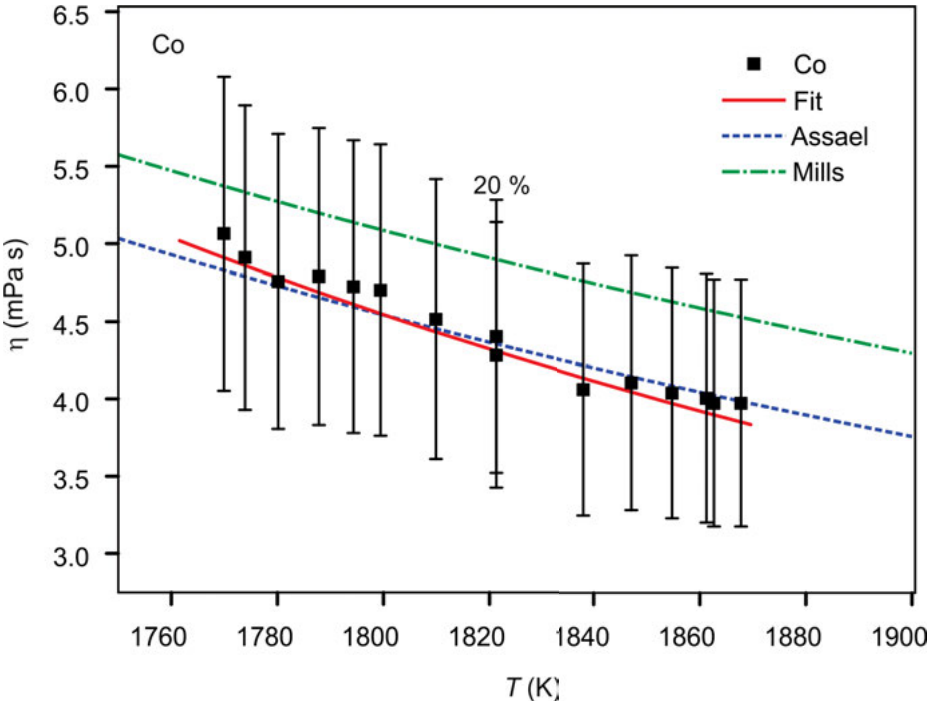

Fig. 5.6. Viscosity η of Co [256] versus temperature using the viscometer "HOC" (squares) at DLR. The data is shown together with results from Assael [92] and Mills [12].

Table 5.6. Parameters η_∞ and E_A for the viscosity of pure liquid Co measured in this work (bold) [256]. The data is compared with selected results from literature. The methods used for their determinations are specified in the third column.

η_∞ (mPa · s)	E_A (10^4J/mol)	Method	Source
0.048	**6.81**	**HOC**	**[256]**
0.125	5.377	R	[92]
0.204	4.813	R	[12]

For liquid Co, the recommended data of Assael [92] and Mills [12] are consulted as reference. The comparison with the results measured in this work is shown in Fig. 5.6 and the corresponding parameters η_∞ and E_A are listed in Tab. 5.6. As visible from Fig. 5.6, the best agreement is obtained with the results of Mills [12], whereas the overall deviation between both sets is within ± 5 % only. The results of Assael [94] are slightly larger. Again, all curves agree with each other within ± 20 %.

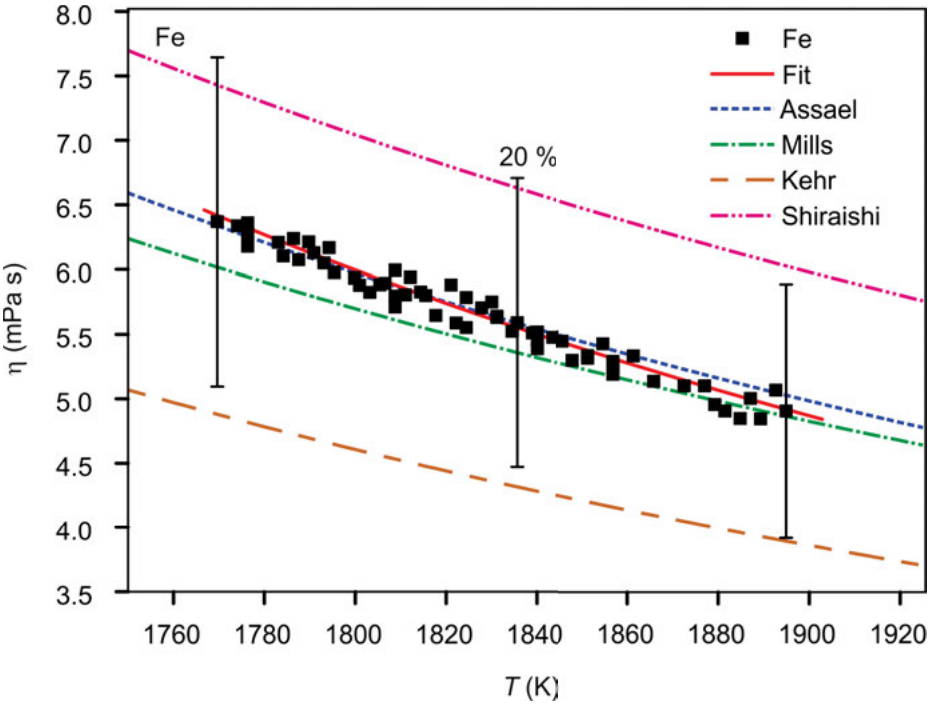

Fig. 5.7. Viscosity η of Fe [160] versus temperature using the viscometer "HOC" (squares) at DLR. The data is shown together with results from Assael [63], Mills [12], Shiraishi [11] and Kehr [86].

Table 5.7. Parameters η_∞ and E_A for the viscosity of pure liquid Fe measured in this work (bold) [160]. The data is compared with selected results from literature. The methods used for their determinations are specified in the third column.

η_∞ (mPa · s)	E_A (10^4J/mol)	Method	Source
0.114 ± 0.02	**5.93± 0.1**	**HOC**	**[160]**
0.24	4.74	R	[12; 13]
0.19	5.16	R	[63]
0.162	5.01	HOC	[86]
0.315	4.65	R	[11]

Finally, the results for liquid Fe are discussed in Fig. 5.7 together with available data from literature, i.e. the viscosities recommended by Assael, [63], Mills [12], and Shiraishi [11]. The data of Mills [12] is identical with those of Iida and Guthrie, [13]. In addition, data measured by Kehr [86] is also shown.

Again, all datasets agree with each other within a band of ± 20 %, whereas the upper limit is set by the recommendation of Shiraishi [11] and the lower limit by the data of Kehr [86]. The data of the present work [160] lies in the middle between these

extremes and agrees within approx. 5 % with the results obtained by Assael [63] and Mills [12].

Among the three transition metals Ni, Co, and Fe, the largest viscosities is exhibited by Fe, followed by Co and Ni for $T < 1850$ K. Above this temperature, $\eta_{Co} > \eta_{Ni}$.

5.2.4 Synopsis

For each element, the parameters η_∞ and E_A are collected in Tab. 5.8 together with their corresponding liquidus temperatures, T_L. In addition, the table lists values of η at the corresponding liquidus temperatures T_L, i.e. $\eta_L := \eta(T_L)$. As a rough tendency, elements with a high melting temperature also exhibit a large viscosity. The only exception from this trend is liquid Si having a comparatively small viscosity, η_L=0.59 mPa · s, paired with a liquidus temperature of T_L= 1687 K which, compared to Al or Cu, is relatively large.

The Hirai equation, Eq. (5.14), provides a comparatively simple relation between η_L and material parameters, such as T_L, ρ_L, and the molar mass, M:

$$\eta_L = 1.7 \cdot 10^{-7} \frac{\rho_L^{\frac{2}{3}} T_L^{\frac{1}{2}}}{M^{\frac{1}{6}}} \tag{5.20}$$

Equation (5.20) is verified in Fig. 5.8 where a plot of η_L versus the right hand side of Eq. (5.20) is shown. Obviously, Eq. (5.20) is fulfilled for liquid metals, as η_L scatters within error bars of ± 20 % around the relation of Eq. (5.20). The latter is indicated in Fig. 5.8 by the solid line. Again, liquid Si forms the only exception from this trend, as η_L is overestimated by more than 100 %. From the Hirai law, Eq. (5.14), one can also derive an expression for the activation energy of viscous flow, $E_{A,Hirai}$:

$$E_{A,Hirai} = 2.65 T_L^{1.27} \left[\text{J/mol}\right] \tag{5.21}$$

As shown by the inset in Fig. 5.8 this provides a good estimation of the activation energies of Al, Cu, and Ni. However, there are also deviations: The activation energy of

Table 5.8. Parameters T_L, η_∞, and E_A for each investigated element. The viscosity η_L, calculated from Eq. (5.9) for $T = T_L$, is also shown. Some of the data is measured more than once.

Element	T_L (K)	η_∞ (mPa · s)	E_A (10^4J/mol)	η_L (mPa · s)	Ref.
Al	933	0.281	1.23	1.372	[158]
Si	1687	0.214	1.43	0.593	[158]
Cu	1358	0.522	2.36	4.221	[248]
Cu	1358	0.657	2.15	4.411	[158]
Ni	1727	0.413	3.49	4.694	[160]
Co	1768	0.048	6.81	4.935	[256]
Fe	1818	0.114	5.93	5.765	[160]

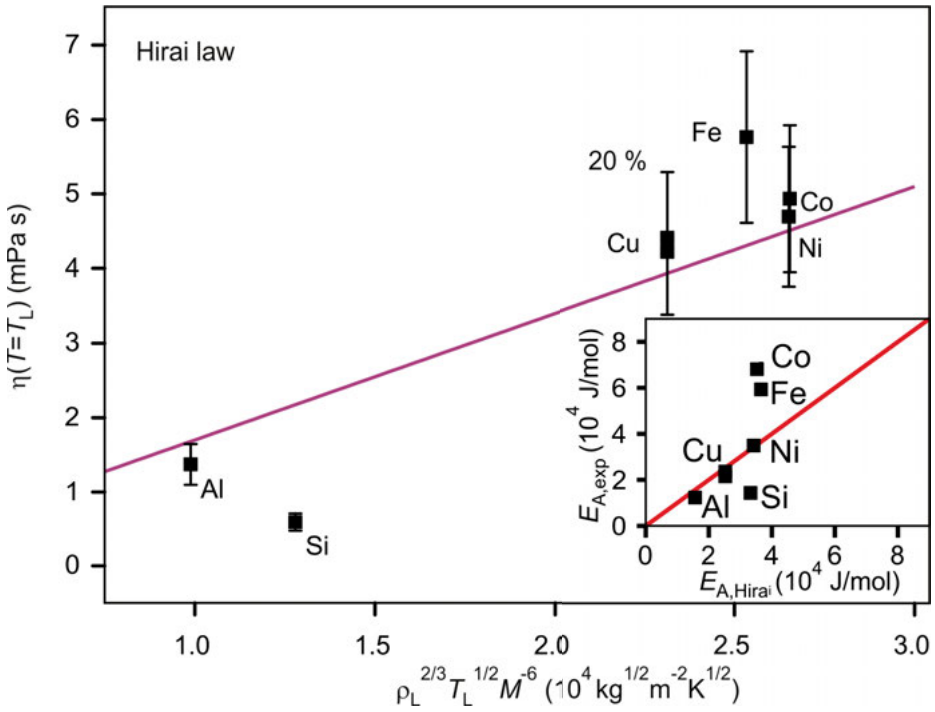

Fig. 5.8. Viscosity η_L versus the right hand side of Eq. (5.20), $\rho_L^{2/3} T_L^{1/2} M^{-1/6}$ (symbols). The solid lines corresponds to Eq. (5.20). The inset shows the measured values of the activation energy $E_{A,exp}$ versus activation energies $E_{A,Hirai}$ calculated from Eq. (5.21).

Si is overestimated by more than 100 % and the activation energies of Fe and Co are underestimated by up to 50 % of their original values.

It is tempting, on the other hand, to test whether or not E_A can be related to the free energies of the standard states, $G_i^0(T)$. This idea is based on the assumption that shear flow is related to a permanent breaking of nearest-neighbor bonds [87] and that the activation energy of viscous flow is generally larger if the interactions between atoms are more attractive. In fact, $G_i^0(T)$ consists of a part being almost independent on temperature, H_i^0, and another one, $-TS_i^0(T) = T\partial G_i^0/\partial T$, depending on temperature almost linearly. This latter part contributes only to η_∞ and can, thus, be neglected for the calculation of the activation energy.

Figure 5.9 shows a plot of E_A versus H_i^0. Generally, one can state that there is indeed a monotonous relation between E_A and H_i^0 for liquid metals. This relation can be expressed by a second order polynomial (dotted line in Fig. 5.9). The simplest relation, however, is linear, $E_A = \alpha_{vis} H_i^0$, with α_{vis} being a coefficient. From the fit to the data of the pure metals, not including Si, one obtains for α_{vis} a value of $0.721 \approx \sqrt{0.5}$. Hence:

$$E_A \approx \sqrt{0.5} H_i^0 \tag{5.22}$$

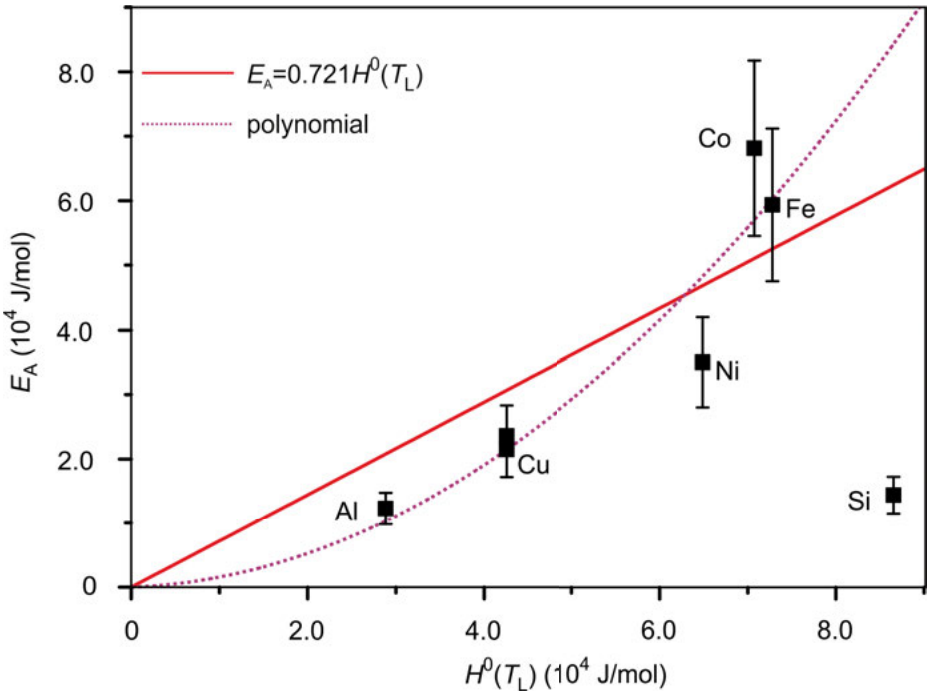

Fig. 5.9. Activation energy E_A of the liquid pure elements versus the standard enthalpy of formation, H_i^0. The data is shown in comparison with a second order polynomial (dotted line) and a linear fit (solid line).

It is striking from Tab. 5.8 and Figs. 5.8 and 5.9 that liquid Si does not follow the trend of the other elements. Neither can η_L be described for liquid Si by the Hirai law, Eq. (5.20), nor can its activation energy be related to H_i^0 via Eq. (5.22). Obviously, this has to do with the significantly larger values of T_L and H_i^0.

In contrast to the other elements, which are metals with nearest neighbor coordination numbers of roughly 12, Si is semiconducting in the solid state and exhibits a coordination number in the liquid of ≈5 [257]. Moreover, covalent bonds coexist with metallic bonds and, due to this, the nature of the atomic interactions strongly differs from those in pure metals, where covalent bonds do not exist. Therefore, it is not too surprising that there is also a different behavior of Si with respect to its viscosity.

5.3 Binary and ternary systems

Systematic viscosity measurements are carried out for binary and ternary systems listed in Tab. 5.9. These systems are: Al-Cu [87], Ag-Al-Cu [157], Co-Sn [256] as well as Cr-Fe-Ni [160], Cu-Fe-Ni [248], Co-Cu-Ni [159] and Al-Cu-Si [158].

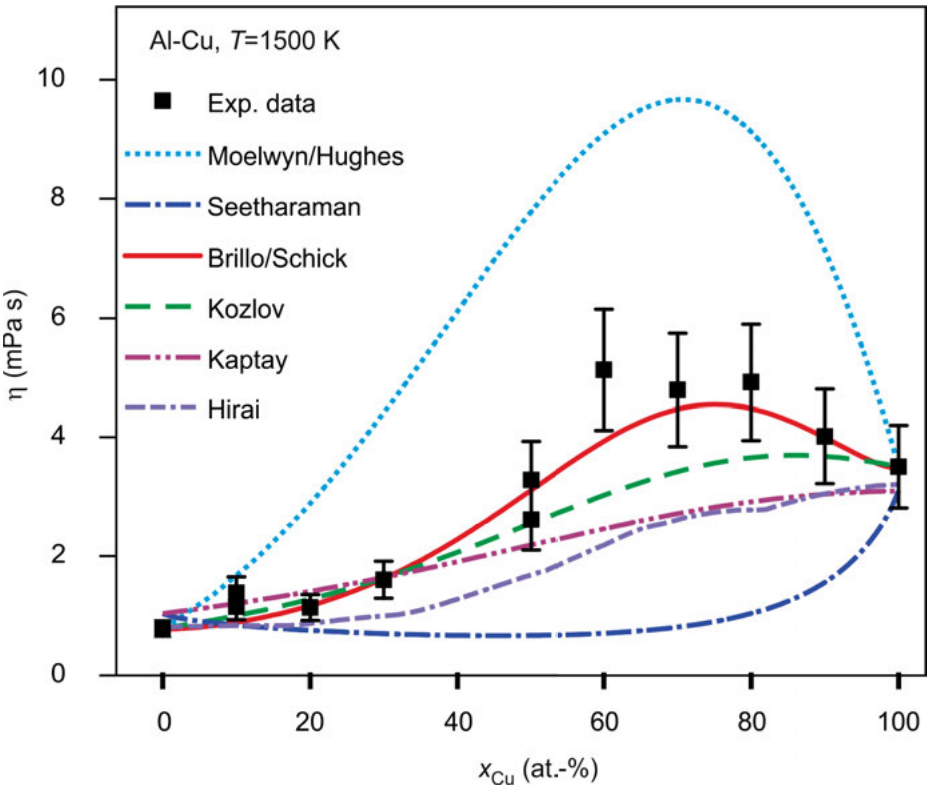

Fig. 5.10. Measured viscosity of Al-Cu versus x_{Cu} at T =1500 K [87]. In addition, calculations of the models of Moelwyn/Hughes (dotted), Seetharaman (dash dotted), Brillo/Schick (solid), Kozlov (dashed), Kaptay (dash double-dotted), and Hirai (dot double-dashed), are also shown.

Data from the binary system Fe-Ni is not measured in the present work. However, results obtained by Sato [258] are discussed in Ref. [160]. The results of this discussion will be exploited in the present section too, i.e. in Tabs. 5.9–5.12, as they support the conclusions drawn below.

As an example, Al-Cu [87] is discussed in more detail: Figure 5.10 shows a plot of the isothermal viscosities of this system at 1500 K versus x_{Cu}. At 1500 K, the viscosity ranges between 0.73 mPa · s, corresponding to pure liquid Al, and 5.1 mPa · s. The latter value corresponds to the viscosity of liquid $Al_{40}Cu_{60}$, which is slightly larger than the viscosity of pure Cu, i.e. than 3.5 mPa · s. Hence, the curve exhibits a maximum around the composition of $Al_{40}Cu_{60}$, see Fig. 5.10.

In an attempt to explain this feature, one might identify the several inter metallic phases that exist around this specific composition in the solid as potential causes [87; 154]. For instance, a maximum in the isothermal viscosity is also evident in Al-Ni [86], Bi-In [259], In-Sn [259] and in ternary Ag-Al-Cu alloys [157]. All these systems exhibit

intermetallic phases at compositions close to the locations of the individual maxima in viscosity. For certain compositions of Al-Ni, intensified chemical short range order in the liquid is discussed as the reason for the observed increase in viscosity [163; 260; 261].

Intermetallic phases, however, are an expression of particularly pronounced attractive interaction in a system. Thermodynamically, the latter is associated with a negative excess free energy. As will be seen shortly, intermetallic phases do not necessarily need to be considered in order to explain the maxima observed.

Together with the experimental data, Fig. 5.10 also shows calculations of the models of Moelwyn/Hughes, Seetharaman, Brillo/Schick, Kozlov, Kaptay, and Hirai. Obviously, the Moelwyn/Hughes model and the Seetharaman model fail to predict the viscosity correctly: Although the Moelwyn/Hughes model accurately predicts the position of the maximum, it overestimates the absolute value of η by more than a factor of 2. The curve calculated from the Seetharaman model exhibits a minimum in viscosity instead of the observed maximum. Moreover, it predicts viscosities that are by a factor of up to 6 too small.

The Hirai model produces a curve with a similar shape to the experimental one but without a pronounced maximum. It still underestimates the data by a factor of up to 2.

A slightly better agreement is found for the Kaptay model. For $x_{Cu} < 60$ at.-%, it deviates from the experimental data only within the errors bars of ± 20 %.

Considerably better agreement is obtained from the Kozlov model for which the agreement with the experiment is within the error bars of ± 20 % for $x_{Cu} \leq 60$ at.-% and $x_{Cu} \geq 90$ at.-%.

The best agreement is found for the Brillo/Schick model, Eqs. (5.18) and (5.19). It reproduces the experimental data in Fig. 5.10 correctly, from both, a qualitative and quantitative point of view [87].

As discussed in Ref. [87] the Brillo/Schick model also correctly predicts the activation energy, E_A. This is shown in Fig. 5.11, where the experimentally determined values of E_A are compared to the ones calculated from Eq. (5.18). The agreement is excellent, again. The same is true for η_∞, as shown by the inset in Fig. 5.11.

It should be noted at this point that the Brillo/Schick model (and also the Kozlov model) do not explicitly consider compound formation in the melt. In principle, ΔH could have any mathematical form. Therefore, it could also be calculated from a compound formation model. However, ΔH is calculated in Eq. (5.18) from the sub-regular solution approximation[3] [242]. Obviously, this is sufficient for the description of the experimental data. As for the surface tension [69], see Chap. 4, a model using compound formation is not necessary for Al-Cu.

3 using the coefficients listed in Refs. Tab. B.3.

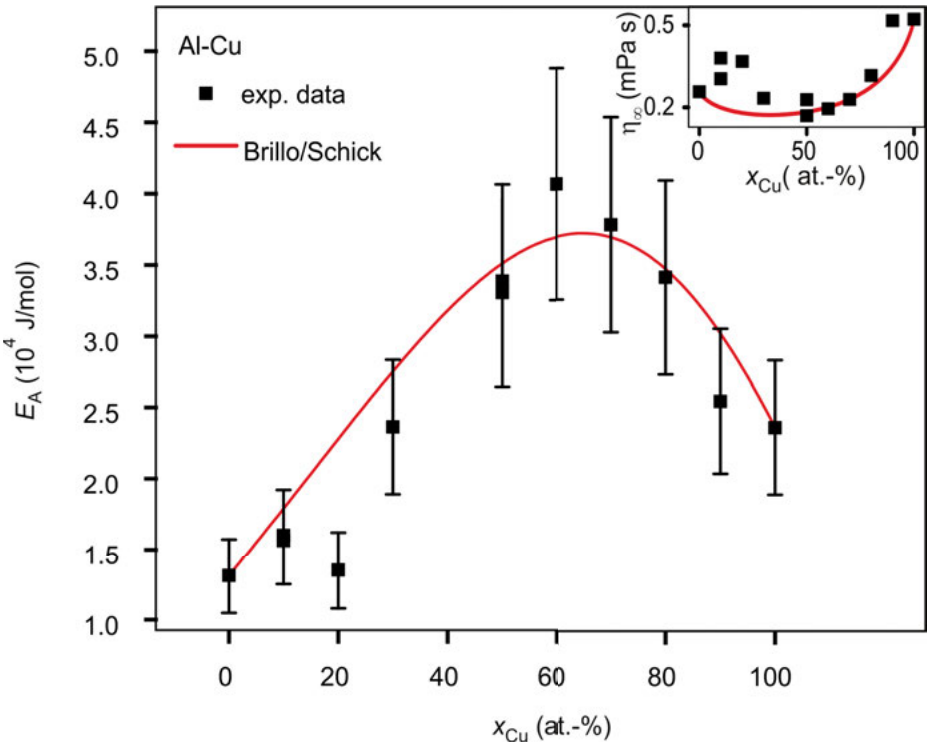

Fig. 5.11. Experimentally determined activation energies E_A versus x_{Cu} for liquid Al-Cu. The experimental data is shown together with a calculation of the Brillo/Schick model. The inset shows the same comparison for the pre-exponential factor η_∞.

This result is also obtained for the ternary system Ag-Al-Cu which is similar to Al-Cu. For this system, the viscosity is measured along a section where the concentration of silver is kept constant at 10 at.-% and the mole fraction of Cu, x_{Cu} is varied from 0 to 90 at.-% [157].

The results for the isothermal viscosity are shown in Fig. 5.12 for $T = 1223$ K. Obviously, they exhibit the same general appearance, i.e. the data monotonously increases with x_{Cu} from 0.9 mPa · s, corresponding to the viscosity of $Ag_{10}Al_{90}$, up to approx. 5.8 mPa · s which corresponds to the viscosity of $Ag_{10}Al_{30}Cu_{60}$. As in the binary system Al-Cu, η exhibits a maximum at x_{Cu}=60 at.-% before it slightly decays down to the value of 4.7 mPa · s corresponding to the viscosity of $Ag_{10}Cu_{90}$.

The experimental data is compared in Fig. 5.12 with the different model calculations. Obviously, the best agreement is found for the Kozlov model which excellently reproduces the experimental data. A nearly equally good agreement is obtained for the Brillo/Schick model. It correctly predicts the maximum and η for $x_{Cu} < 60$ at.-%. However, the decay of η on the right hand side of the maximum is slightly stronger

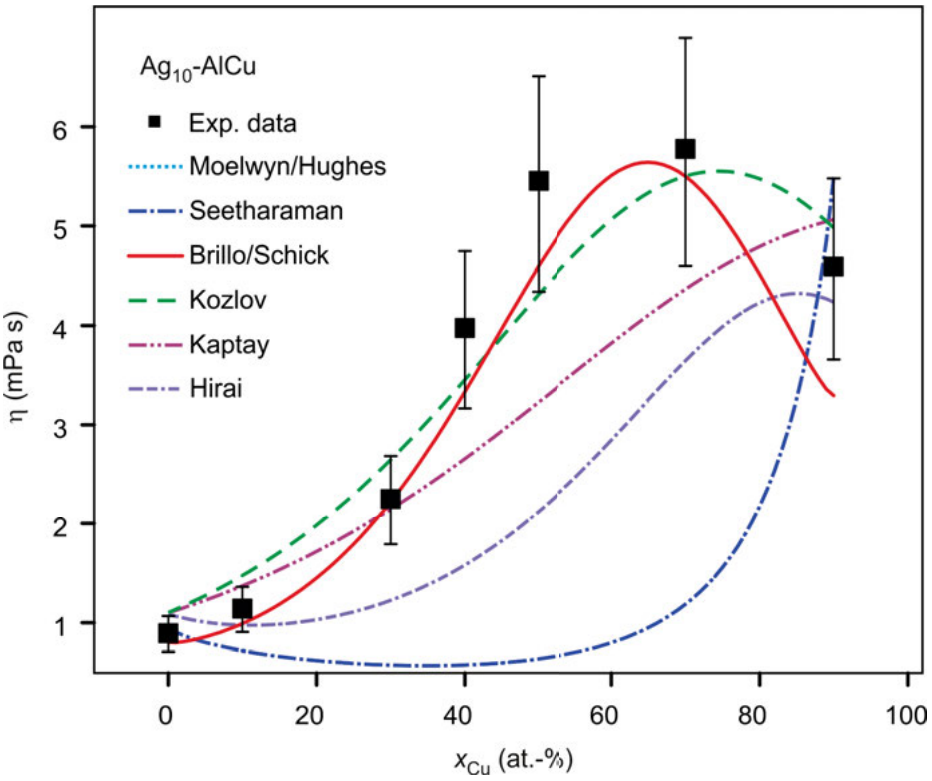

Fig. 5.12. Measured viscosity of Ag_{10}-Al-Cu versus x_{Cu} at T =1223 K. In addition, calculations of the models of Seetharaman (dash dotted), Brillo/Schick (solid), Kozlov (dashed), Kaptay (dash double-dotted), and Hirai (dot double-dashed), are also shown.

as indicated from experiment so that the viscosity of $Ag_{10}Cu_{90}$ is underestimated by more than 20 %. The agreement with the other models is worse.

As already mentioned, the monotectic system Cu-Fe-Ni is different from Al-Cu and Al-Cu-Ag. In particular, because it exhibits a positive excess free energy and the tendency to demix at $T < T_L$. In order to pursue the question, whether or not this has any impact on the viscosity, η is measured along the section $Cu_xFe_{0.6(1-x)}Ni_{0.4(1-x)}$, $0 \le x \le 1$ and plotted in Fig. 5.13 versus the Cu mole fraction x_{Cu} at 1873 K.

Obviously, the experimental data decreases moderately and almost linearly with increasing x_{Cu} from ≈ 4.5 mPa · s to ≈2.9 mPa · s. The curve exhibits a concave shape and there is no maximum in viscosity as function of x_{Cu}.

For this system, the best description of the data is provided by the Kaptay model [248]. Despite its simplicity, the second best description is provided by the Hirai model. For $x_{Cu} < 30$ at.-%, however, the Hirai model underestimates the experimental data slightly. The agreement with the Kozlov model is also good, although the measured viscosities are overestimated by <20 % for x_{Cu} <30 at.-%. In contrast to the two previ-

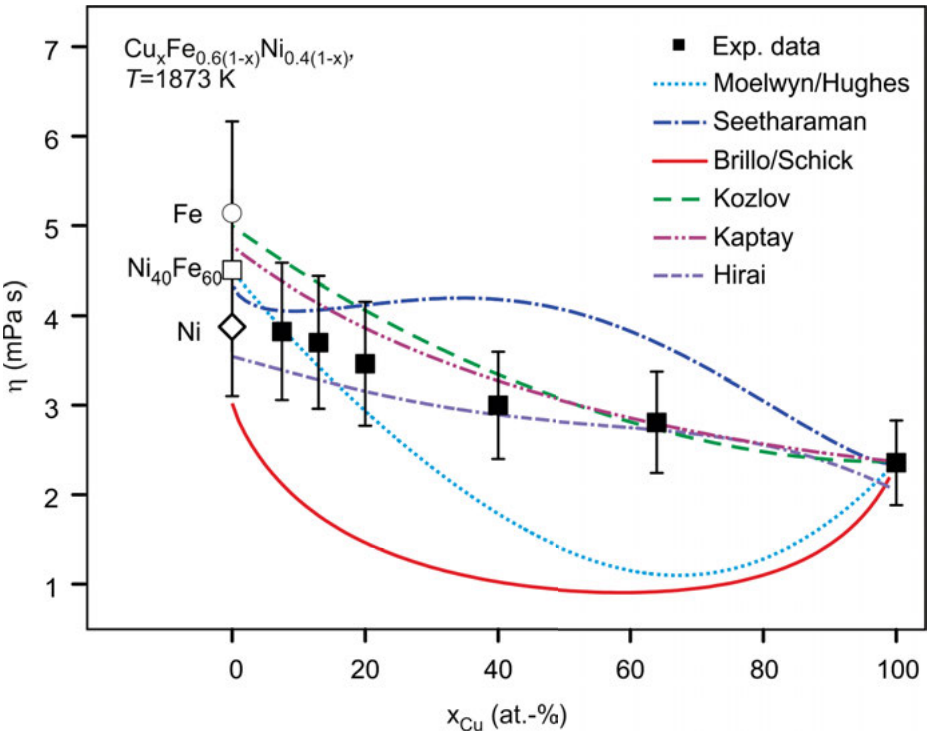

Fig. 5.13. Measured viscosity of $Cu_xFe_{0.6(1-x)}Ni_{0.4(1-x)}$, $0 \le x \le 1$ versus x_{Cu} at T =1873 K. In addition, calculations of the models of Moelwyn/Hughes (dotted), Seetharaman (dash dotted), Brillo/Schick (solid), Kozlov (dashed), Kaptay (dash double-dotted), and Hirai (dot double-dashed), are also shown.

ous examples, the Brillo/Schick model fails to describe the data correctly. In fact, its agreement with the experimental data is even worse than for the Seetharaman or the Moelwyn/Hughes model which also fail to predict the data correctly.

Obviously, the success of each model depends on the system being investigated. This is demonstrated in Tab. 5.9 where it is evaluated how well each model works for each investigated system. A model is hereby regarded as *OK* if the predicted viscosities agree with the experimental data within the error bars over the entire investigated concentration range. It is regarded as "reasonable" (*RS*) if the agreement is, at least, partially within the error bars. If there is no agreement between the model and the experimental data, the model fails (*F*) to predict the viscosity correctly. A model is regarded as "successful" if it doesn't fail and it is rated "best" if it yields the best agreement, compared with the other models.

Applying these criteria, the Moelwyn/Hughes model is tested in the case of Al-Cu, Cu-Fe-Ni and Co-Cu-Ni. The Seetharaman model is tested for Al-Cu, Ag-Al-Cu, Cu-Fe-Ni, and Co-Cu-Ni. Both models do not succeed in any case (=*F*).

The Brillo/Schick model is tested in the case of Al-Cu, Al-Cu-Ag, Co-Sn, Cu-Fe-Ni, Co-Cu-Ni and Al-Cu-Si. It seems to fail when being applied to systems for which $\Delta H > 0$.

The Kozlov model and the Kaptay model are tested for all investigated systems, except Co-Sn. The Hirai model, finally, is also tested for all these systems, except Al-Cu-Si.

In the case of liquid Co-Sn, also two other models are tested in Ref. [256]: the Budai/Kaptay model [249] and the Singh/Sommer model [262]. These models are not discussed in the present work as they pursue different approaches. The results of these tests are summarized in Tab. 5.9.

In order to find out which of the models is best suited in order to describe the viscosity of any system, Tab. 5.9 is evaluated with respect to the success of each model.

The result of this evaluation is summarized in Tab. 5.10. Obviously, the Moelwyn/Hughes and the Seetharaman models fail in 100 % of the cases in which they are tested. The Hirai model is successful in 43 % of the cases, the Brillo/Schick model in 50 %, and the Kaptay model in 57 %.

The Kozlov model is successful in 86 %. In nearly 30 % of all cases in which it is tested, it even provides the best description of the viscosity.

Among the models tested and based on the systems selected in Tab. 5.9, the Kozlov model can be regarded as “the best” one. Indeed, among the models discussed, the Kozlov model is the only one derived purely from physical principles [251].

Table 5.9. Systems investigated and models tested. *F*=failed, *RS*=reasonable= partially within error bars, *OK* = within error bars, and *best*=best model for this system.

System	Model tested		Reference
Ag-Al-Cu	Seetharaman	F	[157]
	Brillo/Schick	OK	
	Kozlov	best	
	Kaptay	RS	
	Hirai	F	
Al-Cu	Moelwyn/Hughes	F	[87]
	Seetharaman	F	
	Brillo/Schick	best	
	Kozlov	RS	
	Kaptay	RS	
	Hirai	F	
Al-Cu-Si	Brillo/Schick	OK	[158]
	Kozlov	OK	
	Kaptay	OK	
Co-Cu-Ni	Moelwyn/Hughes	F	[159]
	Seetharaman	F	
	Brillo/Schick	F	
	Kozlov	OK	
	Kaptay	best	
	Hirai	OK	
Co-Sn	Hirai	RS	[256]
	Brillo/Schick	RS	
	Budai/Kaptay	best	
	Singh/Sommer	F	
Cr-Fe-Ni	Kozlov	OK	[160]
	Kaptay	OK	
	Hirai	OK	
Cu-Fe-Ni	Moelwyn/Hughes	F	[248]
	Seetharaman	F	
	Brillo/Schick	F	
	Kozlov	OK	
	Kaptay	best	
	Hirai	OK	
Fe-Ni	Kozlov	OK (best)	[160]
	Kaptay	RS	
	Hirai	RS	

Table 5.10. Comparison of the performance of the models: *F*=failed, *OK* = within error bars, and *best*=best model for a system. Numbers in brackets denote percentages.

Model	Category								all
	best		OK		Successful		F		
Moelwyn/Hughes							3	(100%)	3
Seetharaman							4	(100%)	4
Brillo/Schick	1	(17%)	2	(33%)	3	(50%)	2	(33%)	6
Kaptay	2	(29%)	2	(29%)	4	(57%)			7
Kozlov	2	(29%)	4	(57%)	6	(86%)			7
Hirai			3	(43%)	3	(43%)	2	(29%)	7

5.4 Ideal solution and excess viscosity

Based on the results of the previous section it is justified to accept the Kozlov model as a basis for the definition of the viscosity, ${}^{\mathrm{id}}\eta$, of an ideal solution and also for the definition of the excess viscosity, ${}^{\mathrm{E}}\eta$.

For an ideal solution $\Delta H = 0$. Hence, Eq. (5.13) transforms into the following expression for a system with N components, i, each having a mole fraction of x_i and a viscosity of η_i:

$$ {}^{\mathrm{id}}\eta = \prod_{i}^{N} \eta_\mathrm{i}^{x_\mathrm{i}} \tag{5.23} $$

In the same way, this expression can also be obtained from the Kaptay model which is the second most successful model in Tab. 5.10.

In contrast to the molar volume, for instance, the ideal viscosity is not a linear combination of the property of the pure component in x_i. Instead, this is rather true for its logarithm which appears to be the additive quantity.

Based on Eq. (5.23), the excess viscosity ${}^{\mathrm{E}}\eta$ can be defined in the following way:

$$ {}^{\mathrm{E}}\eta = \eta - \prod_{i}^{N} \eta_\mathrm{i}^{x_\mathrm{i}} \tag{5.24} $$

Generally speaking, one can also write the activation energy E_A in the following form:

$$ E_\mathrm{A} = \sum_{i}^{N} x_\mathrm{i} E_{\mathrm{A,i}} + \Delta E_\mathrm{A} \tag{5.25} $$

In Eq. (5.25), $E_{\mathrm{A,i}}$ is the activation energy of the pure component i and ΔE_A is the activation energy of mixing.

It is an interesting question, whether or not ${}^{\mathrm{E}}\eta$ and ΔE_A can be related either to ${}^{\mathrm{E}}G$ or ΔH. This question is elucidated within the next section.

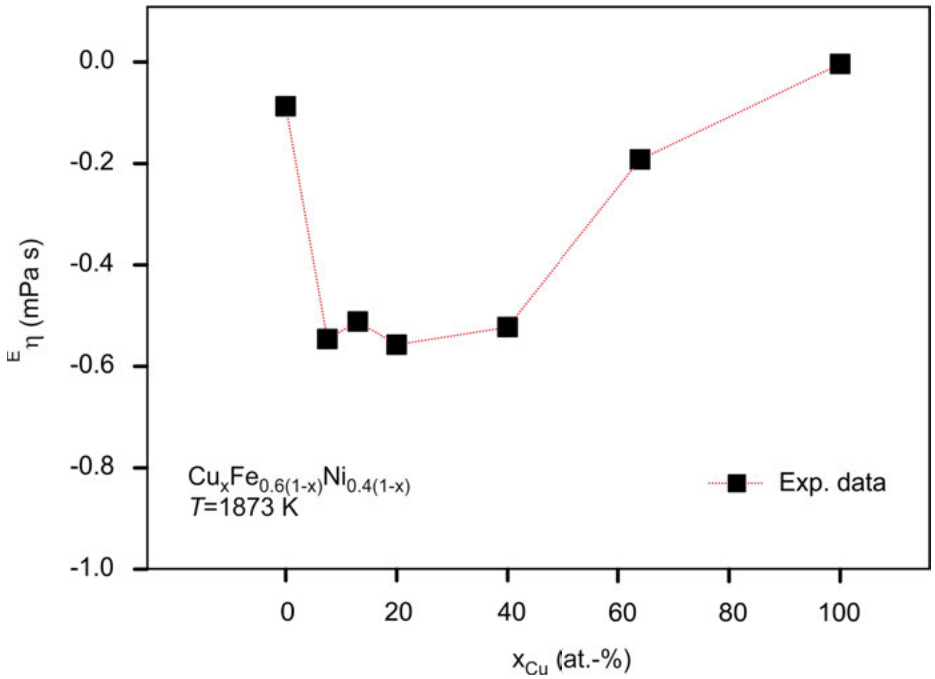

Fig. 5.14. Excess viscosity ${}^{E}\eta$ versus Cu mole fraction x_{Cu} along a cut $Cu_xFe_{0.6(1-x)}Ni_{0.4(1-x)}$, $0 \le x \le 1$ through the Cu-Fe-Ni system at 1873 K.

5.5 Observed trends

If the Kozlov model was strictly valid, ${}^{E}\eta$ and the enthalpy of mixing, ΔH, should exhibit opposite signs. Moreover, one can postulate that this is also true for ΔH and ΔE_A. In the present section this hypothesis will be tested on the basis of the available experimental data.

Figure 5.14 shows a plot of ${}^{E}\eta$ versus the Cu mole fraction, x_{Cu}, along the investigated section, $Cu_xFe_{0.6(1-x)}Ni_{0.4(1-x)}$, $0 \le x \le 1$, of the Cu-Fe-Ni system. The plot is shown for a temperature of 1873 K. The enthalpy of mixing ΔH is positive for Cu-Fe-Ni over the vast compositional range. As visible in Fig. 5.14, ${}^{E}\eta$ is negative, indeed. The minimum of ${}^{E}\eta$ is located at $x_{Cu} \approx 30$ at.-%. At this composition, ${}^{E}\eta \approx -0.6$ mPa · s which is −17 % of the measured viscosity.

The opposite case, $\Delta H < 0$, is tested in Fig. 5.15 for the ternary system Ag_{10}-Al-Cu. The figure shows a plot of ${}^{E}\eta$ versus x_{Cu} along a section $Ag_{0.1}Al_{0.9-x}Cu_x$, $0 \le x \le 0.9$ at 1223 K. As visible, ${}^{E}\eta > 0$ at the vast compositional range. The maximum of ${}^{E}\eta$ is located at $x_{Cu} \approx 50$ % and its value is about 2.7 mPa · s. This is more than 50 % of the measured viscosity and nearly 100 % of the ideal viscosity. Hence, in Ag-Al-Cu is highly non-ideal with respect to viscosity. This is also true for Al-Cu. The contribution

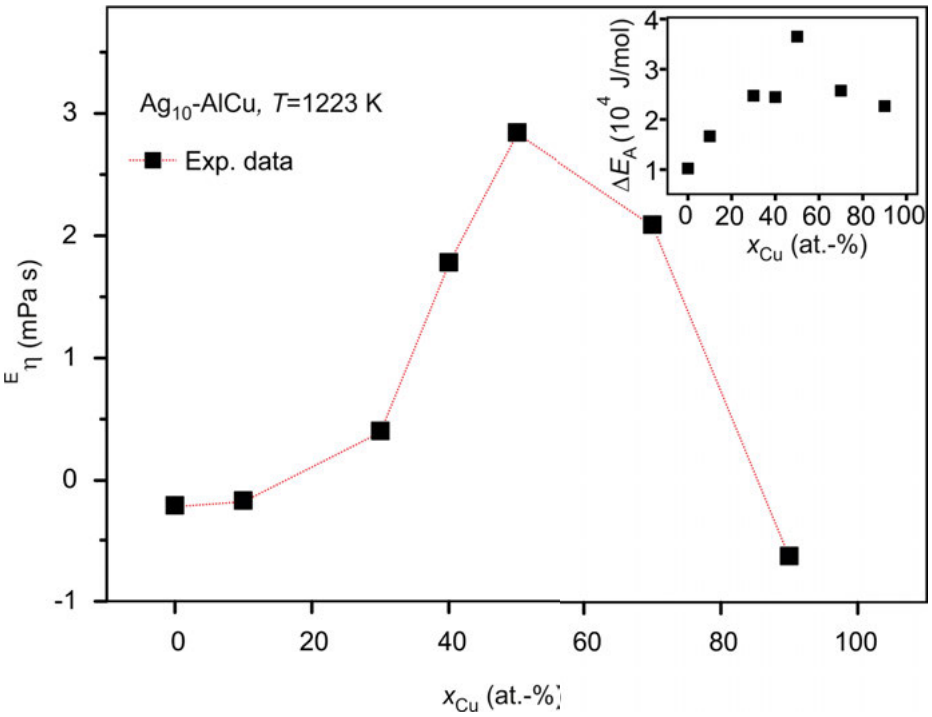

Fig. 5.15. Excess viscosity $^{E}\eta$ versus Cu mole fraction x_{Cu} along a cut $Ag_{0.1}Al_{0.9-x}Cu_x$, $0 \leq x \leq 0.9$, through the Ag-Al-Cu system at 1223 K. The inset shows ΔE_A.

of $^{E}\eta$ to η is 5 times larger in Ag-Al-Cu than, for instance, in Cu-Fe-Ni. With respect to viscosity, the latter, can rather be interpreted as an ideal system.

Comparisons between ΔH, $^{E}\eta$, ΔE_A are shown in Tab. 5.11 for those alloy systems for which viscosity data is measured in the present work. Each system is associated to one of the three classes defined in chapter 3.

In fact, Cu-Fe-Ni is the only system for which ΔH and $^{E}\eta$ are both negative. In the case of Co-Cu-Ni, $^{E}\eta \approx 0$.

Systems for which $\Delta H < 0$ are Cr-Fe-Ni, Fe-Ni, Co-Sn, and Al-Cu-Si. In Cr-Fe-Ni, Fe-Ni, and Co-Sn, $^{E}\eta \approx 0$. For Al-Cu-Si $^{E}\eta$ is slightly negative. Again, the deviation from zero is small in these cases. In addition to the signs of ^{E}G, ΔH, and $^{E}\eta$ also the signs of ΔE_A are listed in Tab. 5.11. No uniform tendency is revealed: In the case of Cu-Fe-Ni, for instance, $\Delta E_A \approx 0$ while $^{E}\eta < 0$. In the case of Co-Cu-Ni, $\Delta E_A < 0$ while $^{E}\eta \approx 0$. For Al-Cu-Si and Co-Sn, both having a strongly negative enthalpy of mixing, $\Delta E_A \approx 0$. In the case of Cr-Fe-Ni, ΔE_A is even negative although also $\Delta H < 0$.

In all these systems, the deviations of $^{E}\eta$ and ΔE_A from zero are actually small. It can, therefore, be concluded that, with respect to viscosity, these systems can be regarded as almost ideal, see Tab. 5.11.

Table 5.11. Observed trends in the viscosity of the investigated alloys.

Class	System	Sign of ΔH	Sign of ${}^{E}\eta$	Sign of ΔE_A	mixing behavior	Source
I	Cu-Fe-Ni	+	-	≈ 0	*ideal*	[248]
	Co-Cu-Ni		≈ 0	-	*ideal*	[159]
II	Cr-Fe-Ni	-	≈ 0	-	*ideal*	[160]
	Fe-Ni				*ideal*	[160]
III	Ag-Al-Cu	-	+	+	*non-ideal*	[157]
	Al-Cu		+	+	*non-ideal*	[87]
	Al-Cu-Si		-	≤ 0	*ideal*	[158]
	Co-Sn		≈ 0	≈ 0	*ideal*	[256]

On the other hand, for Ag-Al-Cu and Al-Cu, $\Delta E_A >> 0$. In fact, these two systems are highly non-ideal with respect to viscosity.

The finding that most systems of Tab. 5.9 are ideal with respect to viscosity explains the success of the Kaptay model, see Tab. 5.10: In Eq. (5.17) ΔH is multiplied by a small factor, 0.155, so that the influence of ΔH on the viscosity is rather small. Hence, the viscosities calculated by this model are close to ${}^{id}\eta$.

The definition whether a system can be regarded as *ideal* or *non-ideal* with respect to viscosity is model-dependent. The Kozlov model is chosen as a basis for this definition, as it is identified in Tab. 5.10 as the most successful one with respect to all systems.

In addition, a look at Tab. 5.12 shows that there might be a certain tendency: Systems belonging to class I can best be described by the Kaptay model, the viscosities of members of class II are best predicted by the Kozlov model and the viscosities of members of class III are predicted best by the model of Brillo and Schick. In view of the limited number of investigated systems, however, this conclusion can only be preliminary.

The models discussed in this section aim to derive η from the thermodynamic potentials, i.e. from ${}^{E}G$ or ΔH. In a ternary system, the influence of a ternary parameter in Eq. (3.17) on the calculated viscosities will be small, as the contributions of the ternary interaction terms to ${}^{E}G$ is usually much smaller in Eq. (3.17) as of the binary terms. Provided the correct model for the calculation of the viscosity is identified for a system, it will also be possible to predict η from the excess free energies only of the binary subsystems.

5.6 Summary and conclusions

In this chapter, viscosities of unary, binary, and ternary liquid metallic systems are studied.

In the case of unary systems, the obtained viscosities are in agreement with data from literature within ±20 %. This margin also corresponds to the deviation among data sets measured in the same apparatus. Moreover, the results are used in order to validate the Hirai law. The energies of activation are empirically found to be functions of the enthalpies of the standard states, H_i^0.

Table 5.12. Best model for the prediction of the viscosity of members of each class. In the case of Cr-Fe-Ni, the Kozlov- the Kaptay, and the Hirai model perform equally well. In the case of Al-Cu-Si, the models of Brillo and Schick, Kozlov, and Kaptay perform equally well.

Class	System	Best viscosity model
I	Cu-Fe-Ni	Kaptay
	Co-Cu-Ni	Kaptay
II	Cr-Fe-Ni	Kozlov ≈ Kaptay ≈ Hirai
	Fe-Ni	Kozlov
III	Ag-Al-Cu	Brillo/Schick
	Al-Cu	Brillo/Schick
	Al-Cu-Si	Brillo/Schick ≈ Kozlov ≈ Kaptay
	Co-Sn	Budai/Kaptay

In the case of binary and ternary systems, the viscosities are measured and compared to a number of thermodynamic models aiming to relate the viscosity to thermodynamic potentials, ${}^{\mathrm{E}}G$ or ΔH. However, these models perform heterogeneously and the comparison does not yield a fully satisfying answer: The viscosity of nearly each system is predicted precisely by one of the models. However, in the case of another system, the same model yields worse agreement or even fails.

As a preliminary tendency, one can state that the Kaptay model works best for class I systems, the Kozlov model is the best choice for class II systems and the viscosities of members of class III are predicted best by the model of Brillo and Schick. On average, the Kozlov model performs most successfully.

Using the Kozlov model in order to generate a definition for the ideal viscosity, does not lead to the establishment of a relation between excess viscosity and enthalpy of mixing, ΔH, or between the mixing contributions to the activation energies, ΔE_{A}. The absolute values of the obtained excess viscosities are small in most cases so that, as a rough trend, the viscosities can be approximated by the ideal solution. Exceptions are the strongly interacting systems Al-Cu and Ag-Al-Cu.

This result may be non-satisfying. However, it also shows that either the relation between η and thermodynamic potentials, i.e. ${}^{\mathrm{E}}G$, ΔH, etc, is not yet understood or that thermodynamics does not have the primary influence on viscous flow. Instead, one may consider other factors such as short range order.

6 Inter-property relations

Two inter-property relations are tested: a relation between viscosity and surface tension as well as the Stokes-Einstein relation.

The relation between surface tension and viscosity works in the case of pure liquid elements with respect to the accuracy of the experimental data. In case of liquid binary and ternary alloys, good agreement is evident for two different systems once the relation is modified slightly. However, the accuracy does not suffice to predict viscosities of alloys from available excess free energies via the Butler equation.

In the case of $Al_{80}Cu_{20}$, the Stokes-Einstein relation holds for temperatures higher than 1400 K. It breaks down for smaller temperatures. In case of the densely packed system $Ni_{36}Zr_{64}$, $D \cdot \eta = const$ is found, heavily contrasting the Stokes-Einstein relation.

6.1 Surface tension - viscosity relation

Attempts, to relate the viscosity of an alloy to the enthalpy of mixing, ΔH, or to the excess free energy, ${}^{\mathrm{E}}G$, are only partially successful as noted in the previous chapter. Instead of directly deriving η from ΔH or ${}^{\mathrm{E}}G$, one can also try to link the viscosity to the surface tension. The surface tension of a sub-regular solution, on the other hand, can be predicted from the excess free energy ${}^{\mathrm{E}}G$ via the Butler equation, as shown in Chap. 4.

Such a relation between surface tension and viscosity can indeed be established. This is seen, for instance, from Eqs. (4.5) and (5.4), which are both well known and often used in order to calculate surface tension and viscosity from the known pair potentials and distribution functions [20].

A remarkable feature of both expressions has been overseen for long, namely, that the integrals in Eq. (4.5) and Eq. (5.4) are identical [23]. Dividing Eq. (4.5) by Eq. (5.4) yields

$$\frac{y}{\eta} = \alpha_{\eta-y}\sqrt{\frac{RT}{M}} \tag{6.1}$$

with $R = 8.314\,\mathrm{J mol^{-1} K^{-1}}$ being the molar gas constant, M the molar mass, and $\alpha_{\eta-y} = 0.94$ is a constant coefficient. Incidentally dividing Eq. (4.40) by Eq. (5.20) yields the same expression with $\alpha_{\eta-y} = 0.82$. In his work [24] Kaptay reports a value of $\alpha_{\eta-y}$ of 0.755.

It may seem surprising at first, that such a relation exists between a surface and a bulk property. On the other hand, when additional surface is created, atoms are displaced and work must be done against their pair potential. The amount of work depends on the distribution of neighboring atoms, described by the pair correlation function and the pair potential. Shear flow is a highly collective process involving the

displacement of atoms relative to the positions of their neighbors [23] so that also in this case work must be done against the pair potential. If surface is created, material flows towards it from the bulk. The energy dissipated during this flow contributes to the energy required to create the new surface. Thus, the origins of viscosity and surface tension lie in the same physical process [23].

Equation (6.1) has already been validated for pure liquid metals by Egry [23], and Kaptay [24]. Both authors report different values of $\alpha_{\eta-y}$. Obviously, Eq. (6.1) must break down sooner or later, as the surface tension depends on temperature linearly while the viscosity obeys an exponential law. Egry [263] found that Eq. (6.1) is valid for temperatures in a range of ≈ 300 K around the melting point. Kaptay noticed that Eq. (6.1) fails in the case of Si, Ge, Sb and Bi [24]. Chemical bonding and coordination are different in their liquid and solid phases for these systems [24].

Based on the results of Chap. 4 and Chap. 5, Eq. (6.1) can easily be checked for pure metals. This is done in the first step. In the second step, it is tested, whether Eq. (6.1) can also be applied to alloy systems or, otherwise, in which way it needs to be modified.

6.1.1 Pure metals

In order to test Eq. (6.1), results obtained for the pure metals Al, Cu, Ni, Co, and Fe, are consulted first. Surface tension data is hereby picked from Chap. 4 and viscosities from Chap. 5. For these systems, the ratios y_L/η_L are plotted in Figure 6.1 versus corresponding values of $\sqrt{RT_L/M}$. Obviously, a linear law is obeyed, except for Al, which deviates from the trend of the other metals.

In addition to the experimental data, Fig. 6.1 also shows Eq. (6.1) using the different values of $\alpha_{\eta-y}$. Obviously, the curve for $\alpha_{\eta-y} = 0.94$ slightly overestimates the data. Most experimental points lie exactly on the curve for $\alpha_{\eta-y} = 0.75$. The only exceptions are Al and Fe measured in Ref. [160]. If, instead, of the latter reference, the results measured by Kehr [86] are used for liquid Fe, Al remains the only exception.

A linear fit of Eq. (6.1) to all data, including liquid Al, yields $\alpha_{\eta-y} = 0.815$. This value equals the one obtained from dividing the phenomenological equations, Eq. (4.40) and Eq. (5.20) by each other. The reason is obvious: Eq. (4.40) and Eq. (5.20) are shown in Chaps. 4 and 5 to work on an average scale. Hence, Eq. (6.1) would also work on an average scale, if $\alpha_{\eta-y} = 0.82$ is used. The agreement in Fig. 6.1 is roughly within ±25 %.

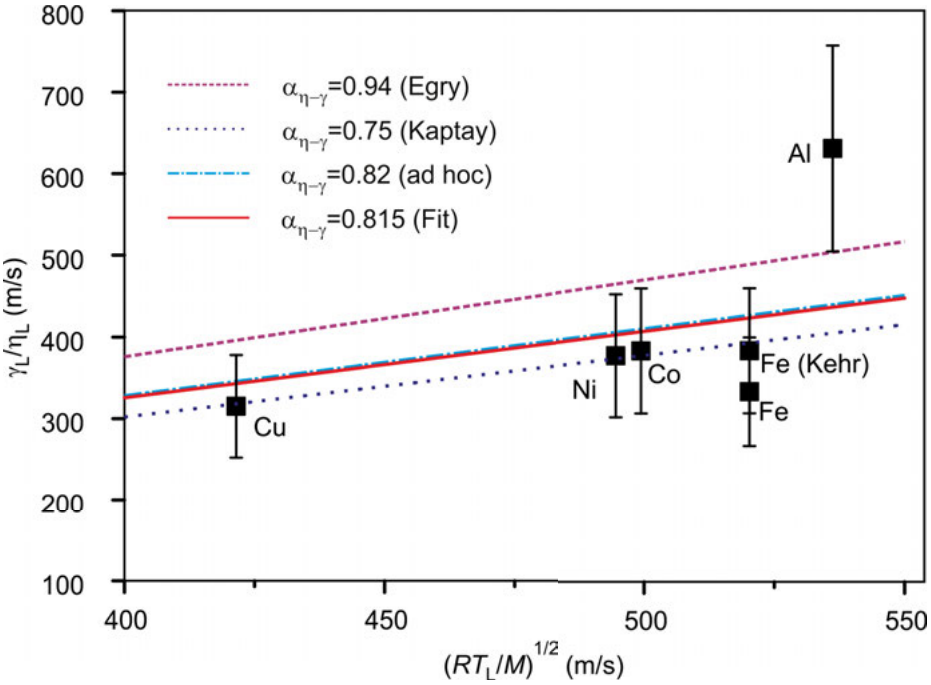

Fig. 6.1. Experimentally obtained ratios γ_L/η_L of Al, Cu, Ni, Co, and Fe versus corresponding values of $\sqrt{RT_L/M}$. In addition, calculations of Eq. (6.1) are shown with different values of α. The error bars, ±20 %, result from the estimated uncertainties of the surface tension, ±5 %, and viscosity, ±20 %.

6.1.2 Al-Cu and Cu-Fe-Ni

The applicability of Eq. (6.1) to alloys is tested by means of of two examples: Al-Cu and Cu-Fe-Ni. These systems are selected because reliable surface tension and viscosity data exist for both [69; 87; 239; 248].

The evaluation of Eq. (6.1) is shown for liquid Al-Cu in Fig. 6.2. Surface tension and viscosity data is taken from Refs. [191] and [87], respectively. In the majority of the results, the experiment is systematically overestimated by the predictions from Eq. (6.1), using $\alpha_{\eta-y} = 0.94$, 0.82 and 0.75. Hence, Eq. (6.1) is no longer valid for alloy systems if it is applied the same as with pure elements. This observation is not too surprising, as the Hirai model fails to predict the viscosity in many alloy systems, as well. As shown in Chap. 5, Eq. (5.14) also drastically underestimates the viscosity of Al-Cu.

Nevertheless, there is a tendency in Fig. 6.2 that the ratio y_L/η_L increases linearly with increasing $\sqrt{RT_L/M}$ which is, at least, in qualitative agreement with Eq. (6.1). Fitting Eq. (6.1) to the data yields a value for $\alpha_{\eta-y}$ of $0.62(\pm 0.03)$.

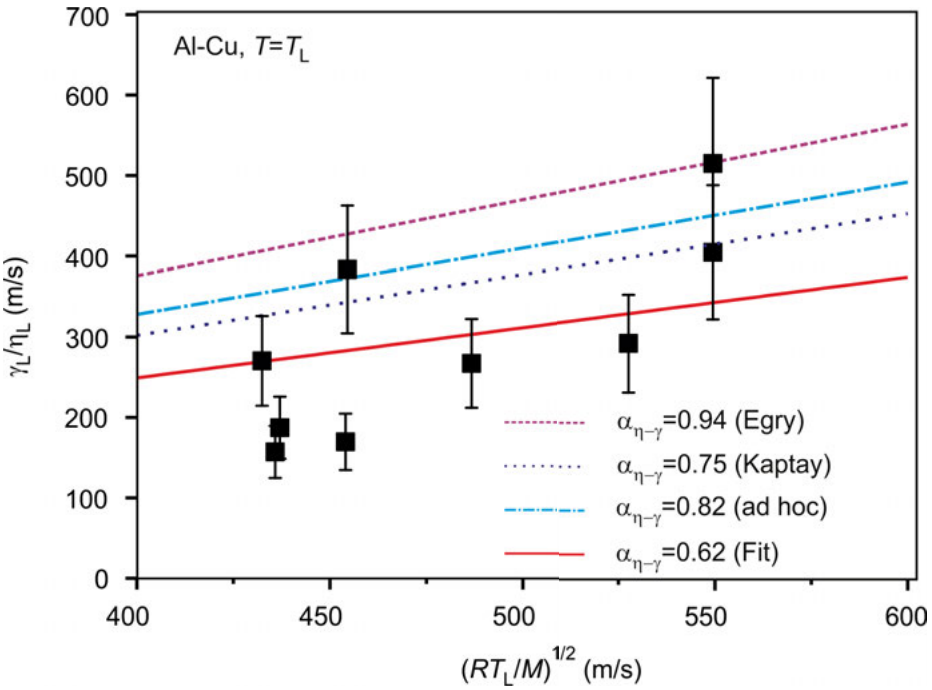

Fig. 6.2. Experimentally obtained ratios γ_L/η_L of Al-Cu alloys versus corresponding values of $\sqrt{RT_L/M}$. In addition, calculations of Eq. (6.1) are shown with different values of $\alpha_{\eta-\gamma}$. The error bars, ±20 %, result from the estimated uncertainties of the surface tension, ±5 %, and viscosity, ±20 %.

In fact, Al-Cu is a mixing system for which ${}^{E}G << 0$. It belongs to class III in Tab. 3.14. The thermophysical properties and their mixing behavior of members of this class are discussed in Chaps. 3–5. In contrast to Al-Cu, the ternary system Cu-Fe-Ni is chemically, structurally and thermodynamically different from Al-Cu. It belongs to class I in Tab. 3.14 and exhibits a miscibility gap in the undercooled regime.

Despite these differences, the same result is obtained in Fig. 6.3: Again, Eq. (6.1) systematically overestimates the experimentally obtained ratios, y_L/η_L, if $\alpha_{\eta-y}$ = 0.94, 0.82, and 0.75 are used. Adjusting Eq. (6.1) to the data, however, yields a value of $\alpha_{\eta-y}$ of 0.595 (±0.03). Within the uncertainty of ±0.03, this value is identical with the one obtained for Al-Cu.

It seems that a relation between y and η is, indeed, found, indeed. This shall be tested for the case of Co-Sn. For this system, viscosity data is published in Ref. [256] from which η_L is calculated and plotted in Fig. 6.4 versus x_{Co}. In Ref. [256], only the data for $x_{Co} \geq 50$ at.-%, are measured using the DLR viscometer "HOC". Moreover, the value of η_L at x_{Co} =80 at.-% is significantly larger than for x_{Co} =70 at.-%

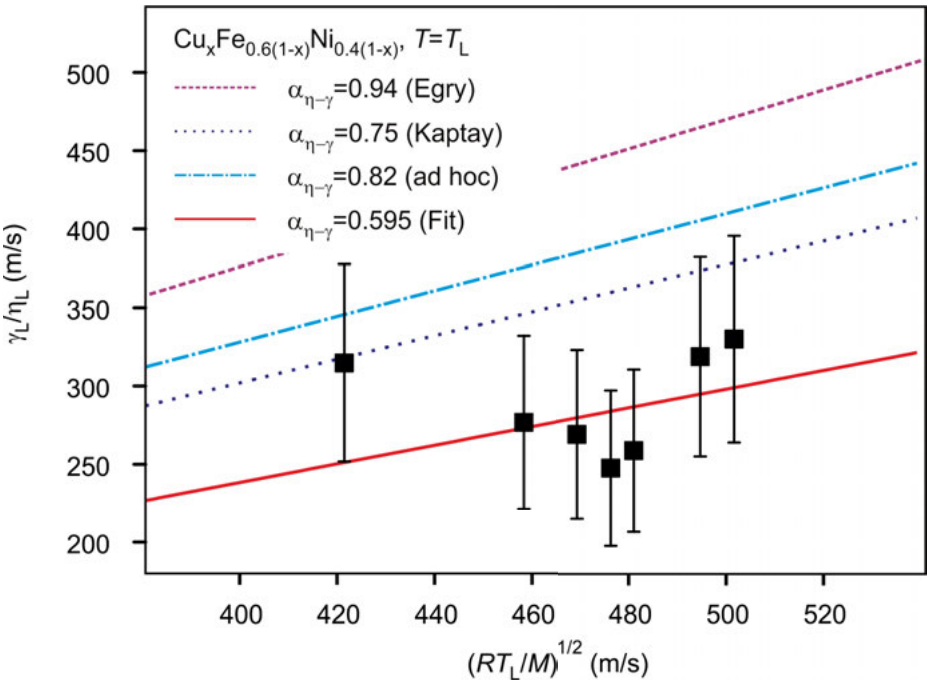

Fig. 6.3. Experimentally obtained ratios γ_L/η_L of Cu-Fe-Ni alloys versus corresponding values of $\sqrt{RT_L/M}$. In addition, calculations of Eq. (6.1) are shown with different values of $\alpha_{\eta-\gamma}$. The error bars, ±20 %, result from the estimated uncertainties of the surface tension, ±5 %, and viscosity, ±20 %.

or x_{Co} =100 at.-%. For this particular alloy, the temperature range was limited during the measurement leading to an increased error in the activation energy E_A.

On the left hand side, in Fig. 6.4, the values of $\eta_L = \eta(T_L)$ start at ≈2.2 mPa · s, corresponding to pure Sn. With increasing x_{Co}, η_L drops down to ≈1.0 mPa · s for $x_{Co} \leq$ 15 at.-%, until it increases back to ≈2.2 mPa · s for x_{Co} =20 at.-%. For $x_{Co} \geq$ 50 at.-%, η_L increases with x_{Co} up to 5.0 mPa · s. This corresponds to the value of pure Co, if the viscosity of $Co_{80}Sn_{20}$ is not considered in the figure.

In order to calculate η from Eq. (6.1), the Butler-equation, Eq. (4.32), is solved using the data of y_{Co} and y_{Sn} from Refs. [196] and [256], respectively. Phase diagram and Redlich-Kister parameters are taken from Ref. [264], see also Tab. B.9.

Figure 6.4 shows the result of this calculation for two different parameters of $\alpha_{\eta-y}$, 0.82 and 0.6. The measured data of Co-Sn agrees for $x_{Co} \leq$20 at.-% with Eq. (6.1) if $\alpha_{\eta-y} = 0.82$ is used. This agreement, however, is not better than within ± 50 %. In the same concentration range, the solution for $\alpha_{\eta-y} = 0.6$ overestimates η_L by nearly 100 %. For $\alpha_{\eta-y} = 0.6$, η_L is almost constant in the vast concentration range

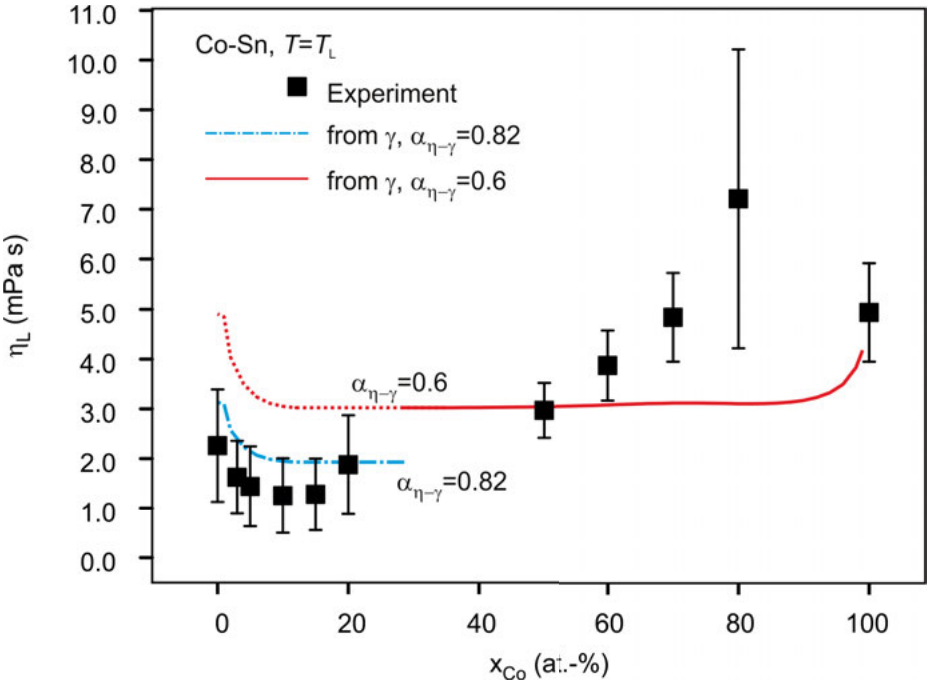

Fig. 6.4. Viscosity η_L of Co-Sn liquid alloys versus x_{Co} (symbols) [256]. For comparison, η_L is calculated from the Butler equation via Eq. (6.1) using $\alpha_{\eta-\gamma} = 0.82$ (dash-dotted) and $\alpha_{\eta-\gamma} = 0.6$ (solid line).

at ≈3.1 mPa · s. Hence, for $x_{Co} > 50$ at.-%, the experimental data is underestimated by more than 20 %.

Averaged over all concentrations, Eq. (6.1) might indeed work for alloy systems, if the parameter $\alpha_{\eta-\gamma}$ is set to 0.6. After all the agreement between experimental data and Eq. (6.1) is not better as compared to the models already discussed in Chap. 5.

6.2 Stokes-Einstein relation

The dynamics in a liquid is governed by two closely related properties: viscosity and atomic diffusion. The viscosity describes the macroscopic transport of momentum. This requires a collective motion of the particles. The atomic diffusion is related to single particle diffusive transport [32].

The atomic diffusion controls processes like nucleation, liquid-liquid phase transitions, crystal growth, and glass formation in an alloy [13; 265; 266]. In order to understand these processes, a precise knowledge of the corresponding diffusion coefficients

is mandatory. In liquid metals and alloys, systematic and reliable information of diffusion data is not available in the majority of cases.

Techniques like, quasi elastic neutron scattering (QNS) provide an option for the measurement of self diffusion coefficients, D_i (i=element). This technique is restricted to alloys containing one component with a dominant incoherent scattering cross section, e.g. Ni, Ti, Co, and Cu [267].

The accurate measurement of diffusion data, using long capillary methods, or alternatively, shear cell methods, is subject to large errors due to the additional transport of mass caused by buoyancy or interface driven flow effects [268; 269]. These techniques have been employed in order to measure the inter diffusion coefficient. The latter can be related to the self diffusion coefficient D_i via the Darken equation. The Darken equation was derived under the assumption that a certain term, called "cross correlation", can be neglected. As shown recently, this assumption leads to an expression which is oversimplified [269]. In addition, the Darken equation is defined solely for binary systems. Contamination of the sample from chemical reactions with the container walls further complicates the measurement.

A common relation, which is often taken for granted in order to calculate diffusion coefficients of atoms in a liquid from the viscosity, or vice versa, is the Stokes-Einstein relation, [25]:

$$\eta D_i = \frac{k_B T}{6\pi r_H}. \tag{6.2}$$

In Eq. (6.2), η is the viscosity, D_i is the self diffusion coefficient of element i, r_H denotes its hydrodynamic radius, T is the absolute temperature and $k_B = 1.38\times10^{-23}$J/K is the Boltzmann constant.

The Stokes-Einstein relation was derived in order to describe the diffusive motion of a mesoscopic particle in a viscous medium [26]. When the diffusing objects are of atomic size, the Stokes-Einstein relation still remains valid in several cases. This has been shown, for instance, for pure liquid metals [266]. Indeed, Eq. (6.2) is a good approximation, at least, on a large scale: For Cu-Ni-P-Pd, [147], Pd self diffusion and viscosity have been measured over a temperature range from 600 K to 1200 K. Both properties vary by 10 orders of magnitude. Equation (6.2) worked within a factor of 2.

The applicability of the Stokes-Einstein relation to liquid metals and alloy systems is well accepted in standard literature [148]. However, there is evidence that D_i and η can significantly deviate from Eq. (6.2): In the case of liquid $Al_{80}Ni_{20}$, molecular dynamics simulations show that Eq. (6.2) is a good approximation when T is large, i.e. $T \geq 1800$ K. Upon lowering the temperature below this limit, the Stokes-Einstein relation becomes increasingly inaccurate [270]. The same is indicated for $ZrCu_2$ [271], Lennard-Jones- [272]–[274], and hard-sphere systems [275], water [276], and silica [277]. For the latter system, η and D even deviate from Eq. (6.2) over the entire investigated temperature range.

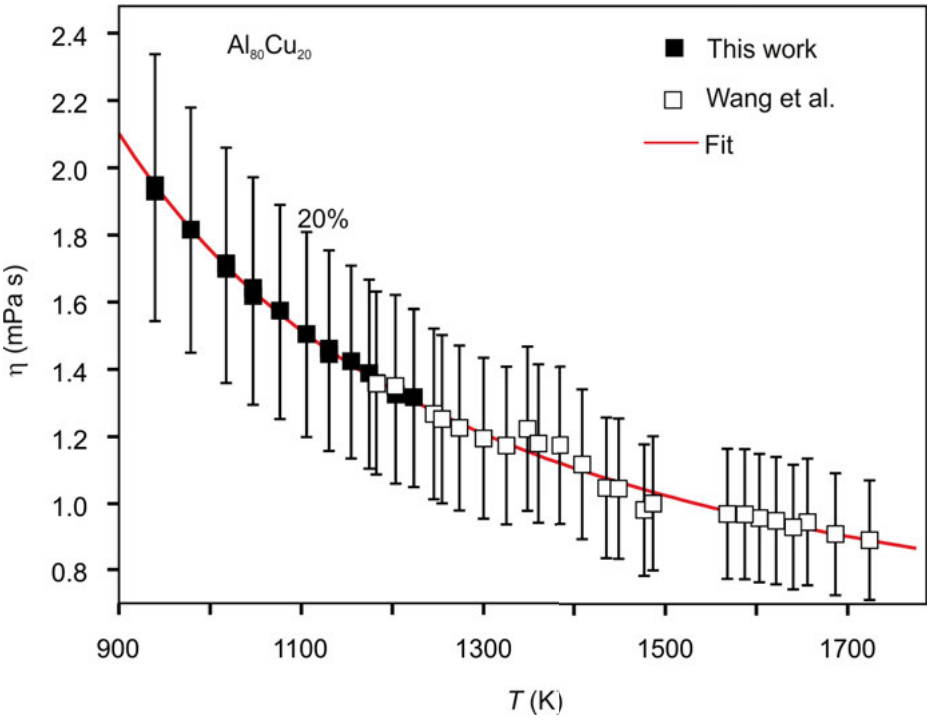

Fig. 6.5. Viscosity of $Al_{80}Cu_{20}$ versus temperature. Shown is data measured using the viscometer "OCN" (solid symbols) and data measured by Wan [279] (hollow symbols). Both data sets can be fitted by the same Arrhenius law (solid line). The uncertainty is estimated as ±20 % [267].

Experimental indications for a deviation from Eq. (6.2) are rare: There is a work from Meyer [278] and there are two publications from Brillo [32; 267] both are discussed below.

6.2.1 $Al_{80}Cu_{20}$

It is the aim of the works presented in Ref. [267] to further investigate the validity of the Stokes-Einstein relation by presenting a comparison of experimental shear viscosity and Cu self diffusion data for an $Al_{80}Cu_{20}$ melt at different temperatures. $Al_{80}Cu_{20}$ is chosen as, due to the incoherent scattering cross section of Cu, it can be investigated using QNS. In addition, $Al_{80}Cu_{20}$ has a low liquidus temperature, T_L =930 K, a low vapor pressure, and with regard to chemical reactivity, it tends to be an inert system. Therefore, container based methods can be employed and the temperatures can be varied over a broad range. Disturbances originating from evaporation of sample material do not occur.

Viscosity data is obtained in the oscillating cup viscometer "OCN" located at NPL, Chap. 5. The uncertainty of the measurement is estimated in Ref. [267] as ±7 %. This is in agreement with the value proposed by Day [280]. It is also in agreement with the error specified for pure Cu in Tab. 5.4 and Fig. 5.4. The latter is ± 10 %. Different, however, from Ref. [267], an uncertainty of ± 20 % is now used. This latter value corresponds to the empirically determined uncertainty of the viscosity of liquid Al, see Tab. 5.2 and Fig. 5.3.

Cu self diffusion coefficients, D_{Cu}, are measured by the co-authors of Ref. [267] in quasi elastic neutron scattering (QNS) experiments. Details of the measurement procedure are described in Refs. [267] and [281]. The uncertainty of the self diffusion data is specified as ± 5 %.

Results of the viscosity measurements are plotted in Fig. 6.5 for $Al_{80}Cu_{20}$ versus temperature, T. They are shown together with data of Wan et al. [279] in order to expand the covered temperature and viscosity ranges. For $T \leq T_L + 600$ K, η embraces values from 1.1 mPa · s to 2.0 mPa · s. In view of the estimated uncertainty of ± 20 %, the agreement between both sets of data is nearly perfect in Fig. 6.5. They can be represented by the same Arrhenius law, Eq. (5.9), with the two parameters $E_A = 1.34{\times}10^4$J/mol[1] and $\eta_\infty = 0.35$ mPa · s.

The self-diffusion coefficients of copper, D_{Cu}, are plotted semi-logarithmically in Fig. 6.6 versus T^{-1}. Values range from D_{Cu} =1.47 (±1.0) × 10^{-8}m^{2}s^{-1} at T =1795 K to 2.4 (±0.2) × 10^{-9}m^{2}s^{-1} at $T = T_L$. These are slightly larger than the Ni self diffusion in $Al_{80}Ni_{20}$ which is $8.74{\times}10^{-9}$m^{2}s^{-1} at T =1795 K [282].

The data in Fig. 6.6 can also be fitted by an Arrhenius law with a thermal activation energy $E_D = -3.28 \times 10^4$J/mol[2] for the Cu self diffusion in $Al_{80}Cu_{20}$. The absolute value is 2.4 times larger than the activation energy for viscous flow, $E_A = 1.34 \times 10^4$J/mol[3], indicating that self diffusion and viscous flow take place on different time scales in this system.

Figure 6.6 also shows self-diffusion coefficients calculated from the experimental viscosity data by the Stokes-Einstein relation, Eq. (6.2). An effective radius of $r_H = r_{Cov} = 1.17$ is used for this calculation which corresponds to the known covalent radius, r_1, of Cu taken from Ref. [146], see Tab. 3.11. At temperatures higher than 1400 K, good agreement between the measured and calculated self diffusion coefficients is evident in Fig. 6.6. At T=1670 K the values of both diffusion coefficients are identical at $1.17{\times}10^{-8}$m^{2}s^{-1}. With respect to the experimental error, the Stokes-Einstein relation is valid at temperatures above 1400 K.

For T < 1400 K, D_{Cu}, calculated via the Stokes-Einstein relation, deviates from the measured ones towards larger values. For instance, at T =1000 K the self dif-

1 0.14 eV

2 -0.34 eV

3 0.14 eV

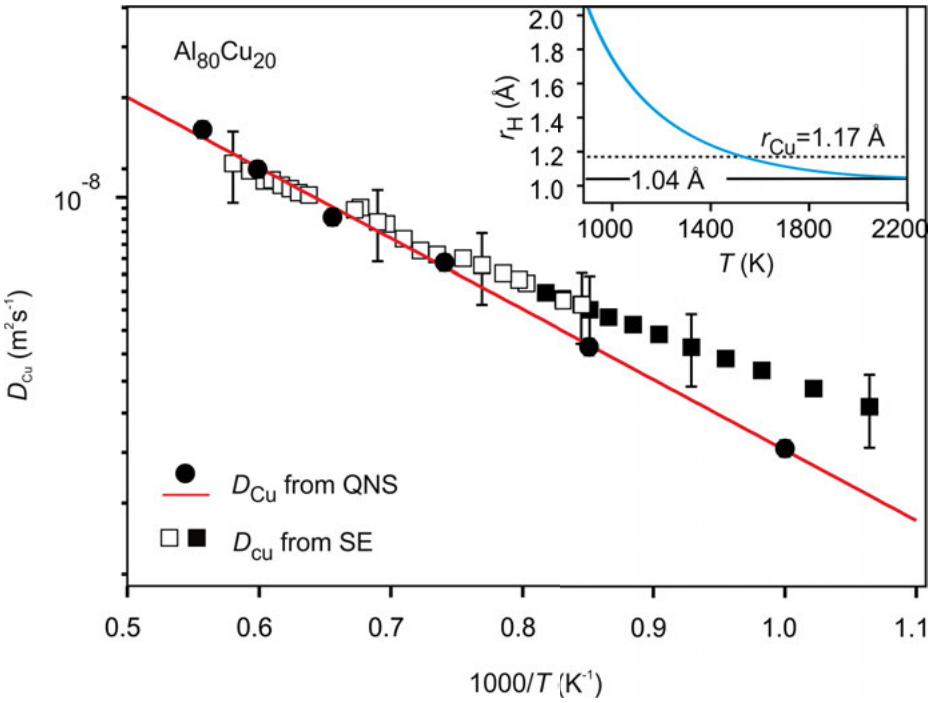

Fig. 6.6. Arrhenius plot of the self-diffusivity D_{Cu} measured by QNS (solid circles) and calculated from Eq. (6.2) (solid squares). The open squares represent D_{Cu} calculated from the data of Ref. [279]. The solid straight line represents an Arrhenius fit to D_{Cu} measured by QNS. The inset shows the effective hydrodynamic radius r_H versus temperature. The covalent radius of Cu is marked by the dotted line. The solid line in the inset marks the limes of r_H for $T \to \infty$ [267].

fusion coefficient equals $2.4\times10^{-9}m^2s^{-1}$ while the Stokes-Einstein relation yields $3.4\times10^{-9}m^2s^{-1}$. This discrepancy is of about 30 %. It becomes increasingly larger when the temperature is lowered.

Due to this deviation, the effective hydrodynamic radius, r_H, deviates in Eq. (6.2) from the covalent radius and becomes temperature dependent. This is shown by the inset in Fig. 6.6, where r_H, calculated from Eq. (6.2), is plotted versus temperature. r_H is hereby calculated using the corresponding fit functions as input to Eq. (6.2). It is seen that, for $T \approx 1500$ K, r_H equals the covalent radius of 1.17 Å. Upon increase of temperature, r_H further decreases and tends towards the constant value of 1.04 Å which is reached at approx. 2000 K. For $T < 1400$ K, r_H diverges with decreasing T. This behavior is clearly no artifact of the use of Arrhenius forms as it is also seen in the plain experimental data.

This investigation of $Al_{80}Cu_{20}$ shows that with respect to the experimental uncertainties, the Stokes-Einstein relation is valid in this system, only above 1400 K. For temperatures lower than 1400 K, the diffusion becomes slower than expected from

the Stokes-Einstein relation. This behavior is atypical. Usually, the opposite is found, namely, that the diffusion becomes faster with a decrease of T [270; 273; 278; 281]. However, as Al-Ni and Al-Cu exhibit otherwise similar properties, no general rule for the direction of this deviation can be given ad hoc. In order to understand this behavior, the role of the Al- self diffusion will need to be clarified in this system.

In the case of $Al_{80}Cu_{20}$ the Stokes-Einstein relation breaks down at temperatures near the melting point. The latter, however, are relevant for processes like nucleation and crystal growth [267].

6.2.2 $Ni_{36}Zr_{64}$

In order to check Eq. (6.2), measurements need to be carried out over a sufficiently large temperature range. Usually, T changes then by a factor of 1.5 - 2, which, in the case of liquid metals, requires high temperatures. Hence, convection and chemical reactivity is favored. The latter is a severe problem, when the sample, as in the case of $Ni_{36}Zr_{64}$, is chemically highly reactive.

The binary alloy $Ni_{36}Zr_{64}$ serves as a model system in order to study a number of phenomena occurring during the glass transition [283]. Precise knowledge of its thermophysical properties of the liquid phase is highly important in this context.

The high reactivity of $Ni_{36}Zr_{64}$, however, rules out most of the classical investigation methods. Correct data can, therefore, only be measured in a contactless way. While it is possible to measure diffusion coefficients in electromagnetic levitation in combination with QNS, the measurement of the viscosity using electromagnetic levitation is not possible under gravity conditions.

Electrostatic levitation (ESL) provides an alternative [19]. Using ESL, quasi elastic neutron scattering (QNS) experiments are carried out by Kordel [54] who determined accurate Ni-self diffusion coefficients in liquid $Ni_{36}Zr_{64}$. This data is measured over a broad temperature range from 1100 K to 1700 K. In addition, density and viscosity data is measured by Brillo [32] over a broad temperature range in which T is varied by a factor of 1.5. Over this range, the viscosity changes by 1.5 orders in magnitude. With these results for a dense glass forming system, the Stokes-Einstein relation can be checked in unequaled detail.

The density of $Ni_{36}Zr_{64}$ follows a linear law with $\rho_L = 6.878(\pm 0.003)\ g \cdot cm^{-3}$ being the density at liquidus temperature, T_L, and $\rho_T = -3.73(\pm 0.01) \times 10^{-4} g \cdot cm^{-3} K^{-1}$ the temperature coefficient. This corresponds to a mean particle density of $\hat{\rho}$=0.052 atoms/Å^3. Using the respective covalent radii of Zr and Ni [146], r_{Zr}=1.45 Å and r_{Ni}=1.15 Å, a value of $\delta = 0.55(\pm 0.002)$ is obtained for the effective volume packing fraction. This value is in agreement with δ from multicomponent bulk glass forming alloys [278]. As for comparison, the packing fraction of liquid Al is ≈0.42, see Tab. 3.11. Hence, $Ni_{36}Zr_{64}$ is a rather densely packed system and glassy behavior should be favored already at temperatures close to the melting point.

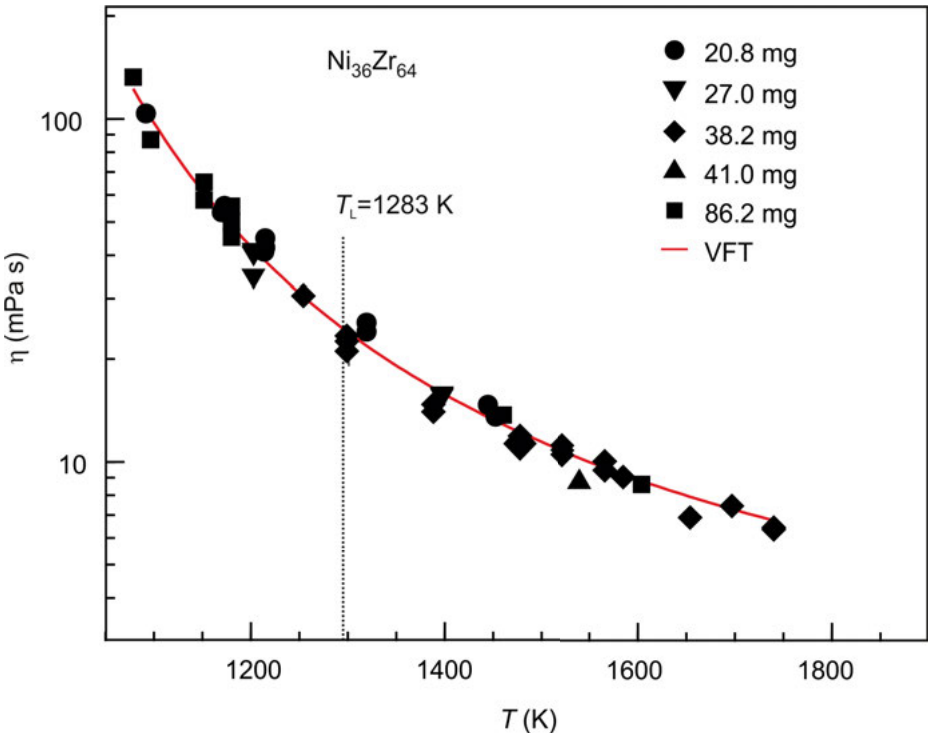

Fig. 6.7. Viscosity of $Ni_{36}Zr_{64}$, measured in ESL, as function of temperature. The solid symbols correspond to data obtained from samples with different masses and the solid line is a corresponding fit of the Vogel-Fulcher-Tammann law, i.e. Eq. (5.10), [32].

Results of the viscosity measurement are shown in Fig. 6.7 as a function of temperature. Values are obtained between 1050 to 1750 K. Large undercoolings of up to 230 K are achieved [32].

Generally, the viscosity increases when the temperature is lowered. At T_L, the viscosity equals η_L =11.5 mPa · s, which is slightly larger than the viscosities of the systems discussed in the previous chapter, see Tab. 5.8. At low temperature, $T \approx$1100 K, η even reaches a value of approximately 130 mPa · s. Again, this is large compared to most non-glass forming metallic alloys. For $T > T_L$, η assumes values between 11.5 mPa · s and 8 mPa · s.

In electrostatic levitation, excitation of flow vortices in the bulk of the droplet might occur when the oscillation amplitude becomes larger than approx. 10 % of the droplet radius at rest [79]. In addition, Ishikawa [284] found that an interference of the surface oscillation with the positioning system takes place under certain conditions. This interference would lead to an exchange of energy between the sample and the generator leading, thus, to an apparently increased or decreased viscosity. If such a non-linear effect existed in the droplet oscillation, using samples with dif-

ferent masses would result in apparently different values of the viscosity [32]. Hence, the experiment in Fig. 6.7 is performed with five different samples having masses of 20.8 mg, 27.0 mg, 38.2 mg, 41.0 mg and 86.2 mg. As shown, however, the same curve, $\eta(T)$, is obtained for each sample mass within the scatter of the viscosity data of ± 5 %, mentioned in Ref. [32]. Thus, systematic errors, due to non-linear droplet oscillations, can be excluded.

The viscosity data in Fig. 6.7 can well be described by the phenomenological Vogel-Fulcher-Tammann (VFT) law, Eq. (5.10), which is typical for many glass-forming systems [266]. The Arrhenius law, used in Chap. 5, is no longer sufficient to represent this data. The parameters obtained from a fit of Eq. (5.10) are $E_A = 1.66 \times 10^4$J/mol[4], T_0 =660.5 K, and $\eta_\infty = 1.1$ mPa · s, see Fig. 6.7.

The Ni self diffusion coefficients, D_{Ni}, are plotted semi-logarithmically in Fig. 6.8 versus the inverse temperature T^{-1} [32; 54]. The uncertainty of D_{Ni} is of the order of ±5 %. Values range from 2.3×10^{-9}m^{2}s^{-1} at $T \approx$1650 K to 2.3×10^{-10}m^{2}s^{-1} at ≈1116 K. At the liquidus temperature, T_L = 1283 K, D_{Ni}=7.8×10^{-10}m^{2}s^{-1}.

The Ni self diffusion data can also be fitted in Fig. 6.8 by a Vogel-Fulcher Tammann (VFT) law, similar to Eq. (5.10). Apart from the scaling factor, absolute values obtained for the activation energy $E_D = -1.60 \times 10^4$J/mol[5] and for the temperature T_0=674 K are identical within error bars with the corresponding values obtained from the viscosity data. Moreover, the activation energies have opposite signs for viscosity and diffusion. This is already different from the case of $Al_{80}Cu_{20}$, Sec. 6.2.1, where the activation energies of the two processes are different.

Obviously, the inverse of the viscosity, η^{-1}, and D_{Ni} are proportional to each other. This is shown in Fig. 6.9 where the measured viscosity data is multiplied by the VFT-fit of D_{Ni}. The product $D_{Ni} \cdot \eta$ equals $1.8(\pm0.25)\times10^{-11}$J/m over the entire temperature range of 1050 K ≤ T ≤ 1750 K.

For comparison, Fig. 6.9 shows the Stokes-Einstein relation with the hydrodynamic radius r_H being set to r_{Ni} =1.15 Å. The experimental data is underestimated by more than a factor of 2 and the temperature dependence is significantly different [32]: While, from experiment $D_{Ni} \cdot \eta = const$ is found, $D_{Ni} \cdot \eta$, calculated from Eq. (6.2) scales with $k_B T$.

The failure of the Stokes-Einstein relation is also visible in Fig. 6.8. In this figure, D_{Ni}, calculated from the viscosity, is also shown. Obviously, the Stokes-Einstein relation, Eq. (6.2) underestimates the measured diffusion coefficients by more than 70 %. The significantly different temperature dependence is already visible by eye [32]. In an attempt to better fit Eq. (6.2) to the experimental data, the hydrodynamic radius, r_H is set to $c_{SE} \cdot r_{Ni}$ with c_{SE} being a coefficient [32]. Using $c_{SE} = 2/3$, Eq. (6.2) transforms into the Sutherland-Einstein relation [285]. In the case of $c_{SE} = 0.467$, Eq. (6.2)

4 0.172 eV

5 -0.166 eV

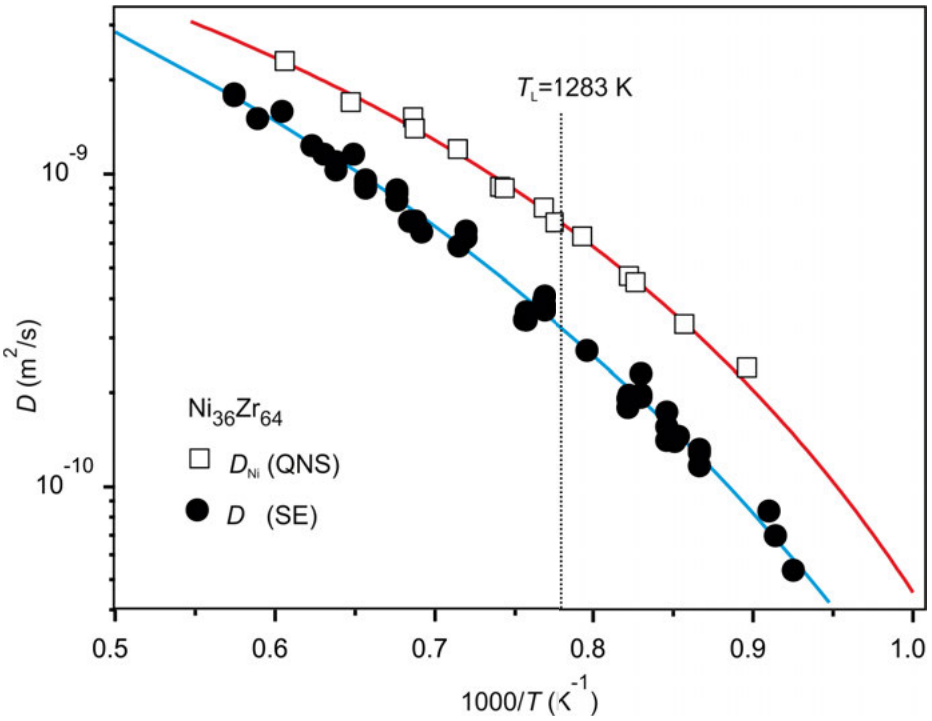

Fig. 6.8. Diffusion constants versus inverse temperature. The circles represent D_{Ni} obtained from η via the Stokes-Einstein relation, Eq. (6.2). The squares correspond to the Ni- self-diffusion constant D_{Ni}, directly measured by QNS. Corresponding fits of the VFT law are shown by solid lines (from Ref. [32]).

is fulfilled in Fig. 6.9, at least at T_L. In this case, $r_H \approx 0.53$ Å, which is non-physically small. Upon decreasing r_H, the product $D_{Ni} \cdot \eta$ can be increased in Fig. 6.9 and, thus, brought closer to the experimental data. However, the agreement of the temperature dependences becomes worse. At this point, it pays off that D_{Ni} and η are measured over a large temperature range.

The only way to resolve the situation, i.e. to "rescue" the Stokes-Einstein relation, is to assume that r_H becomes temperature dependent. In this case, r_H would have to vary by a factor of 1.7 over the investigated temperature range. Obviously, this is unrealistic.

According to Mode-Coupling-Theory (MCT) [247], the dynamics in a liquid is strongly coupled when the particle density is large [32]. Thus, the atomic motion freezes in when T comes close to a critical temperature T_{Fr} upon cooling. In this case, the diffusion coefficient D and the inverse of the viscosity, η^{-1}, become proportional to the same scaling law, Eq. (5.11). Hence, $D \cdot \eta = const$ is asymptotically obtained when $T \rightarrow T_{Fr}$. For $Ni_{36}Zr_{64}$ Voigtmann [283] estimated $T_{Fr} \approx 900$ K. However, the experi-

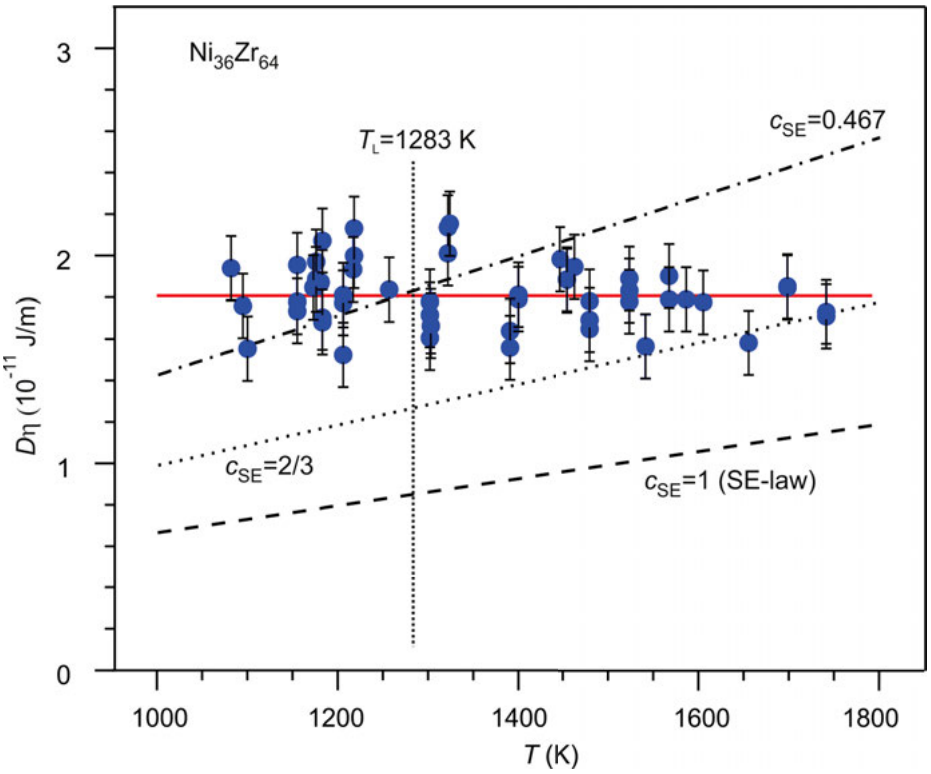

Fig. 6.9. $D \cdot \eta$ versus temperature (symbols). In order to guide the eye, a linear fit to data is also shown (solid line). The dashed and dotted lines correspond to the Stokes-Einstein relation, Eq. (6.2), with different choices of the hydrodynamic radius $r_H = c_{SE} r_{Ni}$. (from Ref. [32]).

mental data on D and η, discussed in the present section, is obtained at temperatures well above T_{Fr} [32].

In conclusion, it is found in the case of $Ni_{36}Zr_{64}$ that $D\eta = const$. This is in agreement with MCT predictions for temperatures close to the temperature of dynamical freezing but contradicts the Stokes-Einstein relation which predicts $D\eta \propto k_B T$.

6.3 Summary and conclusions

In order to elucidate the question whether or not the viscosity can be predicted from ${}^{E}G$ via calculating the surface tension from the Butler equation, Eq. (6.1) is reconfirmed as a valid relation between surface tension and viscosity for pure liquid metallic elements. The parameter $\alpha_{\eta-y}$, hereby, can be set to 0.75 and Eq. (6.1) works within the experimental error of ±20 % for liquid Cu, Ni, Co, and Fe. If Al is included, Eq. (6.1) is valid on an average scale within ±25 % and for $\alpha_{\eta-y} = 0.82$.

Equation (6.1) is also tested for alloy systems. It is found to be valid in the cases of Al-Cu and Cu-Fe-Ni. In both cases, the data can be fitted by Eq. (6.1) yielding a value for $\alpha_{\eta-y}$ of 0.6±0.03. The agreement is within the experimental error of ±20 %. However, it is not possible to predict the viscosity of Co-Sn alloys from solving the Butler equation. Although the results agree on average with the experimentally obtained viscosities, the deviation for each composition between the calculated and experimental value is quite significant. In particular, the agreement is not better than for the models discussed in Chap. 5.

The Stokes-Einstein relation, which relates the viscosity to the self-diffusivity, is shown for liquid alloys to work only as a good approximation. In the case of the less densely packed system $Al_{80}Cu_{20}$, it holds for temperatures larger than 1400 K. For $T \leq 1400$ K D and η deviate from Eq. (6.2), whereas the diffusion becomes slower than expected from the Stokes-Einstein relation. This behavior is atypical and might be explained if the role of the packing density is clarified in this context.

In case of a densely packed system, like $Ni_{36}Zr_{64}$, the Stokes-Einstein is disproved: Instead of $D\eta \propto k_B T$, as predicted from Eq. (6.2), $D \cdot \eta = const$ is found over a broad temperature range. This behavior is predicted from Mode-Coupling theory for temperatures close to the critical point of dynamical freezing. In the case of $Ni_{36}Zr_{64}$, it is observed at already considerably higher temperatures.

These phenomena, which might be coupled to densely packed liquids, are still not fully understood and the subject of ongoing research [22].

7 Application examples

There are multiple overlaps between the broad field of thermophysical property measurement and different, but related, topics. In the present chapter, the aim is to highlight some of these topics using examples of applications to which contributions are made within the present work.

The first of these examples deals with the measurement of solid-liquid interfacial energies[1]. This property and its anisotropy are of tremendous importance for modeling and the understanding of heterogeneous nucleation and crystal growth processes. Within a Ph.-D. thesis solid-liquid boundaries of liquid Al-Cu alloys on differently oriented surfaces of single crystalline sapphire substrates are investigated, see Ref. [286]. Some of these results are outlined in Sec. 7.1.

In the second example, a model for the prediction of liquid-liquid interfacial energies is introduced in Sec. 7.2. In addition to the solid-liquid interfaces, liquid-liquid interfaces play important roles for nucleation and growth processes. Moreover, liquid-liquid interfaces are crucial for liquid phase separation processes. Detailed studies of such processes are performed within a project[2] aiming to also investigate liquid, metastably demixed Co-Cu alloys under microgravity[3].

In Sec. 7.3 of the present chapter it is demonstrated by the example of a magnetic shape memory alloy how the establishment of a comprehensive set of precise thermophysical property data can be used in order to optimize an industrially relevant material.

7.1 Solid-liquid interfacial energy

7.1.1 Liquid metal/sapphire

The kinetics of heterogeneous nucleation and solidification is controlled by processes taking place at the involved solid-liquid interfaces. The respective interfacial energies depend generally on the structure of the solid [287; 288] and its anisotropy.

There is plenty of evidence in literature that this anisotropy also affects the wetting behavior of a liquid single component melt [212; 289; 290; 291]. Among different substrate materials, the effect is greatest for liquid Al on $\alpha - Al_2O_3$ (sapphire) surfaces [291; 292], due to its large surface anisotropy.

---

1 Project in the framework of the priority programme "SPP 1296 - Heterogene Keim- und Mikrostrukturbildung: Schritte zu einem system- und skalenübergreifenden Verständnis" funded by the German Science Foundation (DFG)

2 "Undercooling and Demixing of Copper-Cobalt Alloys - CoolCop", in response to ESA AO -99.

3 Using the EML facility on board the International Space Station ISS. First batch of experiments is scheduled for spring 2015.

Except for the studies carried out in the frame of this work, systematic investigations on this effect are sparse for alloy systems. In the case of Al-Cu, this is indeed surprising as Al-Cu is otherwise an intensively studied system serving as a model for heterogeneous nucleation and crystal growth in binary eutectic alloys [242; 243]. Moreover, Al-Cu is an easy-to-handle system. It has a low melting point and chemically inert substrates, such as $\alpha - Al_2O_3$, are available [286].

Therefore, and in order to contribute to an understanding of the impact of interfacial anisotropies on heterogeneous nucleation, the wetting behavior of Al-Cu alloys, covering the entire composition range, on differently oriented $\alpha - Al_2O_3$ surfaces is studied in detail in a model experiment [293; 294].

In this section, a part of these results, namely the wetting of pure Cu on differently oriented sapphire surfaces, is summarized.

7.1.2 Sessile drop apparatus

In order to study the wetting behavior, contact angle measurements are performed inside a sessile drop chamber, designed and developed by Schmitz [293]. The principal setup is shown schematically in Fig. 7.1. It consists of a stainless steel high vacuum chamber equipped with a drop dispenser and an alumina tube furnace. The tube furnace (diameter = 24 mm, length = 93 mm) is located in the center of the apparatus. Its axis is vertically aligned. Molybdenum wires act as resistive heating elements. The tube has a hole half way along the vertical axis through its walls allowing observation of the sample from the side [286].

Inside the furnace, the substrates are positioned on a boron nitride substrate holder. For position adjustment, it can be moved vertically. A W-5%Re/W-26%Re thermocouple (type C) is placed underneath the substrate supporter in order to determine the temperature.

At the beginning of an experiment, the alloy is contained inside a drop dispenser. The dispenser consists of an alumina tube with a 1 mm nozzle at its bottom and is placed approx. 10 mm above the clean surface of the substrate. As soon as the desired furnace temperature is reached, the liquid alloy is pushed through the nozzle by carefully increasing the gas pressure inside the dispenser.

The sessile droplet is illuminated from one side through the holes in the furnace tube. Shadow graph images are recorded by a camera from the other side, so that the contact angles can be recorded as functions of time.

Further details of the apparatus, as well as of the measurement and image processing procedures, are given in Ref. [293].

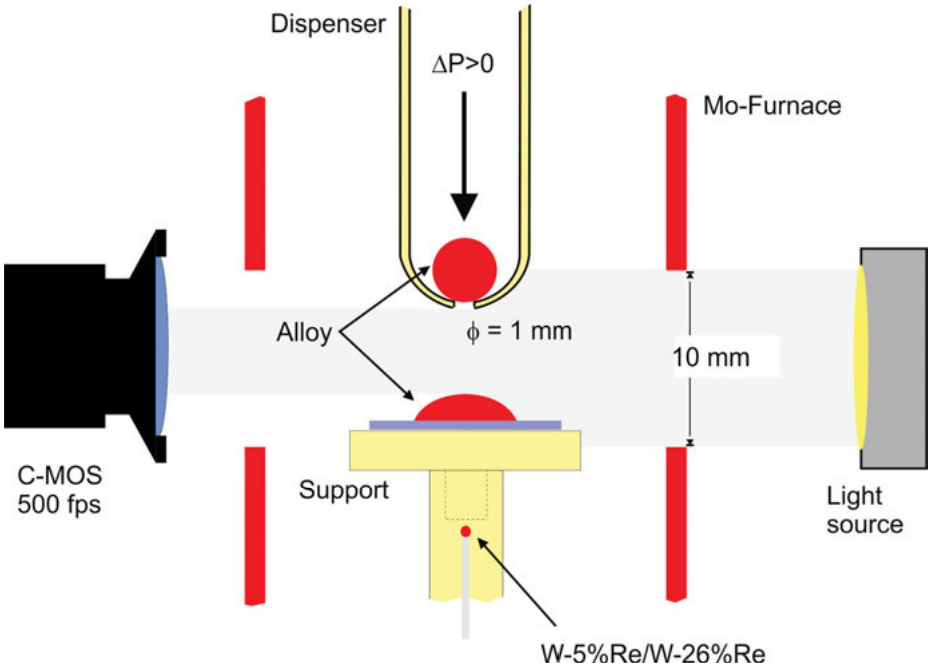

Fig. 7.1. Schematic depiction of the arrangement for contact angle measurements.

7.1.3 Contact angle measurements

A sequence of images, recorded when a droplet is dispensed, is shown in the inset of Fig. 7.2. The typical size of the droplet is 1.5 mm and the temperature in the experiments discussed is ≈1380 K. When the droplet comes out of the nozzle, potentially existing oxide skins are stripped off. After a period of free fall, the droplet touches the surface of the substrate and vibrates strongly [286], so that the contact angle also oscillates around its equilibrium value, Θ_0. This is shown in Fig. 7.2 for the case of the Cu/sapphire-R($1\bar{1}02$) system at 1380 K. After a period of about 1 s, the contact angle becomes constant at $\Theta_0 = 113^\circ$ with respect to a time scale of seconds.

For larger time scales, the contact angle Θ starts to increase slowly. For the first 400 s, the time evolutions of the measured contact angles are shown in Fig. 7.3 for liquid Cu on the C(0001), R($1\bar{1}02$), and A($11\bar{2}0$) surfaces of sapphire [286].

It is found for all substrates that the contact angles increase with time until they become constant after approximately 200 s. This increase is most likely caused by a self purification of the liquid Cu droplets as, under the processing conditions, the equilibrium is shifted towards the reducing regime. This is discussed in detail in Refs. [293]-[295]. The initial values of the contact angles lie between 106° and 113± 5°. For all surfaces, the final contact angle at long times, Θ_∞, is approximately 117±5° [286].

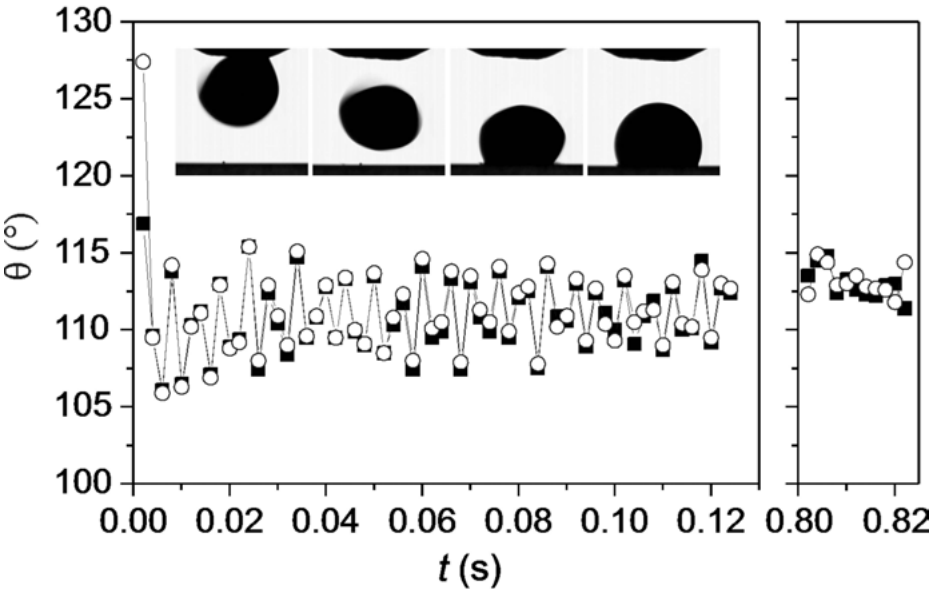

Fig. 7.2. Contact angle, Θ, of liquid Cu on a sapphire R-plane versus time. The diagram is recorded at 1380 K for short times, ≤ 1 s, capturing the moment when the droplet touches the substrate. Solid squares denote contact angles at the left side of the droplet, open circles the ones at the right side. The inset shows a series of frames recorded when the droplet is dispensed: The droplet forms and falls to the surface, touches the substrate and vibrates strongly. After approximately 1 s, it lies stably (last image). From Ref. [286].

This observation is in agreement with recent literature studies [212]. It should be noted that the uncertainty of the data is far less than the 40 % [164] usually encountered in conventional sessile drop experiments.

The evaluation of the measured contact angles can be performed using the Young-equation, provided that the solid substrate is sufficiently stiff and forces vertical to its surface can be neglected [164]:

$$\sigma_{S,L}^{(hklm)} = \sigma_{S,V}^{(hklm)} - y_{Cu}\cos(\Theta) \tag{7.1}$$

In Eq. (7.1), $\sigma_{S,L}^{(hklm)}$ and $\sigma_{S,V}^{(hklm)}$ denote the respective interfacial energies of the solid-liquid and the solid-vacuum interfaces. Their orientation dependence is denoted by the Miller indices, h, k ,l, and m. y_{Cu} is the surface tension of liquid Cu.

The Young equation can be applied in order to calculate $\sigma_{S,L}^{(hklm)}$ when $\sigma_{S,V}^{(hklm)}$, y_{Cu}, and Θ are known. However, the true physics of a solid-liquid interface might be obscured, if $\sigma_{S,V}^{(hklm)}$ depends strongly on ($hklm$). In this case, $\sigma_{S,L}^{(hklm)}$ will do so as well, regardless of the measured contact angles [286]. Moreover, the application of Eq. (7.1) is not always possible due to the limited availability of $\sigma_{S,V}^{(hklm)}$.

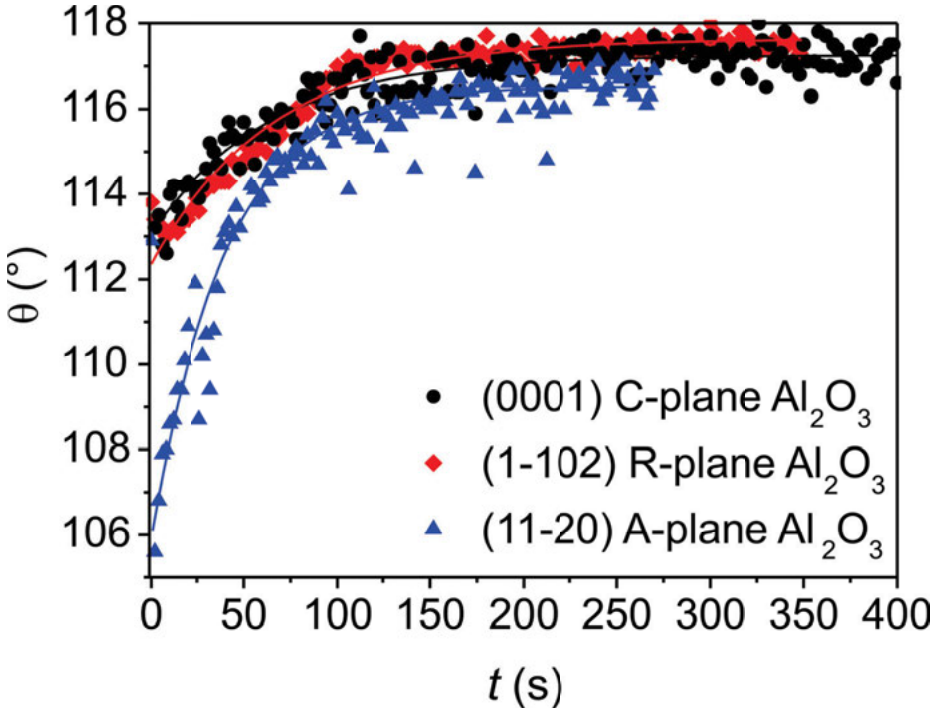

Fig. 7.3. Time evolution of the contact angle, Θ, of liquid Cu on different sapphire surfaces for times greater than 1 s. Measurements are performed at 1380 K on the C(0001)- plane (circles), the A(11$\bar{2}$0)-plane (triangles), and the R(1$\bar{1}$02)-plane (diamonds). From Ref. [286].

This problem can be circumvented by introducing the work of adhesion: $W_{\mathrm{adh}} = \sigma_{\mathrm{S,V}} + y - \sigma_{\mathrm{S,L}}$. It is defined as the energy gain per surface area upon adhesion. W_{adh} is related to the contact angle via the Young-Dupre equation [286]:

$$W_{\mathrm{adh}} = (1 + y_{\mathrm{Cu}}) \cos(\Theta) \tag{7.2}$$

In this equation, the parameter $\sigma_{\mathrm{S,V}}$ does not need to be known.

In order to evaluate Eqs. (7.1) and (7.2), y_{Cu} is taken from Tab. 4.11 and values for $\sigma_{\mathrm{S,V}}$ are taken from Ref. [296]. In this work $\sigma_{\mathrm{S,V}}^{(\mathrm{hklm})}$ is normalized with respect to the value of the C plane. These relative surface energies can be assumed as constant with respect to temperature [286; 295]. The absolute value of $\sigma_{\mathrm{S,V}}^{(0001)}$ of the C-plane is extrapolated to 1380 K using experimentally obtained values reported in Refs. [164; 297].

Table 7.1 lists the measured contact angles, the solid-liquid interfacial energies, obtained from Eq. (7.1) and the works of adhesion, obtained from Eq. (7.2) for the differently oriented sapphire faces. The corresponding uncertainties are estimated to be less than ± 0.1 Jm^{-2} [295].

Since the contact angle Θ_∞ is the same for all three faces, C, A, and R, the work of adhesion, W_{Adh}, is isotropic, see Tab. 7.1. Moreover, $\sigma_{\mathrm{S,L}}^{(\mathrm{hklm})}$ apparently exhibit no

anisotropy within their uncertainties. For a detailed discussion of the error budget, see Refs. [293; 286; 295].

Sessile drop experiments of liquid Cu on sapphire ($\alpha - Al_2O_3$) substrates with C(0001)-, R(1$\bar{1}$02)-, and A(11$\bar{2}$0) orientation confirm the known contact angle of 117°. The solid-liquid interfacial energy, as well as the work of adhesion, do not exhibit any anisotropy within the uncertainties. Hence, in heterogeneous nucleation of liquid Cu, any effect originating from the anisotropy of the solid-liquid interfacial energy should be of subordinate dominance and can be neglected in the first approach [286]. As pointed out in Refs. [293; 294] this situation is completely different for Al/$\alpha - Al_2O_3$ and Al-Cu/$\alpha - Al_2O_3$. In these systems, an anisotropy becomes evident, which is partially due to a reconstruction of the C(0001)-plane that occurs in the presence of adsorbed Al.

Table 7.1. Parameters of the liquid Cu/$\alpha - Al_2O_3$ interfaces at T=1380 K. $\sigma_{S,L}^{(hklm)}$ are determined via Eq. (7.1) using $\sigma_{S,V}^{(0001)}$ from Ref. [297] and relative surface energies normalized to $\sigma_{S,V}^{(0001)}$ from Refs. [164; 297]. The works of adhesions are calculated from Eq. (7.2). Surface tension of Cu at 1380 K: $\gamma_{Cu}(1380K) = 1.30\ Nm^{-1}$, see Tab. 4.11.

	C(0001)	R(1$\bar{1}$02)	A(11$\bar{2}$0)
Θ_0(°)	113 ± 5	112 ± 5	106 ± 5
Θ_∞(°)	117 ± 5	118 ± 5	117 ± 5
$\sigma_{S,L}^{(hklm)}$ (Jm^{-2})	1.72 ± 0.11	1.58 ± 0.12	1.69 ± 0.13
W_{adh} (Jm^{-2})	0.71 ± 0.10	0.69 ± 0.10	0.71 ± 0.10

7.2 Liquid-liquid interfacial energy

Another important parameter in the context of solidification is associated with liquid-liquid interfaces: The liquid-liquid interfacial energy not only limits droplet nucleation during liquid-liquid phase separation, it can also affect crystal growth processes during solidification. For instance, during the growth of a solid phase, the liquid in front of the dendrite may become enriched by one particular component until the solubility limit is exceeded. This process may lead to liquid-liquid phase separation acting as a kinetic barrier. A good overview on these processes is given in Ref. [265]. Contributions on demixing and liquid-liquid interfacial energies are published for the systems Al-Bi, Al-Pb, Al-In, Al-Bi-Si and Co-Cu in Refs. [65] and [298]–[300].

Up to now, there are only a few models for the prediction of the liquid-liquid interfacial energy. One reason for this situation is that its measurement in metallic systems is by no means trivial and, therefore, the amount of experimental data is limited. The most widely used models are the ones proposed by Becker and Landau, [165; 265], Kaban and Merkwitz [165; 298] as well as Antion, Chatain, and Wynblatt [187; 188]. These

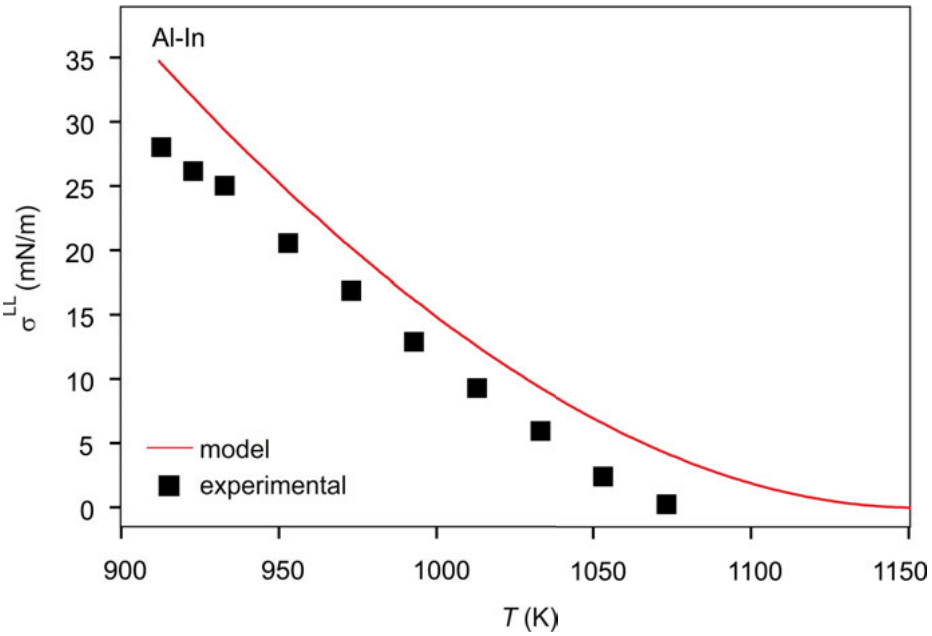

Fig. 7.4. Liquid-liquid interfacial energy σ^{LL} of demixed Al-In versus temperature. The symbols represent the experimental data [298] and the solid line the model [172].

models can be seen as rough estimates [299] with specific advantages and shortcomings [172].

The concept of the Butler equation, on the other hand, provides a recipe for the derivation of an equivalent model for the prediction of liquid-liquid interfacial energies whereas, instead of a single bulk phase, two bulk phases are considered. This approach was first pursued by Kaptay [301]. A more general derivation of such a model is published by Brillo [172].

The derivation is carried out in Ref. [172] in an analogous way to the derivation of Eq. (4.22) and the following similar expression is obtained:

$$\sigma^{LL} = (2u^{LL}{}_i - \mu^{BI}{}_i - \mu^{BII}{}_i)A_i^{-1} \tag{7.3}$$

Here, A_i is the interfacial area, σ^{LL} is the liquid-liquid interfacial energy, and $\mu^{BI}{}_i$ and $\mu^{BII}{}_i$ are the chemical potentials of element i in bulk phase I and bulk phase II, respectively. $u^{LL}{}_i$ is hereby that part of the chemical potential $\mu^{LL}{}_i$ of the interface which does not depend on σ^{LL}. In fact, the chemical potential in the interfacial layer, $\mu^{LL}{}_i$, consists of a part $0.5\sigma^{LL}A_i$ including the interfacial energy, and another one including the rest, i.e. $\mu^{LL}{}_i = u^{LL}{}_i - 0.5\sigma^{LL}A_i$.

This latter condition assures that, in case of thermodynamic equilibrium, the chemical potentials of the three phases can indeed be equal, i.e. $\mu^{LL}{}_i = \mu^{BI}{}_i = \mu^{BII}{}_i$,

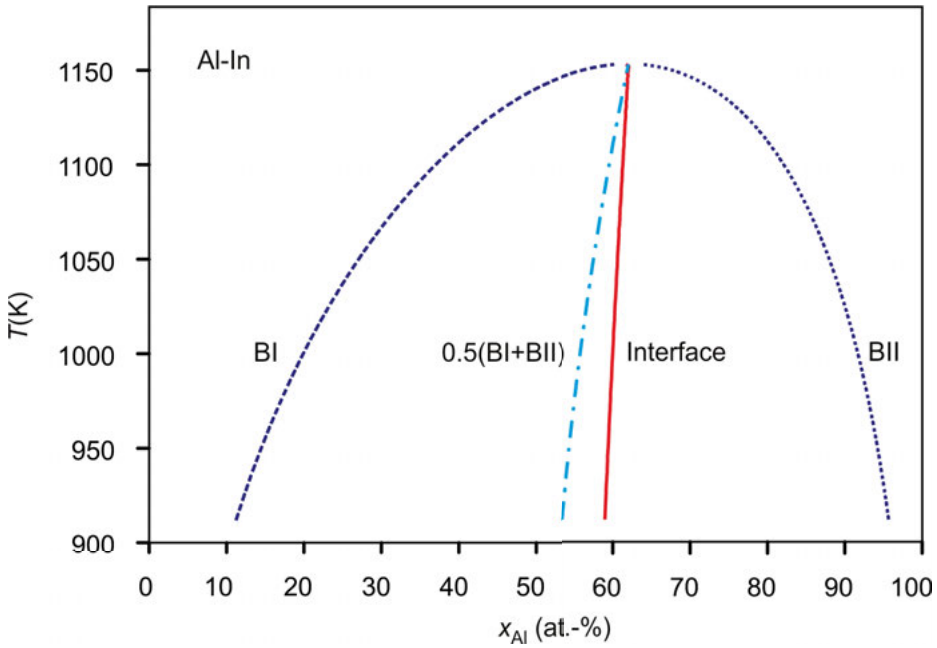

Fig. 7.5. Al- mole fractions of the two bulk phases, BI (dashed) and BII (dotted), as well as of the interface (solid) in demixed Al-In. For comparison, the arithmetic average of the compositions of the two bulk phases is also shown (dash-dotted).

without violating Eq. (7.3) when $\sigma^{LL} \neq 0$ [172]. Moreover, it should be noticed that thermodynamic equilibrium is not explicitly required here.

The factor 2 in front of $u^{LL}{}_i$ assures in Eq. (7.3) that an important condition is fulfilled, namely, that $\sigma^{LL} = 0$ when the compositions of the two bulk phases are equal. In this case, no interface exists [172].

After some transformations and using the fact that the difference of the standard states equals zero, the following, simple expression for the liquid-liquid interfacial energy is obtained, where a_i denotes the activity of each phase:

$$\sigma^{LL} = \frac{RT}{A_i} \ln \left(\frac{a_i^{LL,2}}{a_i^{BI} a_i^{BII}} \right) \tag{7.4}$$

In order to apply this expression, it can be brought into a form similar to Eq. (4.24). The solution procedure is identical to the one described in Chap. 4, except that the factor ξ, accounting in Eq. (4.33) for a difference in coordination number with respect to the bulk and surface phase, can be set to unity. In fact, atoms in a liquid-liquid interfacial layer are coordinated by atoms from the same layer and, in addition, by atoms in the two bulk phases. Consequently, the total coordination number of an atom in the liquid-liquid interface is not much different from an atom in the bulk [172].

The model is tested in Ref. [172] on the examples of the binary systems Al-Pb, Al-In, Al-Bi and Cu-Co. For these systems, experimental data is published in Refs. [65; 298; 299]. For the sake of brevity, the model is demonstrated in the present section by the example of Al-In, only.

Redlich-Kister parameters of Al-In, needed in order to solve Eq. (7.4), are taken from Ref. [302], see Tab. B.7. Using this thermodynamic assessment, the binodal line, i.e. the temperature dependent aluminium mole fractions of the two bulk phases, $x_{\mathrm{Al}}^{\mathrm{BI}}$ and $x_{\mathrm{Al}}^{\mathrm{BII}}$, are calculated by Schmid-Fetzer in Ref. [172] using the software package PANDAT$^{\mathrm{TM}}$.

The result of the model calculation, i.e. the liquid-liquid interfacial energy of Al-In as function of temperature, is shown in Fig. 7.4 together with the experimental data from Ref. [298].

For Al-In, the critical temperature of demixing is $T_{\mathrm{C}} \approx 1150$ K [303]. Experimental data is available for 900 K $\leq T \leq$ 1070 K. Over the investigated temperature range σ^{LL} varies from 28 mNm^{-1} at 900 K to $\approx$ 0 mNm^{-1} at 1070 K. Although the model, Eq. (7.4), overestimates the experimental data slightly by $\approx$5 mNm^{-1}, it correctly reproduces the temperature dependence (slope). In addition, it is correctly reproduced that, with increasing temperature, the calculated interfacial energies asymptotically approach zero and that the curve exhibits a concave shape [172]. Hence, the overall agreement between model and experimental data is very good for this particular system.

Figure 7.5 shows a plot of the temperature versus the mole fraction of Al in the two bulk phases, $x_{\mathrm{Al}}^{\mathrm{BI}}$ and $x_{\mathrm{Al}}^{\mathrm{BII}}$ and in the interface, $x_{\mathrm{Al}}^{\mathrm{LL}}$. $x_{\mathrm{Al}}^{\mathrm{LL}}$ hereby depends only weakly on temperature. It changes steadily from 62 to 59 at.-% with a decrease of T from 1150 K to 900 K. The values of $x_{\mathrm{Al}}^{\mathrm{LL}}$, obtained from solving Eq. (7.4), are very close in Fig. 7.5 to the arithmetic average of the Al mole fractions in the bulk phases which varies from 62 at.-% at 1050 K to 52 at.-% 900 K. This behavior is observed in all three systems discussed in Ref. [172].

A good agreement between model and experimental data is also observed for the system Al-Pb [172]. In the case of the third system, Al-Bi, different results are obtained, depending of the thermodynamic assessment used. Using, for instance, the assessment of Mirkovic [304], the experimental data of Al-Bi is underestimated by a constant factor of 1.5. When, on the other hand, the assessment of Kim [302] is applied, the experimental data is overestimated by up to a factor of 1.7. This shows, that even small differences in the used thermodynamic assessment can have a large effect on the prediction of the interfacial energy. The quality of model developed in Ref. [172], hence, critically depends on the thermodynamic assessment, i.e. parameters for ${}^{\mathrm{E}}G$ used as input.

7.3 Shape memory alloys

It is the goal of the activities described in this section to develop and construct energy efficient actuators, based on magnetic shape memory alloys, for automotive applications.

The energy efficiency of motorized vehicles is mainly determined by the transformation of energy from fossil fuels into motion. Roughly 15 % of engine power is consumed by secondary aggregates, electronic devices etc. [305]. In many of these systems, electromagnetic actuators, of which a typical car can have more than 60, play crucial roles [306]. Hence, they substantially contribute to the energy consumption of a vehicle.

Thus, requirements for an increased energy efficiency and CO_2 reduction currently also[4] drive the development of new actuator technologies. For instance, the Piezo-Common-Rail-system developed by Siemens leads to a reduction of energy consumption by approx. 30 %, whereas it is claimed that the CO_2 emission can be reduced by this technique by roughly 25 % [307].

Obviously, new materials play a key role in the development of new actuator concepts in this, entirely new, socially and technically relevant, field. Beside piezo electric materials, magnetic shape memory alloys (FSMA) seem to be very promising and exhibit the highest potential for applications as actuators. One aim of the BMBF-funded project EFAM[5] is to identify, produce and optimize a material that can be used for such an actuator.

Magnetic shape memory alloys (MSMA) made from Ga-Mn-Ni display the largest shape changes, with magnetic field induced strains (MFIS) reaching 10 %. MSMA showing high MFIS over a wide temperature range and fast frequency response make these alloys attractive for actuator and sensor applications. In addition, the MFIS in single crystalline specimens is reported to be higher than in the corresponding polycrystalline material. Oriented single crystals of Ga-Mn-Ni based alloys can be obtained on a lab scale using Zone melting or Bridgman techniques. The upscaling from laboratory scale to industrial scale with larger amounts of single crystals, however, is still a challenging task. Thus, when optimizing the single crystal growth in terms of crystal quality and size, process simulation tools can be applied to support the development [308].

These process simulation tools require thermophysical properties of the molten and solid material as input parameters. Within the present work these properties are precisely determined and they are used in order to simulate the distribution of the thermal field within the sample and the furnace.

---

4 As specified in Chap. 1 requirements for an increased energy efficiency and CO_2 reduction also drive the development of new technologies for casting processes.

5 "Energieeffiziente Formgedächtnislegierungen für Automobilanwendungen - EFAM (2009–2012)"

Table 7.2. Parameters determined within the EFAM project: EML=electromagnetic levitation, DTA/DSC=differential thermo-analysis/differential scanning calorimetry, LFA=laser flash analysis, SSCCM=steady state concentric cylinder method, TGA=thermal gravimetry, OQB=oscillating quartz balance, HOC=high temperature oscillating cup viscometry.

Parameter	Method	Phase(s)
Density	EML	Liquid
Transition temperature(s)	DTA/DSC	Solid/Liquid
Transition heats	DSC	Solid/Liquid
Specific heat	DSC	Solid
Thermal diffusion	LFA	Solid
Thermal conductivity	DSC/LFA/SSCCM	Solid
	SSCCM	Liquid
Rate of evaporation	TGA/OQB	Liquid/Solid
Viscosity	HOC	Liquid
fraction solid		

Properties which are relevant in this context are listed in Tab. 7.2. These are: density, transition temperatures and corresponding heats, fraction solid, specific heat, thermal diffusion, thermal conductivity, viscosity and rate of evaporation.

The applicability of such process simulation tools on the example of a specific Ga-Mn-Ni alloy is demonstrated in Ref. [308]. In that work, thermophysical properties are determined for a $Ga_{25}Mn_{25}Ni_{50}$ magnetic shape memory alloy with the concentrations known within ±2 at.-%. In a second step, global thermal simulations without melt flow effects are carried out in a Bridgman-Stockbarger type lab furnace. These simulations, carried out by Behnken [308], allow to vary relevant process parameters like sample geometry, heater temperatures and withdrawal rates in the Bridgman-type crystal growth. Finally, the simulations are compared in Ref. [308] with benchmark experiments, carried out by Drevermann, in order to verify the predictive power of the method.

7.3.1 Methods

Details of the sample preparation are described in Ref. [308]. Density data ρ of the liquid phase is measured in electromagnetic levitation. Data for solidus and liquidus temperatures T_S, T_L, latent heat H_f, fraction solid $f_S(T)$ and specific heat $c_P(T)$ is obtained from differential scanning calorimetry (DSC) measurements. The principle of this technique is described in a number of standard textbooks, e.g. Refs. [309; 310]. The device used in Ref. [308] is a Netzsch Pegasus 404 C heat flow calorimeter which can achieve a maximum temperature of 2023 K. The furnace was heated or cooled linearly with a rate, β. When a phase transition occurs, the heat exchange manifests itself as a peak in the temperature difference ΔT and the heat flow Φ. Upon melting, the fur-

nace temperature at the onset of this peak is identical with the solidus temperature T_S. The liquidus temperature T_L is determined from linearly extrapolating the temperature of the peak maximum T_{max} to zero heating rate. For this purpose measurements with different heating rates are performed in Ref. [308].

The latent heat H_f is obtained from integrating the area under the peak taking into account a sigmoidal baseline correction $\Phi_{BSL}(T_F)$ with furnace temperature T_F.

The fraction solid, f_S, is determined from the ratio of the partial peak area to H_f as described in more detail in Refs. [308; 311]. Finally, the specific heat $c_P(T)$ is determined from an additional measurement on a sapphire reference sample.

Thermal diffusivity α_T is measured using the laser flash technique [312; 313]. Short IR laser pulses of 20 J with wavelengths of 1064 nm and durations of each pulse between 0.3 and 1.2 ms hit a flat thin sample at one side. The increase of the temperature response is monitored by a detector on the adjacent side. From the half time of the signal increase and the thickness of the sample the thermal diffusivity is calculated, see Ref. [308]. The sample is solid during the entire experiment.

Knowing α_T, c_P and the density ρ, the thermal conductivity λ can be obtained from the well-known relation:

$$\lambda = \rho c_P \alpha_T \tag{7.5}$$

For liquid materials, the steady state concentric cylinder method (SSCC) [314] is used in Ref. [308] as a complementary approach in order to determine λ directly. These measurements are carried out by Sklyarchuk and Plevachuk [308]. The apparatus consists of two coaxial BN-cylinders separated by a small gap. A radial temperature gradient is produced between the two cylinders and in the solid or liquid sample material. The power ΔP needed to maintain this gradient is measured so that the thermal conductivity can be calculated from the known formula for a cylindrical layer [308].

A detailed description of the experimental setup, the corrections which need to be included, as well as a detailed analysis of the experimental error is given in Ref. [314]. The total error for thermal conductivity measurements is about 7 %.

For the solidification benchmark experiment a cylindrical rod diameter of 10 mm and length 153 mm is prepared from the polycrystalline master alloy material [308]. Six contained thermocouples are placed along the center axis inside the sample at different fixed positions z=25.2 mm, 51 mm, 75.2 mm, 96 mm, 114 mm and 135 mm, relative to the bottom. The sample rod with the thermocouples is then surrounded by a protection tube made from alumina. This tube has an inner diameter of 10 mm and a length of 200 mm so that the sample fits inside. Both, sample and tube, are fixed in the furnace. The setup of the latter is shown schematically in Fig. 7.6.

For an experiment, the temperature is set to 1790 K. This is well above the liquidus temperature of the sample. For the LMC-cooling a Ga-In bath at 300 K is used [308]. The sample is molten directionally by translation from the cold into the hot zone [308]. When the upper 85 % of the sample are molten, a dwelling time of 10 min is inserted in order to allow for thermal equilibration [308]. After this step, solidification is ini-

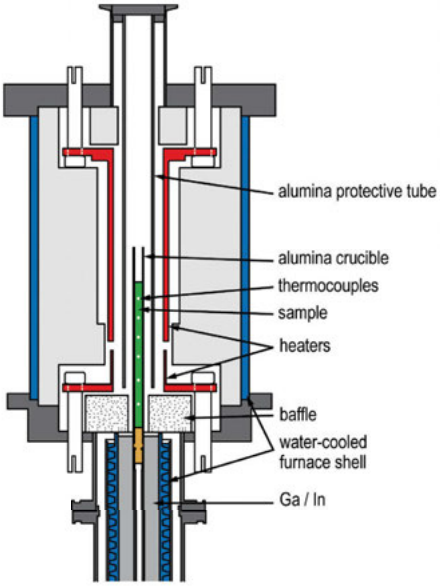

Fig. 7.6. Schematic drawing of the LMC lab-furnace. The marked positions of the thermocouples are at $z = 25.2$ mm, 51 mm, 75.2 mm, 96 mm, 114 mm and 135 mm, relative to the bottom of the rod (from Ref. [308]).

tiated by cooling the heaters with a constant rate of 50 K/min. During this process a solidification front starts moving upwards from within the baffle into the heater zone [308]. The uppermost part of the sample crystallizes simultaneously within a few seconds. At all phases of the experiment, temperatures are measured at the positions of the thermocouples and recorded [308].

For the purpose of thermal simulations a detailed finite-elements (FE-) model of the lab furnace is developed in Ref. [308]. The simulations are performed with the program package StarCAST^{TM} [8].

In the FE- model, the assembly is reduced to the main and relevant components of the furnace [308]. The actual heat transfer from the inner tube to the thermocouples in its center is a mixture of heat conduction and radiation effects, depending on the local contacts of the thermocouples and the wall of the protection tube [308]. The model does not consider the thermocouples explicitly but their inner volume is defined as isolation material [308].

While the sample and its protecting tube are fixed in space, furnace and metal bath are connected and can be moved up and down for directional solidification and melting, respectively [308].

The simulation takes into account the heat conduction within the components, the heat transfer between components directly in contact with each other, the heat

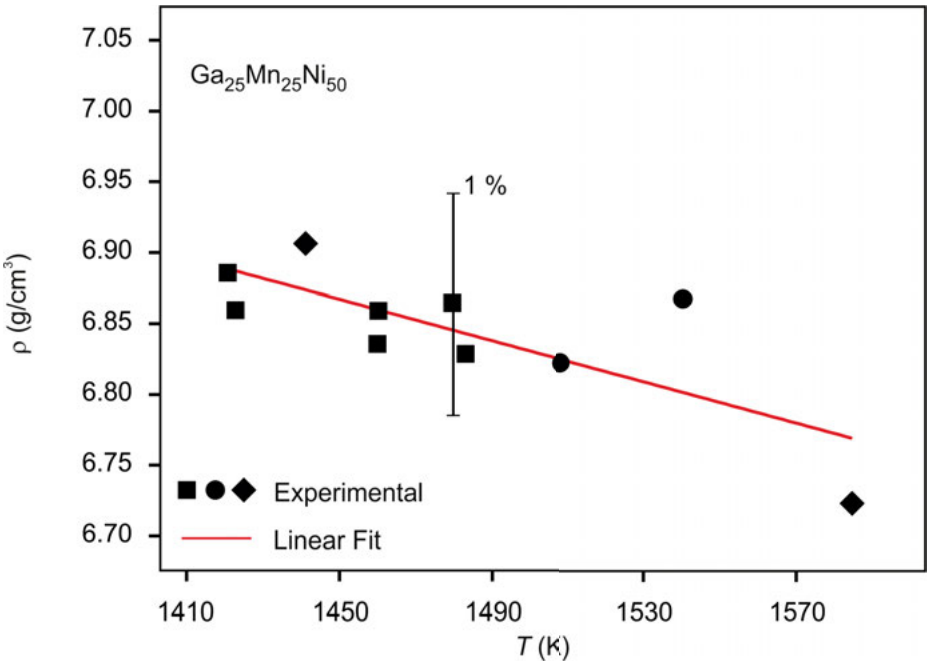

Fig. 7.7. Density of the liquid sample versus temperature. The different symbols correspond to individual experimental runs with different samples. The solid line is the common linear fit. The absolute error of 1.0 % is shown for the example of one data point by the error bar (from Ref. [308]).

radiation between all free surfaces, the latent heat of the solidifying material, and the liquid metal cooling below the baffle [308]. Free element surfaces take part in the heat exchange by radiation. This is simulated in Ref. [308] by using the net-radiation method [315].

7.3.2 Results and conclusion

Density is measured in electromagnetic levitation. Although the samples levitate stably, pronounced mass loss due to evaporation of Mn and Ga is critical. In order to keep the uncertainty caused by the mass loss sufficiently low, measurements at different temperatures are carried out in separate levitation experiments [308]. Figure 7.7 shows the density data obtained this way. It is plotted versus temperature T. Different symbols, hereby, correspond to different experimental runs, each with an individually prepared sample. The scatter of the data is approximately ±0.7 %. This is less than the error of ±1.0 % estimated in Chap. 2.

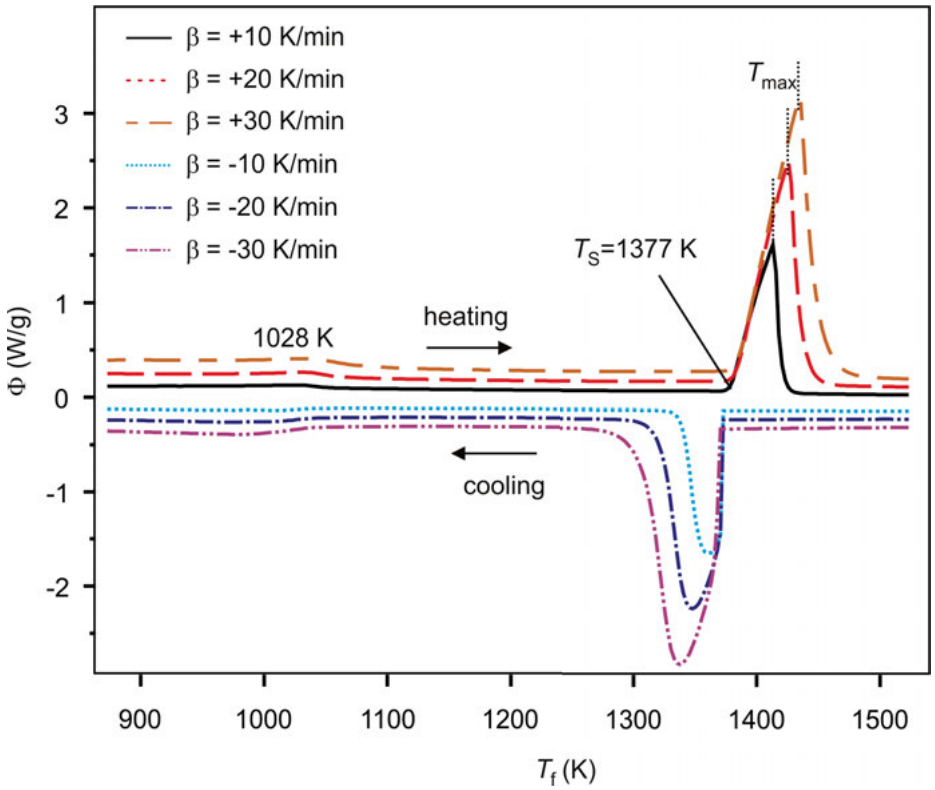

Fig. 7.8. DSC curves for heating and cooling. The used temperature rates, β are ±10 K/min, ±20 K/min, and ±30 K/min. The onsets of the melting peaks collapse onto the solidus temperature T_S. The peak maxima, T_{max}, are marked by dotted vertical lines. The small feature visible around 1028 K in the heating curves and around 970 K in the cooling curves corresponds to the λ-transition (from Ref. [308]).

Between 1410 K and 1570 K, the density decreases linearly from $6.9\,\mathrm{g\cdot cm^{-3}}$ to $6.7\,\mathrm{g\cdot cm^{-3}}$. Fitting Eq. (3.9) yields ρ_L=$6.90\,\mathrm{g\cdot cm^{-3}}$, as the density at T_L = 1405 K, and the temperature coefficient equals ρ_T= $7.3\times10^{-4}\mathrm{g\cdot cm^{-3}K^{-1}}$.

For three different samples, DSC curves are recorded by heating and cooling with rates of β = ±10 K/min, ±20 K/min, and ±30 K/min [308]. The results of such runs are shown in Fig. 7.8. This figure displays the heat flow, Φ, as function of temperature for one specific sample. The maximum temperature is 1573 K.

Two remarkable features are visible in Fig. 7.8: a small peak at ≈ 1028 K in the heating curves and around ≈ 970 K in the cooling curves, as well as a dominant peak between 1370 K and 1570 K in the heating; and between 1270 K and 1370 K in the cooling curves. The feature around 1028 K is caused by a second order phase transition [308]. Due to the shape of the peak, this is usually called a "λ-transition" [310]. At this temperature, such a transition is also found in Mn-Ni binary alloys, where it corresponds

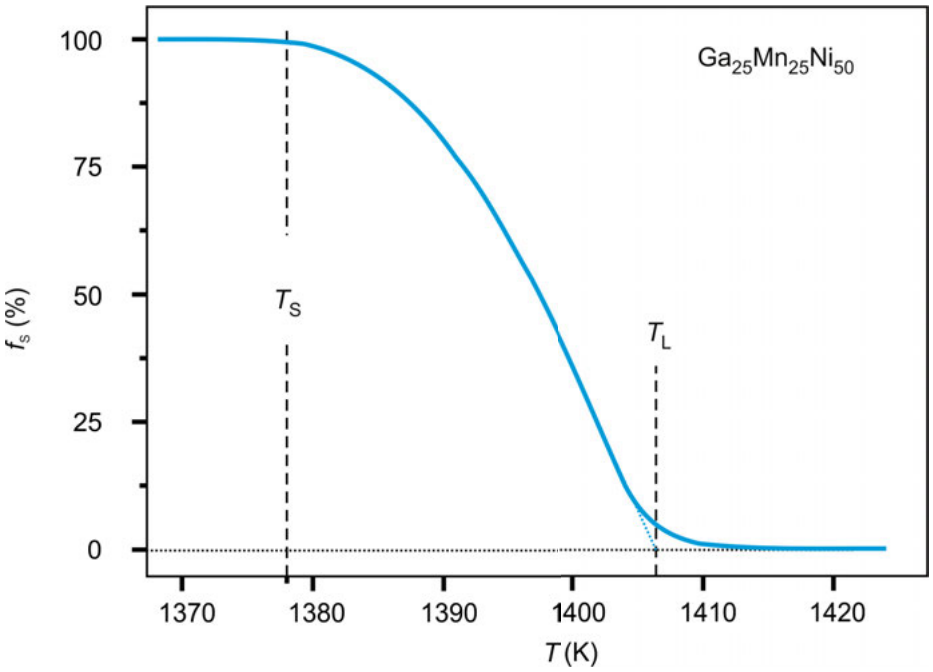

Fig. 7.9. Fraction solid versus temperature calculated from the DSC signal (from Ref. [308]).

to a reordering of atoms [310]. The large peak in the heating curves corresponds to the melting of the alloy. The solidus temperature, T_S, is identified with the onset of the peak. It does not vary with the β. T_S is determined as $T_S = 1377(\pm 1)$ K. Extrapolating the β-dependent temperatures of the peak maxima, T_{max}, to β=0 yields the liquidus temperature as $T_L = 1405(\pm 1)$ K. Finally, the heat of fusion is obtained as H_f= 223 (±15) Jg^{-1}.

The fraction of solid material during melting, $f_S(T)$, is determined from the heating curve for $\beta = 10$ K/min. It is plotted in Fig. 7.9 versus the sample temperature, T. Below T_L, the displayed curve has qualitatively the expected shape: f_S is equal to 100 % for $T < T_S$ and decreases monotonically for $T_S < T < T_L$ [308]. Close to the liquidus temperature, however, the curve gets a concave shape and approximates the horizontal axis when $T > T_L$. Moreover, $f_S \neq 0$ at $T = T_L$. This behavior is a known artifact as under the dynamic conditions in DSC experiments, thermodynamic equilibrium is only approximated [308].

Figure 7.10 shows a curve of c_P, recorded with a heating rate of $\beta = 10$ K/min. It is plotted versus the furnace temperature T_F [308]. The temperature ranges from 500 K and 1370 K which corresponds to the regime where the sample is solid. The curve exhibits a maximum at 1033 K. On the left side of this maximum, between roughly 650 K and 800 K, c_P increases linearly with increasing temperature from ≈ 0.45 $Jg^{-1}K^{-1}$ at

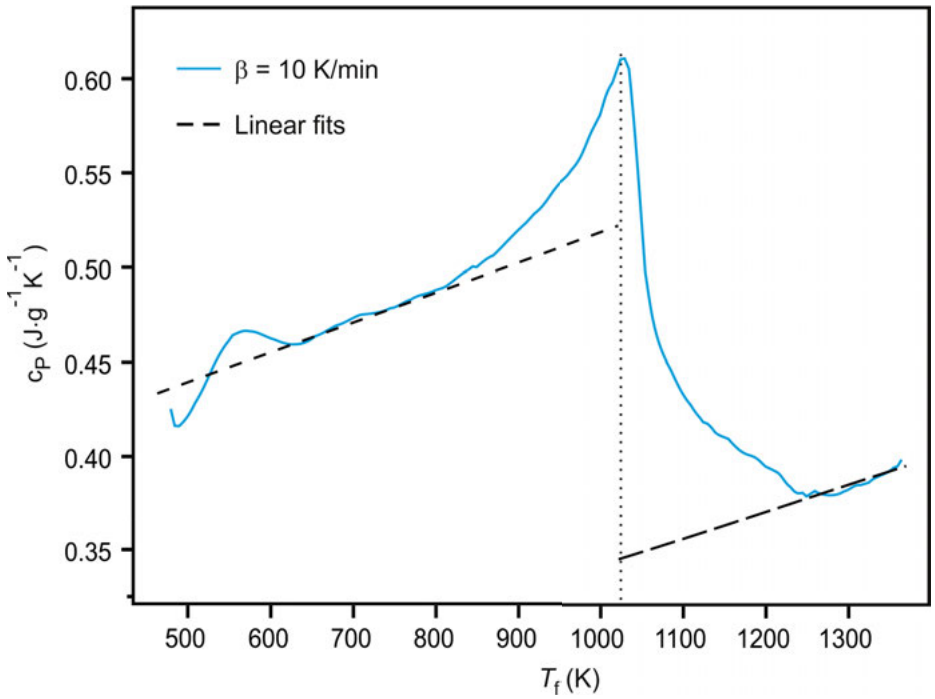

Fig. 7.10. Effective specific heat of the solid sample c_P versus temperature for a heating rate of 10 K/min (solid line). In order to eliminate the distorting effect of the λ-transition, c_P is linearly extrapolated in the region under the peak (dashed lines). From Ref. [308].

650 K to approximately 0.47 $Jg^{-1}K^{-1}$ at 800 K. On the right side of the maximum and above 1253 K, c_P also increases linearly with temperature from 0.37 $Jg^{-1}K^{-1}$ to 0.4 $Jg^{-1}K^{-1}$ at 1400 K. The maximum corresponds to the λ-transition. It is visible in Fig. 7.10 as a peak with an asymmetric shape between approximately 770 K and 1253 K. The system is not a single phase system and the measured curve of c_P must be regarded as an "effective" specific heat. In order to obtain information about c_P in the region under the peak it is extrapolated linearly from both sides in Fig. 7.10 to the phase transition temperature of 1028 K. The following curves are obtained with a precision of approximately ± 10 % [308]:

$$c_P/[\,Jg^{-1}K^{-1}] = 0.38 + 7.5 \times 10^{-5} T \vee 500K < T < 1028K \tag{7.6}$$

$$c_P/[\,Jg^{-1}K^{-1}] = 0.4 + 4.0 \times 10^{-5} T \vee 1028K < T < 1400K \tag{7.7}$$

Thermal diffusivities, $\alpha_T(T)$, obtained by laser flash analysis, are plotted versus temperature in Fig. 7.11. Data is measured for 300 K < T < 1300 K. In this range $T < T_L$ and, therefore, the $Ga_{25}Mn_{25}Ni_{50}$ sample is solid. For T < 700 K, there is nearly a linear increase of α_T with temperature from ≈ 4.5 mm^2s^{-1} at 300 K to 6.0 mm^2s^{-1} at

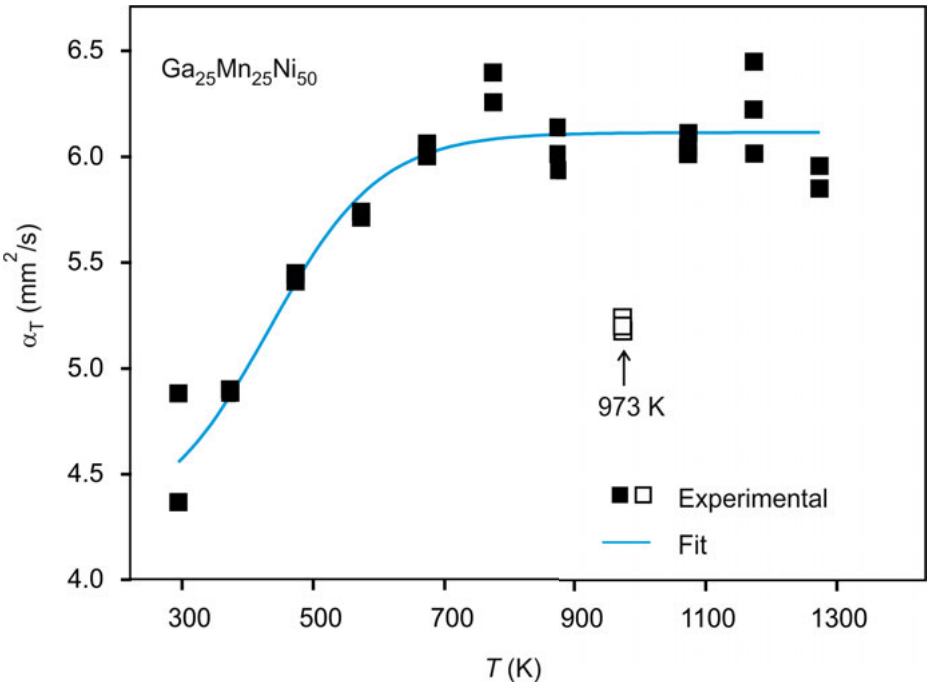

Fig. 7.11. Thermal diffusivity versus temperature. Data of the solid sample (symbols) is obtained using the laser flash method. The line is a fit of Eq. (7.8). The hollow symbols correspond to the data at 970 K. They are not included into the fit (from Ref. [308]).

$T \approx 700$ K. For temperatures above 700 K, the thermal diffusivities become constant at this value (6.0 mm^{2}s^{-1}) with the exception of a minimum indicated in Fig. 7.11 by the data points at 973 K, where $\alpha_T \approx 5.0$ mm^{2}s^{-1}. This minimum is due to an artifact which is related to the phase transition observed in the DSC curves at 1028 K. The laser-flash method can be misleading in temperature ranges where phase transitions occur. The laser energy rises the temperature inside the sample and drives the phase transformation already at lower temperatures [308]. This process consumes a part of the laser energy so that the values of the thermal diffusivity appear to be reduced. The minimum is, therefore, not included when the experimental data is fitted by the following empirical equation (solid line in Fig. 7.11) [308]:

$$\alpha_T = \alpha_{T,max} + \frac{\alpha_{T,min} - \alpha_{T,max}}{1 + \exp\left((T - T_0)/\Delta T\right)} \tag{7.8}$$

In this equation, $\alpha_{T,min}$, $\alpha_{T,max}$, T_0, and ΔT are fit parameters. $\alpha_{T,min}$ and $\alpha_{T,max}$ respectively denote the minimum and maximum value of the thermal diffusivity. T_0 and ΔT specify the shape of the slope. Fitting Eq. (7.8) yields the following values for the adjustable parameters: $\alpha_{T,max} = 6.11$ mm^{2}s^{-1}, $\alpha_{T,min} = 4.26$ mm^{2}s^{-1}, $T_0 = 432.64$ K,

and ΔT = 84.06 K. Obviously, a very good agreement with the experimental data is obtained within an uncertainty of ± 10 % [308].

The thermal conductivity λ is obtained from the product of thermal diffusivity, density and specific heat, using Eq. (7.5). Values of c_P are taken from Eqs. (7.6) and 7.7 for the respective temperature ranges. α_T, finally, is obtained from Eq. (7.8). Data for the density is not available for the solid phase and λ can, hence, only be estimated for the solid sample. For this purpose, the temperature dependent density of the solid sample is calculated from the densities of the solid elements [17; 316; 317] assuming that the excess volume is zero and neglecting possibly existing density differences between coexisting solid phases [308]. This procedure is justified as, in the vast majority of alloys, the excess volume is typically more than one order of magnitude smaller in the solid compared to the liquid state.

Figure 7.12 shows the thermal conductivity λ obtained in this way as a function of temperature. Between 470 K and 1028 K, λ increases moderately with temperature from roughly 17 W(mK)$^{-1}$ to slightly more than 22 W(mK)$^{-1}$. At 1028 K λ suddenly drops to ≈ 15 W(mK)$^{-1}$ due to the phase transition taking place at this temperature. Above 1028 K λ increases linearly with temperature and finally reaches a value of 16 W(mK)$^{-1}$ at $T = T_L$, see Fig. 7.12.

Using the steady state concentric cylinder method (SSCC), λ is measured directly for temperatures above 1270 K. The results are shown by the symbols in Fig. 7.12 [308]. Between approx. 1270 K and the liquidus temperature T_L, the thermal conductivity of the solid phase λ_S can be described by a linear function of temperature with a positive temperature coefficient [308]:

$$\lambda_S = 11.2 + 4 \times 10^{-3} T[\,\mathrm{W(mK)^{-1}}] \tag{7.9}$$

As visible from Fig. 7.12, the thermal conductivities directly measured by the steady state concentric cylinder method are in excellent agreement with the results obtained from Eq. (7.5) using the the laser flash and DSC measurements.

At the liquidus temperature T_L, the thermal conductivity of the melt, λ_L is decreased by approx. 5.0 W(mK)$^{-1}$ compared to λ_S. Again, a linear temperature dependence is found for thermal conductivity of the liquid alloy [308]:

$$\lambda_L = 0.3 + 8.8 \times 10^{-3} T[\,\mathrm{W(mK)^{-1}}] \tag{7.10}$$

The comparison between the benchmark experiment and the corresponding simulations are discussed in detail in Ref. [308]. Here, it shall be mentioned that there is a good agreement between both, demonstrating the functioning of the concept of process simulation.

The benchmark experiment starts with the main part of the mould being below the baffle and cooled by the liquid metal. When the heaters have reached their final temperatures, the specimen starts driving into the hot zone and the melting front moves along the specimen [308]. The maximum heater temperature is determined as 1833 K and 1803 K for the lower and upper heater, respectively.

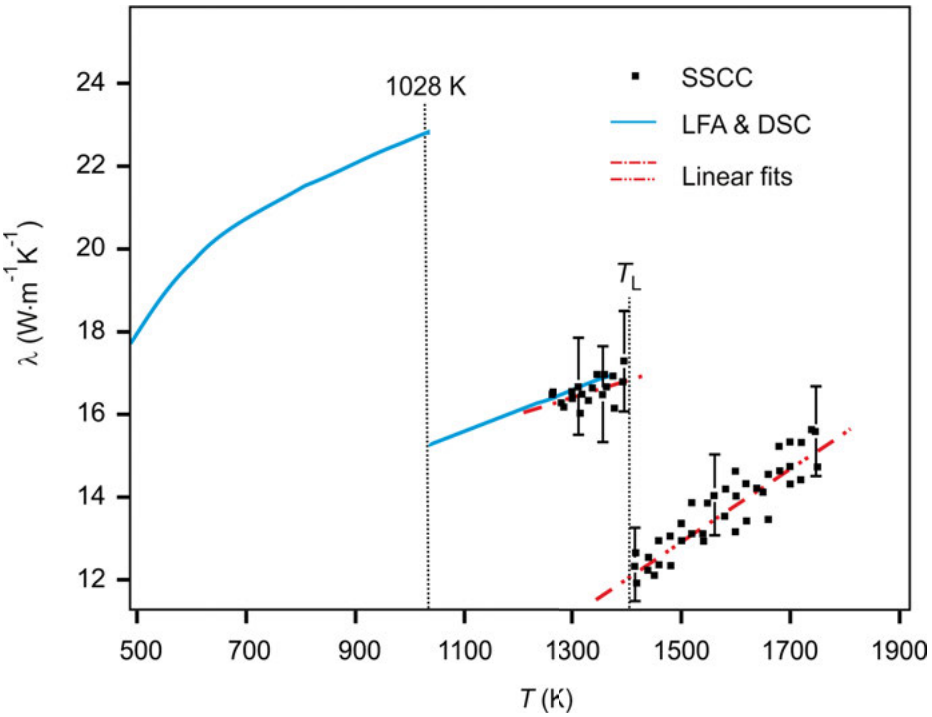

Fig. 7.12. Thermal conductivity as function of temperature calculated by Eq. (7.5) from thermal diffusivity and specific heat obtained by LFA and DSC, respectively. The solid lines are obtained using the linear extrapolations of c_P. The symbols correspond to data of λ measured directly by the steady state concentric cylinder method (SSCC) for both, the solid and liquid sample (from Ref. [308]).

The simulation starts with all components being at room temperature. It uses the measured temperature profile of the heaters as boundary condition at the heater surfaces.

For example, Fig. 7.13 shows the temperature-time profiles of the solidification benchmark experiment and the corresponding calculated profiles for three of the thermocouples at the positions z = 25 mm, 51 mm and 114 mm. For the sake of clarity, the profiles for z = 75 mm, z = 96 mm and z = 135 mm are not plotted, although they show the same good agreement between experiment and simulation [308].

In summary, a comprehensive set of thermophysical property data is raised for a Ga-Mn-Ni alloy with selected composition. It serves for description and characterization of the thermodynamic behavior of the system in both the solid and the liquid state. Using this data of $Ga_{25}Mn_{25}Ni_{50}$, the experimentally performed benchmark experiment is reproduced by the simulation with excellent agreement. The applicability of the entire chain of "process design" from the experimental determination of the relevant thermophysical property data to the correct prediction of the melting and growth process in simulation is demonstrated [308].

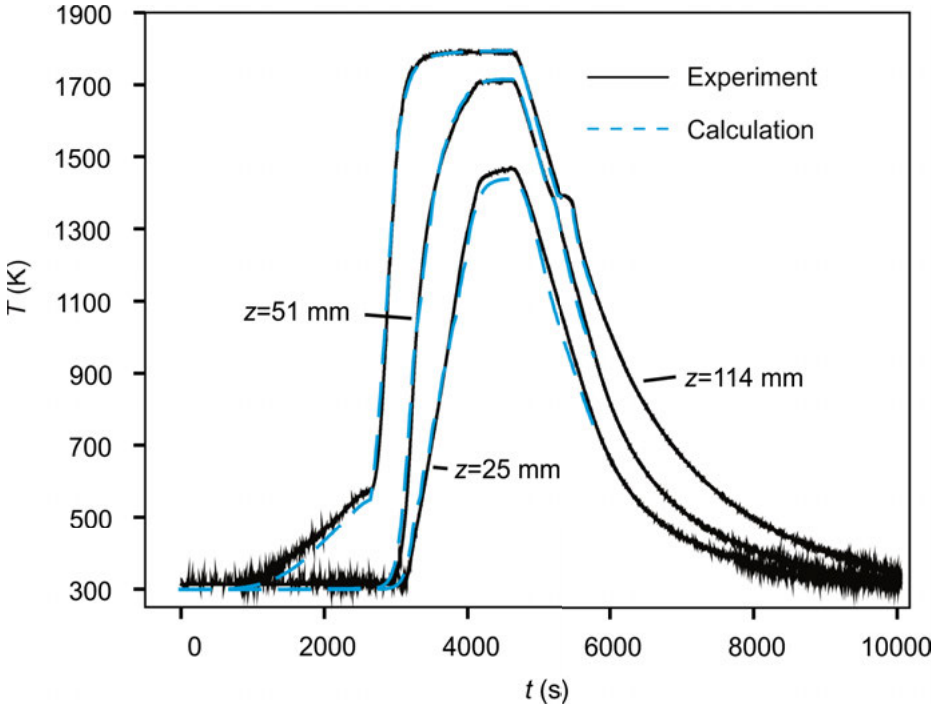

Fig. 7.13. Measured and calculated temperature-time profiles of three of the thermocouples at the marked positions in Fig. 7.6 (from Ref. [308]).

8 Conclusions

8.1 Discussion

In the previous sections, measurements of density, surface tension, and viscosity of binary and ternary systems as functions of temperature and composition are described, discussed, and compared. Furthermore, two inter-property relations are discussed: a relation between surface tension and viscosity as well as the Stokes-Einstein relation between viscosity and self diffusion. In the present chapter, these results are summarized so that general conclusions can be drawn.

In Chapters 3–5, all systems investigated are assigned to three disctinct classes, denoted as class I, class II and class III. Class I contains systems of which the excess free energy is positive, ${}^{\mathrm{E}}G > 0$, and one element is Cu and the others are transition metals. Alloys of class II consist of elements that are similar with respect to their electronic configuration, i.e. which either belong to the same group of the periodic table or which are all transition metals. Despite this definition, Al-Si is also assigned to class II, although Al and Si do not belong to the same group of the period table. On the other hand, the electronic configurations of both elements are similar, (Si: $[\mathrm{Ne}]2\mathrm{s}^2 3\mathrm{p}^2$, Al: $[\mathrm{Ne}]2\mathrm{s}^2 3\mathrm{p}^1$), and they weakly interact in the liquid state. For the latter reasons, Al-Si is also assigned to class II. Class III, finally, contains systems with strong attractive interactions, i.e. where ${}^{\mathrm{E}}G << 0$. Such systems are the Al-based alloys, except Al-Si. In addition, Cu-Si and Cu-Ti are also assigned to the third class as ${}^{\mathrm{E}}G << 0$ for these systems. As Ti is a transition metal, the Cu-Ti system could also have been assigned to class I, but its strongly negative excess free energy is rather typical for alloys in class III.

The results obtained in Chaps. 3–5 are compared for each system in Tab. 8.1 with respect to each property. Table 8.1 is a compilation of Tabs. 3.14, 4.15, and 5.11. It is obvious from this table that attributes like *ideal* or *non-ideal* are not solely system dependent. For instance, in the ternary composition range of Ag-Al-Cu density and surface tension obey ideal laws, see Chaps. 3 and 4. The system, however, exhibits a highly non-ideal behavior with respect to viscosity, see Chap. 5. Moreover, the excess free energy is strongly negative. Hence, attributes like *ideal* or *non-ideal* depend on the corresponding property. A system like Ag-Al-Cu, is therefore neither completely *ideal* nor *non-ideal*, with respect to *all* properties. Another example is Cu-Fe-Ni. It exhibits a non-ideal excess volume with a dominant positive ternary term, a surface tension which strongly deviates from the ideal one and pronounced segregation of copper. Moreover, positive excess free energies cause the system to demix in the undercooled temperature range. At the same time, its viscosity only weakly deviates from an ideal behavior, see Chap. 5.

The comparison of binary and ternary systems teaches the following: The surface tensions of all investigated systems can be described sufficiently by existing thermody-

namic models. These are mainly the Butler equation or, in case of so called compound forming alloys, the Egry model. Basically, there are two classes of systems: those for which ${}^{\mathrm{E}}G < 0$ and those for which ${}^{\mathrm{E}}G \geq 0$. The first exhibit a weak- and the latter a strong segregation behavior. Moreover, the ternary term ${}^{\mathrm{T}}G$ is usually small in Eq. (3.17) as compared to the binary ones. It can, therefore, be neglected without any major influence on the predicted surface tensions, see Chap. 4.

The situation is more complicated with respect to density. It is found in Chap. 3 that the molar volumes of the ternary systems Co-Cu-Fe, Ag-Al-Cu, and Cr-Fe-Ni can be predicted from those of the binary subsystems. For these specific systems, the ternary term is zero in Eq. (3.20), i.e. ${}^{\mathrm{T}}V = 0$. However, for just as many systems, Al-Cu-Si, Co-Cu-Ni, and Cu-Fe-Ni, a dominant ternary term, $|{}^{\mathrm{T}}V| >> 0$, needs be considered in Eq. (3.20) in order to calculate the excess volume. Hence, ${}^{\mathrm{T}}V$ is generally non-zero and the density of a ternary alloy is not implied by only the binary subsystems.

Moreover, no general rule is identified in order to predict the excess volume or, at least, the sign. For instance, the systems Cu-Ni, Co-Cu-Ni, Co-Cu and Cu-Fe all have positive excess free energies. At the same time, the systems Cu-Ni and Co-Cu-Ni exhibit negative excess volumes and the systems Co-Cu and Cu-Fe positive ones.

Nevertheless, the following rough trend becomes obvious among the systems investigated: Alloys assigned to class II, i.e. those that consist of elements with similar electronic structure, exhibit excess volumes that are ≈ 0. Copper based alloys with a positive excess free energy containing one or more transition metals, i.e. alloys that are assigned to class I, tend to have positive excess volumes. Finally, alloys of class III, i.e. those of which ${}^{\mathrm{E}}G << 0$, tend to exhibit excess volumes which are strongly negative. This is true, in particular for Al-based alloys.

Exceptions from this scheme exist in all these cases. Examples are Cu-Ti, which is assigned to class III, and for which ${}^{\mathrm{E}}G << 0$ and ${}^{\mathrm{E}}V > 0$, or Cu-Ni, class I, with ${}^{\mathrm{E}}G > 0$ and ${}^{\mathrm{E}}V < 0$. These exceptions confirm once again that a strict relation between ${}^{\mathrm{E}}G$ and ${}^{\mathrm{E}}V$ is not obvious. This result is also obtained in a simulation study by Amore [162].

Moreover, it is justified to question the assignment of Cu-Ti to class III. As Ti is a transition metal, Cu-Ti might also be accommodated in class I. Cu-Ti exhibits a positive excess volume and fits, therefore, to the trend of the other alloys in this class. However, there is no benefit from this step. On the one hand, it seems that this would decrease the number of exceptions in Tab. 8.1. On the other hand, another exception is created simultaneously, as Cu-Ti exhibits weak segregation while all other members of class I exhibit strong segregation.

Studying the systems with respect to their viscosities reveals that the Kozlov model is most suited for their prediction, if it is not considered to which class the systems belong. The Kozlov model is, hence, choosen in Chap. 5 in order to define whether, with respect to viscosity, a system is *ideal* or *non-ideal*. For the viscosity, this definition is model dependant. In fact it is found that, in the majority of investigated systems, η can be approximated as *ideal*. The only systems that exhibit non-ideal behavior are Al-Cu and Ag-Al-Cu. Both systems are assigned to class III.

Table 8.1. Trends observed in all systems with respect to excess volume, surface segregation, and viscosity.

		^{E}V	Segregation	Viscosity $^{E}\eta$	Viscosity ΔE_A	
class I	Co-Cu-Ni	-	strong	≈ 0	-	*ideal*
	Cu-Fe-Ni	+		-	≈ 0	
	Co-Cu-Fe					
	Cu-Fe					
	Cu-Ni	-				
	Co-Cu	+				
class II	Cr-Fe-Ni	+		0	-	*ideal*
	Fe-Ni	0	weak	0	-	
	Al-Si					
	Ag-Cu		strong			
	Ag-Au					
	Au-Cu					
	Co-Fe					
	Cr-Ni	+				
	Cr-Fe					
class III	Co-Sn			0	0	*ideal*
	Al-Cu-Si	0		-	≤ 0	
	Ag-Al-Cu		weak	+	+	*non-ideal*
	Al-Cu	-		+	+	
	Al-Au					
	Al-Fe					
	Al-Ni					
	Cu-Ti	+				
	Cu-Si	+/-				
	Ag-Al	-				

If the performance of the models is evaluated with respect to each materials class, the following preliminary tendency becomes obvious: Viscosities of alloys assigned to class I can best be described by the Kaptay model. Viscosities of systems belonging to class II are predicted best by the Kozlov model and the viscosities of systems belonging to class III are best described by the Brillo/Schick model. In view of the limited number of systems investigated in Chap. 5, it is clear that further clarification is needed.

Similar to the case of surface tension, the viscosity of a ternary alloy can also be predicted from the properties of its binary subsystems by neglecting ^{T}G.

In addition to the mixing rules, inter-property relations are investigated in Chap. 6. The available base of data allows the testing of a relation between surface tension and viscosity. Such a relation can be derived from a formal similarity in the definitions of the two properties. Its validity is shown in the case of pure metals, except Al. In addition, the validity of the relation between surface tension and viscosity is also demon-

strated for alloys. Deducing a new recipe for the prediction of viscosities from ${}^{E}G$ via the Butler equation fails, however, due to a lack of numerical accuracy.

Moreover, the Stokes-Einstein relation is tested in two cases. For the less densely packed system $Al_{80}Cu_{20}$, it is shown to be valid for temperatures above 1400 K. Below 1400 K, deviations from the Stokes-Einstein behavior occur which increase with decreasing temperature. In the case of $Al_{80}Cu_{20}$, diffusion becomes apparently faster with decreasing temperature than expected from the Stokes-Einstein law. This behavior is opposite from what is usually observed.

Investigations performed on the rather densely packed system $Ni_{36}Zr_{64}$ using electrostatic levitation reveal that the Stokes-Einstein relation is not valid for this system. Already at more than 1000 K above the mode coupling temperature of dynamical freezing the dynamics in $Ni_{36}Zr_{64}$ is obviously collective. As $Ni_{36}Zr_{64}$ is a densely packed system, viscous flow and diffusion take place on the same time scale. Hence, $D \cdot \eta = const$ as convincingly shown in Chap. 6 [32].

8.2 Answers

Based on the findings summarized in Sec. 8.1 it is possible to answer the key questions formulated in Sec. 1.5. Each single issue is addressed:

Q:1. Is there any general rule for predicting the mixing behavior? Moreover, are there commonalities with respect to the mixing behavior among similar materials?

There is no general rule for the prediction of excess volumes. Not even their signs can be predicted in a strict sense. The investigated systems can be assigned to three distinct classes, depending on composition: class I, consisting of Cu-based alloys containing transition metals and with ${}^{E}G > 0$, class II, consisting of alloys with elements of similar electronic structure or of elements from the same periodic group, and, finally, class III consisting of alloys with strongly negative excess free energies. The majority of members of this class are Al- based systems. The following trend is obvious: Alloys of class I exhibit positive excess volumes, alloys of class II exhibit excess volumes that are approximately zero and alloys of class III exhibit strongly negative excess volumes. There are exceptions from this trend in each of the classes.

In the case of surface tension, the Butler equation is found to work reliably. In the case of compound forming systems, the Egry model has to be used instead. With respect to surface tension, the systems dissociate in two classes, depending on the signs of ${}^{E}G$. Pronounced segregation occurs in systems with ${}^{E}G > 0$ and only weak segregation is found in systems for which ${}^{E}G < 0$.

Regarding viscosity, most of the investigated alloys exhibit ideal mixing behavior. The investigations indicate that the viscosities of materials of class I are best predicted by the Kaptay model, viscosities of materials from class II are best described by the Kozlov model and, in the case of a class III system, the Brillo/Schick model yields the

best agreement with the experimental data. Commonalities among similar systems are compared to each other in Tab. 8.1.

Q:2. Is it possible to establish relations between excess thermophysical properties and thermodynamic potentials? If such relations exist, how well will they perform?

In the case of density, such a relation does not exist. The excess volume could principally be derived by ${}^{\mathrm{E}}V = \partial {}^{\mathrm{E}}G/\partial P$ with P being the pressure. However, ${}^{\mathrm{E}}G(P)$ is not normally known. Writing ${}^{\mathrm{E}}V \propto {}^{\mathrm{E}}G$ could be a reasonable approach for such a model. However, it is clearly contradicted by the exceptions evident from Tab. 3.14. Basically, the same answer is obtained from the simulation study performed by Amore and Horbach [162]. The excess volume is still not understood. Few attempts have yet been undertaken in order to change this situation.

The prediction of the surface tension using the Butler equation, or the Egry model in case of a compound forming system, is rather non-problematic.

Most systems investigated with respect to viscosity can be seen as approximately ideal. As pointed out above, viscosities of materials of class I are best predicted by the Kaptay model, viscosities of materials from class II are best described by the Kozlov model and, viscosities of systems of class III are best predicted by the Brillo/Schick model (see answer to question **Q:1**).

Q:3. Is it possible to relate thermophysical properties of a multicomponent alloy to those of its constituent subsystems?

As long as the ternary interaction term can be neglected in Eq. (3.17), i.e. ${}^{\mathrm{T}}G \approx 0$, surface tension and, in principle, also viscosity can be predicted for ternary alloys taking only thermodynamic assessments of the binary subsystems into account. In the case of density, it is generally not possible to predict the excess volume of a ternary liquid alloy from its binary subsystems. The ternary volume interaction term ${}^{\mathrm{T}}V$ is approximately zero purely for certain systems.

Q:4. Is it possible to identify inter-property relations in selected cases? If yes, what are their forms and how well do they perform?

A relation between surface tension and viscosity is tested in Chap. 6 and verified in the case of pure metals (Al formed the only exception) and for alloys.

In the case of $Al_{80}Cu_{20}$, the Stokes-Einstein relation between viscosity and diffusivity holds for $T > 1400$ K. Below 1400 K, diffusion becomes apparently faster with decreasing temperature than expected from the Stokes-Einstein law. In the case of $Ni_{36}Zr_{64}$, the Stokes-Einstein law is rejected. Instead of $D \cdot \eta \propto k_{\mathrm{B}}T$, as predicted by the Stokes-Einstein relation, $D \cdot \eta = const$, is found from experiment [32].

8.3 Implications on computer aided materials design from the melt

It is one of the key motivations of the present work to contribute to an improvement of materials design from the melt. This goal has been is achieved as the results obtained in the present work will have the following implications on computer aided materials design from the melt:

1. The obtained parameterizations of the measured excess volumes, Tabs. 3.12 and 3.13, as well as the measured density data of pure elements, Tab. 3.10, can be used directly by simulation programmes in order to predict density data of liquid alloys.
2. The same is true for surface tension and viscosity. In addition, models for the prediction of this data are evaluated in the present work.
3. The comprehensive set of thermophysical property data established in this work also serves as benchmark data for further theoretical studies aiming to obtain a fundamental understanding of the mixing behavior of liquid alloys.
4. In the case that, in a simulation application melt properties are needed of a material system that is not investigated within the present work, it is even possible, to try an assignment of that material to one of the classes identified in Chaps. 3–5, i.e. class I– class III. In this way, qualitative statements about the mixing behavior can be obtained, allowing the estimation of the desired properties of less investigated materials.
5. Computer Aided Materials Design from the Melt is extended by the results of the present work by an unprecedented predictive power: Instead of just reading the desired data from a database, it is now also possible to make statements about materials and their thermophysical properties that are not explicitly stored in such a database. This will ease the development of new materials and their processing substantially.

8.4 Outlook

Up to now, the studies carried out in the present work have only scratched the tip of the iceberg. In the future, these works will need to be continued to help to complete the picture obtained so far. Hence, further measurements are required, in particular on systems that have not yet been taken into focus. This refers mainly to the study of Ti-based alloys which will be intensified soon.

Ti-based alloys are of enormous technological relevance, for instance, in aerospace applications, as bio-compatible materials or as alloys for turbine blades. The thorough investigation of these materials in their liquid states is possible only through using containerless, i.e. levitation, techniques.

Investigating Ti-based alloys also promises interesting scientific results when studying, for instance, the interactions of these melts with oxygen.

In the next years, a major part of the investigations will also deal with the investigation of the effect of oxygen on thermophysical properties of liquid metals. For this purpose, it is aimed to implement an Oxygen Sensing and Control (OSC) system on board the ISS.

Last, but not least, the combination of the experiments with simulation studies is promising in order to explain and to understand some of the observed phenomena on an atomic scale. Such phenomena are, for instance, the origin of the excess volume.

A Data

In this section, the parameters of the representations of the thermophysical properties, density, surface tension and viscosity, are given for all liquid pure metal and alloy systems discussed in the previous chapters.

In the case of density, ρ is described as function of temperature by a linear law, Eq. (3.9), which reads:

$$\rho(T) = \rho_{\mathrm{L}} + \rho_{\mathrm{T}}(T - T_{\mathrm{L}}) \tag{A.1}$$

Here, ρ_{L} is the density at liquidus temperature T_{L}, and ρ_{T} is the temperature coefficient.

In the case of surface tension, y is also described as function of temperature by a linear law, see Eq. (4.11), which reads:

$$y(T) = y_{\mathrm{L}} + y_{\mathrm{T}}(T - T_{\mathrm{L}}) \tag{A.2}$$

Analogously, y_{L} is the surface tension at T_{L} and y_{T} is the corresponding temperature coefficient.

The viscosities, η, discussed in Chap. 5 are represented by the Arrhenius law, Eq. (5.9), as written below:

$$\eta(T) = \eta_{\infty} \exp\left(\frac{E_{\mathrm{A}}}{RT}\right) \tag{A.3}$$

In this equation, η_{∞} is the pre-exponential factor and E_{A} is the energy barrier of the thermally activated process of viscious flow.

The following table A.1 assigns the investigated binary and ternary alloy systems to tables below listing these parameters for density, surface tension and viscosity, respectively:

Table A.1. Reference to tables showing parameters in order to represent density, surface tension, and viscosity of liquid binary and ternary alloys as functions of temperature.

System	Density	Surface tension	Viscosity
Pure elements	A.2	A.3	A.4
Ag-Al	A.5		
Ag-Au	A.14		
Ag-Cu	A.6	A.7	
Ag-Al-Cu	A.8	A.9	A.10
Al-Au	A.15	A.16	
Ag-Au	A.14		
Al-Cu	A.11	A.12	A.13
Al-Cu-Si	A.17		A.18
Al-Fe	A.22	A.23	
Al-Ni	A.24	A.25	
Al-Si	A.19		
Au-Cu	A.26		
Co-Cu	A.31		
Co-Cu-Fe	A.32	A.33	
Co-Cu-Ni	A.34	A.35	A.36
Co-Fe	A.28		
Co-Sn			A.27
Cr-Ni	A.47		
Cr-Fe	A.46		
Cr-Fe-Ni	A.49		A.50
Cu-Fe	A.29	A.30	
Cu-Fe-Ni	A.41	A.42	A.43
Cu-Ni	A.37	A.38	
Cu-Si	A.20	A.21	
Cu-Ti	A.44	A.45	
Fe-Ni	A.39 A.48	A.40	

A.1 Pure elements

Table A.2. Parameters ρ_L and ρ_T of liquid pure elements obtained from linear fits to the experimental data from the references cited in the last column. For some elements, data is measured more than once.

Element	T_L (K)	ρ_L ($g \cdot cm^{-3}$)	ρ_T ($10^{-4} g \cdot cm^{-3} K^{-1}$)	source
Al	933	2.36	-3.3	[96]
		2.29	-2.5	[15]
		2.36	-3.0	[97]
		2.42	-3.0	[158]
Cu	1358	7.90	-7.65	[17]
Ag	1233	9.15	-7.4	[37]
Au	1333	17.4	-11.0	[104]
Ni	1727	7.93	-10.1	[17]
		7.82	-8.56	[123]
Co	1768	7.81	-8.9	[134]
Fe	1818	7.04	-10.8	[61]
		6.99	-5.6	[123]
Ti	1941	4.1	-3.3	[135]

Table A.3. Parameters γ_L and γ_T of liquid pure elements obtained from linear fits to the experimental data from the references cited in the last column. For some elements, data is measured more than once.

Element	T_L (K)	γ_L (Nm^{-1})	γ_T ($10^{-4} Nm^{-1} K^{-1}$)	source
Al	933	0.866	-1.46	[199]
Cu	1358	1.30	-2.64	[191]
		1.33	-2.6	[67]
		1.33	-2.3	[206]
Ag	1233	0.894	-1.9	[67]
Au	1333	1.140	-1.83	[199]
Ni	1727	1.77	-3.30	[68]
Fe	1818	1.92	-3.97	[68]
Ti	1941	1.49	-1.7	[206]

Table A.4. Parameters η_∞ and E_A of liquid pure elements obtained from linear fits to the experimental data from the references cited in the last column. For some elements, data is measured more than once.

Element	η_∞ (mPa · s)	E_A (10^4J/mol)	Source
Al	0.281	1.23	[158]
Si	0.214	1.43	[158]
Cu	0.522	2.36	[248]
	0.657	2.15	[158]
Ni	0.413	3.49	[160]
Co	0.048	6.81	[256]
Fe	0.114	5.93	[160]
Sn	0.407	0.72	[256]

A.2 Ag-Al-Cu

A.2.1 Ag-Al (Density)

Table A.5. Parameters ρ_L and ρ_T for liquid **Ag-Al** binary alloys obtained from linear fits to the experimental data from Ref. [96]. The liquidus temperatures T_L are extracted from the phase diagram presented in Ref. [154].

System	T_L(K)	ρ_L(g · cm^{-3})	ρ_T (10^{-4}g · cm^{-3}K^{-1})
Al	933	2.36	-3.3
$Ag_{10}Al_{90}$	893	2.83	-2.1
$Ag_{20}Al_{80}$	864	3.83	-4.2
$Ag_{40}Al_{60}$	840	5.38	-4.8
$Ag_{60}Al_{40}$	979	6.81	-10.5
$Ag_{79}Al_{21}$	1049	8.07	-6.8
Ag	1235	9.15	-7.4

A.2.2 Ag-Cu (Density)

Table A.6. Parameters ρ_L and ρ_T for liquid **Ag-Cu** binary alloys obtained from linear fits to the experimental data from Ref. [37]. The liquidus temperatures T_L are extracted from the phase diagram presented in Ref. [154].

System	T_L(K)	ρ_L(g · cm^{-3})	ρ_T (10^{-4}g · cm^{-3}K^{-1})
$Ag_{80}Cu_{20}$	1135	9.0	-6
$Ag_{60}Cu_{40}$	1053	8.9	-7
$Ag_{40}Cu_{60}$	1132	8.6	-6
$Ag_{20}Cu_{80}$	1225	8.4	-12

A.2.3 Ag-Cu (Surface tension)

Table A.7. Parameters γ_L and γ_T for liquid **Ag-Cu** binary alloys from Ref. [67]. Some of the compositions are measured more than once. Liquidus temperatures T_L are obtained from Ref. [154].

System	T_L(K)	γ_L(Nm^{-1})	γ_T (10^{-4}Nm^{-1}K^{-1})
Cu	1358	1.334	-2.6
$Ag_{10}Cu_{90}$	1284	1.129	-0.70
$Ag_{20}Cu_{80}$	1215	1.069	-1.42
$Ag_{40}Cu_{60}$	1113	0.989	-0.51
$Ag_{40}Cu_{60}$	1113	0.951	-0.30
$Ag_{60}Cu_{40}$	1053	0.926	-1.00
$Ag_{60}Cu_{40}$	1053	0.911	-0.59
$Ag_{60}Cu_{40}$	1053	0.930	-0.23
Ag	1234	0.894	-1.91

A.2.4 Ag-Al-Cu (Density)

Table A.8. Parameters ρ_L and ρ_T for liquid **Ag-Al-Cu** ternary alloys obtained from linear fits to the experimental data from Ref. [157]. Liquidus temperatures T_L are obtained by a procedure described in Ref. [157].

System	T_L(K)	ρ_L(g · cm^{-3})	ρ_T (10^{-4}g · cm^{-3}K^{-1})
$Ag_{10}Al_{90}$	920	2.82	-2.1
$Ag_{10}Al_{80}Cu_{10}$	890	3.48	-5.4
$Ag_{10}Al_{60}Cu_{30}$	810	4.49	-6.4
$Ag_{10}Al_{50}Cu_{40}$	840	5.48	-9.8
$Ag_{10}Al_{40}Cu_{50}$	880	6.03	-10.1
$Ag_{10}Al_{20}Cu_{70}$	1190	6.90	-6.46
$Ag_{10}Cu_{90}$	1310	8.12	-10.5

A.2.5 Ag-Al-Cu (Surface tension)

Table A.9. Parameters γ_L and γ_T for liquid **Al-Ag-Cu** ternary alloys from Ref. [176]. Liquidus temperatures T_L are obtained by a procedure described in Ref. [176].

System	T_L(K)	γ_L(Nm^{-1})	γ_T (10^{-4}Nm^{-1}K^{-1})
$Ag_{10}Cu_{90}$	1282	1.15	-2.2
$Ag_{10}Al_{20}Cu_{70}$	1245	1.06	-4.5
$Ag_{10}Al_{40}Cu_{50}$	1134	1.01	-2.1
$Ag_{10}Al_{50}Cu_{40}$	1009	1.01	-3.9
$Ag_{10}Al_{70}Cu_{20}$	818	1.05	-3.7
$Ag_{10}Al_{90}$	901	0.95	-2.7
$Al_{17}Cu_{83}$	1044	1.32	-2.7
$Ag_{30}Al_{55}Cu_{15}$	864	0.90	-1.0
$Ag_{50}Al_{40}Cu_{10}$	961	0.97	-2.9
$Ag_{30}Al_{35}Cu_{35}$	1044	1.01	-2.5
$Al_{40}Cu_{60}$	1228	1.13	-1.54

A.2.6 Ag-Al-Cu (Viscosity)

Table A.10. Parameters η_∞ and E_A for liquid **Al-Ag-Cu** ternary alloys from Ref. [157].

System	η_∞(mPa · s)	E_A (10^{4}J/mol)
$Ag_{10}Cu_{90}$	0.519	2.21
$Ag_{10}Al_{20}Cu_{70}$	0.347	2.85
$Ag_{10}Al_{40}Cu_{50}$	0.172	3.47
$Ag_{10}Al_{50}Cu_{40}$	0.338	2.50
$Ag_{10}Al_{60}Cu_{30}$	0.225	2.39
$Ag_{10}Al_{80}Cu_{10}$	0.229	1.64
$Ag_{10}Al_{90}$	0.327	1.02

A.2.7 Al-Cu (Density)

Table A.11. Parameters ρ_L and ρ_T for liquid **Al-Cu** binary alloys obtained from linear fits to the experimental data from Ref. [96]. The liquidus temperatures T_L are extracted from the phase diagram presented in Ref. [154].

System	T_L(K)	$\rho_L(\mathrm{g \cdot cm^{-3}})$	$\rho_T\ (10^{-4}\mathrm{g \cdot cm^{-3}K^{-1}})$
Al	933	2.36	-3.3
$Al_{80}Cu_{20}$	835	3.32	-5.3
$Al_{70}Cu_{30}$	865	3.76	-4.9
$Al_{60}Cu_{40}$	900	4.44	-5.4
$Al_{50}Cu_{50}$	1087	5.05	-6.1
$Al_{40}Cu_{60}$	1233	5.49	-6.9
$Al_{30}Cu_{70}$	1314	6.17	-8.5
$Al_{20}Cu_{80}$	1315	6.66	-7.7
Cu	1358	7.92	-7.6

A.2.8 Al-Cu (Surface tension)

Table A.12. Parameters γ_L and γ_T for liquid **Al-Cu** binary alloys from Ref. [191]. Liquidus temperatures T_L are obtained by a procedure described in Ref. [191].

System	T_L(K)	$\gamma_L(\mathrm{Nm^{-1}})$	$\gamma_T\ (10^{-4}\mathrm{Nm^{-1}K^{-1}})$
$Al_{10}Cu_{90}$	1347	1.35	-2.1
$Al_{17}Cu_{83}$	1317	1.32	-2.7
$Al_{30}Cu_{70}$	1304	1.19	-1.3
$Al_{40}Cu_{60}$	1638	1.13	-1.5
$Al_{50}Cu_{50}$	1644	1.04	-0.7
$Al_{60}Cu_{40}$	980	1.00	-0.6
$Al_{70}Cu_{30}$	867	0.97	-1.1
$Al_{83}Cu_{17}$	825	0.94	-1.6
$Al_{90}Cu_{10}$	873	0.87	-1.2

A.2.9 Al-Cu (Viscosity)

Table A.13. Parameters η_∞ and E_A for liquid **Al-Cu** binary alloys from Ref. [87]. Liquidus temperatures T_L are obtained by a procedure described in Ref. [87].

System	T_L(K)	η_∞ (mPa · s)	E_A (10^4J/mol)
Al	933	0.257	1.31
$Al_{90}Cu_{10}$	873	0.305	1.60
$Al_{90}Cu_{10}$	873	0.380	1.56
$Al_{80}Cu_{20}$	834	0.358	1.32
$Al_{70}Cu_{30}$	867	0.233	2.36
$Al_{50}Cu_{50}$	1105	0.228	3.31
$Al_{50}Cu_{50}$	1105	0.169	3.39
$Al_{40}Cu_{60}$	1228	0.195	4.07
$Al_{30}Cu_{70}$	1303	0.229	3.71
$Al_{20}Cu_{80}$	1313	0.316	3.4
$Al_{10}Cu_{90}$	1346	0.517	2.54
Cu	1358	0.520	2.35

A.3 Ag-Au

A.3.1 Ag-Au (Density)

Table A.14. Parameters ρ_L and ρ_T for liquid **Ag-Au** binary alloys obtained from linear fits to the experimental data from Ref. [37]. The liquidus temperatures T_L are extracted from the phase diagram presented in Ref. [154].

System	T_L(K)	ρ_L(g · cm^{-3})	ρ_T (10^{-4}g · cm^{-3}K^{-1})
$Ag_{75}Au_{25}$	1276	11.2	-7
$Ag_{50}Au_{50}$	1306	13.3	-6
$Ag_{25}Au_{75}$	1326	15.6	-12

A.4 Al-Au

A.4.1 Al-Au (Density)

Table A.15. Parameters ρ_L and ρ_T for liquid **Al-Au** binary alloys obtained from linear fits to the experimental data from Ref. [15]. The liquidus temperatures T_L are extracted from the phase diagram presented in Ref. [318].

System	T_L(K)	$\rho_L(\mathrm{g \cdot cm^{-3}})$	$\rho_T\ (10^{-4}\mathrm{g \cdot cm^{-3}K^{-1}})$
Al	934	2.291	-2.51
$Al_{85}Au_{15}$	835	4.425	-3.27
$Al_{80}Au_{20}$	847	5.275	-5.90
$Al_{67}Au_{33}$	895	7.231	-6.85
$Al_{55}Au_{45}$	1144	9.163	-6.3
$Al_{50}Au_{50}$	1252	10.05	-10.6
$Al_{33}Au_{67}$	1333	12.842	-10.0
$Al_{27}Au_{73}$	1280	13.84	-10.1
$Al_{20}Au_{80}$	1237	15.02	-10.8
Au	1338	17.192	-11.1

A.4.2 Al-Au (Surface tension)

Table A.16. Parameters γ_L and γ_T for liquid **Al-Au** binary alloys obtained from linear fits to the experimental data from Ref. [199]. The liquidus temperatures T_L are extracted from the phase diagram presented in Ref. [318].

System	T_L(K)	$\gamma_L(\mathrm{Nm^{-1}})$	$\gamma_T\ (10^{-4}\mathrm{Nm^{-1}K^{-1}})$
Au	1338	1.140	–1.83
$Al_{15}Au_{85}$	1039	1.170	–1.73
$Al_{20}Au_{80}$	835	1.240	–2.39
$Al_{27}Au_{73}$	847	1.157	–1.91
		1.21	–2.5
$Al_{33}Au_{67}$	895	1.160	–2.12
$Al_{45}Au_{55}$	951	1.118	–1.82
$Al_{50}Au_{50}$	1144	1.005	–2.03
$Al_{55}Au_{45}$	1252	0.933	–1.33
$Al_{67}Au_{33}$	1333	0.897	–1.9
$Al_{80}Au_{20}$	1280	0.8570	–0.82
$Al_{85}Au_{15}$	1237	0.8609	–1.33
Al	934	0.866	–1.46

A.5 Al-Cu-Si

A.5.1 Al-Cu-Si (Density)

Table A.17. Parameters ρ_L and ρ_T for liquid **Al-Cu-Si** ternary alloys obtained from linear fits to the experimental data from Ref. [158]. The liquidus temperatures T_L are calculated by a procedure described in Ref. [158].

System	T_L(K)	ρ_L(g · cm^{-3})	ρ_T (10^{-4}g · cm^{-3}K^{-1})
Al	933	2.42	-3.0
$Al_{90}Cu_5Si_5$	870	2.69	-4.8
$Al_{80}Cu_{10}Si_{10}$	837	3.07	-5.5
$Al_{60}Cu_{20}Si_{20}$	1035	3.23	-2.4
$Al_{33}Cu_{33}Si_{33}$	1270	3.89	-2.6
$Cu_{50}Si_{50}$	1363	5.26	-5.4
$Al_{30}Cu_{40}Si_{30}$	1245	4.36	-3.7
$Al_{40}Cu_{20}Si_{40}$	1302	3.33	-2.5

A.5.2 Al-Cu-Si (Viscosity)

Table A.18. Parameters η_∞ and E_A for liquid **Al-Cu-Si** ternary alloys from Ref. [158].

System	η_∞(mPa · s)	E_A (10^4J/mol)
Al	0.281	1.23
Cu	0.657	2.15
Si	0.214	1.43
$Al_{90}Cu_5Si_5$	0.259	1.16
$Al_{80}Cu_{10}Si_{10}$	0.212	1.38
$Al_{60}Cu_{20}Si_{20}$	0.270	1.39
$Al_{33}Cu_{33}Si_{33}$	0.292	1.77
$Al_{20}Cu_{40}Si_{40}$	0.244	2.12
$Cu_{50}Si_{50}$	0.336	1.63
$Al_5Cu_{90}Si_5$	0.458	2.80
$Al_{10}Cu_{80}Si_{10}$	0.197	3.46
$Al_{20}Cu_{60}Si_{20}$	0.194	2.84
$Al_{30}Cu_{40}Si_{30}$	0.172	2.53
$Al_{40}Cu_{20}Si_{40}$	0.138	2.15
$Al_{50}Si_{50}$	0.169	1.63
$Al_{80}Cu_{20}$	0.273	1.66
$Al_{80}Cu_{20}$	0.239	1.70
$Al_{40}Cu_{20}Si_{40}$	0.156	2.03
$Cu_{20}Si_{80}$	0.176	2.03

A.5.3 Al-Si (Density)

Table A.19. Parameters ρ_L and ρ_T for liquid **Al-Si** binary alloys obtained from linear fits to the experimental data from Ref. [97]. The liquidus temperatures T_L are calculated according to a procedure described in Ref. [97].

System	T_L(K)	$\rho_L(\mathrm{g \cdot cm^{-3}})$	$\rho_T\ (10^{-4}\mathrm{g \cdot cm^{-3}K^{-1}})$
Al	933	2.36	-3.0
$Al_{88}Si_{12}$	849	2.46	-2.1
$Al_{80}Si_{20}$	970	2.44	-2.3
$Al_{70}Si_{30}$	1104	2.37	-1.6
$Al_{70}Si_{30}$	1104	2.40	-1.7
$Al_{70}Si_{30}$	1104	2.39	-1.8
$Al_{60}Si_{40}$	1225	2.42	-2.9
$Al_{50}Si_{50}$	1334	2.46	-3.2

A.5.4 Cu-Si (Density)

Table A.20. Parameters ρ_L and ρ_T for liquid **Cu-Si** binary alloys obtained from linear fits to the experimental data from Ref. [151]. The liquidus temperatures T_L are picked from Ref. [154]. The parameters of $Cu_{50}Si_{50}$ are taken from Ref. [158], see also Tab. A.17.

System	T_L(K)	$\rho_L(\mathrm{g \cdot cm^{-3}})$	$\rho_T\ (10^{-4}\mathrm{g \cdot cm^{-3}K^{-1}})$
$Cu_{95}Si_5$	1311	7.79	-7.01
$Cu_{90}Si_{10}$	1246	7.59	-6.31
$Cu_{85.1}Si_{14.9}$	1159	7.47	-6.73
$Cu_{84}Si_{16}$	1125	7.38	-6.73
$Cu_{85.4}Si_{16.6}$	1118	7.40	-7.04
$Cu_{80}Si_{20}$	1094	7.21	-6.95
$Cu_{77.5}Si_{22.5}$	1131	7.09	-6.81
$Cu_{76}Si_{24}$	1132	6.80	-5.73
$Cu_{75}Si_{25}$	1131	6.83	-6.27
$Cu_{72.5}Si_{27.5}$	1114	6.70	-5.14
$Cu_{70}Si_{30}$	1075	6.51	-5.92
$Cu_{65}Si_{35}$	1164	6.07	-5.50
$Cu_{60}Si_{40}$	1235	5.74	-5.67
$Cu_{50}Si_{50}$	1363	5.26	-5.40

A.5.5 Cu-Si (Surface tension)

Table A.21. Parameters γ_L and γ_T for liquid **Cu-Si** binary alloys obtained from linear fits to the experimental data from Ref. [151]. The liquidus temperatures T_L are picked from Ref. [154].

System	T_L(K)	γ_L(Nm^{-1})	γ_T (10^{-4}Nm^{-1}K^{-1})
$Cu_{95}Si_5$	1311	1.36	-3.06
$Cu_{90}Si_{10}$	1246	1.33	-2.69
$Cu_{85.1}Si_{14.9}$	1159	1.30	-2.47
$Cu_{84}Si_{16}$	1125	1.32	-1.96
$Cu_{85.4}Si_{16.6}$	1118	1.33	-2.14
$Cu_{80}Si_{20}$	1094	1.27	-1.75
$Cu_{77.5}Si_{22.5}$	1131	1.19	-1.70
$Cu_{76}Si_{24}$	1132	1.15	-0.74
$Cu_{75}Si_{25}$	1131	1.12	-0.14
$Cu_{72.5}Si_{27.5}$	1114	1.10	-0.94
$Cu_{70}Si_{30}$	1075	1.04	0.023
$Cu_{65}Si_{35}$	1164	0.97	0.69

A.6 Al-Fe

A.6.1 Al-Fe (Density)

Table A.22. Parameters ρ_L and ρ_T for liquid **Al-Fe** binary alloys obtained from linear fits to the experimental data from Ref. [21]. The liquidus temperatures T_L are picked from Ref. [154].

System	T_L(K)	$\rho_L(\mathrm{g \cdot cm^{-3}})$	$\rho_T\ (10^{-4}\mathrm{g \cdot cm^{-3}K^{-1}})$
$Al_{80}Fe_{20}$	1430	3.15	-11.5
Al_3Fe	1433	3.32	-4.8
Al_5Fe_2	1452	3.43	-5.7
Al_2Fe	1457	3.83	-7.2
$Al_{60}Fe_{40}$	1505	4.19	-5.4

A.6.2 Al-Fe (Surface tension)

Table A.23. Parameters γ_L and γ_T for liquid **Al-Fe** binary alloys obtained from linear fits to the experimental data from Ref. [232]. The liquidus temperatures T_L are picked from Ref. [154].

System	T_L(K)	$\gamma_L(\mathrm{Nm^{-1}})$	$\gamma_T\ (10^{-4}\mathrm{Nm^{-1}K^{-1}})$
$Al_{90}Fe_{10}$	1289	0.95	-4.8
$Al_{80}Fe_{20}$	1430	1.08	-5.8
Al_3Fe	1433	1.08	-3.7
Al_5Fe_2	1452	1.12	-7.1
Al_2Fe	1457	1.16	-4.4
$Al_{60}Fe_{40}$	1505	1.22	-1.4

A.7 Al-Ni

A.7.1 Al-Ni (Density)

Table A.24. Parameters ρ_L and ρ_T for liquid **Al-Ni** binary alloys obtained from linear fits to the experimental data from Ref. [21]. The liquidus temperatures T_L are picked from Ref. [154].

System	T_L(K)	ρ_L(g · cm^{-3})	ρ_T (10^{-4}g · cm^{-3}K^{-1})
$Al_{82}Ni_{18}$	1221	3.31	-4.8
Al_3Ni	1377	3.55	-7.6
$Al_{70}Ni_{30}$	1565	3.80	-9.4
Al_3Ni_2	1835	4.49	-12.9
AlNi	1913	4.46	-19.2
$AlNi_3$	1670	6.42	-8.0

A.7.2 Al-Ni (Surface tension)

Table A.25. Parameters γ_L and γ_T for liquid **Al-Ni** binary alloys obtained from linear fits to the experimental data from Ref. [190]. The liquidus temperatures T_L are picked from Ref. [154].

System	T_L(K)	γ_L(Nm^{-1})	γ_T (10^{-4}Nm^{-1}K^{-1})
$Al_{82}Ni_{18}$	1221	1.01	-5.1
Al_3Ni	1377	1.21	-8.3
$Al_{70}Ni_{30}$	1565	1.15	-8.8
Al_3Ni_2	1835	1.30	-6.3
AlNi	1913	1.44	-6.7
$Al_{37}Ni_{63}$	1813	1.55	-2.9
$AlNi_3$	1670	1.44	-2.6
$Al_{13}Ni_{87}$	1706	1.58	-5.1

A.8 Au-Cu

A.8.1 Au-Cu (Density)

Table A.26. Parameters ρ_L and ρ_T for liquid **Au-Cu** binary alloys obtained from linear fits to the experimental data from Ref. [104]. The liquidus temperatures T_L are picked from Ref. [154]. For the parameters of pure Au, also compare Tab. A.15.

System	T_L(K)	$\rho_L(\mathrm{g \cdot cm^{-3}})$	$\rho_T\ (10^{-4}\mathrm{g \cdot cm^{-3}K^{-1}})$
$Au_{25}Cu_{75}$	1243	11.39	-19.5
$Au_{50}Cu_{50}$	1193	13.5	-12.6
$Au_{75}Cu_{25}$	1215	15.67	-17.6
Au	1337	17.39	-11.0

A.9 Co-Sn

A.9.1 Co-Sn (Viscosity)

Table A.27. Parameters η_∞ and E_A for liquid **Co-Sn** binary alloys from Ref. [256].

System	η_∞(mPa · s)	$E_A\ (10^4\mathrm{J/mol})$
Co_3Sn_{97}	0.273	1.17
Co_5Sn_{95}	0.256	1.39
$Co_{10}Sn_{90}$	0.246	1.53
$Co_{15}Sn_{85}$	0.254	1.58
$Co_{20}Sn_{80}$	0.318	1.78
$Co_{50}Sn_{50}$	0.245	2.95
$Co_{60}Sn_{40}$	0.186	3.63
$Co_{70}Sn_{30}$	0.214	3.64
$Co_{80}Sn_{20}$	0.072	5.44
Co	0.048	6.81

A.10 Co-Cu-Fe

A.10.1 Co-Fe (Density)

Table A.28. Parameters ρ_L and ρ_T for liquid **Co-Fe** binary alloys obtained from linear fits to the experimental data from Ref. [134]. The liquidus temperatures T_L are picked from Ref. [154].

System	T_L(K)	ρ_L(g · cm^{-3})	ρ_T (10^{-4}g · cm^{-3}K^{-1})
Co	1768	7.81	-8.85
$Co_{75}Fe_{25}$	1752	-9.54	1.26
$Co_{50}Fe_{50}$	1752	7.43	-7.48
$Co_{25}Fe_{75}$	1767	7.21	-3.32
Fe	1811	7.04	-10.8

A.10.2 Cu-Fe (Density)

Table A.29. Parameters ρ_L and ρ_T for liquid **Cu-Fe** binary alloys obtained from linear fits to the experimental data from Ref. [134]. The liquidus temperatures T_L are picked from Ref. [154]. In the case of $Cu_{30}Fe_{70}$, only a single data point is measured at 1756 K due to problems with pronounced evaporation of this material.

System	T_L(K)	ρ_L(g · cm^{-3})	ρ_T (10^{-4}g · cm^{-3}K^{-1})
Fe	1811	7.04	-10.8
$Cu_{30}Fe_{70}$	1728	at 1756 K: 7.14 g · cm^{-3}	
$Cu_{70}Fe_{30}$	1693	7.37	-7.90
$Cu_{80}Fe_{20}$	1673	7.48	-8.13
$Cu_{90}Fe_{10}$	1578	7.67	-8.57
Cu	1357	7.90	-7.65

A.10.3 Cu-Fe (Surface tension)

Table A.30. Parameters γ_L and γ_T for liquid **Cu-Fe** binary alloys obtained from linear fits to the experimental data from Ref. [68]. The liquidus temperatures T_L are picked from Ref. [154]. The parameters of $Cu_{20}Fe_{80}$ in the bottom most line are taken from Ref. [239]. Obviously, the sign of γ_T is positive. This is discussed in detail in Chap. 4.

System	T_L(K)	γ_L(Nm^{-1})	γ_T (10^{-4}Nm^{-1}K^{-1})
$Cu_{80}Fe_{20}$	1658	1.24	-3.8
$Cu_{60}Fe_{40}$	1697	1.22	-4.4
$Cu_{40}Fe_{60}$	1708	1.24	-4.9
$Cu_{20}Fe_{80}$	1736	1.4	-6.4
$Cu_{20}Fe_{80}$	1736	1.30	+1.37

A.10.4 Co-Cu (Density)

Table A.31. Parameters ρ_L and ρ_T for liquid **Co-Cu** binary alloys obtained from linear fits to the experimental data from Ref. [134]. The liquidus temperatures T_L are picked from Ref. [154].

System	T_L(K)	ρ_L(g · cm^{-3})	ρ_T (10^{-4}g · cm^{-3}K^{-1})
Co	1768	7.81	-8.85
$Co_{85}Cu_{15}$	1713	7.74	-11.6
$Co_{75}Cu_{25}$	1687	7.75	-9.4
$Co_{50}Cu_{50}$	1652	7.66	-7.2
$Co_{25}Cu_{75}$	1628	7.69	-7.2
Cu	1357	7.90	-7.65

A.10.5 Co-Cu-Fe (Density)

Table A.32. Parameters ρ_L and ρ_T for liquid **Co-Cu-Fe** ternary alloys obtained from linear fits to the experimental data from Ref. [134]. The liquidus temperatures T_L are picked from Ref. [154].

System	T_L(K)	ρ_L(g · cm^{-3})	ρ_T (10^{-4}g · cm^{-3}K^{-1})
$Co_{50}Fe_{50}$	1752	7.43	-7.48
$Co_{40}Cu_{20}Fe_{40}$	1696	7.47	-13.7
$Co_{30}Cu_{40}Fe_{30}$	1675	7.48	-10.3
$Co_{20}Cu_{60}Fe_{20}$	1662	7.53	-11.7
$Co_{70}Cu_{15}Fe_{15}$	1656	7.57	-11.5
$Co_{10}Cu_{80}Fe_{10}$	1639	7.63	-7.79
$Co_5Cu_{90}Fe_5$	1558	7.71	-4.99
Cu	1357	7.90	-7.65
$Co_{20}Cu_{20}Fe_{60}$	1711	7.26	-8.39
$Co_{40}Cu_{20}Fe_{40}$	1696	7.47	-13.7
$Co_{60}Cu_{20}Fe_{20}$	1693	7.61	-10.5

A.10.6 Co-Cu-Fe (Surface tension)

Table A.33. Parameters γ_L and γ_T for liquid **Co-Cu-Fe** ternary alloys obtained from linear fits to the experimental data from Ref. [240]. For the liquidus temperatures T_L see references in Ref. [240].

System	T_L(K)	γ_L(Nm^{-1})	γ_T (10^{-4}Nm^{-1}K^{-1})
$Co_{50}Fe_{50}$	1752	1.82	-3.72
$Co_{40}Cu_{20}Fe_{40}$	1696	1.30	-2.25
$Co_{30}Cu_{40}Fe_{30}$	1675	1.17	+0.75
$Co_{20}Cu_{60}Fe_{20}$	1662	1.21	-2.85
$Co_{10}Cu_{80}Fe_{10}$	1639	1.22	-2.0
Cu	1358	1.30	-2.34
$Cu_{20}Fe_{80}$	1736	1.30	+1.37
$Co_{20}Cu_{20}Fe_{60}$	1711	1.30	-2.25
$Co_{60}Cu_{20}Fe_{20}$	1693	1.35	-4.8
$Co_{80}Cu_{20}$	1698	1.40	-2.0

A.11 Cu-Co-Ni

A.11.1 Co-Cu-Ni (Density)

Table A.34. Parameters ρ_L and ρ_T for liquid **Co-Cu-Ni** ternary alloys obtained from linear fits to the experimental data from Ref. [159]. The liquidus temperatures T_L are determined by means of the DSC/DTA technique, see Ref. [159].

System	T_L(K)	$\rho_L(\mathrm{g \cdot cm^{-3}})$	$\rho_T\ (10^{-4}\mathrm{g \cdot cm^{-3}K^{-1}})$
$Co_{80}Ni_{20}$	1758	8.10	-7.6
$Co_{70}Cu_{10}Ni_{20}$	1721	8.25	-11.7
$Co_{50}Cu_{30}Ni_{20}$	1654	8.17	-12.6
$Co_{40}Cu_{40}Ni_{20}$	1621	8.22	-8.1
$Co_{30}Cu_{50}Ni_{20}$	1590	8.19	-10.9
$Co_{10}Cu_{70}Ni_{20}$	1508	8.21	-8.0
$Cu_{80}Ni_{20}$	1473	8.13	-9.6
$Co_{50}Cu_{50}$	1650	7.66	-7.2
$Co_{40}Cu_{40}Ni_{20}$	1621	8.22	-8.1
$Co_{35}Cu_{35}Ni_{30}$	1641	8.40	-9.1
$Co_{30}Cu_{30}Ni_{40}$	1642	8.22	-16.7
$Co_{20}Cu_{20}Ni_{60}$	1643	8.24	-14.6
$Co_{15}Cu_{15}Ni_{70}$	1685	8.13	-8.7
$Co_{10}Cu_{10}Ni_{80}$	1685	8.25	-12.1
Ni	1728	7.93	-10.1

A.11.2 Co-Cu-Ni (Surface tension)

Table A.35. Parameters γ_L and γ_T for liquid **Co-Cu-Ni** ternary alloys obtained from linear fits to the experimental data from Ref. [159]. The liquidus temperatures T_L are determined by means of the DSC/DTA technique, see Ref. [159].

System	T_L(K)	γ_L(Nm^{-1})	γ_T (10^{-4}Nm^{-1}K^{-1})
$Co_{50}Cu_{50}$	1650	1.23	-2.9
$Co_{40}Cu_{40}Ni_{20}$	1621	1.35	-6.5
$Co_{30}Cu_{30}Ni_{40}$	1642	1.43	-3.6
$Co_{20}Cu_{20}Ni_{60}$	1643	1.48	-7.6
$Co_{10}Cu_{10}Ni_{80}$	1685	1.59	-1.5
Ni	1728	1.78	-3.8
$Co_{70}Cu_{10}Ni_{20}$	1721	1.61	-4.4
$Co_{30}Cu_{50}Ni_{20}$	1654	1.40	-2.3
$Co_{50}Cu_{30}Ni_{20}$	1590	1.36	-2.6
$Co_{70}Cu_{10}Ni_{20}$	1508	1.33	-5.0
$Co_{80}Ni_{20}$	1473	1.34	-2.2

A.11.3 Co-Cu-Ni (Viscosity)

Table A.36. Parameters η_∞ and E_A for liquid **Co-Cu-Ni** binary alloys from Ref. [159].

System	η_∞(mPa · s)	E_A (10^4J/mol)
$Co_{80}Ni_{20}$	0.21777	4.58
$Co_{70}Cu_{10}Ni_{20}$	0.23702	4.24
$Co_{50}Cu_{30}Ni_{20}$	0.33474	3.74
$Co_{40}Cu_{40}Ni_{20}$	0.35459	3.45
$Co_{30}Cu_{50}Ni_{20}$	0.39665	3.22
$Co_{10}Cu_{70}Ni_{20}$	0.40564	3.11
$Cu_{80}Ni_{20}$	0.40959	3.37

A.12 Cu-Fe-Ni

A.12.1 Cu-Ni (Density)

Table A.37. Parameters ρ_L and ρ_T for liquid **Cu-Ni** binary alloys obtained from linear fits to the experimental data from Ref. [61]. The liquidus temperatures T_L are picked from Ref. [154].

System	T_L(K)	$\rho_L(\mathrm{g \cdot cm^{-3}})$	$\rho_T\ (10^{-4}\mathrm{g \cdot cm^{-3}K^{-1}})$
Cu	1357	7.90	-7.65
$Cu_{90}Ni_{10}$	1409	7.97	-7.95
$Cu_{80}Ni_{20}$	1473	8.09	-9.57
$Cu_{60}Ni_{40}$	1553	8.13	-10.3
$Cu_{50}Ni_{50}$	1593	8.10	-7.72
$Cu_{30}Ni_{70}$	1653	8.06	-9.11
$Cu_{10}Ni_{90}$	1706	7.96	-9.26
Ni	1727	7.92	-10.1

A.12.2 Cu-Ni (Surface tension)

Table A.38. Parameters γ_L and γ_T for liquid **Cu-Ni** binary alloys obtained from linear fits to the experimental data from Ref. [68]. The liquidus temperatures T_L are picked from Ref. [154].

System	T_L(K)	$\gamma_L(\mathrm{Nm^{-1}})$	$\gamma_T\ (10^{-4}\mathrm{Nm^{-1}K^{-1}})$
Ni	1727	1.77	-3.3
$Cu_{10}Ni_{90}$	1706	1.61	-0.67
$Cu_{20}Ni_{80}$	1690	1.51	-0.21
$Cu_{30}Ni_{70}$	1660	1.43	-0.84
$Cu_{40}Ni_{60}$	1620	1.38	-0.45
$Cu_{50}Ni_{50}$	1584	1.37	-0.94
$Cu_{60}Ni_{40}$	1553	1.36	-1.91
$Cu_{70}Ni_{30}$	1508	1.32	-3.24
$Cu_{80}Ni_{20}$	1462	1.34	-2.17
$Cu_{90}Ni_{10}$	1409	1.31	-2.21
Cu	1358	1.29	-2.3

A.12.3 Fe-Ni (Density)

Table A.39. Parameters ρ_L and ρ_T for liquid **Fe-Ni** binary alloys obtained from linear fits to the experimental data from Ref. [61]. The liquidus temperatures T_L are picked from Ref. [154]. Compare with data listed in Tab. A.48.

System	T_L(K)	$\rho_L(\mathrm{g \cdot cm^{-3}})$	$\rho_T\ (10^{-4}\mathrm{g \cdot cm^{-3}K^{-1}})$
Fe	1811	7.04	-10.8
$Fe_{80}Ni_{20}$	1753	7.32	-10.0
$Fe_{60}Ni_{40}$	1725	7.43	-11.5
$Fe_{50}Ni_{50}$	1716	7.50	-10.2
$Fe_{40}Ni_{60}$	1713	7.51	-10.6
$Fe_{20}Ni_{80}$	1713	7.87	-12.3
Ni	1727	7.93	-10.1

A.12.4 Fe-Ni (Surface tension)

Table A.40. Parameters γ_L and γ_T for liquid **Fe-Ni** binary alloys obtained from linear fits to the experimental data from Ref. [68]. The liquidus temperatures T_L are picked from Ref. [154]. The value of γ_L of $Fe_{25}Ni_{75}$ is re-evaluated in this table from the original data, due to an obvious misprint in Ref. [68]. The parameters of $Fe_{60}Ni_{40}$ are taken from Ref. [239], see Tab. A.42.

System	T_L(K)	$\gamma_L(\mathrm{Nm^{-1}})$	$\gamma_T\ (10^{-4}\mathrm{Nm^{-1}K^{-1}})$
Ni	1727	1.77	-3.3
$Fe_{25}Ni_{75}$	1713	1.86	-2.76
$Fe_{50}Ni_{50}$	1713	1.91	-3.27
$Fe_{60}Ni_{40}$	1725	1.91	-3.27
$Fe_{75}Ni_{25}$	1746	1.93	-1.73
Fe	1818	1.92	-3.97

A.12.5 Cu-Fe-Ni (Density)

Table A.41. Parameters ρ_L, β, and ρ_T for liquid **Cu-Fe-Ni** ternary alloys obtained from linear fits to the experimental data from Ref. [161]. The liquidus temperatures T_L are picked from Ref. [154]. ρ_T is hereby obtained from the published values of β via $\rho_T = \rho_L\beta$.

System	T_L(K)	$\rho_L(\mathrm{g \cdot cm^{-3}})$	$\beta(10^{-4}K^{1})$	$\rho_T(10^{-4}\mathrm{g \cdot cm^{-3}K^{-1}})$
$Cu_{13}Fe_{54}Ni_{33}$	1692	7.11	0.4	-2.8
$Cu_{40}Fe_{35}Ni_{25}$	1610	7.14	1.1	-7.9
$Cu_{50}Fe_{30}Ni_{20}$	1591	7.20	0.5	-3.6
$Cu_{60}Fe_{24}Ni_{26}$	1580	7.53	2.6	-19.6
$Cu_{70}Fe_{13}Ni_{27}$	1546	7.76	1.5	-11.6
$Cu_{20}Fe_{65}Ni_{15}$	1701	7.16	2.0	-14.3
$Cu_{20}Fe_{48}Ni_{32}$	1669	7.40	2.3	-17.0
$Cu_{20}Fe_{35}Ni_{45}$	1663	7.42	1.4	-10.4
$Cu_{20}Fe_{20}Ni_{60}$	1668	7.56	1.1	-8.3
$Cu_{20}Fe_{10}Ni_{70}$	1673	7.79	1.1	-8.6

A.12.6 Cu-Fe-Ni (Surface tension)

Table A.42. Parameters γ_L and γ_T for liquid **Cu-Fe-Ni** ternary alloys obtained from linear fits to the experimental data from Ref. [161]. The liquidus temperatures T_L are picked from Ref. [154].

System	T_L(K)	γ_L(Nm^{-1})	γ_T (10^{-4}Nm^{-1}K^{-1})
$Fe_{60}Ni_{40}$	1725	1.91	-3.27
$Cu_{13}Fe_{54}Ni_{33}$	1692	1.45	-1.88
$Cu_{30}Fe_{42}Ni_{28}$	1638	1.29	-1.09
$Cu_{40}Fe_{35}Ni_{25}$	1610	1.28	-2.95
$Cu_{50}Fe_{30}Ni_{20}$	1591	1.26	-2.36
$Cu_{60}Fe_{24}Ni_{16}$	1580	1.24	-4.93
$Cu_{70}Fe_{13}Ni_{17}$	1546	1.30	-5.30
$Cu_{20}Fe_{80}$	1736	1.30	+1.37
$Cu_{20}Fe_{65}Ni_{15}$	1701	1.34	-2.9
$Cu_{20}Fe_{48}Ni_{32}$	1669	1.38	-2.11
$Cu_{20}Fe_{35}Ni_{45}$	1663	1.42	-1.78
$Cu_{20}Fe_{20}Ni_{60}$	1668	1.44	-1.9

A.12.7 Cu-Fe-Ni (Viscosity)

Table A.43. Parameters η_∞ and E_A for liquid **Cu-Fe-Ni** ternary alloys from Ref. [248]. For the source of the liquidus temperatures T_L, see Ref. [248].

System	T_L(K)	η_∞(mPa · s)	E_A (10^{4}J/mol)
$Cu_{64}Fe_{19}Ni_{17}$	1564	0.375	3.141
$Cu_{40}Fe_{35}Ni_{25}$	1612	0.313	3.519
$Cu_{20}Fe_{48}Ni_{32}$	1668	0.242	4.151
$Cu_{13}Fe_{54}Ni_{33}$	1690	0.244	4.232
$Cu_{7.5}Fe_{55.5}Ni_{37}$	1706	0.252	4.240

A.13 Cu-Ti

A.13.1 Cu-Ti (Density)

Table A.44. Parameters ρ_L and ρ_T for liquid **Cu-Ti** binary alloys obtained from linear fits to the experimental data from Ref. [135]. The liquidus temperatures T_L are picked from Ref. [319].

System	T_L(K)	$\rho_L(\mathrm{g \cdot cm^{-3}})$	ρ_T ($10^{-4}\mathrm{g \cdot cm^{-3}K^{-1}}$)
Cu	1358	7.9	-7.6
$Cu_{90}Ti_{10}$	1293	7.3	-3.2
$Cu_{80}Ti_{20}$	1204	6.9	-8.7
$Cu_{70}Ti_{30}$	1190	6.3	-5.8
$Cu_{60}Ti_{40}$	1238	6.1	-12.3
$Cu_{50}Ti_{50}$	1254	5.3	-5.5
$Cu_{40}Ti_{60}$	1253	5.0	-6.2
$Cu_{30}Ti_{70}$	1415	4.6	-1.3
$Cu_{20}Ti_{80}$	1641	4.6	-1.0
$Cu_{10}Ti_{90}$	1807	4.3	-4.6
Ti	1941	4.1	-3.3

A.13.2 Cu-Ti (Surface tension)

Table A.45. Parameters γ_L and γ_T for liquid **Cu-Ti** binary alloys obtained from linear fits to the experimental data from Ref. [206]. The liquidus temperatures T_L are picked from Ref. [319].

System	T_L(K)	$\gamma_L(\mathrm{Nm^{-1}})$	γ_T ($10^{-4}\mathrm{Nm^{-1}K^{-1}}$)
Cu	1358	1.33	-2.3
$Cu_{90}Ti_{10}$	1293	1.37	-2.2
$Cu_{80}Ti_{20}$	1204	1.42	-2.2
$Cu_{70}Ti_{30}$	1193	1.45	-2.1
$Cu_{60}Ti_{40}$	1235	1.47	-2.1
$Cu_{50}Ti_{50}$	1256	1.50	-2.1
$Cu_{40}Ti_{60}$	1255	1.51	-1.9
$Cu_{30}Ti_{70}$	1414	1.51	-1.9
$Cu_{20}Ti_{80}$	1638	1.49	-1.8
Ti	1943	1.49	-1.7

A.14 Cr-Fe-Ni

A.14.1 Cr-Fe (Density)

Table A.46. Parameters ρ_L and ρ_T for liquid **Cr-Fe** binary alloys obtained from linear fits to the experimental data from Ref. [123]. The liquidus temperatures T_L are picked from Ref. [154].

System	T_L(K)	ρ_L(g · cm^{-3})	ρ_T (10^{-4}g · cm^{-3}K^{-1})
$Cr_{10}Fe_{90}$	1805	6.98	-5.40
$Cr_{20}Fe_{80}$	1800	6.92	-8.62
$Cr_{40}Fe_{60}$	1873	6.78	-5.42
$Cr_{60}Fe_{40}$	2006	6.52	-5.97

A.14.2 Cr-Ni (Density)

Table A.47. Parameters ρ_L and ρ_T for liquid **Cr-Ni** binary alloys obtained from linear fits to the experimental data from Ref. [123]. The liquidus temperatures T_L are picked from Ref. [154].

System	T_L(K)	ρ_L(g · cm^{-3})	ρ_T (10^{-4}g · cm^{-3}K^{-1})
$Cr_{10}Ni_{90}$	1710	7.69	-7.90
$Cr_{20}Ni_{80}$	1700	7.51	-7.92
$Cr_{40}Ni_{60}$	1648	7.28	-6.08
$Cr_{60}Ni_{40}$	1710	6.97	-6.57

A.14.3 Fe-Ni (Density)

Table A.48. Parameters ρ_L and ρ_T for liquid **Fe-Ni** binary alloys obtained from linear fits to the experimental data from Ref. [123]. The liquidus temperatures T_L are picked from Ref. [154]. See also Tab. A.39.

System	T_L(K)	$\rho_L(\mathrm{g \cdot cm^{-3}})$	$\rho_T\ (10^{-4}\mathrm{g \cdot cm^{-3}K^{-1}})$
Ni	1728	7.82	-8.56
$Fe_{20}Ni_{80}$	1726	7.69	-7.60
$Fe_{40}Ni_{60}$	1723	7.37	-5.58
$Fe_{60}Ni_{40}$	1723	7.21	-6.60
$Fe_{70}Ni_{30}$	1748	7.10	-5.66
$Fe_{80}Ni_{20}$	1773	7.06	-6.05
Fe	1808	6.99	-5.55

A.14.4 Cr-Fe-Ni (Density)

Table A.49. Parameters ρ_L and ρ_T for liquid **Cr-Fe-Ni** ternary alloys obtained from linear fits to the experimental data from Ref. [160]. The liquidus temperatures T_L are picked from Ref. [320].

System	T_L(K)	$\rho_L(\mathrm{g \cdot cm^{-3}})$	$\rho_T\ (10^{-4}\mathrm{g \cdot cm^{-3}K^{-1}})$
$Cr_{10}Fe_{18}Ni_{72}$	1724	7.50	-3.76
$Cr_{10}Fe_{36}Ni_{54}$	1724	7.33	-4.10
$Cr_{10}Fe_{54}Ni_{36}$	1722	7.18	-5.72
$Cr_{10}Fe_{63}Ni_{27}$	1734	7.10	-6.13
$Cr_{10}Fe_{72}Ni_{18}$	1748	7.09	-6.04
$Cr_{20}Fe_{16}Ni_{64}$	1690	7.16	-6.87
$Cr_{20}Fe_{32}Ni_{48}$	1690	7.05	-5.58
$Cr_{20}Fe_{48}Ni_{32}$	1698	6.95	-6.36
$Cr_{20}Fe_{56}Ni_{24}$	1710	6.93	-7.03
$Cr_{20}Fe_{64}Ni_{16}$	1710	6.89	-9.39
$Cr_{40}Fe_{12}Ni_{48}$	1640	8.011	-6.34
$Cr_{40}Fe_{24}Ni_{36}$	1635	8.064	-7.47
$Cr_{40}Fe_{36}Ni_{24}$	1723	7.882	-6.27
$Cr_{40}Fe_{48}Ni_{12}$	1798	7.911	-7.92

A.14.5 Cr-Fe-Ni (Viscosity)

Table A.50. Parameters η_∞ and E_A for liquid **Cr-Fe-Ni** ternary alloys from Ref. [160].

System	η_∞(mPa · s)	E_A (10^4J/mol)
$Cr_{20}Ni_{80}$	0.256	4.48
$Cr_{20}Fe_{16}Ni_{64}$	0.299	4.13
$Cr_{20}Fe_{32}Ni_{48}$	0.264	4.55
$Cr_{20}Fe_{48}Ni_{32}$	0.455	3.98
$Cr_{20}Fe_{64}Ni_{16}$	0.191	5.22
$Cr_{20}Fe_{80}$	0.082	6.78
Fe	0.114	5.93

B Redlich-Kister parameters

The tables in this chapter contain Redlich-Kister parameters used in order to calculate the excess free energy ${}^{\mathrm{E}}G$ from Eqs. (3.17) and 3.16. The references to these parameters are specified as well as the chapters, tables and figures in which they are used in the present work.

In order to ease working with this chapter, the following Tab. B.1 assigns all systems, binary and ternary ones, to tables below where the corresponding parameters for the calculation of ${}^{\mathrm{E}}G$ are listed.

Table B.1. Reference to tables showing Redlich-Kister parameters for the calculation of ${}^{E}G$ using Eqs. (3.16) and (3.17) for binary and ternary liquid alloy systems.

System	Table
Ag-Al	B.3
Ag-Al-Cu	B.3
Al-Au	B.4
Ag-Cu	B.3
Al-Cu	B.3
	B.2
	B.5
Al-Cu-Si	B.5
Al-Fe	B.6
Al-In	B.7
Al-Ni	B.8
Al-Si	B.5
Co-Cu	B.10
	B.11
Co-Cu-Ni	B.11
Co-Cu-Fe	B.10
Co-Fe	B.10
Co-Ni	B.11
Co-Sn	B.9
Cu-Fe	B.12
	B.10
Cu-Fe-Ni	B.12
Cu-Ni	B.11
	B.12
Cu-Si	B.5
Fe-Ni	B.12
	B.14
Cu-Ti	B.13
Cr-Fe	B.14
Cr-Ni	B.14
Cr-Fe-Ni	B.14

B.1 Ag-Al-Cu

Parameters used in order to calculate the excess free energy ${}^{\mathrm{E}}G$ using Eqs. (3.17) and (3.16) for binary and ternary liquid alloys of the Al-Cu-Ag system are shown in Tab. B.3. These parameters are used in order to calculate the surface tension via the Butler equation, Eq. (4.32) and the Chatain model Eq. (4.36). The surface tension of liquid Al-Cu, however, is calculated in [69] using the parameters listed in Tab. B.2. For further explanation, see Ref. [69].

Results of these calculations are shown in Figs. 4.24, 4.25, 4.26 and 4.28. Moreover, they are summarized in Tabs. 4.13 and 4.15.

In addition to surface tension, the viscosity is calculated using the parameters in Tab. B.3. Results are shown in Figs. 5.10, 5.11 and 5.12 as well as in Tabs. 5.9, 5.10 and 5.12.

Table B.2. Redlich-Kister parameters of **Al-Cu** used in Eq. (3.16). The parameters are taken from Ref. [321].

Parameter	(J mol^{-1})
${}^{0}L_{\mathrm{Al,Cu}}$	$-66622 + 8.1T$
${}^{1}L_{\mathrm{Al,Cu}}$	$46800 - 90.8T + 10T\ln(T)$
${}^{1}L_{\mathrm{Al,Cu}}$	-2812

Table B.3. Redlich-Kister parameters of **Al-Cu-Ag** used in Eq. (3.17). The parameters are taken from Refs. [242; 243]. Note that the parameters corresponding to binary Al-Cu differ from those in Tab. B.2.

Parameter	(J mol^{-1})
${}^{0}L_{\mathrm{Al,Cu}}$	$-67094 + 8.555T$
${}^{1}L_{\mathrm{Al,Cu}}$	$32148 - 7.118T$
${}^{2}L_{\mathrm{Al,Cu}}$	$5915 - 5.889T$
${}^{3}L_{\mathrm{Al,Cu}}$	$-8175 + 6.049T$
${}^{0}L_{\mathrm{Ag,Al}}$	$-15022 - 20.538T$
${}^{1}L_{\mathrm{Ag,Al}}$	$-20456 - 17.291T$
${}^{2}L_{\mathrm{Ag,Al}}$	$-3821 - 17.17T$
${}^{3}L_{\mathrm{Ag,Al}}$	$7028 - 12.247T$
${}^{4}L_{\mathrm{Ag,Al}}$	$7661 - 5.857T$
${}^{0}L_{\mathrm{Ag,Cu}}$	$14463 - 1.516T$
${}^{1}L_{\mathrm{Ag,Cu}}$	$-934 - 0.319T$

B.2 Al-Au

Parameters used in order to calculate the excess free energy ${}^{\mathrm{E}}G$ using Eq. (3.16) for liquid Al-Au are shown in Tab. B.4. These parameters are used in order to calculate the surface tension from the Butler equation, Eq. (4.32) and the Chatain model, Eq. (4.36). Results of these calculations are shown in Figs. 4.20, 4.21 and 4.28. They are summarized in Tabs. 4.13 and 4.15.

Table B.4. Redlich-Kister parameters of **Al-Au** used in Eq. (3.17). The parameters are taken from Ref. [322].

Parameter	(J mol^{-1})
${}^{0}L_{\mathrm{Al,Au}}$	$-131996.19 + 36.42T$
${}^{1}L_{\mathrm{Al,Au}}$	$40781.83 - 1.896T$

B.3 Al-Cu-Si

Parameters used in order to calculate the excess free energy ${}^{\mathrm{E}}G$ using Eqs. (3.17) and (3.16) for binary and ternary liquid alloys of the Al-Cu-Si system are shown in Tab. B.5. These parameters are used in order to calculate the surface tension via the Butler equation, Eq. (4.32).

Results of these calculations are summarized in Tabs. 4.13 and 4.15. In addition to surface tension, the viscosity is also calculated using the parameters in Tab. B.5. The results are discussed in Tabs. 5.9, 5.10 and 5.12.

Table B.5. Redlich-Kister parameters of **Al-Cu-Si** used in Eq. (3.17). The parameters are taken from Ref. [323].

Parameter	(J mol^{-1})
${}^{0}L_{\mathrm{Al,Cu}}$	$-66622 + 8.1T$
${}^{1}L_{\mathrm{Al,Cu}}$	$46800 - 90.8T + 10T\ln(T)$
${}^{2}L_{\mathrm{Al,Cu}}$	-2812
${}^{0}L_{\mathrm{Al,Si}}$	$-11340.1 - 1.23394T$
${}^{1}L_{\mathrm{Al,Si}}$	$-3530.93 + 1.35993T$
${}^{2}L_{\mathrm{Al,Si}}$	2265.39
${}^{0}L_{\mathrm{Cu,Si}}$	$-38763.5 + 12T$
${}^{1}L_{\mathrm{Cu,Si}}$	$-52431.2 + 27.4571T$
${}^{2}L_{\mathrm{Cu,Si}}$	$-29426.5 + 14.775T$
${}^{T}G$	$x_{\mathrm{Al}}{}^{0}L_{\mathrm{Al,Cu,Si}} + x_{\mathrm{Cu}}{}^{1}L_{\mathrm{Al,Cu,Si}} + x_{\mathrm{Si}}{}^{2}L_{\mathrm{Al,Cu,Si}}$
whereas ${}^{\nu}L_{\mathrm{Al,Cu,Si}}$ are defined as follows:	
${}^{0}L_{\mathrm{Al,Cu,Si}}$	$129.758.274 - 152.551977T$
${}^{1}L_{\mathrm{Al,Cu,Si}}$	$154448.454 - 8.5615T$
${}^{2}L_{\mathrm{Al,Cu,Si}}$	$-88726.6292 + 40T$

B.4 Al-Fe

Parameters used in order to calculate the excess free energy ${}^{\mathrm{E}}G$ using Eq. (3.16) for binary liquid alloys of the Al-Fe system are shown in Tab. B.6. These parameters are used in order to calculate the surface tension using the Butler equation, Eq. (4.32).

Results of these calculations are shown in Fig. 4.28 and summarized in Tabs. 4.13 and 4.15.

Table B.6. Redlich-Kister parameters of **Al-Fe** used in Eq. (3.17). The parameters are taken from Ref. [324].

Parameter	(J mol^{-1})
${}^{0}L_{\mathrm{Al,Fe}}$	$-88090 + 19.8T$
${}^{1}L_{\mathrm{Al,Fe}}$	$-3800 + 3T$
${}^{2}L_{\mathrm{Al,Fe}}$	-2000

B.5 Al-In

Parameters used in order to calculate the excess free energy ${}^{\mathrm{E}}G$ using Eq. (3.16) for binary liquid alloys of the Al-In system are shown in Tab. B.7. These parameters are used in order to calculate the liquid-liquid interfacial energy via the model proposed in Sec. 7.2.

Results of these calculations are shown in Fig. 7.4 and 7.5.

Table B.7. Redlich-Kister parameters of **Al-In** used in Eq. (7.4). The parameters are taken from Ref. [302].

Parameter	(J mol^{-1})
${}^{0}L_{\mathrm{Al,In}}$	$39887.4 - 19.1T$
${}^{1}L_{\mathrm{Al,In}}$	$254.64 - 0.8T$

B.6 Al-Ni

Parameters used in order to calculate the excess free energy ${}^{\mathrm{E}}G$ using Eq. (3.16) for binary liquid alloys of the Al-Ni system are shown in Tab. B.8. These parameters are used in order to calculate the surface tension via the Butler equation, Eq. (4.32), and the Chatain model, Eq. (4.36).

Results of these calculations are shown in Figs. 4.19 and 4.28 and summarized in Tabs. 4.13 and 4.15.

Table B.8. Redlich-Kister parameters of **Al-Ni** used in Eq. (3.17). The parameters are taken from Ref. [325].

Parameter	(J mol^{-1})
${}^{0}L_{\mathrm{Al,Ni}}$	$-197088 + 30.353T$
${}^{1}L_{\mathrm{Al,Ni}}$	5450
${}^{2}L_{\mathrm{Al,Ni}}$	$54624 - 11.383T$

B.7 Co-Sn

Parameters used in order to calculate the excess free energy ${}^{\mathrm{E}}G$ and the enthalpy of mixing, ΔH, using Eq. (3.16) of the Co-Sn system are shown in Tab. B.9. ΔH is hereby related to ${}^{\mathrm{E}}G$ via the following relation:

$$\Delta H = -T^2 \left(\frac{{}^{\mathrm{E}}G}{T} \right) \tag{B.1}$$

These parameters are used in order to calculate the viscosity using the models discussed in Section 5.

Results of these calculations are summarized in Tabs. 5.9, 5.10 and 5.12.

Table B.9. Redlich-Kister parameters of **Co-Sn** used in Eq. (3.17). The parameters are taken from Ref. [326].

Parameter	(J mol^{-1})
${}^{0}L_{\mathrm{Co,Sn}}$	$-75466.9610 + 39.6726T$
${}^{1}L_{\mathrm{Co,Sn}}$	$-30685.2702 + 15.0835T$

B.8 Cu-Co-Fe

Parameters used in order to calculate the excess free energy ${}^{E}G$ using Eqs. (3.17) and (3.16) for binary and ternary liquid alloys of the Cu-Co-Fe system are shown in Tab. B.10. These parameters are used in order to calculate the surface tension via the Butler equation, Eq. (4.32) and, additionally for Cu-Fe, the Chatain model Eq. (4.36).

Results of these calculations are shown in Figs. 4.15, 4.16, 4.21 and 4.27. They are summarized in Tabs. 4.13 and 4.15.

Table B.10. Redlich-Kister parameters of **Cu-Co-Fe** used in Eq. (3.17). The parameters are taken from Ref. [327].

Parameter	(J mol^{-1})
${}^{0}L_{\mathrm{Co,Cu}}$	$35200 - 4.95T$
${}^{1}L_{\mathrm{Co,Cu}}$	$-6695 + 4.68T$
${}^{0}L_{\mathrm{Fe,Co}}$	-9312
${}^{1}L_{\mathrm{Fe,Co}}$	1752
${}^{0}L_{\mathrm{Cu,Fe}}$	$36078.99 - 2.33T$
${}^{1}L_{\mathrm{Cu,Fe}}$	$324.53 - 0.033T$
${}^{2}L_{\mathrm{Cu,Fe}}$	$10355.39 - 3.60T$

B.9 Cu-Co-Ni

Parameters used in order to calculate the excess free energy ${}^{\mathrm{E}}G$ using Eqs. (3.17) and (3.16) for binary and ternary liquid alloys of the Cu-Co-Ni system are shown in Tab. B.11. These parameters are used in order to calculate the surface tension using the Butler equation, Eq. (4.32).

Results of these calculations are shown in Fig. 4.27 and are summarized in Tabs. 4.13 and 4.15.

In addition to surface tension, the viscosity is also calculated using the parameters in Tab. B.11. This is done by means of the models discussed in Section 5. The results are summarized in Tabs. 5.9, 5.10 and 5.12.

As the calculations are not part of Ref. [159], they are shown below in Fig. B.1.

Table B.11. Redlich-Kister parameters of **Cu-Co-Ni** used in Eq. (3.17). The parameters are taken from Ref. [328].

Parameter	(J mol^{-1})
${}^{0}L_{\mathrm{Co,Cu}}$	$31451.078 - 1.3140133T$
${}^{1}L_{\mathrm{Co,Cu}}$	-595.04051
${}^{2}L_{\mathrm{Co,Cu}}$	3701.3751
${}^{0}L_{\mathrm{Co,Ni}}$	1331
${}^{0}L_{\mathrm{Cu,Ni}}$	$11760 + 1.084T$
${}^{1}L_{\mathrm{Cu,Ni}}$	-1671.8
${}^{T}G$	$(-27500 + 15T)x_{\mathrm{Co}} - (15150)x_{\mathrm{Cu}}$

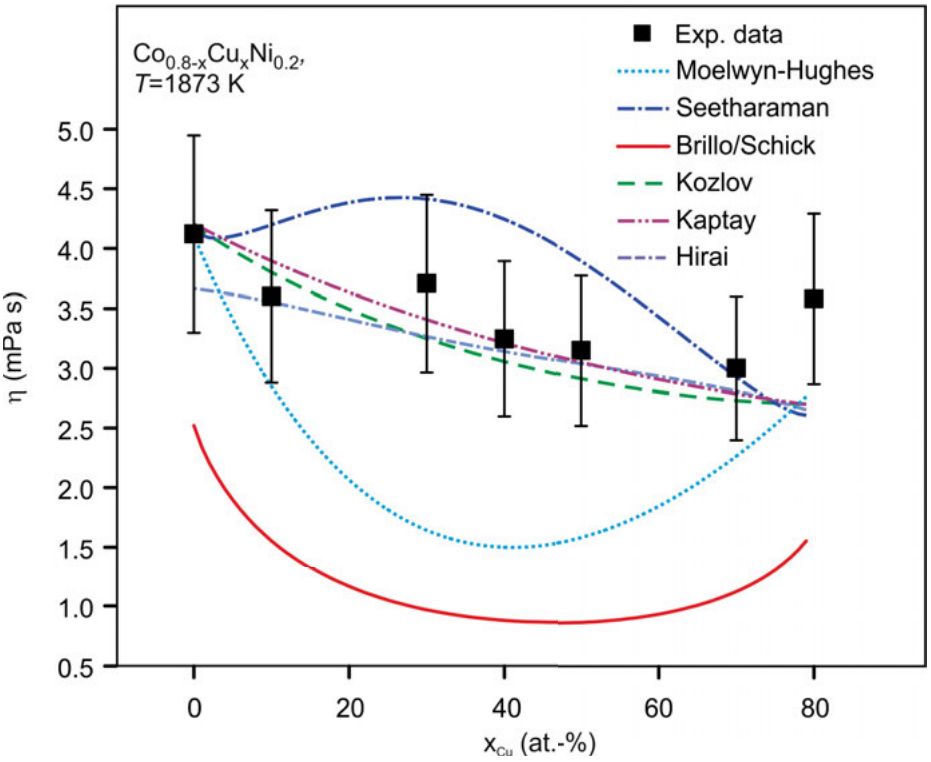

Fig. B.1. Measured viscosity of $Co_{0.8-x}Cu_xNi_{0.2}$ [159] versus x_{Cu} at T =1873 K. In addition, calculations of the models of Moelwyn/Hughes (dotted), Seetharaman (dash dotted), Brillo/Schick (solid), Kozlov (dashed), Kaptay (dash double-dotted), and Hirai (dot double-dashed) are shown.

B.10 Cu-Fe-Ni

Parameters used in order to calculate the excess free energy ${}^{\mathrm{E}}G$ using Eqs. (3.17) and (3.16) for binary and ternary liquid alloys of the Cu-Fe-Ni system are shown in Tab. B.12. These parameters are used in order to calculate the surface tension using the Butler equation, Eq. (4.32), as well as the Chatain model Eq. (4.36) for liquid Cu-Fe.

Results of these calculations are shown in Figs. 4.15, 4.16, 4.17, 4.18, 4.21, 4.22, 4.23, and 4.27. They are summarized in Tabs. 4.13 and 4.15.

In addition to surface tension, the viscosity is calculated using the parameters in Tab. B.12. This is done by means of the models discussed in Section 5. The results are shown in Fig. 5.13 and summarized in Tabs. 5.9, 5.10 and 5.12.

Table B.12. Redlich-Kister parameters of **Cu-Ni-Fe** used in Eq. (3.17). The parameters are taken from Ref. [235].

Parameter	(J mol^{-1})
${}^{0}L_{\mathrm{Fe,Ni}}$	$-18380 + 6.04T$
${}^{1}L_{\mathrm{Fe,Ni}}$	$9228 - 3.55T$
${}^{0}L_{\mathrm{Cu,Ni}}$	$11760 + 1.084T$
${}^{1}L_{\mathrm{Cu,Ni}}$	-1672
${}^{0}L_{\mathrm{Cu,Fe}}$	$36087.98 - 2.33T$
${}^{1}L_{\mathrm{Cu,Fe}}$	$324.53 - 0.033T$
${}^{2}L_{\mathrm{Cu,Fe}}$	$10355.39 - 3.603T$
${}^{T}G$	$-68786 + 30.9T$

B.11 Cu-Ti

Parameters used in order to calculate the excess free energy ${}^{\mathrm{E}}G$ using Eq. (3.16) for binary liquid Cu-Ti alloys are shown in Tab. B.13. These parameters are used in order to calculate the surface tension via the Butler equation, Eq. (4.32).

Results of these calculations are shown in Fig. 4.27 and summarized in Tabs. 4.13 and 4.15.

As the Butler equation, Eq. (4.32), is not discussed in Ref. [206], a depiction with this calculation is shown in Fig. B.2.

Table B.13. Redlich-Kister parameters of **Cu-Ti** used in Eq. (3.16). The parameters are taken from Ref. [329].

Parameter	(J mol^{-1})
${}^{0}L_{\mathrm{Cu,Ti}}$	$(-19330 + 7.651T)$
${}^{1}L_{\mathrm{Cu,Ti}}$	0
${}^{2}L_{\mathrm{Cu,Ti}}$	$9382 - 5.448T$

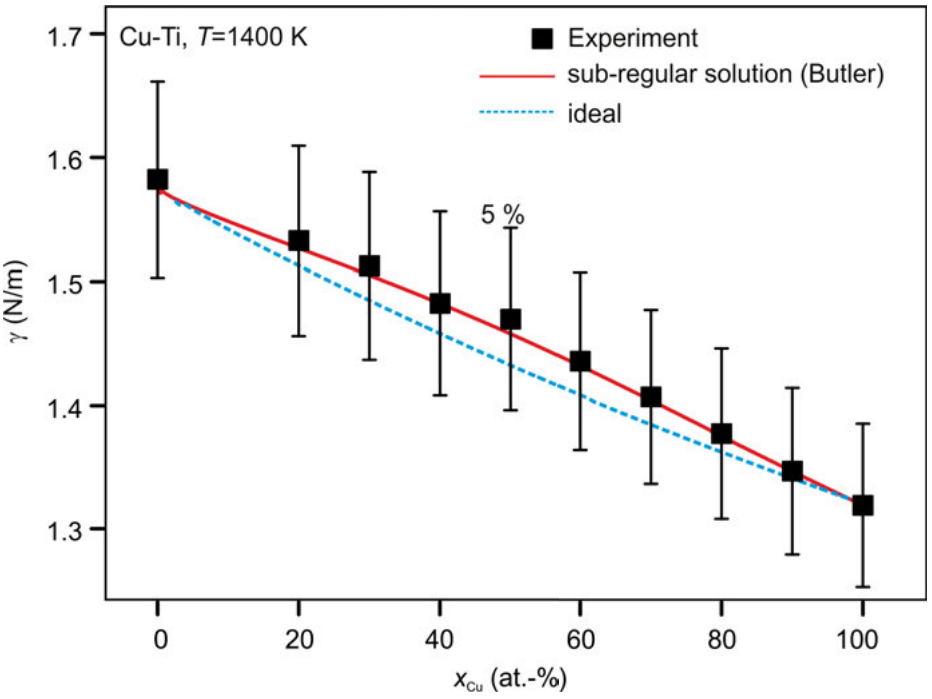

Fig. B.2. Isothermal surface tension γ versus x_{Ti}^{B} for liquid Cu-Ti at 1400 K (symbols). For comparison, calculations of the ideal solution model, Eq. (4.29) (dashed) and the Butler model, Eq. (4.32), (solid) are shown. Redlich-Kister parameters are used from Tab. B.13.

B.12 Cr-Fe-Ni

Parameters used in order to calculate the excess free energy ${}^{\mathrm{E}}G$ using Eqs. (3.17) and (3.16) for binary and ternary liquid alloys of the Cr-Fe-Ni system are shown in Tab. B.14. These parameters are used in order to calculate the surface tension via the Butler equation, Eq. (4.32). In the case of liquid binary Fe-Ni, however, the parameters listed in Tab. B.12 are used.

Results of these calculations are summarized in Tabs. 4.13 and 4.15.

In addition to surface tension, the viscosity is calculated using the parameters in Tab. B.14 in combination with the models discussed in Section 5. These parameters are used in [160] in order to apply the models for the viscosity of ternary Cr-Fe-Ni as well as for binary Fe-Ni alloys. The results are summarized in Tabs. 5.9, 5.10, 5.11 and 5.12.

Table B.14. Redlich-Kister parameters of **Cr-Fe-Ni** used in Eq. (3.17). The parameters are taken from Ref. [330].

Parameter	(J mol^{-1})
${}^{0}L_{\mathrm{Fe,Cr}}$	$-17737 + 7.997T$
${}^{1}L_{\mathrm{Fe,Cr}}$	1331
${}^{0}L_{\mathrm{Cr,Ni}}$	$318 - 7.332T$
${}^{1}L_{\mathrm{Cr,Ni}}$	$16941 - 6.37T$
${}^{0}L_{\mathrm{Fe,Ni}}$	$-16911 + 5.162T$
${}^{1}L_{\mathrm{Fe,Ni}}$	$10180 - 4.147T$
${}^{T}G$	$(80000 - 50T)x_{\mathrm{Fe}} + (130000 - 50T)x_{\mathrm{Cr}} + (60000 - 50T)x_{\mathrm{Ni}}$

Bibliography

[1] http://en.wikipedia.org/wiki/Timeline_of_ancient_history.

[2] SNL Metals and Mining, Raw Materials Group (RMG) Consulting and Analysis, Stockholm. Report - available on demand at http://go.snl.com/MEG-MS-FreeReport.html (2014).

[3] M. Holtzer, R. Danko, S. Ymankowska-Kumon. Metalurgija 51 (2012) 337.

[4] EUROPEAN COMMISSION, ENTERPRISE AND INDUSTRY DIRECTORATE-GENERAL. High-level round table on the future of the european steel industry recommendations. COM 121 (2013).

[5] http://de.statistika.com.

[6] EUROPEAN COMMISION, COMMUNICATION FROM THE COMMISSION TO THE PARLIAMENT, THE COUNCIL, THE EUROPEAN ECONOMIC AND SOCIAL COMMITTEE AND THE COMMITTEE OF REGIONS. Action plan for a competitive and sustainable steel industry in europe. COM 407 (2013).

[7] OECD. OECD/DSTI/SU/SC 21 (2012).

[8] http://www.starcast.org.

[9] I. Steinbach, B. Böttger, J. Eiken, N. Warnken, S. G. Fries. J. Phase Equilib. Diff. 28 (2007) 101.

[10] H. J. Fecht. High Temperature Materials And Processes 27 (2014) 385.

[11] Y. Kawai, Y. Shiraishi. *Handbook of Pysico-chemical Properties at High Temperatures*. (The Iron and Steel Institute of Japan ISIJ, Osaka, Japan, 1988).

[12] K. C. Mills. *Recommended values of thermophysical properties for selected commercial alloys*. (Woodhead Publishing Ltd., Cambridge, 2002).

[13] T. Iida, R. Guthrie. *The Physical Properties of Liquid Metals*. (Clarendon Press, Oxford, 1993).

[14] G. Pottlacher. *High Temperature Thermophysical Properties of 22 Pure Metals*. (edition keiper, Graz, 2019).

[15] H. Peng, T. Voigtmann, G. Kolland, H. Kobatake, J. Brillo. Phys. Rev. in preparation B (2015).

[16] N. Eustathopoulos, B. Drevet. J. Cryst. Growth 371 (2013) 77.

[17] J. Brillo, I. Egry. Int. J. Thermophys. 24 (2003) 1155.

[18] J. Brillo, G. Lohöfer, F. Schmid-Hohagen, S. Schneider, I. Egry. Int. J. Materials and Product Technology 26 (2006) 247.

[19] P. F. Paradis, T. Ishikawa, G. W. Lee, D. Holland-Moritz, J. Brillo, W. K. Rhim, J. T. Okada. Mat. Sci. Eng. R76 (2014) 1.

[20] M. Shimoji. *Liquid Metals*. (Academic press, London, 1977).

[21] Y. Plevachuk, I. Egry, J. Brillo, D. Holland-Moritz, I. Kaban. Int. J. Mat. Res. 98 (2007) 107.

[22] F. Yang, T. Unruh, A. Meyer. Europhys. Lett. 107 (2014) 26001.

[23] I. Egry. Scripta Met. et Mat. 26 (1992) 1349.

[24] G. Kaptay. Z. Metallkd 96 (2005) 24.

[25] A. Einstein. *Investigation on the theory of the Brownian movement*. (Dover, New York, 1926).

[26] A. Einstein. Ann. Phys. 17 (1905) 549.

[27] H. Fukuyama, Y. Waseda. *High-Temperature Measurements of Materials* volume 11 of *Advances in Materials Research*. (Springer-Verlag, Berlin - Heidelberg - New York, 2009).

[28] I. Egry, A. Diefenbach, W. Piller. Int. J. Thermophys. 22 (2001) 569.

[29] C. Notthoff, H. Franz, M. Hanfland, D. M. Herlach, D. Holland-Moritz, W. Petry. Rev. Sci. Instr. 71 (2000) 3791.

[30] D. Herlach, D. Matson. *Materials Science, Solidifation of Containerless Undercooled Melts*. (Wiley-VCH, Weinheim, 2012).

[31] I. Egry, D. Herlach, M. Kolbe, L. Ratke, S. Reutzel, C. Perrin, D. Chatain. Adv. Eng. Mat. 5 (2003) 819.

[32] J. Brillo, A. I. Pommrich, A. Meyer. Phys. Rev. Lett. 107 (2011) 165902.

[33] Westinghouse Electric Corp. *Magnetic levitation and heating of conductive materials*. US Patent 2686864 (08/07/1954).
[34] P. R. Sahm, I. Egry, T. Volkmann. *Schmelze, Erstarrung, Grenzflächen*. (Friedrich Vieweg & Sohn, Braunschaweig, 1999).
[35] J. Jackson. *Classical Electrodynamics*. (Wiley, New York, 1967).
[36] P. R. Roney. In M. A. Cocca, editor, *Trans. Vacuum Met. Conference, A* Boston 1965. Vacumm Society.
[37] J. Brillo, I. Egry, I. Ho. Int. J. Thermophys. 27 (2006) 494.
[38] S. Krishnan, G. P. Hansen, R. H. Hauge, J. L. Margrave. High Temp. Sci. 29 (1990) 17.
[39] S. Krishnan, K. Yugawa, P. C. Nordine. Phys. Rev. B55 (1997) 8201.
[40] D. L. Cummings, D. A. Blackburn. J. Fluid Mech. 224 (1991) 395.
[41] S. Sauerland. *Messung der Oberflächenspannung an levitierten flüssigen Metalltropfen*. Ph.-D. thesis. (RWTH Aachen, Aachen, Germany, 1993).
[42] R. W. Hyers, G. Trapaga, B. Abedian. Met. Trans. B34 (2003) 29.
[43] A. D. Sneyd, H. K. Moffatt. J. Fluid Mech. 117 (1982) 45.
[44] S. R. Berry, R. W. Hyers, B. Abedian, L. M. Racz. Met. Trans. B31 (2000) 171.
[45] R. W. Hyers. Meas. Sci. Technol. 16 (2005) 394.
[46] J. Priede, G. Gerbeth. IEEE Trans. on Magnetics 36 (2000) 349.
[47] J. Priede, G. Gerbeth. IEEE Trans. on Magnetics 36 (2000) 354.
[48] S. Schneider. *Viskositäten unterkühlter Metallschmelzen*. Ph.-D. thesis. (RWTH Aachen, Aachen, Germany, 2002).
[49] R. P. Liu, T. Volkmann, D. M. Herlach. Acta Mat. 49 (2001) 439.
[50] P. F. Clancy, E. G. Lierke, R. Grossbach, W. M. Heide. Acta Astron. 7 (1980) 877.
[51] W. K. Rhim, M. Collender, M. T. Hyson, W. T. Simms, D. D. Elleman. Rev. Sci. Instr. 56 (1985) 56.
[52] W. K. Rhim, S. K. Chung, D. Barber, K. F. Man, G. Gutt, A. Rulison, R. E. Spjut. Rev. Sci. Instr. 64 (1993) 2961.
[53] T. Meister. *Aufbau und Regelung eines elektrostatischen Levitators*. Ph.-D. thesis, Fortschritt-Berichte VDI, Reihe 8. (RU-Bochum, Bochum, Germany, 2000).
[54] T. Kordel, D. Holland-Moritz, F. Yang, J. Peters, T. Unruh, T. Hansen, A. Meyer. Phys. Rev. B83 (2011) 104205.
[55] P. F. Paradis, T. Ishikawa, S. Yoda. Space Technol. 22 (2002) 81.
[56] A. D. Myshkis, V. G. Babskii, N. D. Kopachevskii, L. A. Slobozhanin, A. D. Tyuptsov. *Low-Gravity Fluid Mechanics*. (Springer, Berlin, Heidelberg, New York, Paris, Tokyo, 1986).
[57] P. F. Paradis, T. Ishikawa, J. Yu, S. Yoda. Rev. Sci. Instrum. 72 (2001) 2811.
[58] S. Sauerland, K. Eckler, I. Egry. J. Mat. Sci. Lett. 11 (1992) 330.
[59] P. F. Paradis, T. Ishikawa, S. Yoda. J. Mat. Sci. 36 (2001) 5125.
[60] P. F. Paradis, T. Ishikawa, S. Yoda. Int. J. Thermophys. 23 (2002) 555.
[61] J. Brillo, I. Egry. Z. Metallkd. 95 (2004) 8.
[62] Y. Sato, T. Nishizuka, T. Takamizawa, K. Sugisawa, T. Yamamura. In *Proceedings of the 16th European Conference on Thermophysical Properties* volume available on CD 58 London 2002.
[63] M. J. Assael, R. M. Banish, J. Brillo, I. Egry, R. Brooks, P. N. Quested, K. C. Mills, A. Nagashima, Y. Sato, W. A. Wakeham. J. Phys. Chem. Ref. Data 35 (2006) 285.
[64] Lord Rayleigh. Proc. Roy. Soc. 29 (1879) 71.
[65] I. Egry, L. Ratke, M. Kolbe, D. Chatain, S. Curiotto, L. Battezatti, E. Johnson, N. Pryds. J. Mater. Sci. 45 (2010) 1979.
[66] F. H. Busse. J. Fluid Mech. 142 (1984) 1.
[67] J. Brillo, G. Lauletta, L. Vaianella, E. Arato, D. Giuranno, R. Novakovic, E. Ricci. JJAP (2014).
[68] J. Brillo, I. Egry. J. Mat. Sci. 40 (2005) 2213.

[69] J. Schmitz, J. Brillo, I. Egry, R. Schmid-Fetzer. Int. J. Mat. Res. 100 (2009) 1529.
[70] S. Z. Beer edt. *Liquid Metals - Chemistry and Physics*. (Marcel Dekker Inc., New York, 1997).
[71] Team TEMPUS. Lecture Notes in Physics 464 (1996) 233.
[72] I. Egry. *Properties, Nucleation and Growth of Undercooled Liquid Metals: Results of the TEMPUS MSL-1 Mission*. J. Jpn. Microgravity Appl. 15, special issue: MSL-11 (1998) 215.
[73] T. Ishikawa, P. F. Paradis, J. T. Okada, Y. Watanabe. Meas. Sci. Technol. 23 (2012) 025305.
[74] S. Mukherjee, J. Schroers, Z. Thou, W. L. Johnson, W. K. Rhim. Acta. Mat. 52 (2004) 3689.
[75] W. K. Rhim, K. Ohsaka, P. F. Paradis, R. E. Spjut. Rev. Sci. Instr. 70 (1999) 2796.
[76] R.C. Bradshaw, M. E. Warren, J. R. Rogers, T. J. Rathz, A. K. Gangopadhyay, K. F. Kelton, R. W. Hyers. Annals of the New York Academy of Sciences 107 (2006) 63.
[77] H. Lamb. *Hydrodynamics, 6th edt*. (Cambridge University Press, Cambridge, 1932).
[78] S. Chandrasekhar. Proc. London Math. Soc. A135 (1959) 141.
[79] E. Becker, W. J. Hiller, T. A. Kowalewski. J. Fluid Mech. 258 (1994) 191.
[80] M. Kehr, W. Hoyer, I. Egry. Int. J. Thermophys. 28 (2007) 1017.
[81] R. Roscoe. Proc. Roy. Soc. 72 (1958) 576.
[82] R. Brooks, A. Day, R. Andon, L. Chapman, K. Mills, P. Quested. High Temp.-High Press. 33 (2001) 72.
[83] J. Kestin, G. F. Newel. Z. Angew. Math. Phys. 8 (1957) 433.
[84] D. A. Beckwith, G. F. Newell. Appl. Surf. Sci. 8 (1957) 450.
[85] W. Brockner, K. Torklep, H. A. Oye. Ber. Bursenges. Phys. Chem. 83 (1979) 1.
[86] M. Kehr. *Aufbau eines Hochtemperaturviskosimeters und Messung der Viskosität von Schmelzen des Systems Aluminium-Nickel*. Ph.-D. thesis. (TU-Chemnitz, Chemnitz, Germany, 2009).
[87] M. Schick, J. Brillo, I. Egry, B. Hallstedt. J. Mater. Sci. 47 (2012) 8145.
[88] C. Lüdecke, D. Lüdecke. *Thermodynamik - Physikalisch-chemische Grundlagen der Verfahrenstechnik*. (Springer-Verlag, Berlin - Heidelberg - New York, 2000).
[89] M. Watanabe, M. Adachi, T. Morishita, K. Higuchi, H. Kobatake, H. Fukuyama. Faraday Discuss. 136 (2007) 279.
[90] L. Vegard. Z. Phys. 5 (1921) 17.
[91] R. S. Schmid-Fetzer, J. Gröbner. Adv. Eng. Mat. 3 (2001) 947.
[92] M. J. Assael, I. J. Armyra, J. Brillo, S. V. Stankus, J. Wu, W. A. Wakeham. J. Phys. Chem. Ref. Data 41 (2012) 033101–1.
[93] M. J. Assael, A. E. Kalyva, K. Antoniadis, R. M. Banish, I. Egry, J. Wu, E. Kashnitz, W. A. Wakeham. J. Phys. Chem. Ref. Data 39 (2010) 033105–1.
[94] M. J. Assael, A. E. Kalyva, K. D. Antoniadis, R. M. Banish, I. Egry, J. Wu, E. Kaschnitz, W. A. Wakeham. High Temp.-High Press. 41 (2012) 161.
[95] P. F. Paradis, Ishikawa T, N. Koike. Gold Bulletin 41 (2008) 242.
[96] J. Brillo, I. Egry, J. Westphal. Int. J. Mat. Res. 99 (2008) 162.
[97] J. Schmitz, B. Hallstedt, J. Brillo, I. Egry, M. Schick. J. Mater. Sci. 47 (2012) 3706.
[98] E. Gebhardt, M. Becker, S. Dorner. Aluminium 31 (1955) 315.
[99] W. J. Coy, R. S. Mateer. Trans Amer. Soc. Metals 58 (1955) 99.
[100] E. S. Levin, G. D. Ayushina, P. V. Gel´d. High Temperature 6 (1968) 416418.
[101] S. A. Yatsenko, V. I. Kononenko, A. L. Sukhman. High Temperature 10 (1972) 55.
[102] P. M. Smith, J. W. Elmer, G. F. Gallegos. Scripta Mat. 40 (1981) 937.
[103] P. M. Nasch, S. G. Steinemann. Phys. Chem. Liq. 29 (1995) 43.
[104] J. Brillo, I. Egry, H. S. Giffard, A. Patti. Int. J. Thermophys. 25 (2004) 1881.
[105] A. Saito, S. Watanabe. Nipp. Kinz. Gakk. 35 (1971) 554.
[106] A. E. El-Mehairy, R. G. Ward. Trans. Met. Soc. AIME. 227 (1963) 1226.

[107] E. Gorges. *Bestimmung der Dichte und Oberflächenspannung von levitierten flüssigen Metallegierungen am Beispiel des Systems Kupfer-Nickel*. Ph.-D. thesis. (Rheinisch- Westfälische-Technische Hochschule, Aachen, Aachen, Germany, 1996).
[108] M. S. Bian, L. M. Ma, J. T. Wang. Acta. Metall. Sin. B90 (1986) 29.
[109] M. G. Frohberg, R. Weber. Arch. Eisenhüttenwes. 35 (1964) 877.
[110] J. A. Cahill, A. D. Kirshenbaum. J. Inorg. Nucl. Chem. 66 (1962) 1080.
[111] L. D. Lucas. Mem. Sci. Rev. Metall. 61 (1964) 1.
[112] M. Kucharski, P. Fima, P. Skrzyniarz, W. Przebinda-Stefanowa. Arch. Met. Mat. 51 (2006) 389.
[113] W. Krause, F. Sauerwald. Z. Anorg. Allg. Chem. 181 (1929) 347.
[114] S. V. Stankus, P. V. Tyagelsky, P. V. Russ. J. Engin. Thermophys. 2 (1992) 93.
[115] L. D. Lucas. Compt. Rend. 253 (1961) 2526.
[116] A. D. Kirshenbaum, J. A. Cahill. Trans Amer. Soc. Metals. 56 (1963) 281.
[117] L. Martin-Garin, M. Gomez, P. Bedon, P. Desre. J. Less Common Met. 41 (1975) 65.
[118] E. Gebhardt, S. Dorner. Z. Metallkd. 42 (1951) 353.
[119] P. Fima, N. Sobczak. Int. J. Thermophys. 31 (2010) 1165.
[120] M. Gomez, L. Martin-Garin, P. Bedon, P. Desre. Bull. Soc. Chim. Fr. 7-8 (1976) 1027.
[121] G. P. Khilya, Yu. N. Ivachshenko, V. N. Eremenko. Iz. Akad. Nauk. SSSR, Met. 6 (1975) 87.
[122] E. Gebhardt, J. Worwag. Z. Metallkd. 42 (1951) 358.
[123] H. Kobatake, J. Brillo. J. Mater. Sci. 48 (2013) 4934.
[124] S. K. Chung, D. B. Thiessen, W. K. Rhim. Rev. Sci. Instr. 67 (1996) 3175.
[125] T. Ishikawa, P. F. Paradis, Y. Saito. J. Jap. Inst. Metals. 68 (2004) 781.
[126] S. Y. Shiraishi, R. G. Ward. Can. Met. Quat. 3 (1964) 117.
[127] A. Sharan, T. Nagasaka, A. Cramb. Met. Trans. 25B (1994) 939.
[128] L. Fang, F. Xiao, Y. F. Wang, Z. N. Tao, K. Mukai. Mat. Sci. Eng. B132 (2006) 174.
[129] L. D. Lucas. Mem. Sci. Rev. Metall. 69 (1972) 479.
[130] L. D. Lucas. Compt. Rend. 250 (1960) 1850.
[131] Z. Morita, Y. Ogino, H. Kaito, A. Adachi. J. Jap. Inst. Metals. 34 (1970) 248.
[132] T. Saito, Y. Siraishi, Y. T. Sakuma. Trans. Iron. Steel. Inst. Japan 9 (1969) 118.
[133] T. Saito, M. Amatatsu, S. Watanabe. Bull. Res. Inst. of Min. Dres. Met., Tohoku Univ. 25 (1969) 67.
[134] J. Brillo, I. Egry, T. Matsushita. Int. J. Mat. Res. 97 (2006) 1526.
[135] S. Amore, S. Delsante, H. Kobatake, J. Brillo. J. Chem. Phys. 139 (2013) 064504.
[136] S. V. Stankus. Ph.-D. thesis. (Institute of Thermophysics, Novosibirsk, Novosibirsk, USSR, 1992).
[137] S. Watanabe. Trans. Jap. Inst. Met. 12 (1971) 17.
[138] E. S. Levin, G. D. Ayushina, V. K. Zavyalov. Trans. UPI-Sverdlovsk 186 (1970) 92.
[139] A. D. Kirshenbaum, J. A. Cahill. Trans. Metal. Soc. AIME 224 (1962) 816.
[140] S. Watanabe, Y. Tsu, K. Takano, Y. Shiraishi. J. Jap. Inst. Met. 45 (1981) 242.
[141] T. Ishikawa, P. Paradis. J. Electron. Mater. 34 (2005) 1526.
[142] P. F. Paradis, T. Ishikawa, S. Yoda. Adv. Space Res. 41 (2008) 2118.
[143] P. F. Paradis, W. K. Rhim. J. Chem. Thermodyn. 32 (2000) 123.
[144] T. Ishikawa, J. Okada, P. Paradis, Y. Watanabe. Jpn. J. Appl. Phys. 50 (2011) 11RD03.
[145] D. B. Miracle, J. D. Miller, O. N. Senkov, C. Woodward, M. D. Uchic, J. Tiley. Entropy 16 (2014) 494.
[146] L. Pauling. J. Amer. Chem. Soc. 69 (1947) 542.
[147] A. Bartsch, K. Rätzke, A. Meyer, F. Faupel. Phys. Rev. Lett. 104 (2010) 195901.
[148] J. P. Hansen, I. R. McDonald. *Theory of simple liquids*. (Academic Press, London, 1986).
[149] P.-F. Paradis, T. Ishikawa, S. Yoda. Appl. Phys. Lett. 86 (2005) 151901.

[150] J. D. Bernal. *Liquids: Structure, Properties, Solid Interactions*. (Elsevier, Amsterdam, London, New York, 1965).
[151] M. Adachi, M. Schick, J. Brillo, I. Egry, M. Watanabe. J. Mater. Sci. 45 (2010) 2002.
[152] D. V. Khantadze, N. I. Topuridze. Translated from Inzhenerno-Fizicheskii Zhurnal 33 (1977) 120.
[153] C. Lemaignan. Acta Met. 28 (1980) 1657.
[154] T. B. Massalski. *Binary Alloy Phase Diagram*. (ASM, Materials Park, Ohio, 1986).
[155] J. Brillo, I. Egry. *Phase Transformations in Multicomponent Melts*. (Wiley-VCH, Weinheim, 2008).
[156] J. Brillo, I. Egry. Jpn. J. Appl. Phys. 50 (2011) 11RD02.
[157] J. Brillo, R. Brooks, I. Egry, P. Quested. High Temp. - High Press. 37 (2008) 371.
[158] H. Kobatake, J. Schmitz, J. Brillo. J. Mater. Sci. 49 (2014) 3541.
[159] M. Schick, J. Brillo, I. Egry. Int. J. Cast. Met. Res. 22 (2009) 82.
[160] H. Kobatake, J. Brillo. J. Mater. Sci. 48 (2013) 6818.
[161] J. Brillo, I. Egry, T. Matsushita. Int. J. Thermophys. 27 (2006) 82.
[162] S. Amore, J. Horbach, I. Egry. J. Chem. Phys. 134 (2011) 044515.
[163] J. Brillo, A. Bytchkov, I. Egry, L. Hennet, G. Mathiak, I. Pozdnyakova, D. L. Price, D. Thiaudiere, D. Zanghi. J. Non-Cryst. Solids 352 (2006) 4008.
[164] N. Eustathopoulos, M. G. Nicholas, B. Drevet. *Wettability at High Temperatures*. (Pergamon Materials Series, New York, 1999).
[165] H. D. Dörfler. *Grenzflächen und kolloid-disperse Systeme*. (Springer, Berlin, 2001).
[166] P. A. Egelstaff. *An Introduction to the Liquid State*. (Clarendon Press, Oxford, 1994).
[167] E. Ricci, D. Giuranno, E. Arato, P. Costa. Mat. Sci. Eng. A495 (2008) 27.
[168] J. Zhu, K. Mukai. ISIJ International 38 (1998) 1039.
[169] Y. Su, Z. Li, K.C. Mills. J. Mat. Sci. 40 (2005) 2201.
[170] H. Fujii, T. Sato, S. Li, K. Nogi. Mat. Sci. Eng. A495 (2008) 296.
[171] J. Butler. Proc. Roy. Soc. A135 (1935) 348.
[172] J. Brillo, R. Schmid-Fetzer. J. Mater. Sci. 49 (2014) 3674.
[173] T. Turkdogan. *Physical Chemistry of High Temperature Technology*. (Academic Press, New York, 1980).
[174] G. Kaptay. In *Proceedings of microcad, section: materials science* 45 Miskolc 2002. University of Miskolc.
[175] T. Tanaka, T. Iida. steel research 65 (1994) 21.
[176] J. Brillo, Y. Plevachuk, I. Egry. J. Mater. Sci. 45 (2010) 5150.
[177] T. P. Hoar, D. A. Melford. Trans. Faraday Soc. 53 (1957) 315.
[178] O. Akinlade, F. Sommer. J. Alloys. Compd. 316 (2001) 226.
[179] G. Kaptay. Mat. Sci. Forum 473 (2005) 1.
[180] T. Tanaka, K. Hack, T. Iida, S. Hara. Z. Metallkd. 87 (1996) 380.
[181] P. Koukkari, R. Pajarre. Pure Appl. Chem. 83 (2011) 1243.
[182] W. D. Kaplan, D. Chatain, P. Wynblatt, W. C. Carter. J. Mater. Sci. 48 (2013) 5681.
[183] R. Defay, I. Prigorine. Trans Faraday Soc. 46 (1950) 199.
[184] J. W. Taylor. Acta Met. 4 (1956) 460.
[185] M. J. de Olivera, R. B. Griffiths. Surf. Sci. 71 (1978) 687.
[186] R. Pandit, M. Schick, M. Wortis. Phys. Rev. B26 (1982) 5112.
[187] P. Wynblatt, A. Saul, D. Chatain. Acta Mater. 46 (1998) 2337.
[188] C. Antion, D. Chatain. Surf. Sci. 601 (2007) 2232.
[189] P. Wynblatt, S. Curiotto, D. Chatain. Surf. Sci. 604 (2010) 1369.
[190] J. Brillo, D. Chatain, I. Egry. Int. J. Mat. Res. 100 (2009) 53.
[191] J. Schmitz, J. Brillo, I. Egry, R. Schmid-Fetzer. Int. J. Mat. Res. 100 (2009) 1529.

[192] F . Sommer. Z. Metallkd. 73 (1982) 72.
[193] I. Egry. J. Mat. Sci. 39 (2004) 6365.
[194] B. C. Allen. *Liquid Metals: Chemistry and Physics*. (Marcel Dekker, New York, 1972).
[195] G. Kaptay. Mat. Sci. Eng. A495 (2008) 19.
[196] R. Eichel, I. Egry. Z. Metallkd. 90 (1999) 372.
[197] J. M. Molina, R. Voytovych, E. Louis, N. Eustathopouls. Int. J. Adh. & Adh. 27 (2007) 394.
[198] F. Milot, V. Sarou-Kanian, J. C. Rifflet, B. Vinet. Mat. Sci. Eng. A495 (2008) 8.
[199] G. Kolland, J. Brillo. J. Mater. Sci, submitted (2014).
[200] L. Goumiri, J. C. Joud, P. Desre, J. M. Hicter. Surf. Sci. 83 (1979) 471.
[201] P. A. Pamies, C. G. Cordovilla, E. Louis. Scripta Met. 18 (1984) 869.
[202] P. Laty, J. C. Joud, P. Desre. Surf. Sci. 69 (1977) 508.
[203] C. Garcia-Cordovilla, E. Louis, A. Pamies. J. Mater. Sci. 21 (1986) 2787.
[204] L. Goumiri, J. C. Joud. Acta Met. 30 (1982) 1397.
[205] B. Keene. Int. Mater. Rev. 38 (1993) 157.
[206] S. Amore, J. Brillo, I. Egry, R. Novakovic. Appl. Surf. Sci. 257 (2011) 7739.
[207] R. F. Brooks, K. C. Mills, I. Egry, D. Grant, S. Seetharaman, B. Vinet. NPL Report CMMTD (1998) 136.
[208] T. Hibiya, K. Morohoshi, S. Ozawa. J. Mater. Sci. 45 (2010) 1986.
[209] I. Egry, S. Sauerland. High Temp.- High Press. 26 (1994) 217.
[210] E. Ricci, R. Novakovic. Gold Bulletin 34 (2001) 41.
[211] I. Egry, G. Lohöfer, G. Jacobs. Phys. Rev. Lett. 75 (1995) 4043.
[212] P. Shen, H. Fujii, T. Matsumoto, K. Nogi. J. Mat. Sci. 40 (2005) 2329.
[213] R. Novakovic, E. Ricci, D. Giuranno, A. Passerone. Surf. Sci. 576 (2005) 175.
[214] J. Lee, A. Kiyose, S. Nakatsuka, M. Nakamoto, T. Tanaka. ISIJ International 44 (2004) 1793.
[215] J. Lee, W. Shimoda, T. Tanaka. Mater. Trans. 45 (2004) 2864.
[216] K. C. Mills, Y. C. Su. Int. Mat. Rev. 51 (2006) 329.
[217] M. Kucharski, P. Fima. Monatshefte f. Chemie 136 (2005) 1841.
[218] J. Lee, M. Nakamoto, T. Tanaka. J. Mat. Sci. 40 (2005) 2167.
[219] Y. Kim, J. Lim, J. Choe, J. Lee. Met. Mat. Trans. B (2014 DOI: 10.1007/s11663-014-0033-z).
[220] P.-F. Paradis, T. Ishikawa, S. Yoda. Int. J. Thermophys. 23 (2002) 825.
[221] B. Allen. Trans. Metall. Soc. AIME 227 (1963) 1175.
[222] K. Man. Int. J. Thermophys. 2 (2000) 793.
[223] S. Ozawa, S. Suzuki, T. Hibiya, H. Fukuyama. J. App. Phys. 109 (2011) 014902.
[224] J. Tille, J. Kelly. Brit. J. Appl. Phys. 14 (1963) 717.
[225] V. Arkhipkin, A. Agaev, G. Grigorev, V. Kostikov. Ind. Lab. 39 (1973) 1340.
[226] A. Peterson, H. Kedesdy, P. Keck, E. Schwartz. J. Appl. Phys. 29 (1958) 213.
[227] V. Elyutin. Iz. AN. SSSR. OTN 4 (1956) 129.
[228] B. Vinet, L. Magnusson, H. Fredriksson, P. Desre. J. Colloid Interface Sci. 255 (2002) 363.
[229] G. Kuppermann. *The determination of the surface tension with the help of the levitierten reciprocating drop under terrestrial conditions and in space*. Ph.-D. thesis. (University of Technology Berlin, Berlin, 2000).
[230] R. Hultgren, P. D. Desai, D. T. Hawkins, M. Gleiser, K. K. Kelly, D. D. Wagman. *Selected Values of Thermodynamic Properties of the Elements*. (American Society for Metals, Metals Park, Ohio, USA, 1973).
[231] R. Schmid-Fetzer. *personal communication* 121 (2014).
[232] I. Egry, J. Brillo, D. Holland-Moritz, Y. Plevachuk. Mater. Sci. Eng. A495 (2008) 14.
[233] D. Kim, R. Abbaschian. J. Phase Equilibria 21 (2000) 25.
[234] G. Wilde. *Makroskopische Eigenschaften unterkühlter metallischer Schmelzen*. Ph.-D. thesis. (Technische Universität Berlin, DLR, Berlin, Germany, 1997).

[235] C. Servant, B. Sundmann, O. Lyon. Calphad 25 (2001) 79.
[236] S. Gruner, M. Köhler, W. Hoyer. J. Alloys Compd. 482 (2009) 335.
[237] S. Amore, E. Ricci, T. Lanata, R. Novakovic. J. Alloys Compd. 452 (2008) 161.
[238] Z. Moser, W. Gasior, J. Pstrus. J. Electr. Mat. 30 (2001) 1104.
[239] J. Brillo, I. Egry, T. Matsushita. Z. Metallkd. 97 (2006) 28.
[240] J. Brillo, I. Egry. Int. J. Thermophys. 28 (2007) 1004.
[241] I. Egry, J. Brillo, T. Matsushita. Mat. Sci. Eng. A460 (2005) 413.
[242] V. T. Witusiewicz, U. Hecht, S. G. Fries, S. Rex. J. Alloys Compd. 385 (2004) 133.
[243] V. T. Witusiewicz, U. Hecht, S. G. Fries, S. Rex. J. Alloys Compd. 387 (2004) 217.
[244] J. P. Boon, S. Yip. *Molecular Hydrodynamics*. (Dover Publications, New York, 1980).
[245] K. Binder, J. Horbach, W. Kob, W. Paul, F. Varnik. J. Phys.: Condens. Matter 16 (2004) 429.
[246] M. Born, H. S. Green. Proc. Roy. Soc. A190 (1947) 455.
[247] W. Götze. *Liquids, Freezing and the Glass Trasition*. In *Proceedings of the Les Houches Summer School of theoretical Physics, Session LI edited by J.-P. Hansen, D. Levesque, and J. Zinn-Justin* 287 Amsterdam 1989. North-Holland.
[248] J. Brillo, R. Brooks, I. Egry, P. Quested. Int. J. Mat. Res. 98 (2007) 457.
[249] I. Budai, M. Z. Benkö, G. Kaptay. Mater. Sci. Forum 309 (2005) 473.
[250] E. A. Moelwyn-Hughes. *Physical Cemistry*. (Pergamon Press, Oxford, UK, 1961).
[251] L. Y. Kozlov, L. M. Romanov, N. N. Petrov. Izv. vysch. uch. zav. Chernaya Metallurgiya russ. 3 (1983) 7.
[252] M. Hirai. ISIJ International 33 (1993) 251.
[253] S. Seetharaman, D. Sichen. Metall. Mater. Trans. B25 (1994) 589.
[254] G. Kaptay. In *Proc. of microCAD 2003 Conference, Section Metallurgy* 23. Univ. of Miskolc 2003.
[255] R. J. L. Andon, L. Chapman, A. P. Day, K. C. Mills. NPL Report A (CMMT) 167.
[256] A. Yakymovych, Y. Plevachuk, S. Mudry, J. Brillo, H. Kobatake, H. Ipser. Phys. Chem. of Liquids http://dx.doi.org/10.1080/00319104.2013.876639 (2014).
[257] H. Kimura, M. Watanabe, K. Izumi, T. Hibiya, D. Holland-Moritz D. Holland-Moritz, T. Schenk, K. R. Bauchspiess, S. Schneider, I. Egry, K. Funakoshi, M. Hanfland. Appl. Phys. Lett. 78 (2014) 604.
[258] Y. Satao, K. Sugisawa, D. Aoki, T. Yamamura. Meas. Sci. Technol. 16 (2005) 363.
[259] H. Walsdorfer, I. Arpshofen, B. Predel. Z. Metallkd. 79 (1988) 503.
[260] M. Maret, T. Pomme, A. Pasturel. Phys. Rev. B42 (1990) 1598.
[261] S. K. Das, J. Horbach, M. M. Koza, S. M. Chatoth, A. Meyer. Appl. Phys. Lett. 86 (2005) 011918.
[262] R. N. Singh, F. Sommer. Monatsh. Chem. 143 (2012) 1235.
[263] I. Egry. Scripta Met. et Mat. 28 (1993) 1273.
[264] M. Jiang, J. Sato, I. Ohnuma, R. Kainuma, K. Ishida. Calphad 28 (2004) 213.
[265] L. Ratke, P. W. Voorhees. *Engineering Materials, Growth and Coarsening*. (Springer, Berlin, 2002).
[266] K. Binder, W. Kob. *Glassy Materials and Disorderd Solids, An Introduction to Their Statistical Mechanics*. (World Scientific Publishing Co. Pte. Ltd., Singapore, 2005).
[267] J. Brillo, S. M. Chathoth, M. M. Koza, A. Meyer. Appl. Phys. Lett. 93 (2008) 121905.
[268] A. Meyer. Phys. Rev. B81 (2010) 012102.
[269] B. Zhang, A. Griesche, A. Meyer. Phys. Rev. Lett. 104 (2010) 035902.
[270] S. K. Das, J. Horbach, T. Voigtmann. Phys. Rev. B78 (2008) 064208.
[271] X. J. Han, H. R. Schober. Phys. Rev. B83 (2011) 224201.
[272] F. Affouard, M. Descamps, L. C. Valdes, J. Habasaki, P. Bordat, K. L. Nagi. J. Chem. Phys. 131 (2009) 104510.

[273] P. Bordat, F. Affouard, M. Descamps, F. Müller-Plathe. J. Phys.: Condens. Matter 15 (2003) 5397.
[274] W. Kob, H. C. Andersen. Phys. Rev. E51 (1995) 4626.
[275] S. K. Kumar, G. Szamel, J. F. Douglas. J. Chem. Phys. 124 (2006) 214501.
[276] S. R. Becker, P. H. Poole, F. W. Starr. Phys. Rev. Lett. 97 (2006) 055901.
[277] J. Horbach, W. Kob. Phys. Rev. B60 (1999) 3169.
[278] A. Meyer, W. Petry, M. Koza, M. P. Macht. Appl. Phys. Lett. 83 (2003) 3894.
[279] L. Wan, X. Bian, J. Liu. Phys. Lett. A326 (2004) 429.
[280] R. F. Brooks, A. P. Day, R. J. L. Andon, L. A. Chapman, K. C. Mills, P. N. Quested. High Temp.-High Press. 33 (2001) 72.
[281] A. Meyer. Phys. Rev. B86 (2002) 011918.
[282] S. K. Das, J. Horbach, M. M. Koza, S. M. Chathoth, A. Meyer. Appl. Phys. Lett. 83 (2003) 3894.
[283] T. Voigtmann, A. Meyer, D. Holland-Moritz, S. Stüber, T. Hansen, T. Unruh. Europhys. Lett. 82 (2008) 66001.
[284] T. Ishikawa, P. F. Paradis, N. Koike, Y. Watanabe. Rev. Sci. Instr. 80 (2009) 013906.
[285] W. Sutherland. Phil. Mag. 9 (1905) 781.
[286] I. Egry J. Schmitz, J. Brillo. Eur. Phys. J. special Topics 223 (2014) 469.
[287] E. Schleip, D. M. Herlach, B. Feuerbacher. Europhys. Lett. 11 (1990) 751.
[288] D. M. Herlach, B. Feuerbacher, E. Schleip. Mat. Sci. Eng. A133 (1990) 795.
[289] K. Landry, S. Kalogeropoulou, N. Eustathopoulos. Mat. Sci. Eng. A254 (1998) 99.
[290] B. Drevet, K. Landry, P. Vikner, N. Eustathopoulos. Scripta Mat. 35 (1996) 1265.
[291] A. Glinter, G. Mendoza-Suarez, R. A. L. Drew. Mat. Sci. Eng. A495 (2008) 147.
[292] P. Shen, H. Fujii, T. Matsumoto, K. Nogi. Acta Mat. 51 (2003) 4897.
[293] J. Schmitz. *Untersuchung der Anisotropie im Benetzungsverhalten flüssiger Al-Cu Legierungen auf einkristallinen orientierten Al_2O_3-Substraten*. Ph.-D. thesis. (RWTH-Aachen, Aachen, Germany, 2011).
[294] J. Schmitz, I. Egry, J. Brillo. J. Mater. Sci. 49 (2014) 2286.
[295] J. Schmitz, J. Brillo, I. Egry. J. Mater. Sci. 45 (2010) 2144.
[296] K. Kitayama, A. Glaeser. J. Am. Ceram. Soc. 85 (2002) 611.
[297] D. Chatain. Annu. Rev. Mater. Res. 38 (2008) 45.
[298] I. Kaban, M. Köhler, L. Ratke, W. Hoyer, N. Mattern, J. Eckert, A. L. Greer. Acta Mat. 59 (2011) 6880.
[299] I. Kaban, S. Curiotto, D. Chatain, W. Hoyer. Acta Mat. 58 (2010) 3406.
[300] I. Kaban, J. Gröbner, W. Hoyer, R. Schmid-Fetzer. J. Mater. Sci. 45 (2010) 2030.
[301] G. Kaptay. Acta Mater. 60 (2012) 6804.
[302] S. S. Kim, T. H. Sanders. Modelling Simul. Mater. Sci. Eng. 14 (2006) 1181.
[303] W. Cao, S. Chen, F. Zhang, K. Wu, Y. Yang, Y. Chang, R. Schmid-Fetzer, W. A. Oates. Calphad 33 (2009) 328.
[304] D. Mirkovic, J. Gröbner, I. Kaban, W. Hoyer, R. Schmid-Fetzer. Int. J. Mat. Res. 100 (2009) 176.
[305] H. Wallentowitz, D. Neunzig. *Reduzierung der Schadstoffbelastung*. (RWTH Aachen, Aachen, 2000).
[306] M. Adeogun. *Smart Materials*. Viewpoints, SRI Business Intelligence (2003).
[307] http://www.vdo.com/press/pictures/powertrain/sv_pp_common_diesel_rail.hthm.
[308] J. Brillo, H. Behnken, A. Drevermann, Y. Plevachuk, E. Pagounis, V. Sklyarchuk, L. Sturz. Int. J. Heat and Mass Trans. 54 (2011) 4167.
[309] G. Höhne, W. Hemminger, H. J. Flammersheim. *Differential Scanning Calorimetry*. (Springer, Berlin, 1996).

[310] W. F. Hemminger, H. K. Cammenga. *Methoden der Thermischen Analyse*. (Springer, Berlin, 1989).
[311] S. J. Qu, A. H. Feng, L. Geng, Z. Y. Ma, J. C. Han. Scripta Mater. 56 (2007) 951.
[312] H. Shibata, H. Ohta, Y. Waseda. *High Temperature Measurements of Materials*. (Springer, Berlin, 2009).
[313] H. Sagara Y. Maeda, R. P. Tye, M. Masuda, N. Ohta, Y. Waseda. Int. J. Thermophys. 17 (1996) 253.
[314] V. Sklyarchuk, Y. Plevachuk. Meas. Sci. Technol. 16 (2005) 467.
[315] C. De Micco, C. M. Aldao. Eur. J. Phys. 24 (2003) 81.
[316] Y. Tsu, K. Takano, S. Watanabe Y. Shiraishi. Daigaku, Senko, Seiren Kenkyusho, Iho 34 (1987) 131.
[317] E. Mathiak, W. Nistler, W. Waschowski, L. Koester. Z. Metallkd. 74 (1983) 793.
[318] J. L. Murray, H. Okamoto, T. B. Massalski. Bull. Alloy Phase Diagr. 8 (1987) 20.
[319] H. Okamoto. *Desk Handbook Phase Diagram for Binary Alloys*. (ASM International, Materials Park, Ohio, 2000).
[320] M. Hillert, C. Qiu. Met. Mat. Trans. A21 (1990) 1673.
[321] I. Ansara, A. T. Dinsdale, M. H. Rund, editors. *COST-507; Thermochemical Database for Light Metal Alloys*. (European Communities, Luxembourg, 1998).
[322] M. Li, C. Li, F. Wang, D. Luo, W. Zhang. J. Alloys Compd. 385 (2004) 199.
[323] C. Y. Hea, Y. Du, H. L. Chen, H. Xu. Calphad 33 (2009) 200.
[324] B. Sundman, I. Ohnuma, N. Dupin, U. R. Kattner, S. G. Fries. Acta Mater. 57 (2009) 2896.
[325] W. Huang, Y. A. Chang. Intermetallics 7 (1999) 625.
[326] A. Yakymovych, S. Fürtauer, A. Elmahfoudi, H. Ipser, H. Flandorfer. J. Chem Thermodyn. 74 (2014) 269.
[327] M. Bamberger, A. Munitz, L. Kaufman, R. Abbaschian. Calphad 26 (2002) 375.
[328] S. Curiotto, L. Battezzati, E. Johnson, N. Pryds. Acta Mat. 55 (2007) 6642.
[329] J. Wang, C. Liu, C. Leinenbach, U. E. Klotz, P. J. Uggowitzer, J. F. Loffler. Calphad 35 (2011) 82.
[330] J. Mietinen. Calphad 23 (1999) 231.

Index